COMPUTER-AIDED DESIGN AND SIMULATION OF CURRENT SENSITIVE ELECTROMAGNETIC ACTUATORS

ERPING LI

A thesis submitted in partial fulfilment of the
requirements of the Council for National Academic Awards
for the Degree of **Doctor of Philosophy**

December 1991

School of Engineering Information Technology
Sheffield City Polytechnic in the collaboration with G H Scholes, Wylex Limited

Acknowledgements

I would like to thank the following people for their guidance and assistance in my work.

Professor P M McEwan, Director of School of Engineering Information Technology, Sheffield City Polytechnic, without whom this would never have been finished. I am indebted to him for his guidance and enthusiastic supervision. Dr Bob Green for his advice and technical support.

Professor Chen Degui and Professor Wang Jimei of Xi'an Jiaotong University for their advice and encouragement from thousands of miles away.

My industrial sponsor, Wylex Ltd, Manchester, and especially Alan Kidd, the Technical Director, for his support, experimental facilities and words of encouragement during the investigation.

Mr John Burgan and staff of the electrical engineering laboratories for providing valuable technical assistance, especially John for his friendly help.

Everyone else who fed me, argued with me and pointed out the error of my ways, Ian Robinson, Cliff Laycock, Tony Bell

Finally, a special word of thanks to my wife,Sue Lin,and boy Jun for their patience and encouragement.

Contents

List of Figures

FIGURES

Chapter 3

FIGURES

Chapter 4

Chapter 5

Chapter 6

Chapter 7

List of Tables

List of Principal Symbols and Abbreviations

AT	Ampere Turns
B	Magnetic flux density
Br	Permanent magnet remanent flux density
CSEMA	Current Sensitive ElectroMagnetic Actuator
CSSMA	Current Sensitive Stepper Motor Actuator
Fm	Magnetic force
g	Length of airgap
H	Magnetizing field strength
Hc	Magnetic coercive force
i	Current
MMF	MagnetoMotive Force
PM	Permanent Magnet
r_1	Radius
R, R_1	Reluctance
RCD	Residual Current Device
SM	Stepper Motor
Tm	Magnetic torque
μ_0	Permeability of free space
μ_r	Relative permeability
φ	Magnetic flux

Abstract

The thesis presents the development of CAD techniques in the design and simulation of electromagnetic actuators. It also demonstrates the application of analytical and finite element CAD techniques on the behaviour, evaluation and optimal design of current sensitive electromagnetic actuators.

Both clapper and stepper motor actuators are investigated based on the magnetic saturation and polarisation principles. An analytical method is outlined and applied in the design of the actuators and their evaluation. The two scalar potential approach is investigated in 3D nonlinear magneto-static finite element computation which is used in the simulation and prediction of the performance of the actuators. A 2D nonlinear transient electromagnetic finite element method, taking account of the 3rd dimension, is developed and the actuators for time-varying current control is evaluated. A decoupled 3D finite element integral method is postulated to predict the dynamic transient response characteristics of the actuators.

Analysis is used to examine the relationships of the actuator sensitivity to manufacturing tolerances which cover a wide range of design and control variables. The actuator sensitivity is quantified in terms of critical design factors and a range of airgap settings. The actuators are optimised and quantitative comparisons between the predictions and the test results for the clapper actuators are discussed.

The deficiencies of the clapper type actuators are examined. A novel approach electromagnetic actuator is proposed to obviate these deficiencies. This actuator is based on the combination of the principles of magnetic saturation and the stepper motor. A disc magnet stepper motor is investigated and employed in the actuator. The dependency of the actuator performance on specific key factors is obtained and optimised. A technique is developed to reduce detent torque to a low level.

The optimal design of the stepper motor actuator is presented, together with the evaluation of its static and dynamic characteristics. Finally, an actuator combining the stepper motor and clapper actuator is postulated and evaluated.

Aims

The aims of the work presented here are to

•explore the use of Computer Aided Design techniques in the design and analysis of high sensitivity current-operated electromagnetic actuators, to optimise actuators and improve the sensitivity

•develop design and evaluation approaches capable of solving the magnetic actuators transient dynamic performance and practical engineering design problems

•investigate the actuators dependence on the key design parameters in order to determine the range of manufacturing tolerances and to optimise the actuator

•develop a novel magnetic actuator capable of operating with the highest possible sensitivity to current, diminishing the need for very finely machined surfaces and obviating the separate use of the toroid transformer. This also involves developing the analytical techniques.

Chapter 1

Introduction

1.1 Review of Current Sensitive Electromagnetic Actuators

In many applications magnetic actuators are required to possess high sensitivity to current flow and also to provide sufficient tripping force to ensure reliable functioning. They must, for example, be able to trip a residual current circuit breaker reliably[3,4]. Such a magnetic actuator is referred to as a current sensitive electromagnetic actuator(CSEMA).Typical application areas of the current sensitive magnetic actuators are processcontrol, small current detection and electrical protection. Important criteria[4,7] when selecting an actuator include torque level, travel displacement, sensitivity to input current, dynamic response and the factors associated with cost reliability and environmental considerations.

The current sensitive magnetic actuator is one of the most common magnetic actuators which may be classified according to the sensitivity to the input, and according to the construction. The conventional magnetic actuators can be divided into two main categories from their construction, (i) direct-limited motion actuators[4,5,9,10,13-16];(ii) actuator based electric motors[7,8,70]. Actuators based on all sorts of force-producing principles are

designed and widely used in the automobile industry[6,37], hydraulic,pneumatic[8], vibration and switching[9,30,55,59] for an industrial control application.

One of the most popular applications of the current sensitive electromagnetic actuator is in residual current devices(RCD)[3,4,47] which are widely used in domestic and small commercial installations to protect humans and installations against electric shock and the hazards caused by overcurrents and excessive leakage currents. An RCD incorporates a current sensor, which may be either electronic or a precision electromagnetic actuator, to monitor the level of differential current flow, in order to operate an electromechanical release means to actuate a RCD circuit breaker when the current exceeds a set level. In so doing the device isolates the harmful electric circuits. The RCD provides a valuable contribution to the safety of installations and in preventing ventricular fibrillation occurring in humans and other harmful physiological effects[12].

Some overcurrent conditions can be reliably interrupted by a fuse or MCB as found in a typical installation to clear the faults within the safe limits of conductor heating[3,10]. For other overcurrent conditions a fault must exist and currents must flow through an extraneous path, usually to earth. The level of differential current in the system to attain safe circuit-breaking conditions generally is extremely small, typically 10 to 30mA, with a balanced current of the order of 100Amps[4,12]. RCD devices have to be able to detect this level of imbalance and to break the faulted electric circuit before permanent damage occurs to the circuit.

Conventional RCD devices generally comprise a current monitoring system including differential transformer and electromechanical release means, such as an actuator, together with a contact system involving contacts and

arc quenching system as shown in the schematic diagram figure 1.1. The current monitoring system is designed to detect the difference between the current flowing in the live conductor and the current returning in the neutral conductor. When the currents are in balance then the current monitoring system or device remains inoperative. Once an imbalance current occurs and exceeds a preset value, the electromechanical means will be released and the RCD contacts will open to clear the unbalanced fault condition. The contact system actuates a mechanical release of the main circuit breaker to break the electric circuit.

The current monitoring system or device of the RCD comprises a toroidal core with the primary winding formed by the main circuit conductors and a secondary winding. By appropriate selection of core, primary and secondary conductor turns, it is possible to detect a differential current less than10mA which produces a signal to trip an electromechanical release means, which is generally a form of current sensitive electromagnetic actuator. Its operating principle is generally described as having a release lever which is normally held on the keeper by the magnetic force produced by a permanent magnet against the opposing force of a spring. When the current from the current monitoring system exceeds a predetermined level, it causes the flux to be diverted other than through the release lever which is then released by the opposite spring. This movement is utilized to operate a latch to release a switch mechanism thereby opening the contacts of the residual current-operated circuit breakers.

Early actuators were all magnetic polarized types used in RCD[17]. The design of this type of actuator used the principle of electromagnetic polarisation, the operation of which introduces a delay up to 10ms for one half cycle of 50Hz current when an alternating current fault condition occurs. It

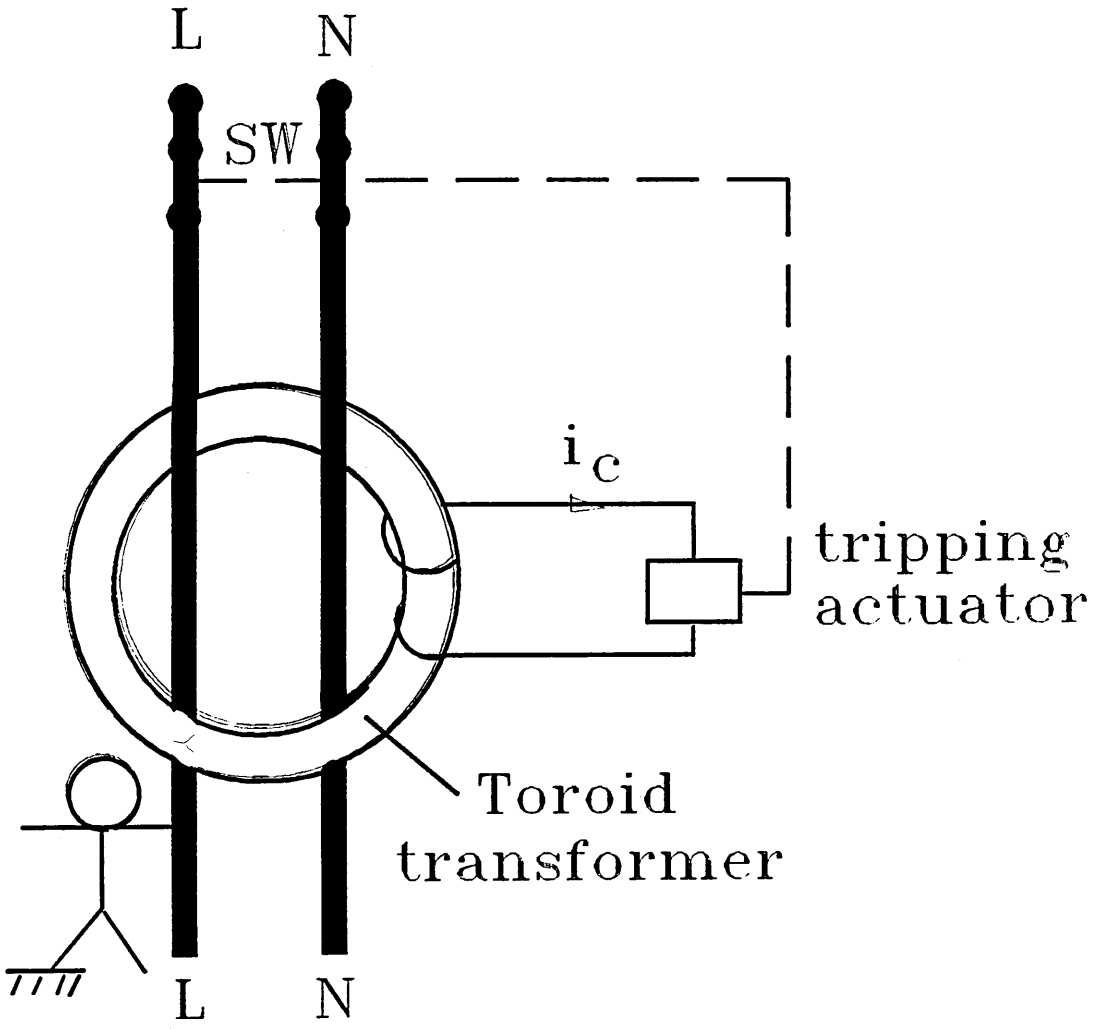

Figure 1.1 Application of CSEM actuator in residual current operated device

can not be used in a direct current system. To overcome the delay defect the modern saturation electromagnetic actuator was developed, which could immediately respond to a.c. current systems without delay[14][15][16]. The designs of these actuators were based on the principle of magnetic saturation. The armature of this type actuator normally is held close to the yoke by the force produced from the permanent magnet. This type actuator has one shunt path as before but the other two paths have constricted regions before combining into the armature. One of the constricted regions is saturated by the exciting flux and the other subtracted. This causes the flux to be diverted into the shunt path, both constrictions causing reduction of the total armature flux until the spring can pull it away. An initial design of saturation actuator had many components due to requiring a number of laminations also the permanent magnet needs to be well-finished[14]. The assembly and clearing surface were expensive and difficult to produce. For these reasons the improved actuator consisted of only one single plane contact surface without pole-pieces and two parallel ferromagnetic laminations[15]. These improvements made it easier to manufacture and reduced the cost, however, the permanent magnet and the armature were still in one plane, which had the disadvantage of lessening the pulling force the wider the armature opening. Therefore, the permanent magnet was mounted on the end of the yoke, not in the same plane as the armature[16]. The force of attraction and current sensitivity of this actuator can be more easily adjusted and the pulling force of the spring is kept constant.

In most types of current sensitive magnetic actuators, the performance is critically dependent upon the size of airgap between its armature and keeper and especially upon the quality of the facing machined surfaces[4]. Generally the airgaps are very small(less than 0.5μm) and the machined

facings are very difficult and expensive. These requirements greatly add to the devices manufacturing cost and to the need for very careful inspection, setting up and final testing procedures. The sensitivity of the actuator is not only critically dependent upon the airgap, but also significantly upon the leakage shunt reluctance, the size of constricted slot, magnetic material properties, the coil window, control variables and the size of the magnetic circuit etc. These design parameters are also dependent on each other. It is desirable to obtain the precise dependency of the actuator sensitivity on each critical design parameter and the optimal value for each parameter.

During the design-development process, it has been found that the clapper type actuator has a number of disadvantages[4], these are: (a) the use of a toroid which isolates the actuator winding, (b) the winding process for toroidal components is difficult and expensive and consequently the transfer of energy between the two components is inefficient, (c) in conventional RCDs where a wound toroid drives an electro mechanical release, the current monitoring device is inherently sensitive only to alternating currents and special measures have to be taken to produce a satisfactory response to any form of direct current such as smooth d.c. or pulsating D.C. obtained from rectification of alternating current, (d) this type of actuator requires a very finely-finished machine surface, which is very expensive to produce as described earlier. The general object here is to develop a new type of actuator which possesses the highest possible tripping sensitivity and overcomes the disadvantages of the clapper type mentioned above.

1.2 Review of CAD Design of Electromagnetic Devices

1.2.1 General Review

In recent years electrical industrial designs have made extensive use of CAD techniques to design such as nuclear devices, electronic devices, electrical machines, electrical circuit breakers , etc. Computer aided analysis (CAA) or design(CAD) for electromagnetic devices is a process based on electromagnetic field modelling and computing(EMC) to analyse and modify the magnetic circuit until the required performance specifications are satisfied. The use of EMC CAD techniques have resulted in many improvements in electromagnetic code design. The early 1960's saw the research of EMC with the arrival of the large batch computers. The early 1970's saw vigorous developments in electromagnetic fields computation, especially for analysing the static models. During this period the finite element method had been introduced into the electromagnetic field computation[18][19], which was to prove in the succeeding years to be of major importance. The reliable algorithms had been constructed to solve the three dimensional problems, particularly with the successful use of integral methods [18]. Furthermore, the finite difference method was successfully used in the solution of 3D problems associated with turbo-generator design[19]. In the early 70's the use of interactive graphics techniques was expanded especially the first interactive code for magnet design ,GFUN [20]. This work assisted , for example, designers to represent complex magnetic circuits and to expand its applications in engineering designs.

Since 1976 many significant developments in electromagnetic computation have been made, these include the introduction of preconditioned conjugate

gradient methods in equation solving [21], two dimensional non-linear time dependent solutions, fully automatic mesh generation, at least for two dimensional geometry[22,23,24], and the tentative beginnings of a posterior errors analysis. In addition reliable packages for three dimensional non-linear static fields were realized in the magnet design [20,27],which gave electromagnetic devices design in particular a big push forward.

However, there are still many problems for which present techniques are either inadequately inefficient at best or as yet non existent. For example non linear 3D time dependent fields including moving systems are still to be solved[20]. Computing fully coupled systems, consisting of mechanical, thermal and electrical components, is relatively easy to formulate using finite element technology but has yet to be realized. Indeed one of the strengths of this method is the elegant formalism which allows such couplings to be introduced. However these systems usually lead to prohibitively large matrices which for serial computing is unlikely to be cost effective, until computing speeds and costs significantly change.

1.2.2 EMC-CAD Techniques in electromagnetic devices

The electromagnetic device designers are fascinated with the CAD techniques now being used. In the 1980's much activity in the application of EMC-CAD to circuit breaker design concerned with electromagnetic actuators, electric contacts and arc quenching chutes was seen[29,32,33,34]. There was also a rapid expansion in circuit breaker CAD design. During this period, the lumped magnetic circuit method was used to analyse the static and dynamic performance of an electromagnet, which was successfully achieved using computers and mathematic models[29], however this method can not model more complicated problems.

The finite element technique has been successfully applied to design of electromagnetic actuators associated with the E type magnetic actuator used in low voltage circuit breaker to trip the latch mechanism, which evaluated the magnet static performance[27,28,30] .

Coupled two dimensional finite element and mechanical systems were successfully used for modelling in simple non-linear electromagnetic actuators in order to evaluate the static and dynamic characteristics [29,30,50,59,60]. There was also vigorous activity in the construction of algorithms for solving the electromagnetic field in the switching arc. In particular the two dimensional finite element method was used to calculate the magnetic field within arc chutes and contact arms and the interactive force between the two contact arms, in which the contact arms were simulated as infinite[25]. At this time electromagnetic computation was also used to analyse the effects of the electromechanical system on the switching arc behaviour[32,34,35].

Some magnetic actuators can be modelled in 2D or axisymmetrical fields, which can be solved either for static or for transient dynamic performance. Some magnetic actuators may be neither modelled in 2D nor in axisymmetrical field problems if the electromagnetic and mechanical system are complex such as for this clapper type actuator used in RCD devices[4], where these designs require good prediction accuracy. Some problems in the actuators make prediction and design by experiment impossible , for example, the measurement of flux distributions in the airgaps and the magnetic saturation in slot, the dependency of the sensitivity on the leakage flux and airgap flux as well as magnetic force associated with the size of airgap etc. Even if the experimental approach was possible, it would be very expensive, i.e. to find the manufacture tolerances,etc. The validity of the sophisticated

analytical approach is degraded. The main causes of this are (a) heavy saturation and very low flux density at the same time within a smaller piece of slot; (b) non-symmetric electromagnetic field existing in a symmetric geometry; (c) larger nonuniformities of flux in the leakage path.

Hence, full 3D electromagnetic field predictions are required to determine the force and flux distributions. The design requirements for the complicated problems both in magnetic and geometric structures make the use of three dimensional nonlinear numerical technique essential. A valid 3D finite element package[45] with the aid of experiment was used to analyse the design of a current sensitive actuator and optimise the design. A decoupled 3D-FE combined with the mechanical systems as well as the electric circuit technique was developed and used to evaluate the dynamic performance of the actuator, in order to design a high quality electromagnetic device, and consequently reduce the design and manufacture cost.

1.3 The Problems and Main Work

As is described earlier, the current sensitive electromagnetic actuators are required to operate with great precision with the highest possible tripping sensitivity at very low current (less than 30mA) and also to provide sufficient tripping mechanical forces. The sensitivity of the actuator critically depends upon these design parameters: size of airgaps, leakage shunt reluctance, size of constricted slot, magnetic material properties and the control ampere turns in the coil. Hence, it is desirable to find the optimal design of the actuator, together with developing some corresponding prediction tools. Solution of the problem necessitates obtaining a range of manufacturing tolerances and predicting the output tripping characteristics and dynamic responses of the actuators since the

response time must be within a permitted value. Each case requires predictions of the dependency of the sensitivity on a number of design parameters with the aid of experiments.

During the design-development process of these clapper type magnetic actuators, the disadvantages have been found as mentioned above. Therefore, to develop new approaches with high sensitivity, for a wide range of manufacturing tolerances, perhaps eliminating the need for a toroid and finely machined surfaces, became desirable and necessary.

Hence,the aims of the investigation become to simulate actuator concepts using numerical computation methods and analytical approaches, develop 2D nonlinear transient electromagnetic fields with the permanent magnet using the finite element technique to deal with this special magnetic problem, investigate the dependencies of the actuator sensitivity on the design and control variables, optimise the design of the actuators, find a range of manufacturing tolerances, predict the operating performances and the output behaviours, investigate the designs, develop new approaches to obtain the highest possible sensitivity and fully to eliminate the deficiencies of previous designs, to reduce the detent torque existing in the stepper motor actuator, and to evaluate the performances of the designs.

The presented studies here were directed to achieve these aims. A commercially available 3D nonlinear finite element electromagnetic field CAD package (TOSCA) was used, with the facility to deal with highly nonlinear iron and with pre-and postprocessing graphics facilities for rapid mesh generation, problem formulations and results interpretations.

The simulations of the magnetic actuators were made using the 3D finite element technique. The analysis of non-energised and energised states were made to determine the effects of the critical design parameters of the actuator on the sensitivity. 3D magnetic fields with permanent magnets were reduced

into 2D nonlinear electromagnetic fields for transient computation purpose. A program of nonlinear transient with permanent magnet fields,which took the 3rd dimensions into account, was developed and used to evaluate the transient characteristics of the actuators. The comparisons were made between the results simulated in 2D transient and 3D static fields. It was found that the 3D magneto-static computation could only be used to precisely determine the performance of the actuators subjected to sinusoidal current at frequencies less than 100Hz.

The analysis permitted characterisation of the performance of the actuator in terms of the critical design and control variables, which correlated very closely with the results of test and measurements. The improvement of the magnetic actuators were made based on optimization design of the current sensitive clapper type magnetic actuators.

Development of a novel actuator was based on using the stepper motor principle combined with the principle of magnetic saturation. A multi-pole permanent magnet rotor disc , which energises the relatively larger airgap, was employed as the actuator's electromechanical release means.

The evaluations for this stepper motor magnetic actuator(SMMA) was carried out using the analytical approach and 3D finite element CAD technique. The design of SMMA was optimised to eliminate the toroid transformer as originally proposed[1]. A pole spacing arrangement and shape was postulated to reduce the detent torque existing in the SMMA actuators to a reasonable value. The problem found during the design-development process was that the stepper motor magnetic actuator cannot be operated without a toroidal transformer. Finally, the optimum design of stepper motor type actuator was proposed and evaluated.

Chapter 2

CAD in Current Sensitive Electro-magnetic Clapper Type Actuators

2.1 Introduction

Clapper type current sensitive magnetic actuator[4] is one of the most common non-electronic actuators used in electrical installations, primarily for tripping tasks. Although the majority are employed in simple tripping applications, the need for actuators to be able to respond faster and be highly sensitive to residual current continues to increase.

The designs of the actuators are mostly based on the magnetic saturation principle. The armature is normally kept closed by the holding force of a small permanent magnet. and it is actuated by a small current from closed to open positions. It can be operated with great precision and highly sensitive at very low current. Magnetic operating characteristics of the actuators are such that once the armature leaves its seating the attractive force dramatically decreases to release a tripping mechanism acting by an opposing spring.

The operating process of the actuator is generally divided into three stages. The first is the non-energised state which applies when the current in the coil is negligible. The second is the energised state which starts when the imbalance current appears. The third is the dynamic state which occurs when the armature commerces the release.

This chapter presents performance analysis and predictions for the first two stages. A 3D finite element program was applied to predict the effects of critical design parameters on the actuator sensitivity. The force characteristics related to a range of airgap and tripping characteristics were discussed with the aid of histograms of magnetic distributions. The permitted tolerances and the magnet setting were also obtained. Finally, the comparisons between the measured results and computed results were made , and conclusions about the nature of possible improvement to the system were presented.

2.2 3D Non-linear Finite Element CAD Technique

2.2.1 Electromagnetic Equations and Elementary FE Magnetic Models

In general terms the elementary model for specifying a electromagnetic field problem is shown in Figure 2.1, in which a volume of conducting material Ω_k bounded by a surface Γ_k with magnetic permeability μ and electrical conductivity σ is immersed in a global volume of free space Ω bounded by a surface Γ which may be extended to infinity if required. The global region may also contain a number of prescribed conductor sources Ω_j. This configuration arises in a very large number of applications of practical importance in industry and problems of this type are the starting points for developers of computer algorithms.

If the dimensions of the regions Ω_k and Ω_J are small compared with the wavelength of prescribed fields then the displacement current term in Maxwell's equations will

be small compared to free current density **J** and there will be, essentially, no radiation. This regime means a return to the pre-Maxwell field equations, the so called quasi-static case , where Ampere's law is good approximation.

The field equations are expressed by:

$$\nabla \cdot D = \rho \tag{2.1}$$

$$\nabla \cdot B = 0 \tag{2.2}$$

$$\nabla \times E = -\frac{\partial B}{\partial t} \tag{2.3}$$

$$\nabla \times H = J \tag{2.4}$$

where **D** is the electric displacement,

B is the magnetic flux density,

E is the electric field intensity,

H is the magnetic field strength,

J=Js+Je

Js is the source current density,

Je is the eddy current density.

ρ is the free charge. The field vectors are related by the material constituent properties,

$$D = \varepsilon E$$

and

$$B = \mu H$$

where ε and μ are the material permittivity and permeability respectively. The relationship between the eddy current density and the field is given by;

$$J_e = \sigma E \tag{2.5}$$

where σ is the material conductivity. The current continuity condition is given below;

$$\nabla \cdot J = 0 \tag{2.6}$$

2.2.2 Magnetic Scalar Potentials for Static Field Computations

It follows from equation (2.4) that free space region Ω can modelled with a scalar potential, when the current density **J=0.** In this case, $\nabla \times H = 0$ and the total field **H** can be represented by a negative gradient of a scalar potential,as follows;

$$H = -\nabla\psi \tag{2.7}$$

where ψ is called the total scalar potential which can be used to calculate the total field.

The governing equation for the regions with permanent magnet without currents is given by

$$B = \mu(H - H_c) = -\mu\nabla\psi - \mu H_c \tag{2.8}$$

where Hc is the magnetic coercive force. Since $\nabla \cdot B = 0$,hence;

$$\nabla \cdot \mu\nabla\psi = -\nabla \cdot \mu H_c \tag{2.9}$$

Equation (2.9) is a non-linear Poisson's equation.

Generally, there are many sources in fields besides permanent magnets, which include current sources. For permanent magnet and current sources, the magnetic field **H** at any point in the field can be partitioned into two fields, namely the field generated by the prescribed current source Hs and the field arising from induced magnetism in ferromagnetic materials Hm. Thus,

$$H = H_m + H_s \tag{2.10}$$

where the **Hm** is,

$$H_m = \frac{1}{4\pi}\nabla \int M(r')\cdot\nabla'\left(\frac{1}{|r-r'|}\right)dv = -\nabla\phi \tag{2.11}$$

where ϕ is called the reduced scalar potential, which describes the magnetization region of the total field, and it follows,

$$H = -\nabla\phi + H_S \tag{2.12}$$

where the source field **Hs** can be defined by the Biot-Savart Law for the conductor regions with current density **Js** Thus,

$$H_S = \frac{1}{4\pi}\int_\Omega J_S \times \nabla\left(\frac{1}{R}\right)d\Omega, \tag{2.13}$$

where R=|**r-r'**| is the distance from the source point **r'** to the field point **r.**

From the equation (2.2) $\nabla\cdot B = 0$,the governing equation (2.8) for the reduced scalar potential is given by,

$$\nabla\cdot\mu\nabla\phi = -\nabla\cdot\mu H_c + \nabla\cdot\mu H_s \tag{2.14}$$

Whilst direct solution of equation (2.14) is possible, in magnetic materials, the two parts of the field **Hm** and **Hs** tend to be of similar magnitude but opposite in direction, so that cancellation occurs in computing the field intensity **H,** giving a loss in accuracy as the difference becomes small. This loss is particularly critical in computing field when μ is large.

It is clear that the total scalar potential can be used to avoid cancellation errors, but unfortunately it cannot represent the whole problem, since in regions where there are current sources this potential is multi-valued.

In a numerical algorithm however the two potentials can be combined to avoid the cancellation associated with reduced potential and yet allow the inclusion of electric currents.

In the iron region Ω_K that does not contain current, as shown Figure 1-1, the total scalar potential ψ can be used,

$$\Omega_K: \qquad \nabla \cdot \mu \nabla \psi = -\nabla \cdot \mu H_C \tag{2.15}$$

and the region Ω_J that contains currents, the reduced scalar potential should be used. Thus,

$$\Omega_J: \qquad \nabla \cdot \mu \nabla \phi = \nabla \cdot \mu H_s \tag{2.16}$$

Since $\mu = \mu_0$ in this region, and $\nabla \cdot H_S = 0$, the equation (2.16) follows that,

$$\nabla^2 \phi = 0 \tag{2.17}$$

The solutions can be coupled at the interfaces of the regions by applying the boundary continuity conditions,

$$B_{1n} = B_{2n}, H_{1t} = H_{2t} \tag{2.18}$$

Figure 2.2 shows the interfaces of the regions, in region Ω_K which contains all the ferromagnetic and permanent magnets sources, e.g. the field $H = -\nabla\psi - H_C$, and in region Ω_J which contains all the conductor sources , $H = -\nabla\phi + H_S$. based on these conditions at the interface Γ_{JK},

$$-\mu_K\left(\frac{\partial \psi}{\partial n_K} + H_{cn}\right) = \mu_J\left(H_{sn} - \frac{\partial \phi}{\partial n_K}\right) \tag{2.19}$$

$$-\frac{\partial \psi}{\partial t} - H_{ct} = -\frac{\partial \phi}{\partial t} + H_{St} \tag{2.20}$$

where **n** and **t** are the unit outward normal and tangent directions respectively. Equation (2.20) can be integrated over interface Γ_{JK},

$$\int\left(-\frac{\partial\psi}{\partial t}-H_{\alpha}\right)dt=\int\left(-\frac{\partial\phi}{\partial t}+H_{St}\right)dt \tag{2.21}$$

hence,

$$\psi=\phi-\int H_s\cdot tdt+\int H_c\cdot tdt \tag{2.22}$$

If the equation (2.20) is integrated from any two points A to B on the interface, then the equation (2.22) can be written as,

$$(\phi-\psi)_B=(\phi-\psi)_A+\int_A^B H_s\cdot tdt-\int_A^B H_c\cdot tdt \tag{2.23}$$

where **Hs** is obtained explicitly from equation (2.13) ,say, at point A,($\psi=\phi$). Two points A and B may selected anywhere providing they do not intersect current regions. For example, the point A can defined at a symmetry central point or far-field point as the zero point. Then the equation (2.23) can be expressed by,

$$(\phi-\psi)_B=\int_0^B H_s\cdot tdt-\int_0^B H_c\cdot tdt \tag{2.24}$$

and equation (2.24) can be integrated over any path except current conductors.

The differential equations and boundary conditions of the static fields for the scalar Potentials can be summarized as,

$$\begin{aligned}
&\Omega_K:\nabla\cdot\mu\nabla\psi+\nabla\cdot\mu H_c=0\\
&\Omega_J:\nabla\cdot\mu_0\nabla\phi=0\\
&\Gamma_{1K}:\psi=\psi_1\\
&\Gamma_{1J}:\phi=\phi_1
\end{aligned} \tag{2.25}$$

$$\Gamma_{2K}: \mu \frac{\partial \psi}{\partial n} = p_{\psi}$$

$$\Gamma_{2J}: \mu_0 \frac{\partial \phi}{\partial n} = p_{\phi}$$

$$\Gamma_{KJ}: -\mu \frac{\partial \psi}{\partial n} - \mu H_{cn} = \mu_0 \left(H_{sn} - \frac{\partial \phi}{\partial n} \right)$$

$$\psi_{AB} = \phi_{AB} - \int_A^B H_s \cdot tdt + \int_A^B H_c \cdot tdt$$

where Γ_{1K} and Γ_{1J} are the first(Dirichlet) boundary condition of regions Ω_K and Ω_J; Γ_{2K} and Γ_{2J} are the second (Neumann) boundary condition; Γ_{KJ} is the interface of the regions.

2.2.3 3D Finite Element Method in Static Field

The stationary electromagnetic field equations are described in equation (2.25), which can be solved using the Finite Element Method. The approach is based on the discrete linked domains ,in which the equation is satisfied. The geometry to be analysed is divided into finite elements, in order to approximate solution in each element

$$\phi(r) = \Sigma N_i \phi_i \tag{2.26}$$

where Ni are shape functions based on the element geometry,

ϕ_i are nodal values of ϕ

The equation (2.25) is solved by means of a weighted residual, as given

$$\int_{\Omega_K} \mu \nabla W_i . \nabla \psi d\Omega + \int_{\Omega_J} \mu_0 \nabla W_i . \nabla \phi d\Omega$$

$$= \int_{\Gamma_{KJ}} W_i \left(\mu \frac{\partial \psi}{\partial n} - \mu_0 \frac{\partial \phi}{\partial n} \right) d\Gamma - \int_{\Omega_K} W_i \nabla . \mu H_c d\Omega \tag{2.27}$$

where Wi is the weighting, set to the shape function. From (2.25),

$$\mu \frac{\partial \psi}{\partial n} - \mu_0 \frac{\partial \phi}{\partial n} = -\mu_0 Hsn - \mu Hcn \tag{2.28}$$

Setting $\phi_A = 0, \psi_A = 0$, and choosing point 'k' on the interface to replace point 'B', equation (2.20) reduces to

$$\phi_K = \psi_k + \int_0^k H_{St} dt - \int_0^k H_{ct} dt \tag{2.29}$$

Therefore the equation (2.27) can be rewritten as,

$$\psi_j \int_{\Omega_K} \mu \nabla Ni . \nabla N_j d\Omega + \psi_K \int_{\Omega_J} \mu_0 \nabla N_i \nabla_K d\Omega + \psi_l \int_{\Omega_J} \mu_0 \nabla N_i \nabla_l d\Omega$$

$$= - \int_{\Gamma_{KJ}} Ni(\mu H_{cn} + \mu_0 H_{sn}) d\Gamma - \int_0^k (H_{St} - H_{ct}) dt \cdot \int_{\Omega_J} \mu_0 \nabla Ni . \nabla N_k d\Omega$$

$$- \int_{\Omega_K} Ni \nabla . \mu H_c d\Omega \tag{2.30}$$

where point j is located in domain Ω_K, point K is on the interface Γ_{KJ}, and l is in the domain Ω_J.

The equation (2.30) can be simplified as a matrix form, and is given below:

$$A\Phi = F \tag{2.31}$$

where $A_{ij} = \int_{\Omega} \nabla Ni \cdot \mu \nabla N_j d\Omega$ (2.32)

Φ are scalar potential values at the element nodes, they being the total scalar potential and reduced scalar potential in the domains Ω_k and Ω_J respectively. The right hand side

of the equation (F) is expressed as

$$F_i = -\int_{\Gamma_{KJ}} Ni(\mu H_{cn} + \mu_0 H_{sn}) d\Gamma$$

$$-\int_0^k (H_{st} - H_{ct}) dt \cdot \int_{\Omega_J} \mu_0 \nabla N_i \cdot \nabla N_k d\Omega - \int_{\Omega_K} Ni \nabla \cdot \mu H c d\Omega \qquad (2.33)$$

Equation (2.31) can be solved by non-linear iterative methods, to obtain the potential values,from which the flux density in the domains may be calculated directly from equations (2.7and 2.12).

This mathematics model and numerical computation method were mostly used in the program of tosca which was mainly applied to analyse the magneto-static problems of the actuators.

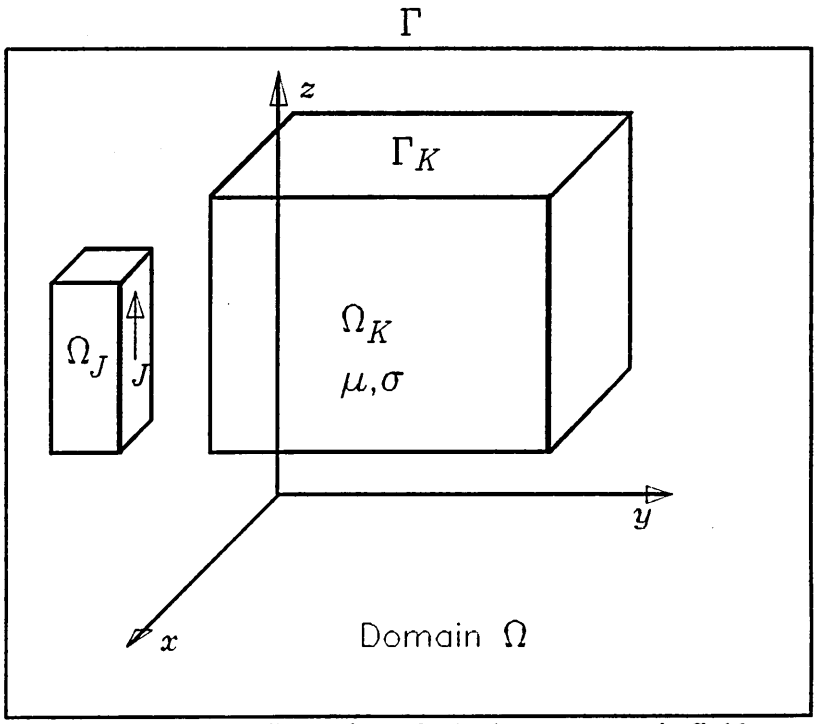

Figure 2.1 Configuration of 3D electromagnetic field

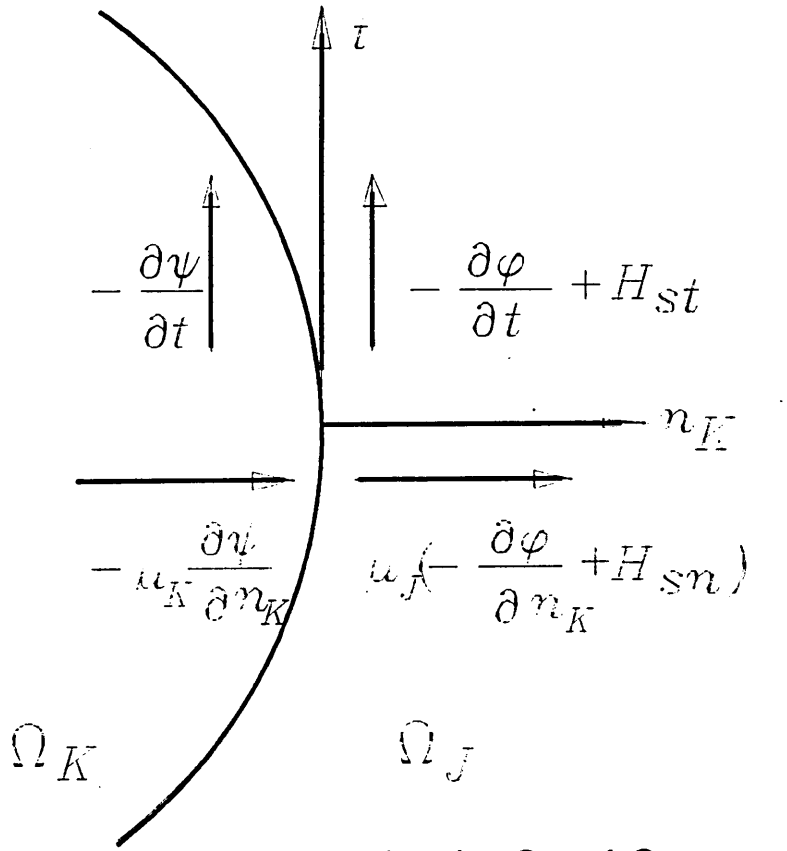

Figure 2.2 Interface of domians Ω_J and Ω_K

2.3 3D-FE Simulation of Clapper Type Actuator

2.3.1 Description of Clapper Type Actuator

A typical current sensitive electromagnetic clapper type actuator is shown in fig.2.3. This actuator is required to operate within 5ms-10ms from the moment when the fault current occurs to the armature in the open position and also to operate at very low current (10- 30mA). This actuator is also required to provide upto 0.6N mechanical actuating forces to trip the latch mechanism.

In this design the magnetic circuit consists of two parallel iron yoke plates (4) and (5) which are separated by a intermediate layer (6) of an non-ferro-magnetic material, which forms a relatively high reluctance path for the leakage flux from the permanent magnet (1). The permanent magnet bridges the two yoke plates , the polarization strength and angular direction of which can be adjusted to change the magnitude of attracting force acting on the armature, in relative to the tripping current, by rotating the magnet about its N-S axis. The armature (3) is normally held on to the yoke by the force produced by the permanent magnet against the action of the opposing spring force (7). The machined air gap between the contact surface (3c) of the tripping armature and the yoke keeper is referred to as the 'working airgap', in which the flux of the permanent magnet produces an electromagnetic force acting on the armature. The air gaps between the contact surfaces (3a) and (3d) and the yoke plates are referred as 'residual airgap' which forms the residual flux path of the permanent magnet. The magnetic circuit has con-stricted sections denoted by x and x' which are the zones to be saturated by the control flux. The control current coil(2) is wound to produce opposing flux as shown in figure 2.3.

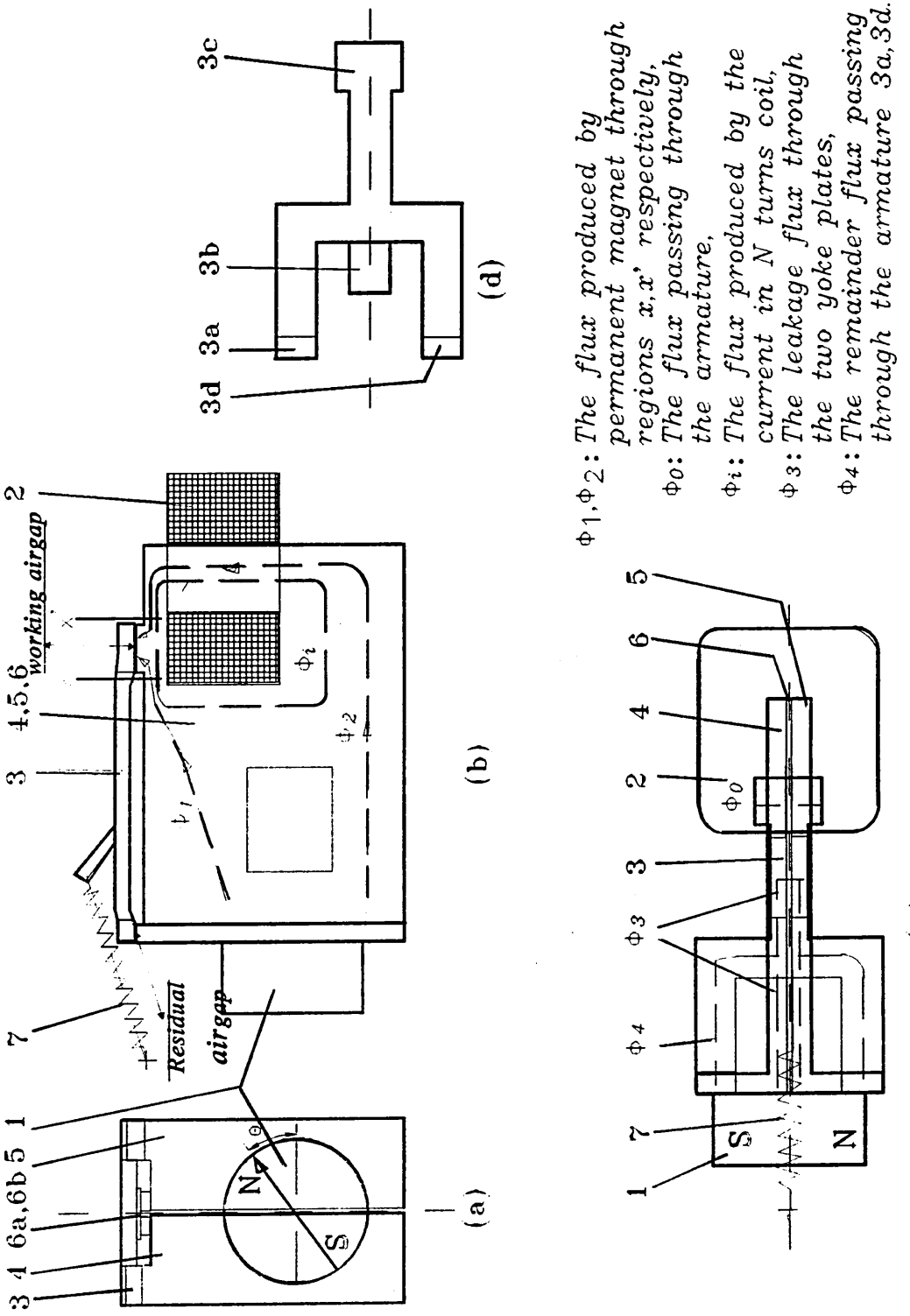

Φ_1, Φ_2: *The flux produced by permanent magnet through regions x,x' respectively,*
Φ_0: *The flux passing through the armature,*
Φ_i: *The flux produced by the current in N turns coil,*
Φ_3: *The leakage flux through the two yoke plates,*
Φ_4: *The remainder flux passing through the armature 3a,3d.*

Figure 2.3 Current sensitive electromagnetic clapper type actuator general arrangement

The intermediate layer(6) is normally arranged with one part of non-ferro-magnetic material and the other of ferro-magnetic material to make the distance between the two yoke plates not too small, so that it is easy to clear the yoke stack. On the other hand the magnetic reluctance of the circuit, which forms the shunt for the flux of the permanent magnet when saturation occurs, must not be too high.

The construction of clapper type actuator shown in fig.2.3 has 4 separate parallel flux paths for the permanent magnet. The first and second paths ϕ_1, ϕ_2 from the permanent magnet have a constricted portion before combining into ϕ_o to pass into the armature. The third path ϕ_3, comprising the two yoke plates and intermediate layer, forms the shunt path which plays a significant role in the sensitivity of the actuator to control current. Path ϕ_4 provides the path for residual flux from the permanent magnet.

The winding is arranged so that current supplied from a toroid is injected into it to produce the flux ϕ_i which adds to the flux produced by the permanent magnet in one constriction (either x or x') and subtracts in other. As a result, the constriction zone with the added flux is to be saturated, which causes part of the flux to be diverted into the shunt leakage path rather than the airgap. The fluxes in other constrictions are also reduced. Both of them cause the reduction of the total flux in the airgap, and consequently reduce the attraction force acting on the armature. The electromagnetic force therefore decreases as the coil current is increased until the armature opens under the action of the opposing release spring.

The flux in the airgap is critically diminished by the coil current in this actuator, so that the operation of the release takes place with a relatively small current. Adjusting the angular alignment of the permanent magnet also

changes the attractive force acting on the armature and consequently its sensitivity to tripping current setting of the actuator.

The magnetic operating characteristics of the actuator are such that once the armature leaves its seating, the attractive force decreases rapidly and the release of the circuit breaker mechanism by the opposing spring is very positive, so that the circuit can be switched off quickly.

In design, the airgaps of the magnetic actuators have significant effects on the force of attraction and consequently the sensitivity to tripping current setting. For example, increasing 1μm for the airgap could lead to approximately 25 percent declination of the force, for the airgap with increasing larger than 3 μm the actuators could fail to work. The dimensions of leakage shunt path and constricted slot critically affect the sensitivity of the actuator. The magnetic material properties have the influences both on the force of attraction and tripping current setting. The performance of the actuators are associated with the design parameters, for example, for a permitted airgap less than 1μm and a reasonable optimum value of the leakage shunt reluctance, if the size of constricted slot is larger or smaller than a critical design value, the sensitivity could dramatically drop down even fail to control. Therefore, the critical design parameters such as airgap spacing, leakage shunt path, constricted slot, material properties and control variables are most important in the design.

In practice, the current-sensitive magnetic actuator requires some means for tuning out the effects of variations in manufacture and enables to constituent tripping and the declared current setting. The change of magnetisation strength of the permanent magnet by rotating the magnet can achieve this purpose.

2.3.2 3D-FE Electromagnetic Modelling of the actuator

The electromagnetic field distribution in the magnetic circuit of the actuator must be determined to enable the influences of the critical design factors such as the airgap dimensions, constricted sections, magnetic material properties and current to be analysed. The geometry of the actuator is symmetrical as shown in figure 2.3, but the electromagnetic field is only symmetrical when the magnetic displacement angle is zero. Therefore, it is necessary to utilise the three dimensional modelling for this problem. A non-linear 3D finite element package was chosen to solve this problem.

The finite element method, used to obtain the solutions of the partial differential equations (2.25) derived from the electromagnetic equations, is based on dividing the physical magnetic circuit into twelve electromagnetic domains (figure 2.4), the planes of which are shown in figure 2.5. Each domain is divided into number of small volumes. The generated finite element mesh model is shown in figure 2.6. The boundary condition of the problem is determined by assigning a zero magnetic scalar potential(Dirichlet condition) in a finite region out of the model.

The descretisation of the magnetic circuit into finite elements (small volumes) as described enables the field distribution in the magnetic material and airgap to be obtained using TOSCA. The electromagnetic force acting on the armature is determined by Maxwell's stress tensor:

$$T=\frac{1}{\mu_o}(B.n)B-\frac{1}{2\mu_0}B^2n$$

$$F_m=\int_s Tds \qquad (2.34)$$

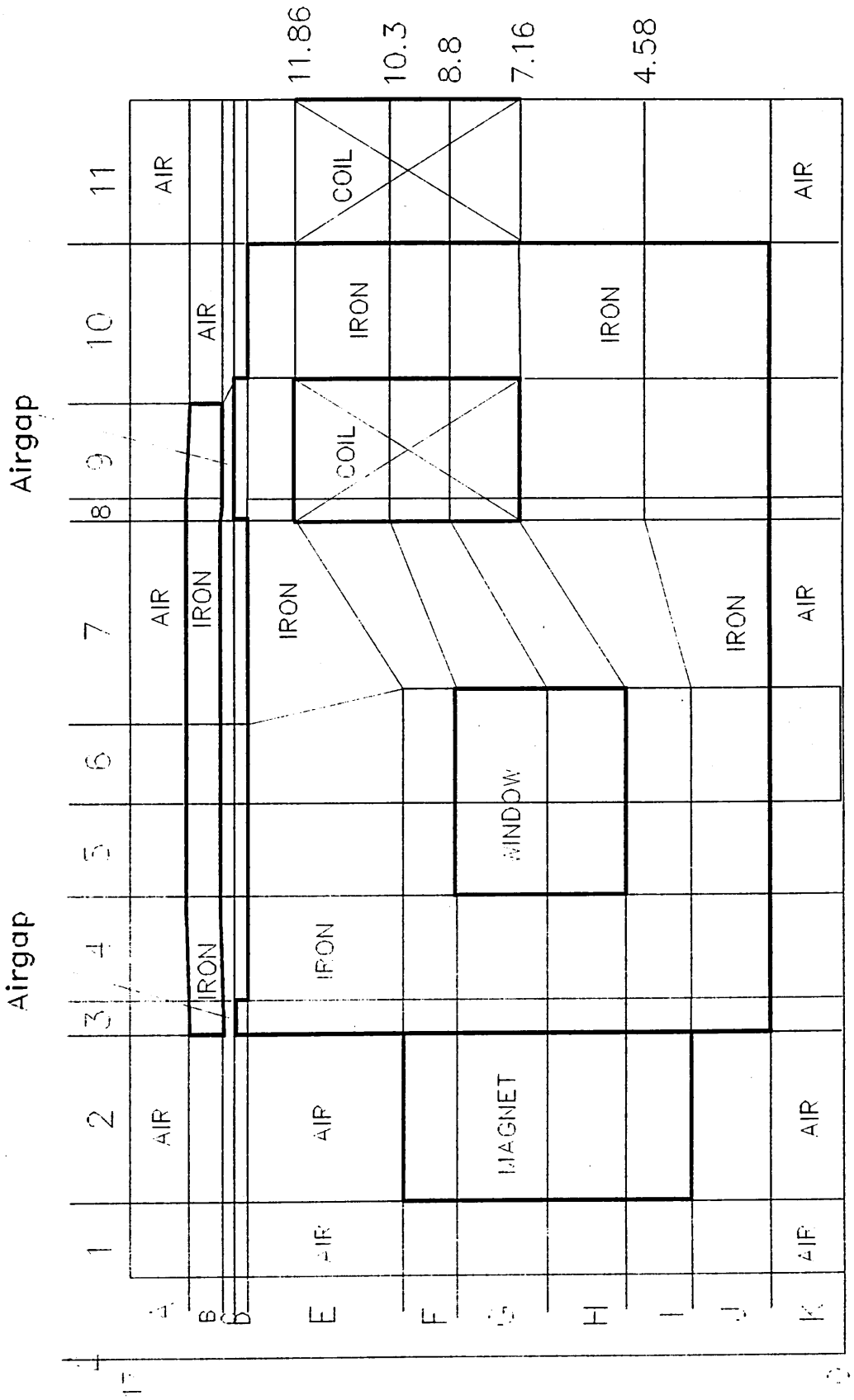

Figure 2.4 Electromagnetic field domains of the actuator

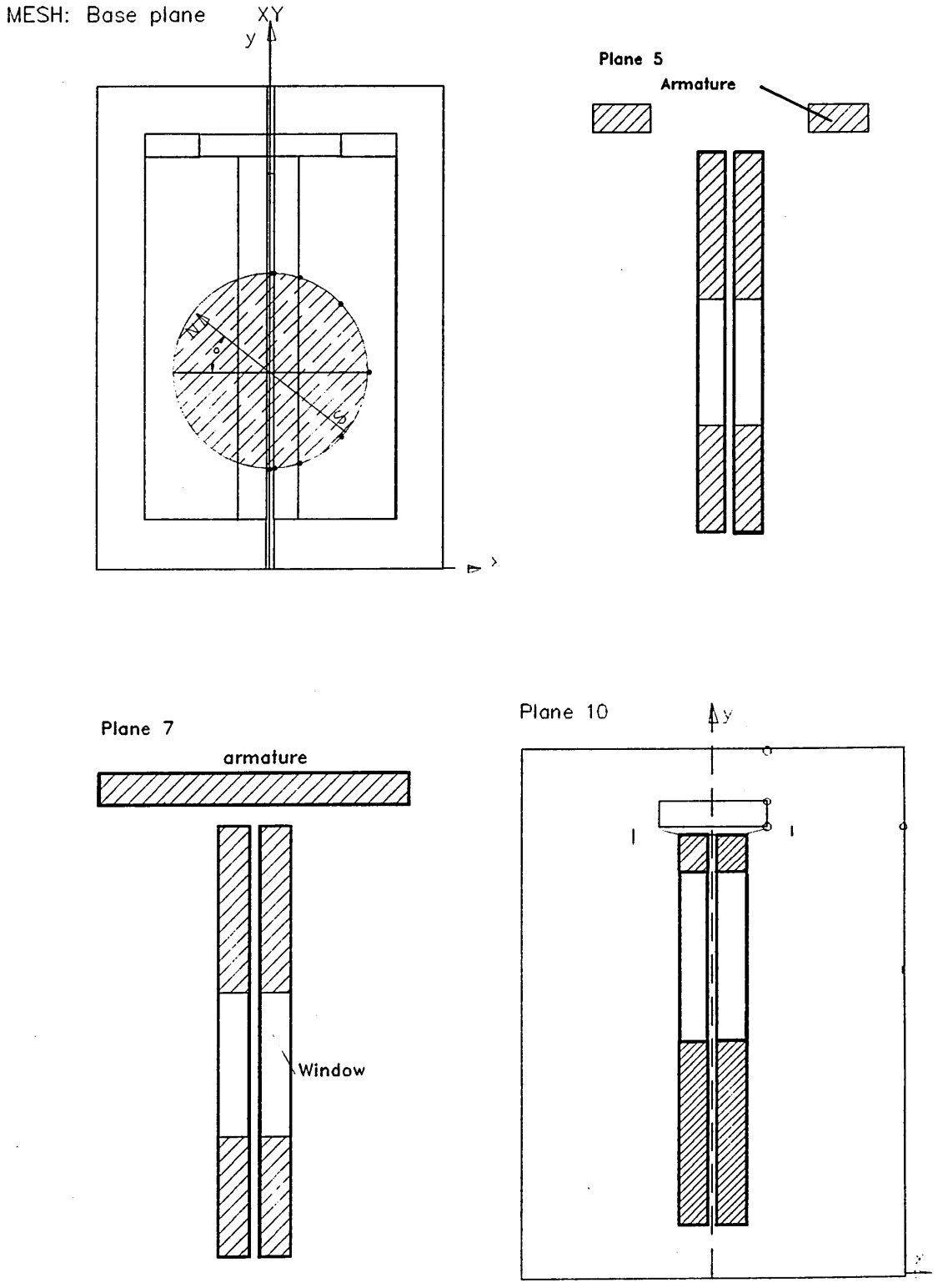

Fig. 2.5 Finite element logical planes

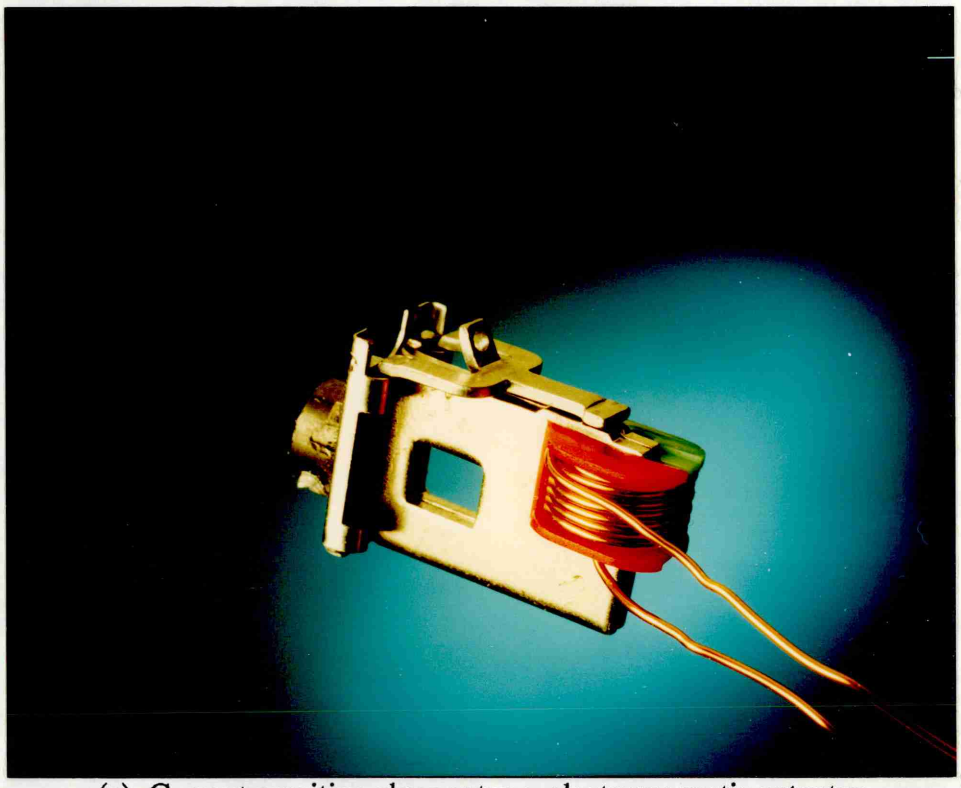

(a) Current sensitive clapper type electromagnetic actuator

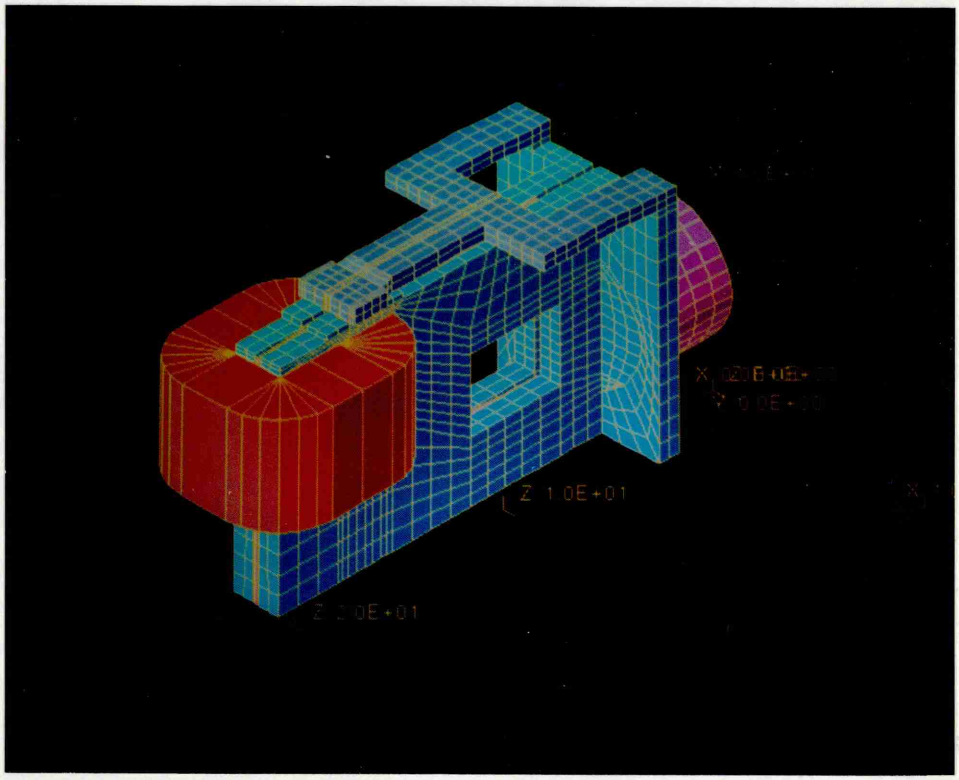

Figure 2.6(b) 3D Finite Element mesh model of the clapper type actuator

where s is the integrated surface;

n is the unit normal vector outwards the surface s;

Fm is the magnetic force acting on armature.

The integration over the region of the airgap is performed within the TOSCA program to permit the calculation of the electromagnetic force and also to plot the flux distribution to enable optimization of the dimensions of the magnetic circuit. The specification of the problem takes account of the magnetic material properties, the shape and the dimensions of the magnetic circuit and airgap, the number of coil turns and the magnitude of the coil current.

2.3.3 Simulation of Small Airgap

To achieve a precise magnetic design, it is necessary to calculate the magnetic field in the very small airgap. However, if the elements with aspect ratios larger than 1000 are used in the computation, the solution accuracy will be significantly affected. When the aspect ratios rise above 2500:1, the solution may not converge to the standard numerical convergence tolerance. For this actuator geometry, the airgaps are between 0.5μm-3μm and the length of the actuator is 20mm. The dimensions of the element in

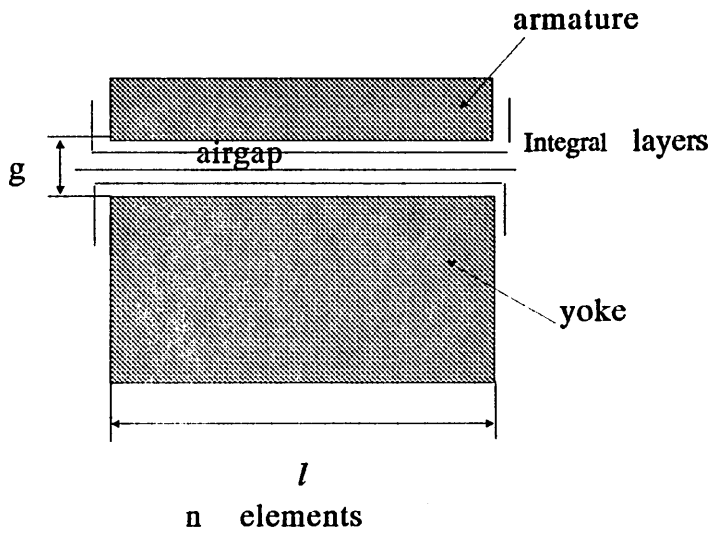

Figure 2.7

the airgap are quite small compared to the feature being modelled. The restriction is also reasonable in all directions where the field is changing rapidly. The finite element discretisation was therefore created to be satisfactory for modelling the actuator field changes. Here let's set the aspect ratio of an element to be λ, then the number of elements(n) in the airgap, refer to fig 2.7, is expressed as follows:

$$n=m \times \lambda \frac{l}{g} \qquad 2.35$$

where m is the layers of element in the airgap;

n is the number of elements shown in Figure 2.7.

λ is the aspect ratio of an element.

The parameters (m and λ) came from the computation. Figure 2.8 shows the relationship between the computed magnetic force(Fm) and mesh layers (m) in the airgap. It can be seen that if the layers of division is equal to or over 3, the computed forces corresponding to each airgap converged to a constant value. Thus the number of layers (m) should be taken as at least 3. From the computation data, the aspect ratio (λ) ≥ 1/1000. Hence, the number of elements can be obtained from equation (2.35).

Assuming when airgap g=0, the flux density on the contact surface is approximately uniform, which can be seen from the predicted histogram of the flux distribution in the surface in the later, then the Maxwell' stress tensor formula(2.34) can be simplified as,

$$Fm=\frac{1}{2\mu_0}B\int Bds=\frac{\varphi^2}{2\mu_0 A} \qquad (2.36)$$

where A is the area of the contact surface;

φ is the flux in the airgap.

Hence the attractive force can be obtained from the computed flux in the airgap divided by the area of the surface.

When the airgap is very small and the reluctance cannot be ignored compared to the iron reluctance, the direct mesh generation cannot model such a problem. Even doing it would require a large number of elements, for which the computation will take a rather long time to obtain one solution. This is not appropriated for the design.

Here, a method is proposed to use a nonferromagnetic material with permeability (μ) instead of air. Assuming the fringing flux in the airgap to be negligible and the reluctance of airgap be equal to the reluctance of the introduced material, then , the permeability of the material is given by

$$\mu = l_m / g$$

where *lm* is the length of the nonferromagnetic material, the cross section area of the material is same as the air gap (A).

g is the length of the airgap.

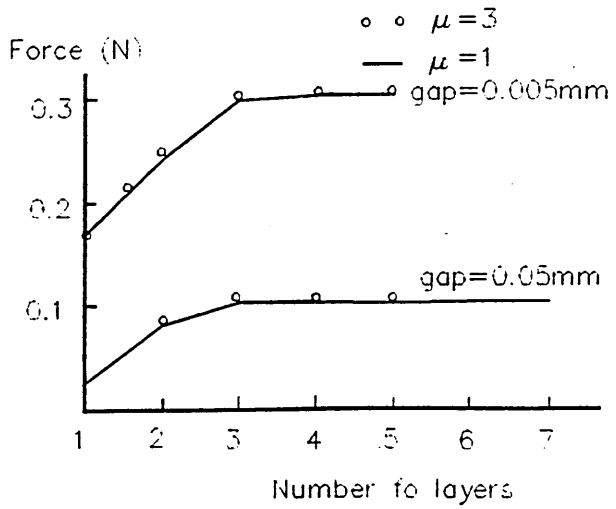

Figure 2.8 Electromagnetic force acting on armature versus number of mesh layers for two kinds of material with μ=1 and μ=3

The force exerted by a magnetostatic field on the nonferromagnetic is obtained by evaluating the integral

$$F_m = \int_s [\mu H(H.n) - \frac{\mu}{2} H^2 n] ds \tag{2.37}$$

Hence the attractive force on the armature involves the magnetic force equation 2.34 and equation (2.37). The comparison between the forces computed in the airgap and in the equivalent material for different mesh layers is shown in figure 2.8. This figure indicates that the equivalent material can be used instead of the air corresponding to the different μ. The mesh layers in the airgap must be divided by 3 to obtain a reasonable accuracy solution.

2.3.4 Magnetic Material Properties

The Nickel-Iron alloy material used in the yoke of the actuator was analysed and found to have a very high permeability. The composition of the specimen material is illustrated in table 2.1.

Elements	Alloy Compositions (wt.%)
Si	0.409
Mo	4.325
Mn	0.36
Fe	14.25
Ni	80.66

The saturation level of the Ni-Fe alloy at room temperature is 0.7161 Tesla and the initial permeability is between 40-80 kilogauss/oersted. The magnetization curves of the permanent magnet and Ni-Fe alloy are shown in Figure 2.9 and 2.10

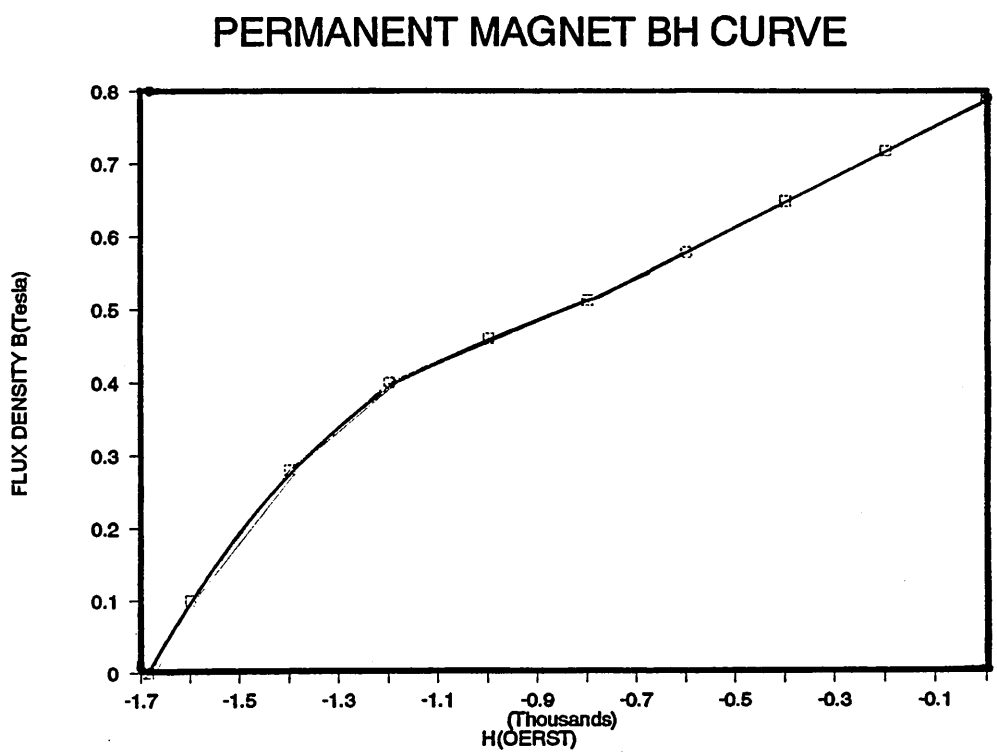

Figure 2.9 Magnetization Curve of the Permanent Magnet

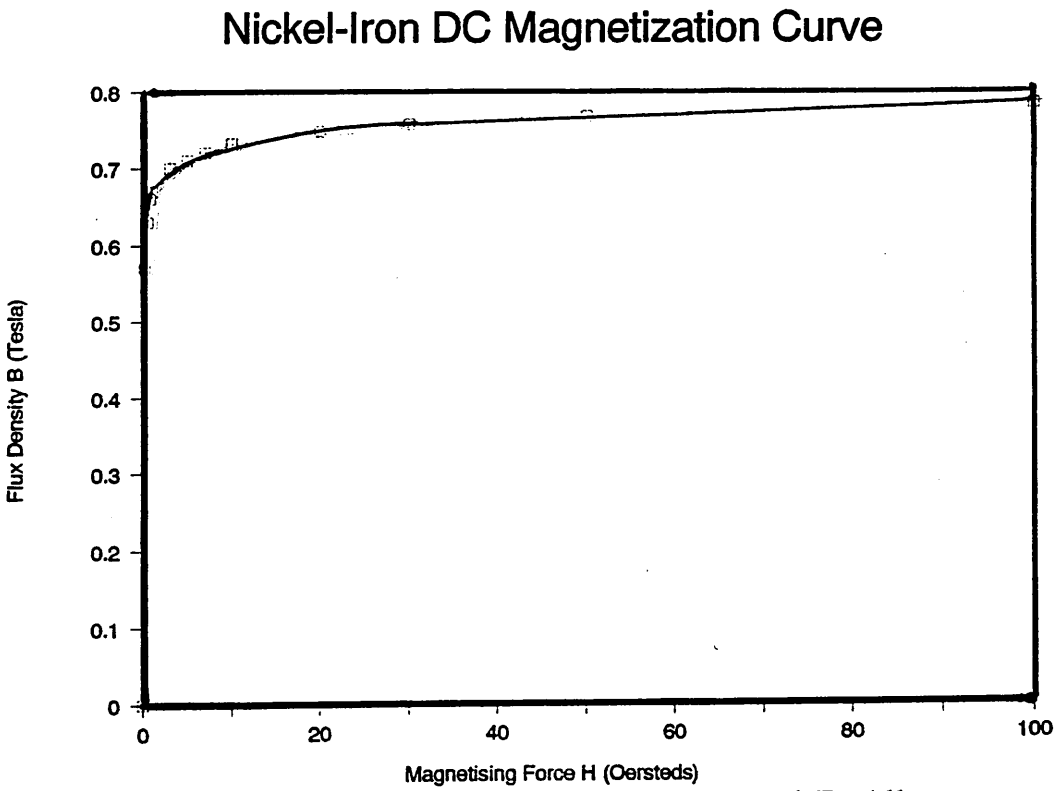

Figure 2.10 DC Magnetization Curve of the Ni-Fe Alloy

2.4 Non-energised Actuator State

2.4.1 Opposing Spring Force Acting on Armature

The force diagram of the actuator is shown in Figure 2.11 where the opposing spring is used to release the armature when the attractive force(Fe) of the armature reduces to value less than the opposing spring force(Fs).

The equation for the spring force was determined by measurement as,

$$Fsp(l) = 0.48 + k(l - lo) \text{ (N)} \qquad (2.38)$$

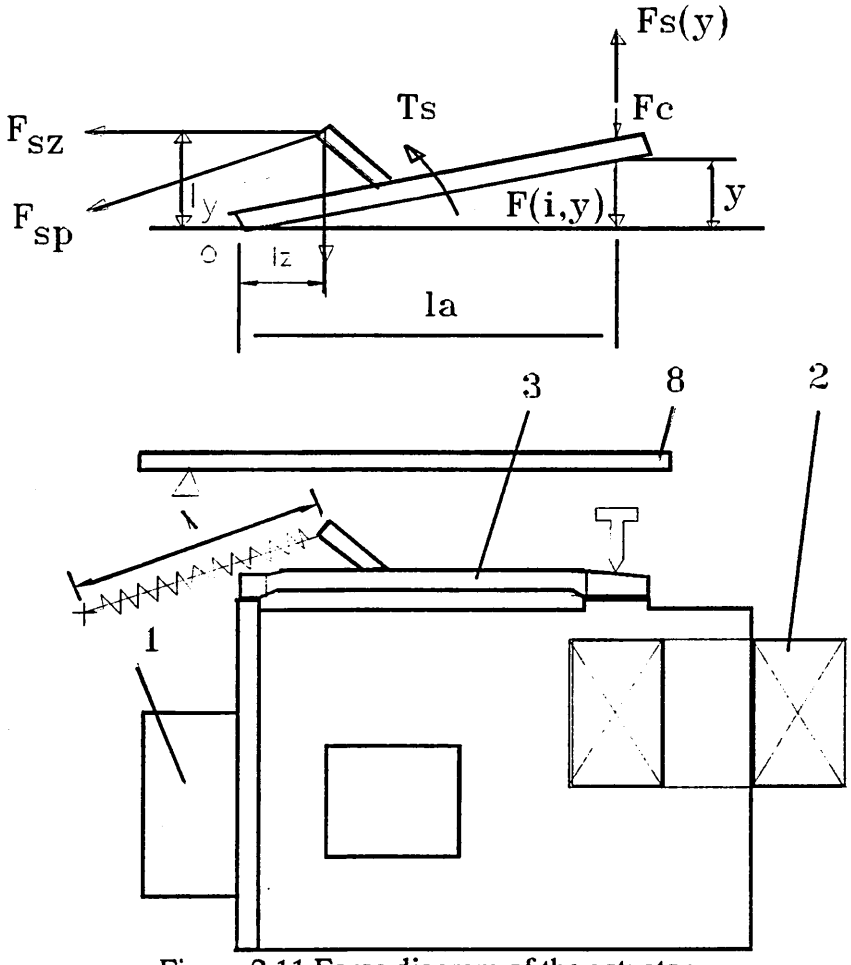

Figure 2.11 Force diagram of the actuator

1 Permanent magnet , 2 Coil. 3 Armature, 8 Latch mechanism

where k=0.38 N/mm is the spring coefficient,

l is the length of the spring along the axis,

lo=4.5mm is the primary length.

The initial spring force when l=7.6mm, acting along the axis of the spring is, Fsp(7.6)=1.658(N)

The component forces Fsz and Fsy are derived from the force diagram 2.11 as; $Fsz=\sin(70^0)Fsp=1.558(N)$

and $Fsy=\cos(70^0)Fsp=0.567(N)$.

The torque acting on the point 'o' is given by,

$$T_s=F_{sz}\, l_y - F_{sy}\, l_z = 2.58 \text{ (N.mm)}$$

where lz=3.5mm, l_y=2.9 and the opposing spring force acting on the armature in 'y' direction is

$Fs\,|_y=Ts/12.28=0.21$ (N) hence Fs=0.21 (N)

2.4.2 Characteristics of the Non-energised State

The non-energised state applies when the control current in the coil is negligible. At this state, the electromagnetic force acting on the armature must exceed the opposing spring force by a sufficient margin to enable the devices to withstand the effects of mechanical shock. Under these conditions, the work-

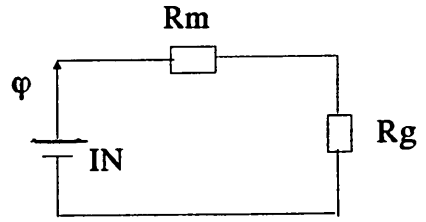

Figure 2.12 Single magnetic circuit

ing air gap (g) and consequently the quality of the machined surfaces of the armature and contact surfaces are most critical.

Firstly, considering the reluctance of the airgap and ferro-magnetic material in the simple magnetic circuit referred to figure 2.12, of which, the airgap reluctance is given by

$$R_g=\frac{g}{\mu_0 A} \tag{2.39}$$

and the magnetic material reluctance by

$$R_m=\frac{l_m}{\mu_m A_m} \tag{2.40}$$

then, $$\varphi=\frac{IN}{(R_g+R_m)} \tag{2.41}$$

where *lm* is the equivalent length of the magnetic circuit;

IN is the coil ampere turns;

g is the length of airgap;

φ is the flux in the magnetic circuit.

Here, the permeability of the ferro-magnetic material is very high compared to air, typically for the maximum permeability, for example, $\mu_m : \mu_0 = 2x10^5 : 1$, so it is clear from equation (2.39), (2.40) and (2.41) that the $R_g >> R_m$ and the magnitude of flux depends on the airgap reluctance when the excitation ampere turn is constant. This consideration is very important in manufacturing to achieve the consistent airgaps and to find the optimum alignment of the permanent magnet angular setting to turn out the effects of manufacturing inconsistencies within a range of practical tolerances.

The 3D finite element package TOSCA was used to compute the electromagnetic field of the actuator , together with the corresponding to the magnetic forces. The experimental device to measure the force of attraction is shown in figure 2.13.

Figure 2.14 shows the computed characteristics of the electromagnetic force of attraction acting on the armature versus airgaps. From these predictions, it is confirmed that the airgaps have a significant effect on the magnitude of the airgap flux and consequently the electromagnetic force acting on the armature.

To arrive at the optimum airgap it is necessary to find the radial alignment of the magnet. Variation of the airgap and the angular alignment can be readily simulated using TOSCA. These results were checked by measurements as shown in figure 2.15. This figure also shows the calculated mag-

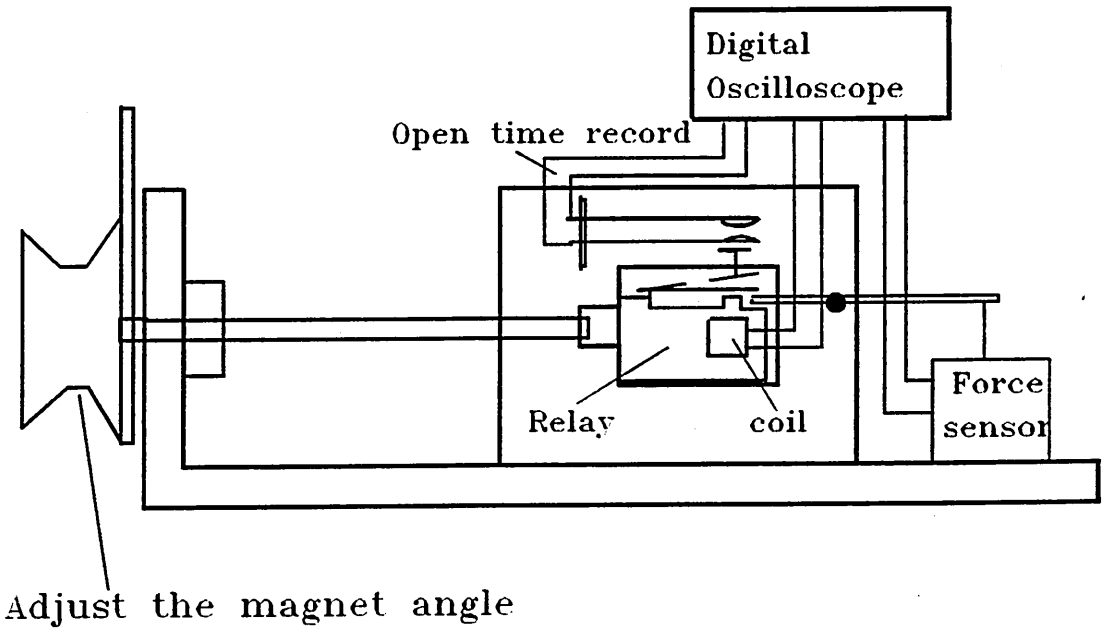

Figure 2.13 Experimental device

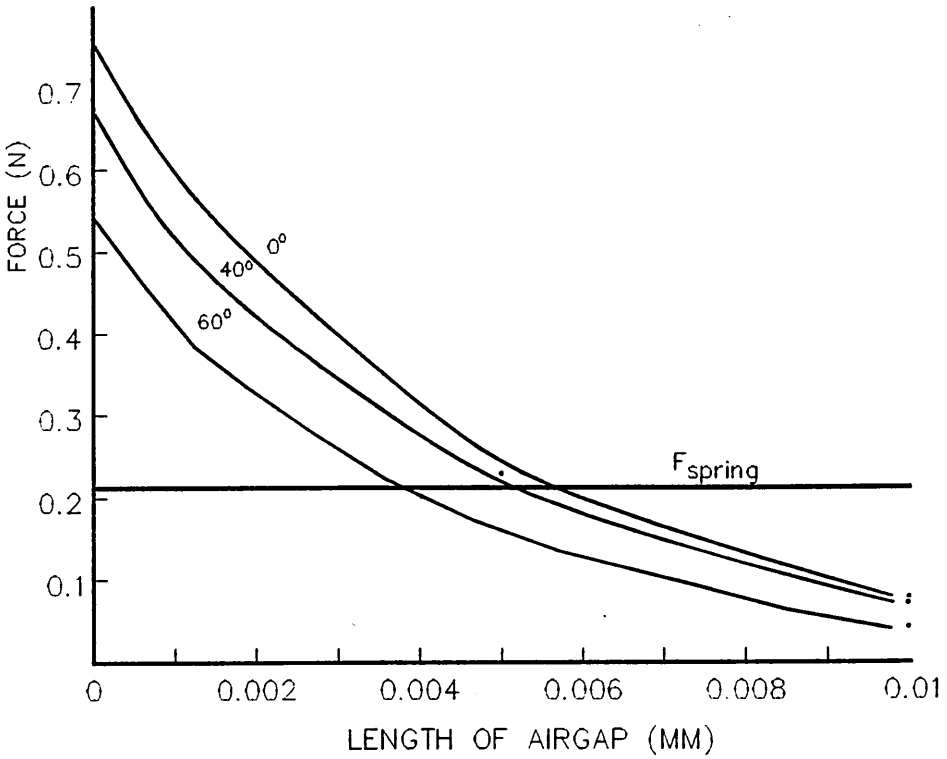

Figure 2.14 Electromagnetic force acting on the armature versus the airgap for different permanent magnet displacement angles

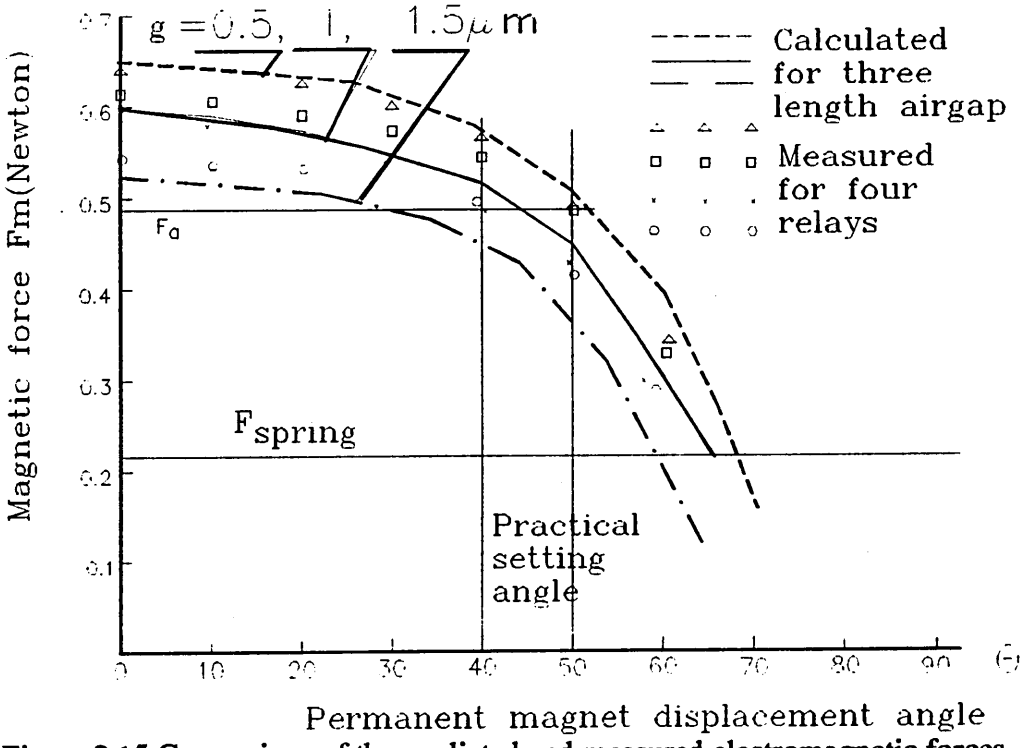

Figure 2.15 Comparison of the predicted and measured electromagnetic forces versus permanent magnet displacement angles

netic forces for three airgaps (0.5, 1 ,1.5μm) over the range of magnet displacement angle from 0^0 to 70^0 degrees. These characteristics indicate the need to preset the permanent magnet angular alignment between40^0-50^0 to minimise the sensitivity of the actuator to variations in manufacturing tolerances and other vagaries on the performance of the actuator in order to retain the magnetic force at a value (typically up to twice that of opposing force) in order to withstand the effects of the mechanical shock.

It is instructive to compare the calculated and measured forces at the same magnet displacement angle as shown in figure 2.15, since each relay corresponds to a different value of airgap. For the number of actuators, the tested results were located in the range of the computed force curves for the computed airgaps in the range from 0.5 to 1.5μm.

The roughness and flatness of the machined surfaces for the number of actuators were also measured, a typical test curve of roughness is shown in figure 2.16. The measured airgaps are in the range 0.2-0.6μm(see appendix II) compared to the computed airgaps 1±0.5μm.

The fluxes in the working airgap, residual airgap and leakage flux are significant as shown in figure 2.17 and 2.18. These figures show the relationships between the fluxes φ_0 in the working airgap , φ_4 in the residual airgap, the leakage flux φ_3 and the airgaps for magnetic displacement angles of 0^0 and 60^0 degrees. It can be seen from figure 2.17 that the fluxes $\varphi_0{}^0$ and $\varphi_0{}^{60}$ go down with increasing air-gap which corresponds to the electromagnetic force characteristics in figure 2.14. But the other fluxes $\varphi_4{}^0$ and $\varphi_4{}^{60}$ reduce slightly when the airgap is below 3μm, since the reluctance of the residual airgap remains constant. However. the leakage flux $\varphi_3{}^0$ and $\varphi_3{}^{60}$ in figure 2.18 increases as the air gap is increased.

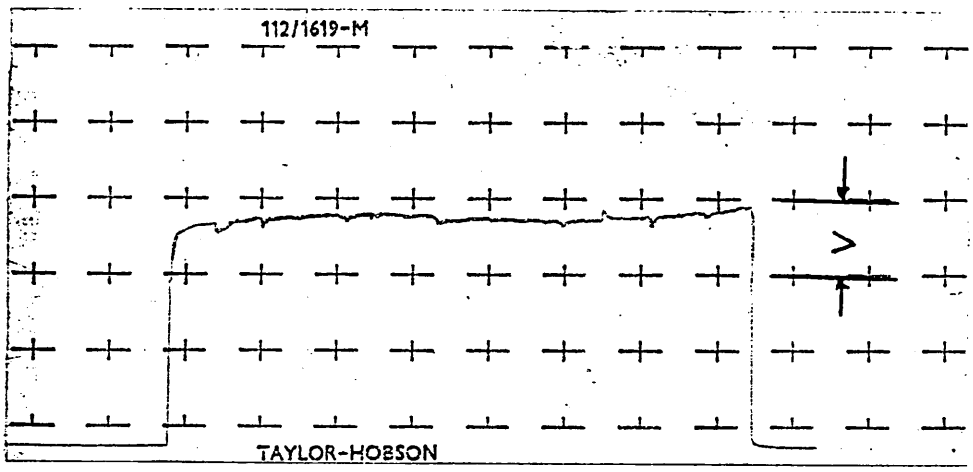

Roughness V(10mm)=0.5µm

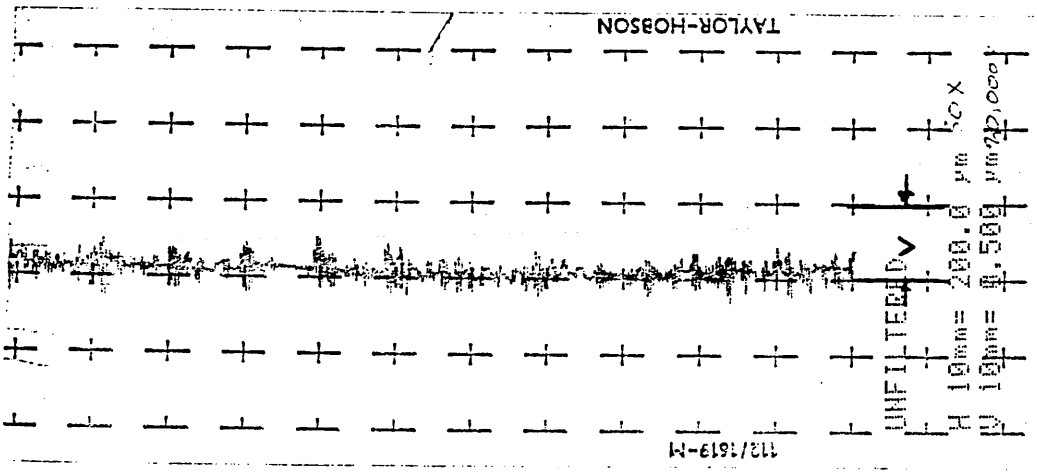

Flatness V(10mm)=0.5µm

Figure 2.16 Measured roughness and flatness of the actuator airgap surface

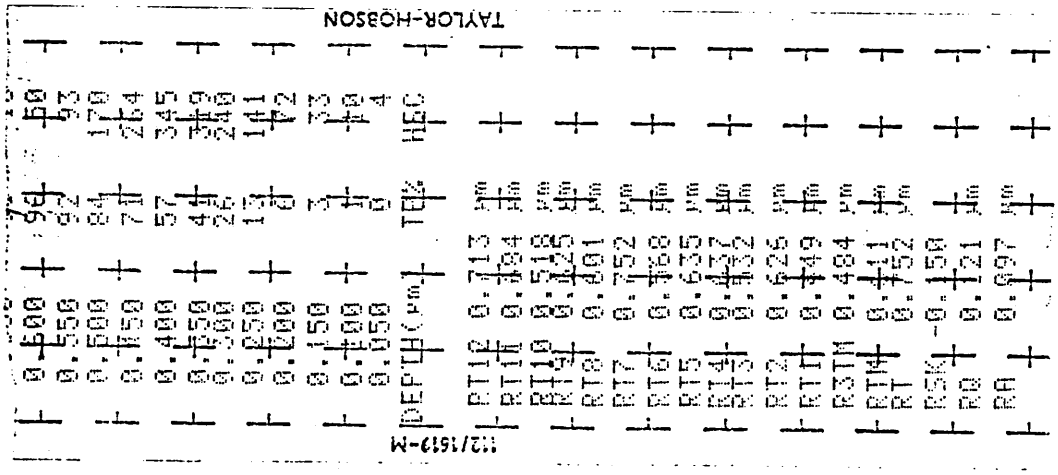

Parameters for the roughness (see appendix 2)

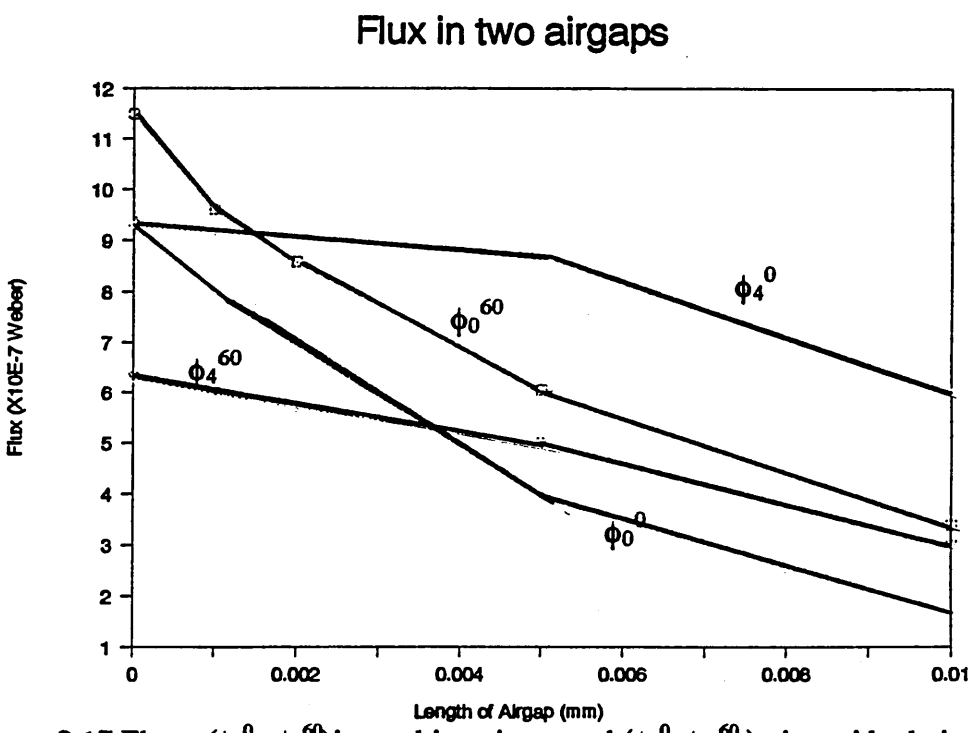

Figure 2.17 Fluxes(ϕ_0^0, ϕ_0^{60})in working airgap and (ϕ_4^0, ϕ_4^{60}) in residual airgap versus airgap length for magnetic displacement angles 0^0 and 60^0

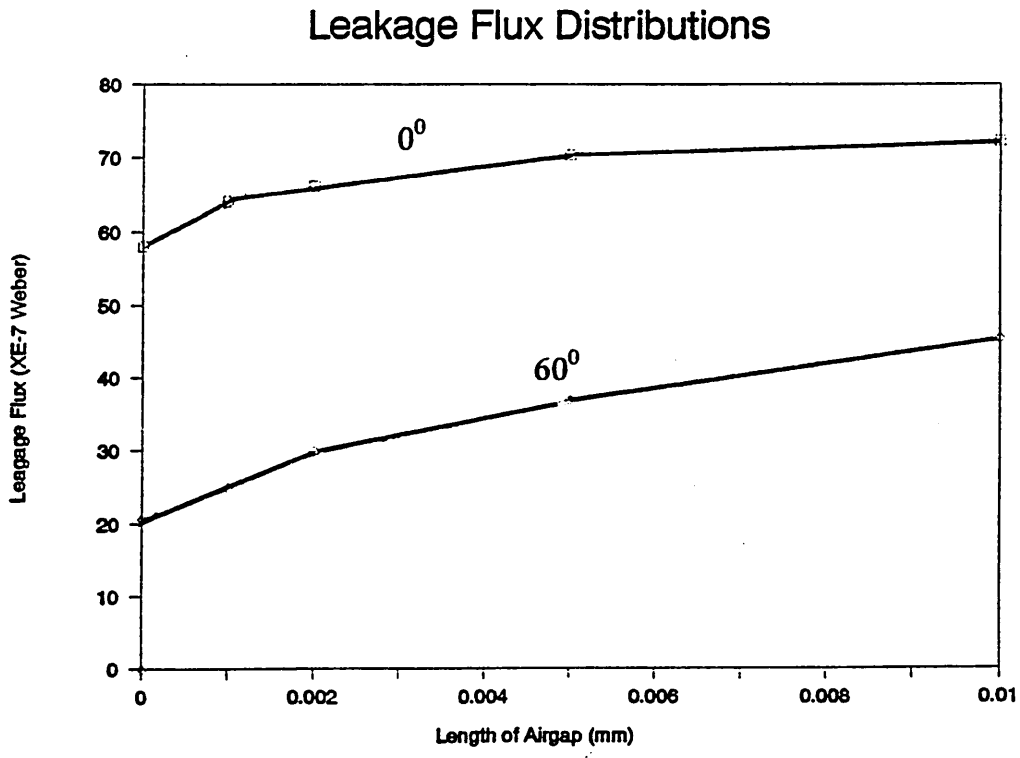

Figure 2.18 Leakage flux (ϕ_3) versus airgap length for magnetic displacement angles 0^0,60^0

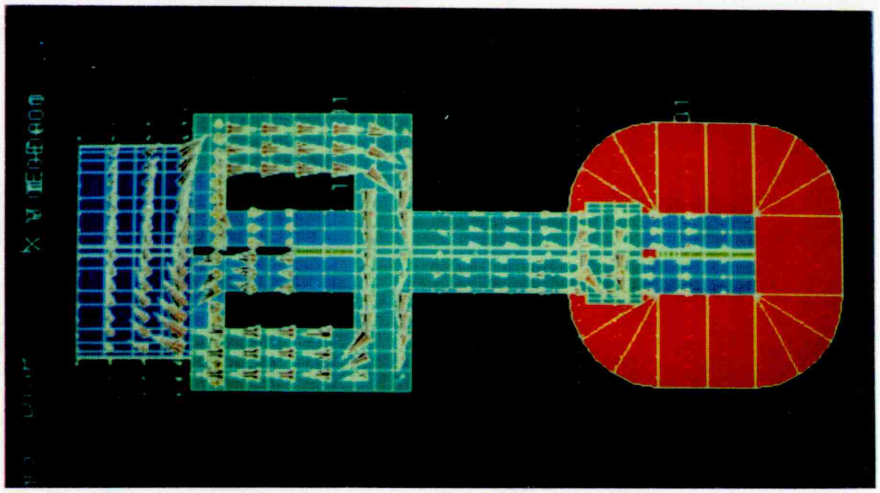

Vector field in armature

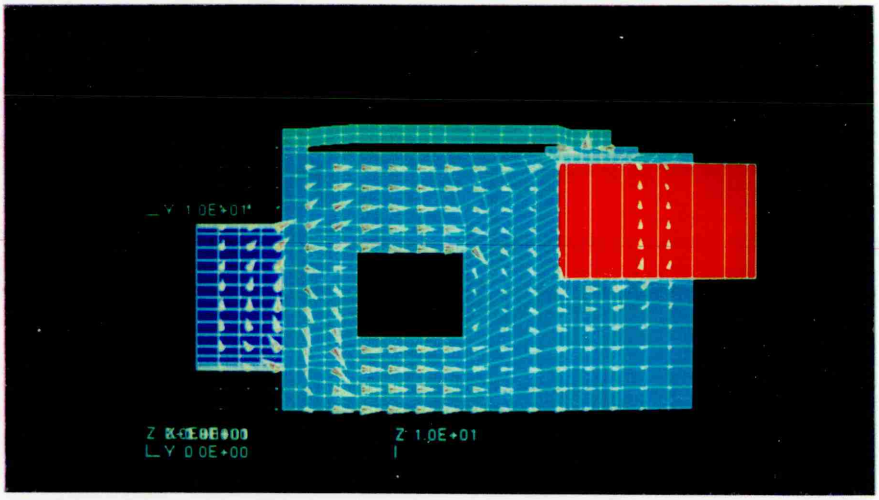

Vector field in yoke

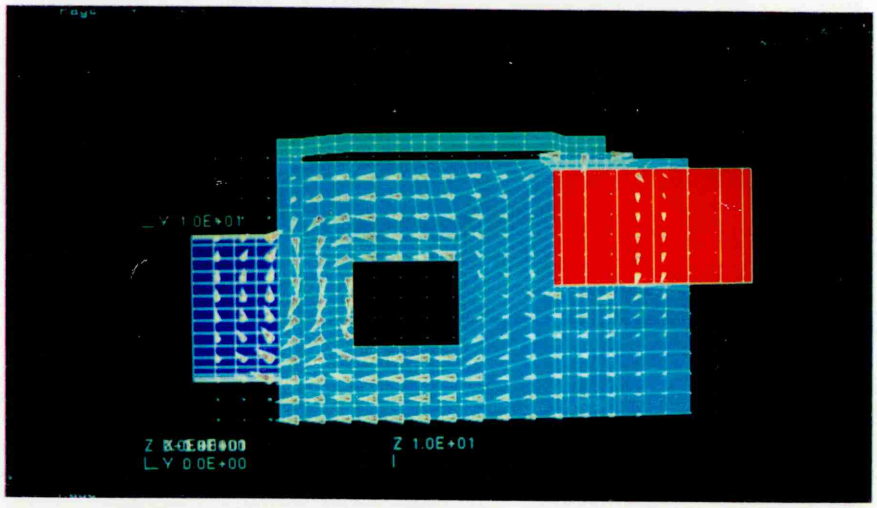

Figure 2.19 Vector magnetic field in the clapper type actuator

2.5 Actuator Energised Steady-State

2.5.1 Characteristics of Force with Tripping Current

Energised steady-state is when the coil current appears until the current is reached at which the tripping occurs. Since the coil current is time varying, the analysis of the actuator magnetic field should take account of the transient variation, which will be returned to in the next chapter. In this section the simulation of the actuator is based neglecting the eddy current and time varying effects. The measurements were made using the dc power supply. Figure 2.20 presents the measured and computed values of the electromagnetic force and initial spring force against trip current

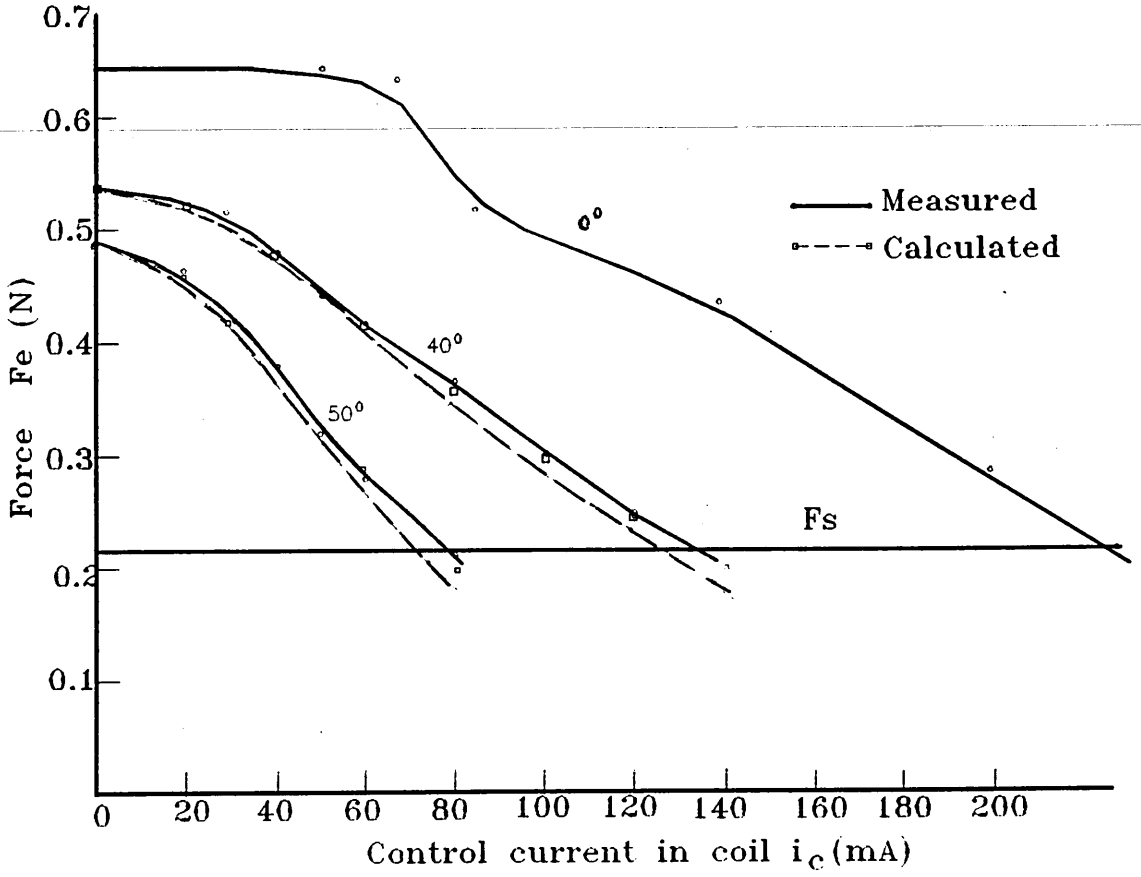

Figure 2.20 Steady-state Electromagnetic force acting on the armature versus the coil current for different magnetic displacement angles

in the coil for three values (0^0,40^0,50^0) of magnet displacement angles for a number of actuators . The attractive forces acting on the armature were measured using the experimental device (shown in figure 2.13). The computation of the electromagnetic field is performed by the magneto-static FE-CAD program described before . The figure also indicates the variation of the electromagnetic force acting on the armature for a specific level of control coil current all of which are shown to be in good agreement.

To precisely detect or set the trip current, the margin of the difference between the two forces is critical and can only be set by permitting the desired trip control current to flow in the coil and then to adjust the magnetic displacement angle to adjust the effect of tripping the armature. The determination of force(Fe) acting on the armature when carrying current is compared by superimposing the force(Fi) produced by the coil current on the constant force (Fm) produced by permanent magnet. The resultant value of the instantaneous forces was computed by setting the value of the current at the time corresponding to the instantaneous value of current. The former technique was used as a means of assuring good quality control in manufacture and test, the latter is used in analysing the relationship between the electromagnetic force and current. In this way the response of the actuator to a sinusoidal current is easily measured and computed.

Figure 2.21 shows the electromagnetic force(Fm) from the permanent magnet and the equivalent forces(Fi) produced by sinusoidal currents of different magnitude , and the effects of the armature force(Fe) of attraction for a typical permanent magnet displacement angle of 50^0 with the time. The pseudo-time-varying force(Fi) can not be directly calculated within the method, but it can be indirectly obtained from Fm-Fe. The measured results

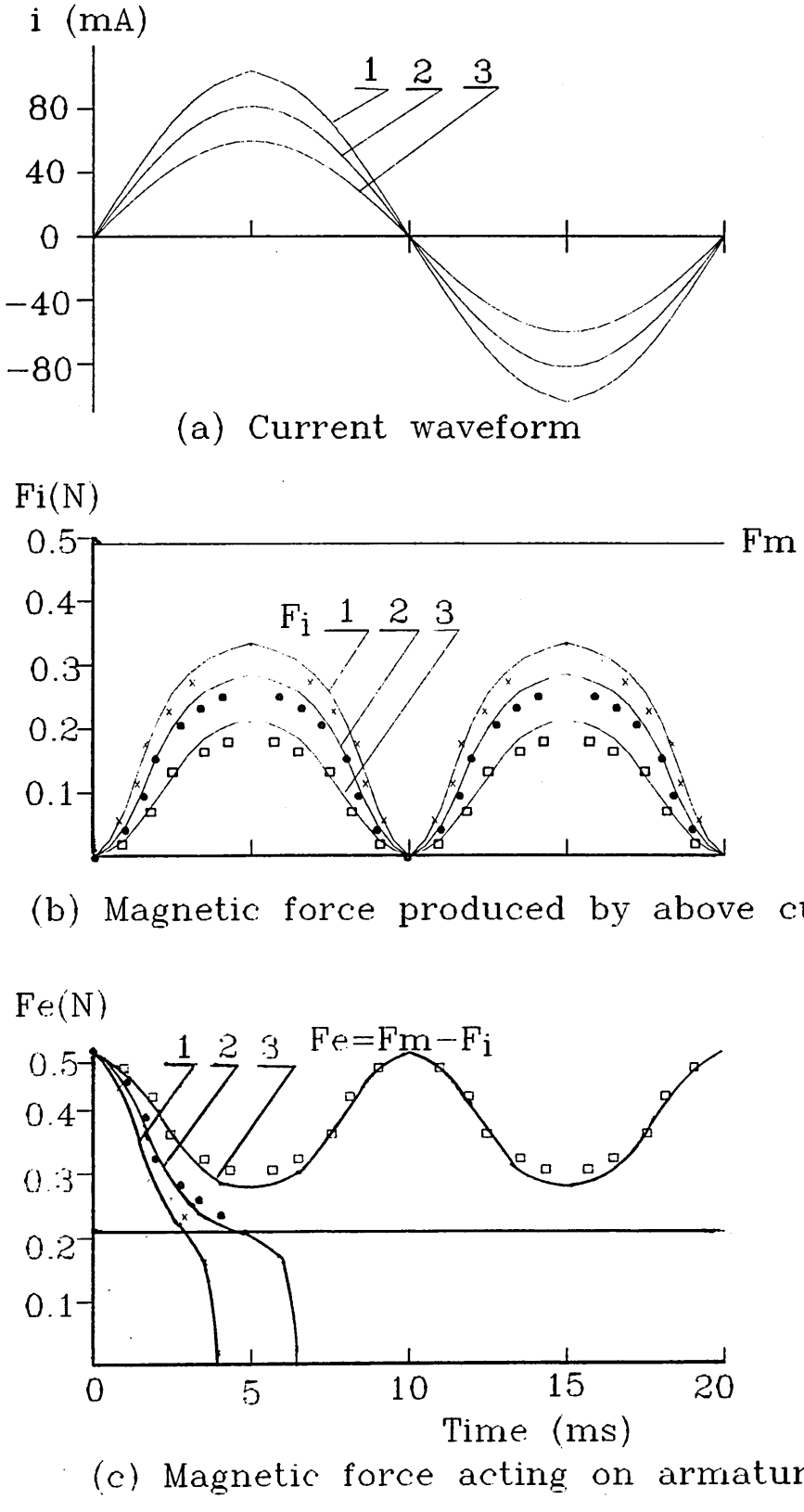

Figure 2.21 Relationship between magnetic force(Fe), current force,Fi(t), and electromagnetic force (Fm)acting on the armature

presented in this figure are the average values of a number of actuators tested. The response of the actuator to sinusoidal current may be explained as follows: when a sinusoidal current (curve 3 in fig. 2.21a) flows into the control coil, the armature force(Fe) (curve 3 in fig. 2.21c) is higher than the spring force, thus the armature remains closed on to the yoke plate. As the current approaches the trip value (curve 2 in fig. 2.21a), the current force(Fi) is increased, consequently the armature force(Fe) reduces to the level of the opposing force. At this moment, the armature begins to move under the action of the spring force, at which instant the force(Fe) will reduce slowly to zero. Consequently, if the current increases in accordance with curve 1 in figure 2.21a, the force (Fe) dramatically decreases to the trip level at approximately 3ms as shown in figure 2.21c. The difference in performance characteristics indicates the precision to which the imbalance current can be detected or the control trip current can be set.

2.5.2 Flux Distributions at Actuator Energised State

To better understand the electromagnetic force characteristics and saturation principle, it is necessary to look at the flux distributions in the field, particularly in the constriction regions when the coil is carrying current. When a sinusoidal current is injected into the control coil, an instantaneous flux φ_i is superimposed on the dc flux φ_1 and φ_2 in the regions x and x' as described,

hence,

$$\varphi_1' = \varphi_1 + \varphi_i$$

$$\varphi_2' = \varphi_2 - \varphi_i$$

The flux (φ_0) in the airgap is the resultant of two fluxes, see figure 2.22. However, the flux φ_1' remains constant rather than increases , flux φ_2' decreases , and consequently the airgap flux φ_0 decreases as current increases, which corresponds to the reduction in the electromagnetic force shown in figure 2.20. The flux density in the constriction regions are given by;

$$B_x = \frac{\varphi_1 + \varphi_i}{A_s}$$

$$B_x' = \frac{\varphi_2 - \varphi_i}{A_s}$$

where As is the area of the cross section denoted by x and x'.

As the coil current increases, the flux density (Bx) increases and Bx' decreases until Bx reaches the saturated flux density of the material as shown in figure 2.23. The TOSCA plots of the histograms of the flux distribution in figure 2.24 highlight the saturation and flux reduction in the regions.

It is instructive to query what happens to the residual flux after the saturation of one of the constriction regions. Figure 2.25 shows the airgap flux and leakage flux versus the control current for a typical permanent magnet displacement angle of 50^0 degrees. This figure confirms that the residual flux goes through the shunt path between the yoke plates rather than path φ_4 after saturation. The figure also demonstrates that the dependency of actuator sensitivity upon the shunt reluctance is significant for this design. Some other interesting points are that the leakage flux φ_3 increases as current increases, but airgap flux decreases. These effects show the flux from the permanent magnet is diverted in to the shunt path, although, the flux φ_4 keeps nearly constant. The conclusion is that decreasing the leakage shunt reluctance increases the leakage flux φ_3' in figure 2.25 and reduces the airgap flux φ_0', thereby increasing the sensitivity of the actuator.

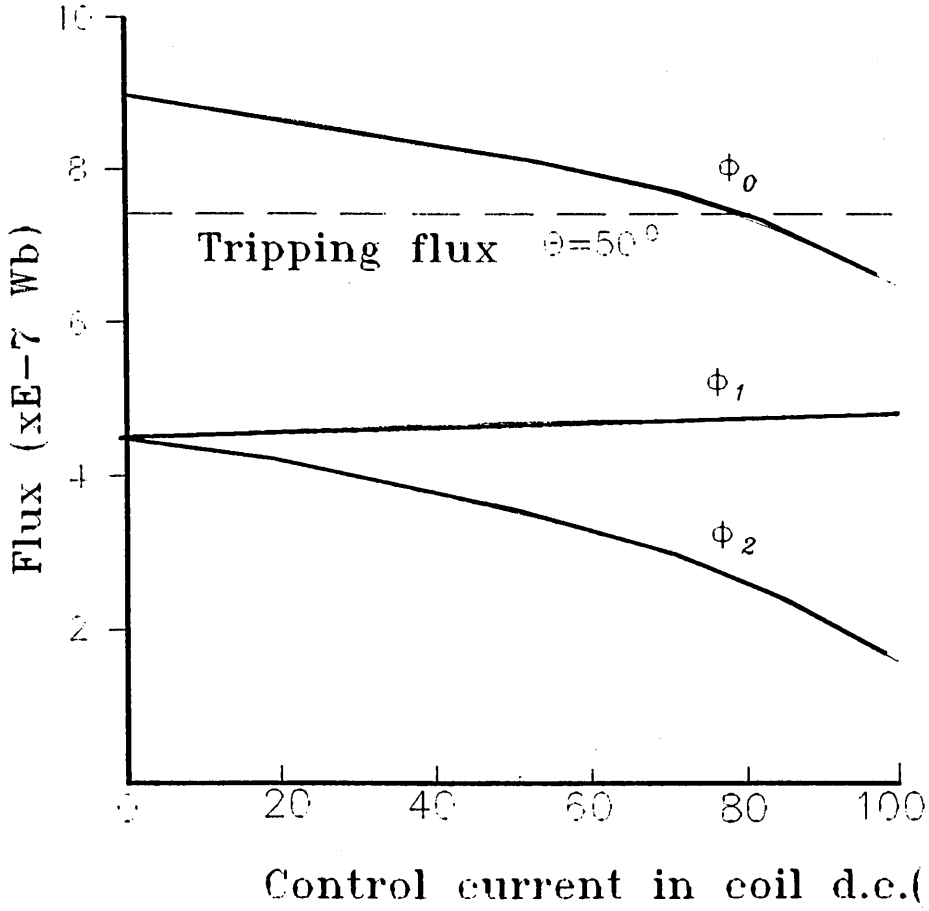

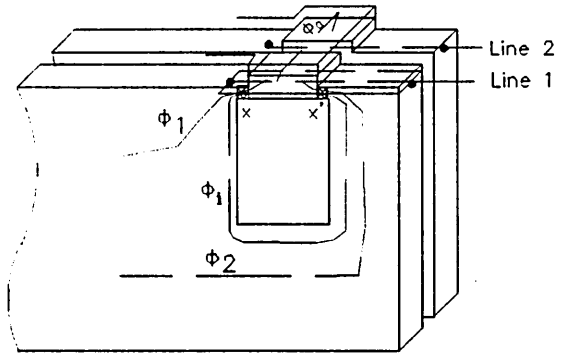

Constriction regions x,x'

Φ_1 Φ_2 —— *Flux produced by permanent magnet through regions x and x' respectively,*

$\Phi_0 = \Phi_1 + \Phi_2$ —— *flux through armature,*

Φ_i —— *flux produced by the excitation current in coil of N turns.*

Figure 2.22 Fluxes in constrictin slots and airgap versus coil control current

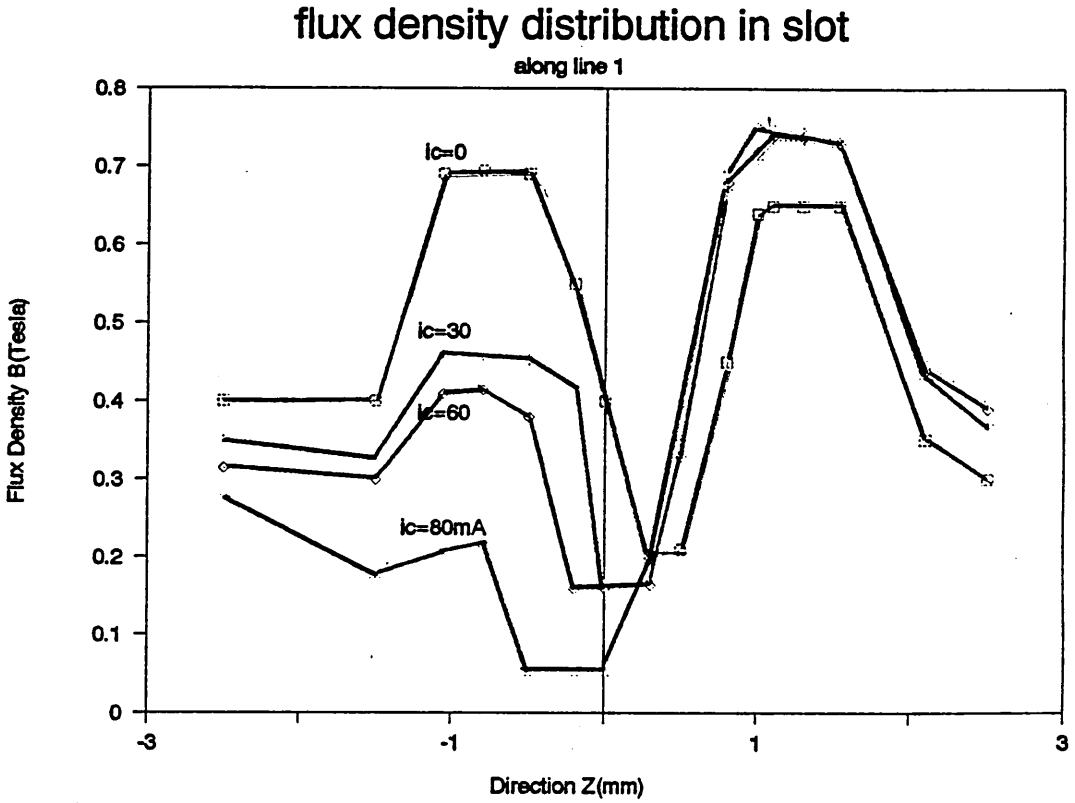

(a) Flux density distribution in the constriction regions in (+) yoke plate

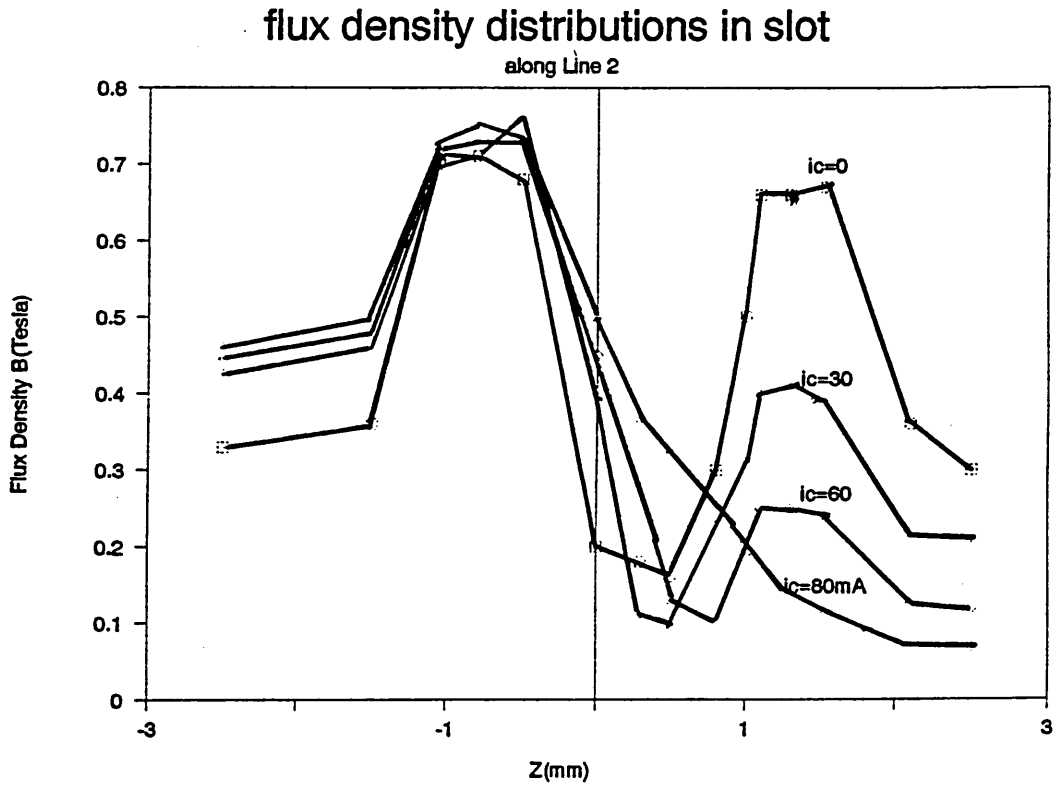

Figure 2.23 (b) Flux density distribution in the constriction regions in (-) yoke plate

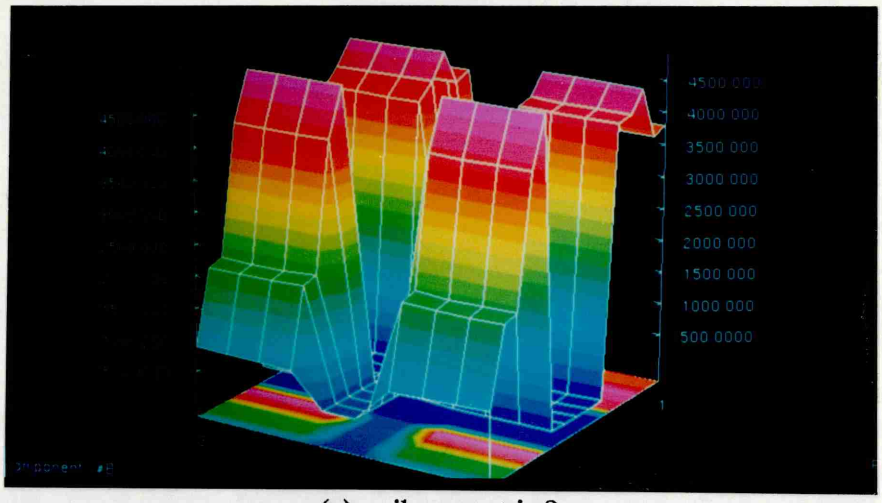

(a) coil current i=0

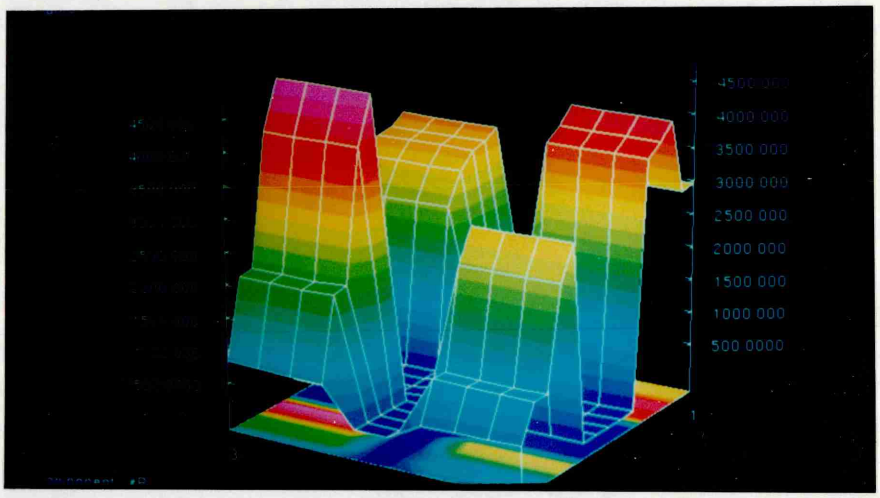

(b) coil current i=30mA

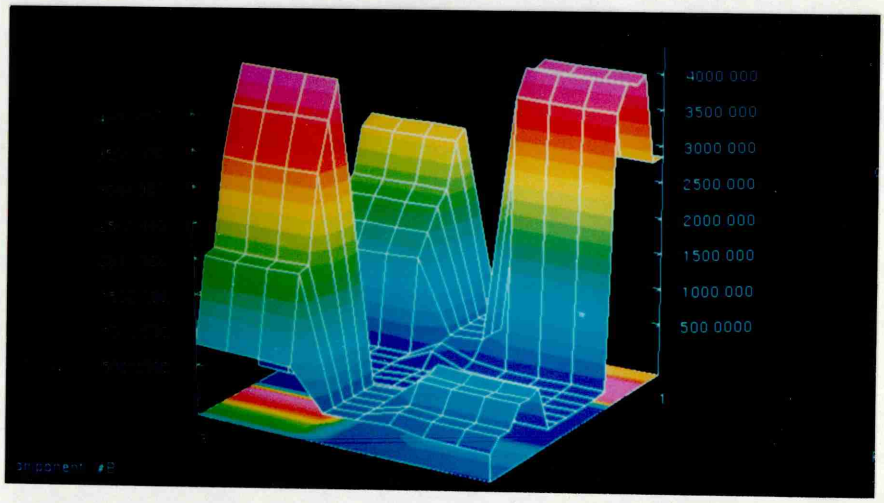

(c) coil current i=80mA

Fig. 2.24 Histograms of flux in constriction slot with coil current i=0,30,80mA

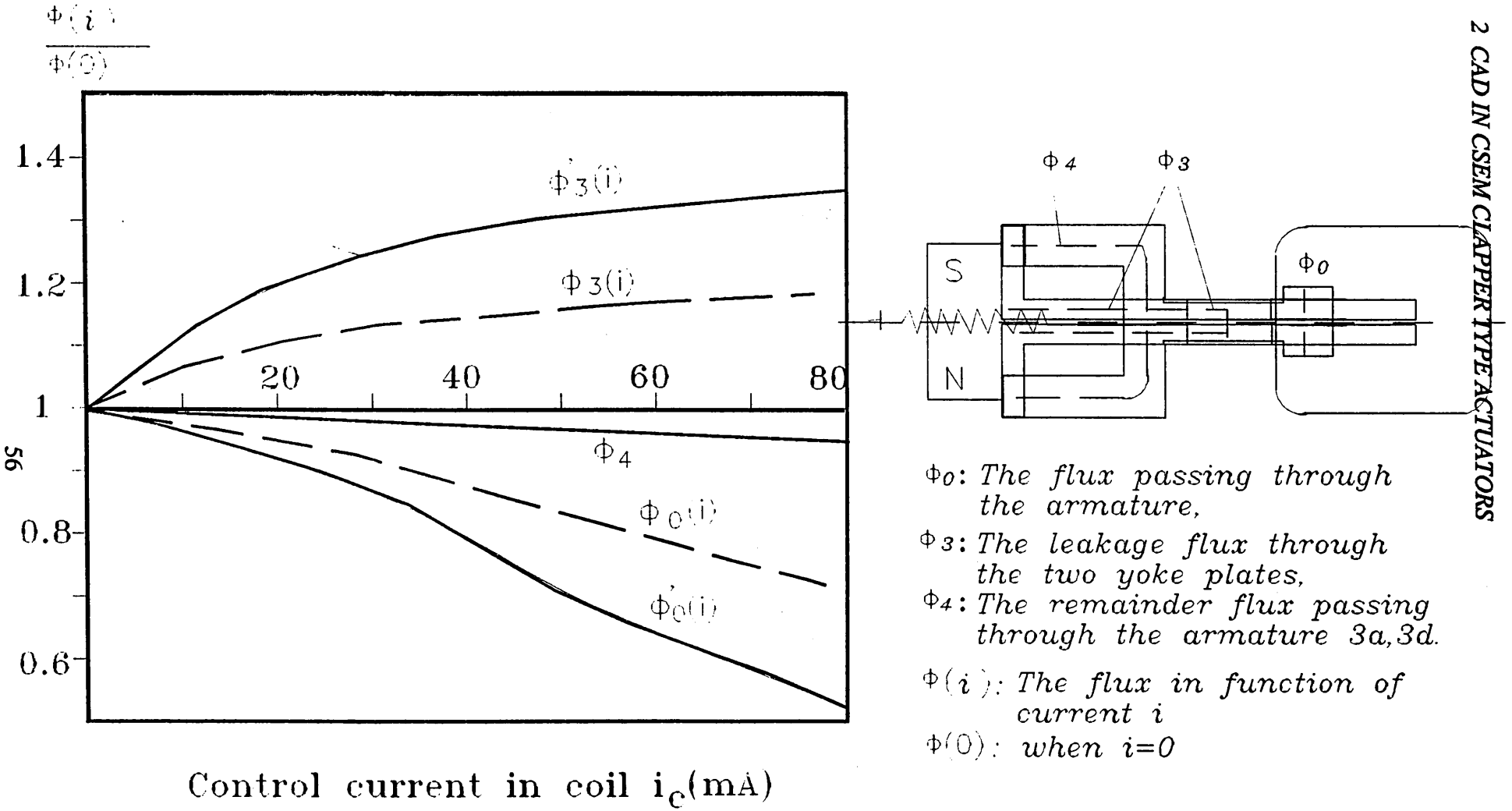

Figure 2.25 Fluxes in working airgap,residual airgap and leakage path against coil current

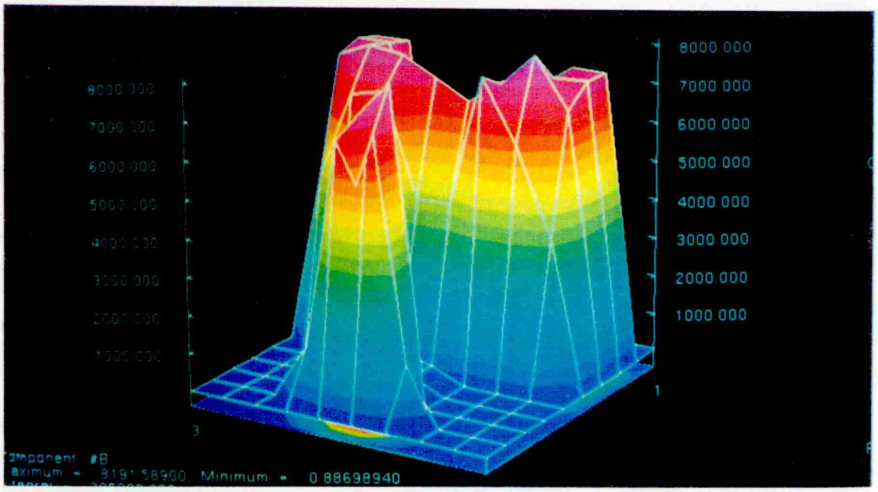

(a) coil current i=0

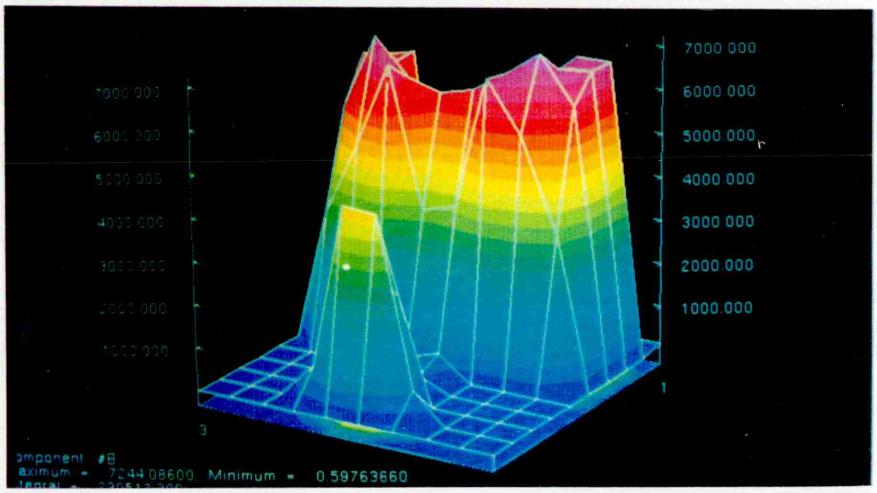

(b) coil current i=30mA

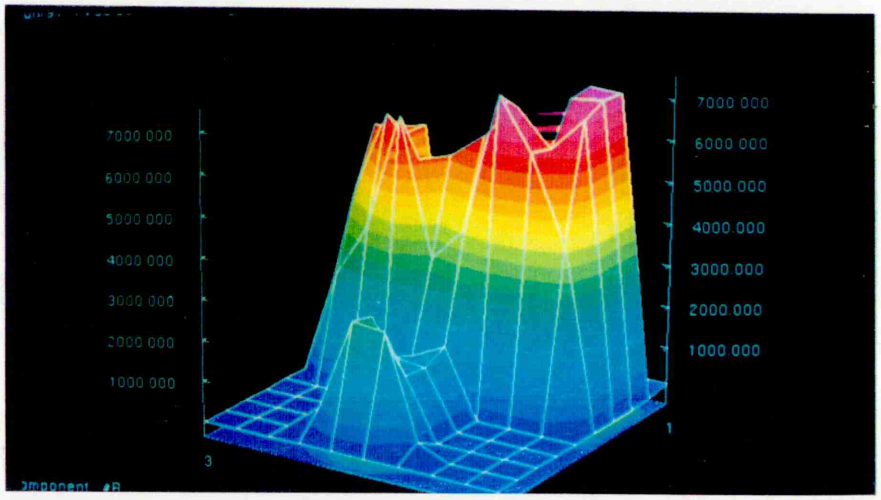

(c) coil current i=80mA

Figure 2.26 Histogram of flux density in the armatures for coil current i=0,30,80mA

2.5.3 Actuator Tripping Characteristics

The actuator tripping characteristics shown in figure 2.27 indicate the trip current variation with magnet alignment for four actuators and confirms the spread of characteristics typically due to manufacturing tolerances . The figure also indicates the need to set the displacement angle between 40^0-50^0 where the curves converge to enable consistent tripping and minimum sensitivity to manufacturing tolerances. The correlation between the measured and computed results is sensible and confirms industrial process manufacturing test practice for setting the magnet displacement. It furthermore highlights the dependency of the actuator performance on high precision manufacture and how practical tolerances can be permitted without producing excessive variations and inconsistency of performance.

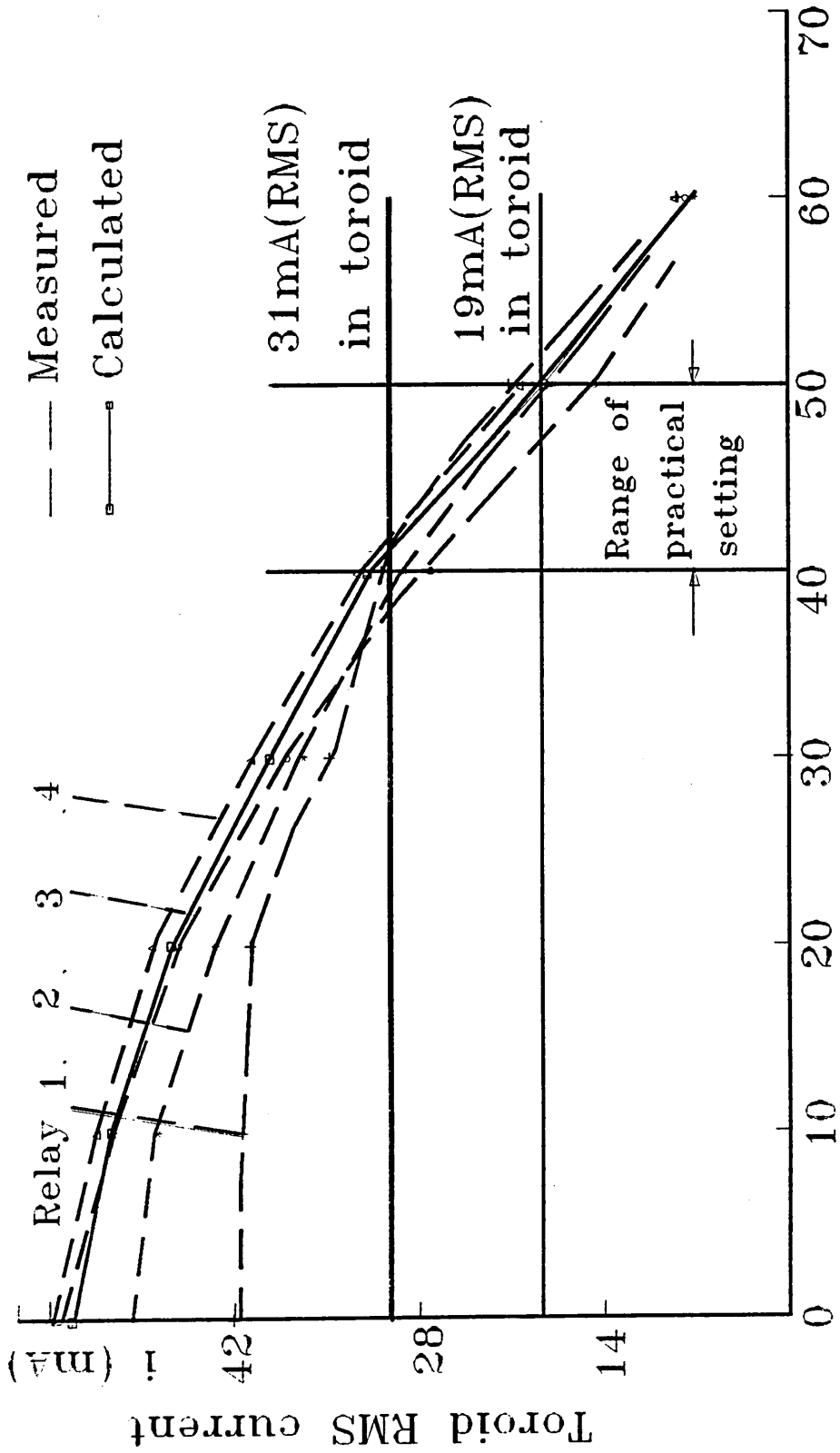

Figure 2.27 Comparison of calculated and measured values of trip current versus magnetic displacement angles

2.6 Conclusions

This chapter has demonstrated, through comparison between experimental and theoretical results, the successful use of the prediction technique for the current sensitive clapper type actuator based on the 3D finite element computation. This technique was employed to predict the performance for two operating stages, namely, the non-energised and energised steady-states of the actuator. These predictions and analysis highlighted some peculiar features of the particular design which were known about but not fully understood.

The analysis permitted characteristics of the performance of the actuator to be predicted in terms of the critical design and control variables. Electromagnetic force acting on the armature was found to be critically dependent on the airgap. The permitted range of manufacture tolerance of the machined surface was obtained between $0.5\pm0.5\mu m$. The analysis further highlighted the sensitivity of operation to the magnetic saturation and polarisation in the design of the actuator. The analytical results compared very closely with the results of test and measurements. This investigation also shows the way in which the optimization design could be undertaken.

Chapter 3

Actuator Energised Transient and Dynamic States

3.1 Introduction

Current sensitive electromagnetic actuators are most commonly designed to operate with AC currents which produce eddy currents in the actuator when operating. The eddy currents produce a flux which diminishes the control flux in the magnetic circuit,which in turn causes a higher tripping current to be required.

The analysis of the actuators using 3D finite element method was based on neglecting the eddy currents, which may lead to unacceptable results when the high frequency current is used to control the actuator. It, therefore, is necessary to know the difference between the static prediction and the transient computation.

In this chapter, the 3D electromagnetic field of the clapper type actuator was modelled as a 2D transient problem, which involves the modelling of the permanent magnet and leakage paths A 2D FEM transient magnetic computation combined with permanent magnet taking account of the 3rd dimension technique was developed and applied to predict the characteristics of the actuators with different tripping current frequencies.

The tripping actuator performs the major role, for example, in the residual current circuit breaker. The response of the actuator is very critical in the operating process. This study investigated the dynamic characteristics of a current-sensitive electromagnetic actuator operated by alternative current with a range of frequencies. The model coupled the electrical, mechanical and magnetic systems of these devices. The decoupled three dimensional finite element integral method was used for determining the dynamic response of the actuator, which took account of the moving armature , and the non-linear properties of the magnetic circuit. The mechanical system of the model included the moving masses and the spring characteristics.

3.2 2D Transient with Permanent Magnet Field Taking 3rd Dimension

3.2.1 Non-linear Transient Magnetic Field with Permanent Magnet Problems

The method to be described is a discretisation approach involving finite elements, since this method is particularly appropriate to numerical solution of complicated geometries. The governing equation for the electromagnetic field involving permanent magnets is

$$B = \mu_0(H + M) \tag{3.1}$$

in which the magnetisation M is a function of the field and the relationship between **B** and **H** is simply represented in the form of BH curves. In equation (3.1) flux density **B** for a region containing no magnetic materials is simply equal to $\mu_0 H$ and, in a region

containing soft iron, is a function of **H.**

The equation can be rewritten as

$$B = \mu_0(H + M' + M_0) \tag{3.2}$$

where $M' = \chi H$ and $\mu_0 M_0 = B_r$ in a region containing the permanent magnet and χ is the incremental susceptibility. This means that one can conveniently represent the flux density in terms of a constant magnetisation vector, together with a single function of H, that is

$$B = \mu' H + \mu_0 M_0 \tag{3.3}$$

where $\mu' = \mu_0(1+\chi)$, it is called the apparent permeability in the permanent magnet region as shown in figure 3.1, which is slightly different from the normal permeability. The permeability of the material is normally defined as $\mu = B/H$.

Taking the curl of each side of equation (3.3) and rearranging it, we obtain

$$\nabla \times H = \nabla \times \frac{B}{\mu'} - \mu_0 \nabla \times \frac{M_0}{\mu'} \tag{3.4}$$

Since the field Vector **B** satisfies the divergence condition, equation(2-2), it can be expressed in terms of a vector potential **A** as follows:

$$B = \nabla \times A \tag{3.5}$$

with $$\nabla \times \left(E + \frac{\partial A}{\partial t} \right) = 0$$

Thus from equations (3.5) the field equation in terms of **A** in two dimensions is given as follows:

$$\nabla \times \nu \nabla \times A - \mu_0 \nabla \times \frac{M_0}{\mu'} = Jc - \sigma \frac{\partial A}{\partial t} \tag{3.6}$$

then

$$\nabla \times \nu \nabla \times A + \sigma \frac{\partial A}{\partial t} = Jc + Jm \tag{3.7}$$

where

$$Jm = \mu_0 \nabla \times (M/\mu') \tag{3.8}$$

is the equivalent current density of the magnet. M is an unknown permanent magnetic source distribution, which in general is nonuniform. ν is the reluctivity of material:

e.g. $\nu = 1/\mu_0$ in the non magnetic regions;

$\nu = 1/\mu$ in soft magnetic material regions;

$\nu = 1/\mu'$ in permanent magnet regions.

With A satisfying the Coulomb gauge $\nabla . A = 0$, the equation (3.7) for the two dimensional field becomes

$$\nabla \cdot \nu \nabla A + \sigma \frac{\partial A}{\partial t} = Js \tag{3.9}$$

where Js=Jc+Jm

In a 2-D x-y Cartesian coordinate system, A,Js have only single vector components Az, Jz.

The equation (3.9) reduces in Cartesian coordinate system to

Cartesian:

$$\frac{\partial}{\partial x}\left(\nu \frac{\partial A_z}{\partial x}\right) + \frac{\partial}{\partial y}\left(\nu \frac{\partial A_z}{\partial y}\right) - \sigma \frac{\partial A_z}{\partial t} = -J_z \tag{3.10}$$

Assuming $\beta = \nu, \gamma = \sigma, u = A_z$ in the 2-D Cartesian coordinate system, equation (3.10) reduces to,

$$\nabla \cdot \beta \nabla u - \gamma \frac{\partial u}{\partial t} = -J_s \tag{3.11}$$

3.2.2 2D Transient FEM Calculation Taking 3rd Dimension into Account

The finite element method was applied to obtain numerical solutions of the non-linear transient problem incorperating a permanent magnet. In the finite element method all domains are subdivided into simpler geometric regions, e.g. into 2D triangles and quadrilaterals etc. The local values of the vector are then approximated by simple functions as follows:

$$u = \Sigma N_j U_j$$
$$J = \Sigma N_j J_j \qquad (3.12)$$

where Uj and Jj are the values of the potential and the current density at the element nodes respectively , the function Nj is the shape function depending on the geometric shape of element. The defining partial differential equations now can be reduced using these local element approximations to a set of algebraic equations using the Galerkin form of the weighted residual method. In this approach equation(3.11) is multiplied by weighting functions, and integration is performed over the solution domains. Thus,

$$\int_{\Omega} N \cdot \left(\nabla \cdot \beta \nabla u - \sigma \frac{\partial u}{\partial t} + Jc + Jm \right) d\Omega = 0 \qquad (3.13)$$

Using the Green theorem the equation (3.13) becomes,

$$\int_{\Omega} \beta \nabla Ni \cdot \nabla u + \int_{\Omega} N_i . \gamma (\partial u / \partial t) d\Omega = \int_{\Omega} N_i (Jc + J_m) d\Omega \qquad (3.14)$$

The Galerkin finite element form for the simply connected eddy current problem for the jth,discretised equation is given by

$$\int_{\Omega_e} \beta \nabla N_i \Sigma \nabla N_j^e u_j d\Omega + \int_{\Omega_e} N_i . \gamma \Sigma N_j^e u_j d\Omega = \int_{\Omega_e} N_i J_c^e d\Omega + \int_{\Omega_e} Ni J_m^e d\Omega \qquad (3.15)$$

which is expressed in matrix notation as

$$[S]\{u\}+[C]\{\dot{u}\}=[P]+[Q] \tag{3.16}$$

where

$\dot{u} = \partial u/\partial t$

$$S_{ij}^{e} = \int_{\Omega_e} \beta \nabla Ni \cdot \nabla N_j d\Omega \tag{3.17a}$$

$$C_{ij}^{e} = \int_{\Omega_e} \gamma N_i N_j d\Omega \tag{3.17b}$$

$$p_i = \int_{\Omega_e} NiJ_c^e d\Omega \tag{3.17c}$$

The integration of permanent magnet term is written by:

$$q_i = \int_{\Omega_e} N_i J_m^e d\Omega$$

$$= \int_{\Omega_e} N_i \mu_0 \nabla \times (M/\mu') d\Omega \tag{3.18}$$

For the permanent magnet with a nonuniform magnetisation distribution, an equivalent current-density distribution exists within the magnet volume, i.e.$J_m \neq 0$ In this case, the magnet boundary surface current model, widely used in magnet-field computations, no longer holds. If the magnet region is discretised into elements, the equation(3.18) is written as:

$$q_i = \int_{\Omega_e} N_i \frac{\mu_0}{\mu'} \left(j \frac{\partial M}{\partial x} + i \frac{\partial M}{\partial y} \right) dxdy \tag{3.19}$$

Assuming each element being an uniform source distribution, in which case Jm=0 in the interior of each magnet element. Figure 3.2 shows the neighbouring magnet

elements e_1 and e_2, the magnetisation vectors of which are in the same direction, but with different magnitude. Applying Stokes theorem to the integral equation(3.19), the equivalent surface current density at the boundary can be easily determined as follows:

$$J_{se} = \frac{\mu_0}{\mu' \Delta l}[\Delta x(M_1^x - M_2^x) + \Delta y(M_1^y - M_2^y)]$$

$$q_i = \int_{\Omega_e} J_{se} N_i dxdy \tag{3.20}$$

Applying the weighted residual approach to the time direction, a general 'θ' method can be established, so that the solution to (3.16) can be obtained by finding the solution to

$$\left[\theta S + \frac{C}{\Delta t}\right]\{u^{n+1}\} + \left[(1-\theta)S - \frac{C}{\Delta t}\right]\{u^n\}$$

$$= \theta(p^{n+1} + q^{n+1}) + (1-\theta)(p^n + q^n) \tag{3.21}$$

which can be simply written as

$$[A]\{u^{n+1}\} + [D]\{u^n\} = [P] + [Q] \tag{3.22}$$

where

$$a_{ij} = \theta \Delta t S_{ij} + C_{ij} \tag{3.23a}$$

$$d_{ij} = (1-\theta)\Delta t S_{ij} - C_{ij} \tag{3.23b}$$

$$p_i = \Delta t[\theta p_i^{n+1} + (1-\theta)p_i^n] \tag{3.23c}$$

$$q_i = \Delta t[\theta q_i^{n+1} + (1-\theta)q_i^n] \tag{3.23d}$$

and $\Delta t = t^{n+1} - t^n$

This gives rise to the standard numerical solution techniques for specific values of theta (e.g. θ=1/2 gives Crank Nicholson method). The Newton-Raphson method can also be implemented to solve this type of non-linear equation (3.22). In the context of non-linear finite element solutions to the electromagnetic field equations, the reliability of the Newton-Raphson method is strongly linked to the smoothness of the equation used to relate the permeability, alternatively to how close the estimate of initial values are to the converged solution. The eddy currents are determined using a simple difference expression for the nth time step. The eddy current density Je in this case is given by

$$J_e^n = \sigma \frac{u^{n+1} - u^n}{\Delta t} \tag{3.24}$$

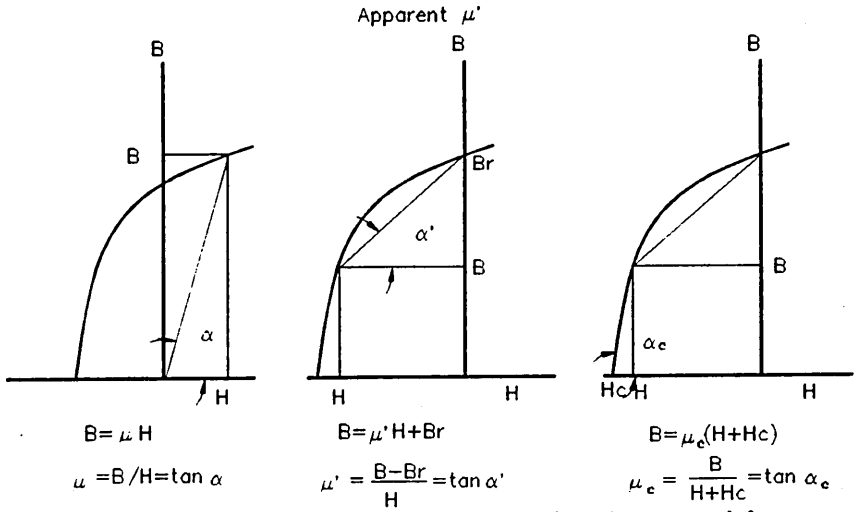

Figure 3.1 Alternative methods of representing demagnetising curve

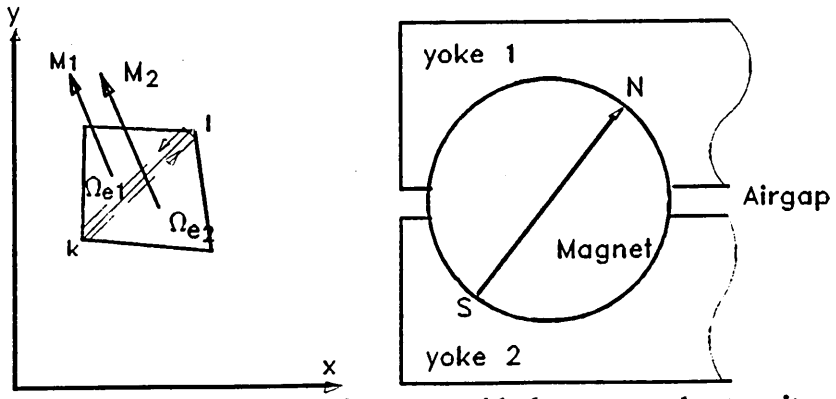

Figure 3.2 Cross section view of magnet with the current sheet on its surface

3.3 2D Simulation of the Actuators

3.3.1 2D Electromagnetic Modelling

The solutions of the actuators described in chapter 2 neglected the eddy currents. In fact, the operation of this type of current sensitive actuator is time-varying, thus solution of the magnetic field is a transient problem. The computation for the saturation characteristics is very significant, since the saturation property greatly affects the performance of the actuator when it is energised. These make the use of linear simulation impossible, and the use of nonlinear transient numerical computation essential. In order to quickly solve this transient nonlinear problem, an approach employed is to use a 2D to model a 3D magnetic field.

The following assumptions are made using 2D to model 3D actuator magnetic field:

(i) the airgaps and size of yoke plates in modelling 2D are same as in 3D,

(ii) the leakage shunt reluctance in modelling 2D is same as in 3D,

(iii) the fringing flux from the edges are neglected in modelling 2D,

(iv) the variations in 3rd axis are neglected but a correction factor in 3rd dimension is introduced,

(v) the dimensions of the permanent magnet are modelled to produce the same magnetization strength MMF in2D and 3D,

(vi) since the fluxes only pass through the contact surfaces of the armature, therefore the armature was assumed to be two pieces of magnetic material where the areas of the contact surfaces are same as the corresponding of the 3D surfaces.

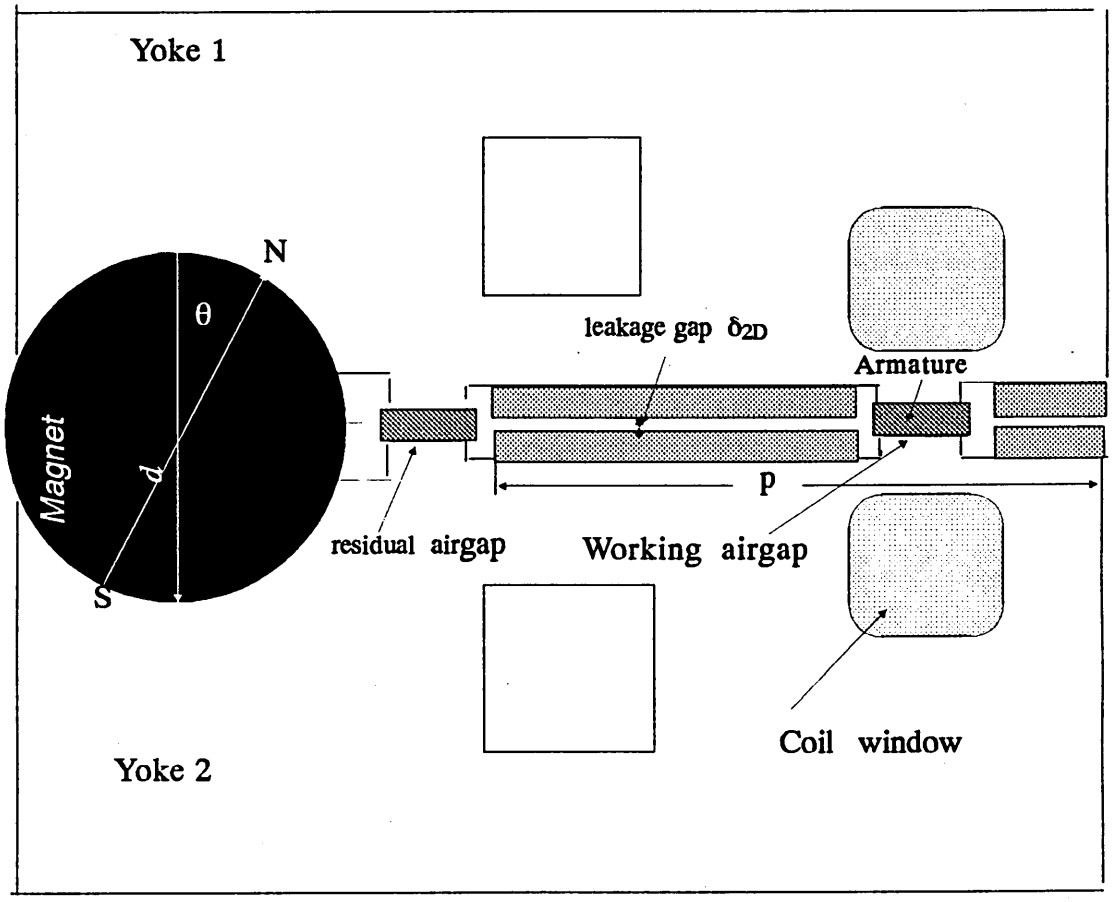

Figure 3.3 2D modelling of the actuator magnetic field

The modelled 2D electromagnetic field of the actuator is shown in figure 3-3. The permanent magnet is inserted into the yoke plates and the magnetic polarisation can be changed by means of rotating the magnetic angle (θ). The size of leakage gap (δ) in 2D is calculated, as follows:

The magnetic leakage shunt reluctance in 3D model is

$$R_{3D}=\frac{\delta_{3D}}{\mu_0 S_{3D}} \tag{3.25}$$

where R_{3D} is the leakage shunt reluctance in the 3D model;

S_{3D} is the face-to-face area of the yoke plates;

δ_{3D} is the distance between the two yoke plates.

The equivalent leakage shunt reluctance in the model 2D is given by

$$R_{2D}=\frac{\delta_{2D}}{\mu_0 S_{2D}} \tag{3.26}$$

where R_{2D} is the leakage shunt reluctance in the 2D model;

δ_{2D} is the length of leakage gap in 2D model;

S_{2D} is the area of leakage faces .

Assuming the 2D equivalent leakage reluctance(R_{2D}) being equal to the reluctance (R_{3D}), hence, the equivalent length of leakage airgap in 2D is given by

$$\delta_{2D}=\frac{\delta_{3D}}{S_{3D}} S_{2D} \tag{3.27}$$

For one of the actuators investigated in last chapter, the dimensions are δ_{3D}=0.12mm,S_{3D}=10.61x16.41=174.1mm^2 ,S_{2D} =pxa=16.41x0.9=14.8mm^2 then the size of leakage airgap in the model 2D is approximated as δ_{2D} =0.01mm. The dimensions of the permanent magnet,see figure 3.3, are the thickness a=0.9mm and the diameter(d) of magnet is varied according to the equivalent magnetisation strength. The magnetisation strength in 2D corresponding to each magnetic angle θ is expressed as:

$$M_{2D}(\theta)=M_o\cos\theta \tag{3.28}$$

where Mo is the maximum magnetisation strength when $\theta=0$;

M_{2D} is the equivalent magnetisation strength for a magnetic angle(θ).

3.3.2 2D Static Computation

The 2D magnetic field model is generally symmetrical along the centre line, but its magnetic field is non-symmetrical except at magnetic angle($\theta=0$), therefore, the whole region has to be taken into account. The characteristics of the actuators performed in the simplified 2D magnetic field may not cope with corresponding to the characteristics in 3D. The objects here are to simulate a 2D model which could produce the approximately same characteristics as in 3D. The following two-step method is applied to calculate the dimensions of the 2D field domain. Firstly, the 2D dimensions of the permanent magnet modelling from 3D are calculated by means of the equivalent volume, then the 2D magnetic field system can be computed and analysed and corresponding force. The results computed in 3D and compared with measured results necessitate adjustment of the parameters of the model by trial and error and recalculation of the field to obtain good solutions. These two steps are required to be repeated until the results converge to corresponding 3D solutions.

The magnetic material properties in 2D computing are the same as in 3D. Setting the airgap g=1μm for the non-energised state, the 2D magneto-static FEM was used to compute the magnetic field, and the magnetic forces acting on the armature for different model dimensions of the permanent magnet are listed in table 3.1

Table 3.1 2D computed magnetic forces $\theta=40^0$

a(mm)	d(mm)	δ(mm)	F_{2D}(N)	F_{3D}(N)
0.9	10	0.008	0.4	
0.9	11	0.008	0.43	0.5
0.9	11	0.01	0.45	
0.9	12	0.01	0.53	
0.9	12	0.012	0.57	
0.9	11	0.012	0.53	
0.9	12	0.008	0.48	

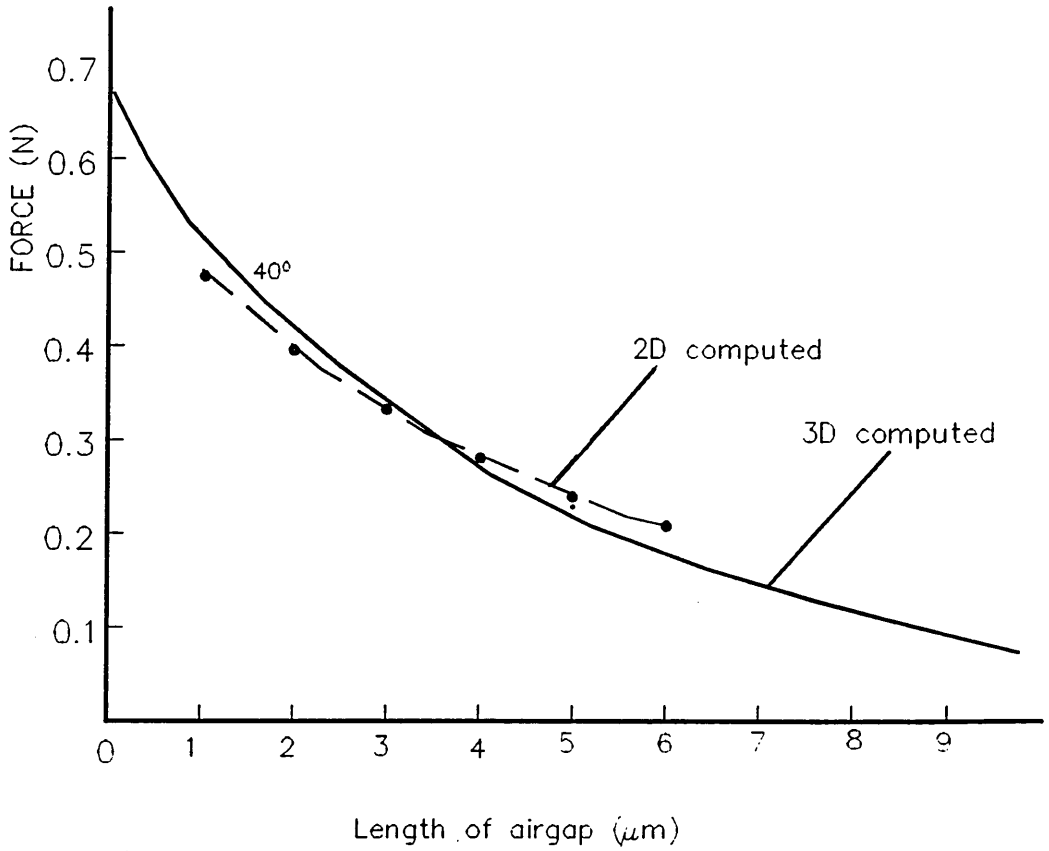

Figure 3.4 Electromagnetic force acting on armature computed in 2D model and 3D static magnetic fields

The results indicates that if the dimensions of the permanent magnet are taken as a=0.9 and d=12mm and δ=0.008-0.01mm, the forces computed in 2D magnetic field are reasonably close to the force (0.5) performed in 3D.

The magnetic forces of attraction were computed based on the classified permanent magnet size of a=0.9,d=12mm for the range of airgaps(1μm-5μm) as shown in figure 3.4. This figure also shows the comparisons between the forces predicted in model 2D and in 3D for each corresponding airgap.

3.3.3 3rd Dimension Effect on 2D Computation

The fringing flux from the edges was neglected in the 2D magnetic field simulation. However, when the constricted regions are heavily saturated, particularly, when current is injected into the coil, the fringing flux cannot be ignored, since this may affect the computation accuracy. In order to diminish this effect, the influences of 3rd dimension has to be taken into account. Two diagrams of the leakage flux are plotted in figures 3.5a and fig3.5b. Fig.3.5a shows the fringing flux to be negligible for unsaturated fields, and figure 3.5b shows the fringing flux distribution along the edges for the saturated field.

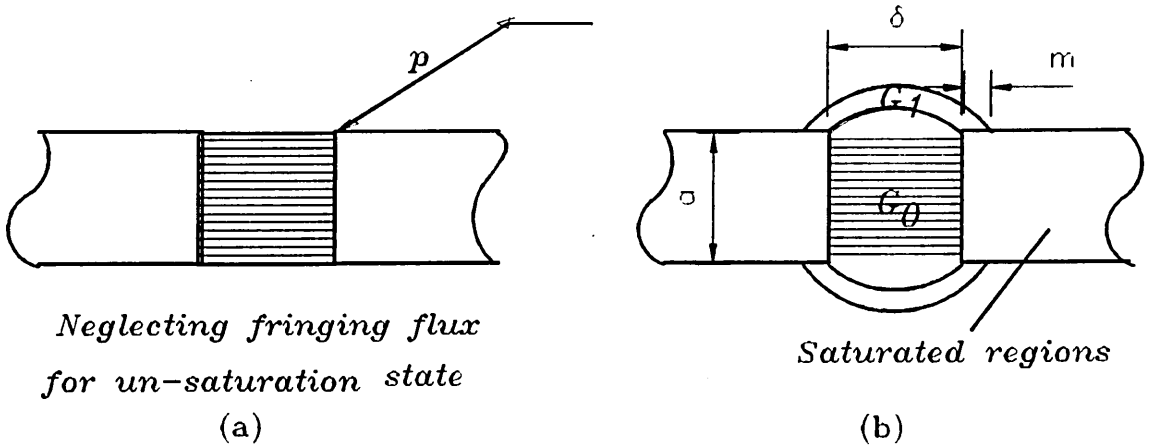

Figure 3.5 Fringing flux distribution in the leakage gap

The reluctance for figure 3.5b is given by

$$R_\delta=\frac{1}{G_0+G_1} \tag{3.29}$$

$$R_\delta=1/G_\delta \tag{3.30}$$

where G_δ is the inverse reluctance to R_δ , $G_\delta=G_0+G_1$ and they are given:

$$G_0=\mu_0\frac{a\,p}{\delta} \tag{3.31}$$

$$R_1=\frac{1}{G_1}=\frac{p}{8\mu_0}\left(\frac{\pi}{2}-\tan^{-1}\frac{a}{\delta}\right)\left(\delta^2+4m\sqrt{a^2+\delta^2}+4m^2\right) \tag{3.32}$$

Since the leakage flux (φ_δ) is inversely proportional to the leakage reluctance(R_δ) and the magnetic force acting on the armature is proportional to the square of the flux in airgap (φ_a), thus

$$\varphi_\delta \infty \frac{1}{R_\delta}=G_\delta \ , \ \varphi_a \infty R_\delta$$

and $F \infty \varphi_a^2$

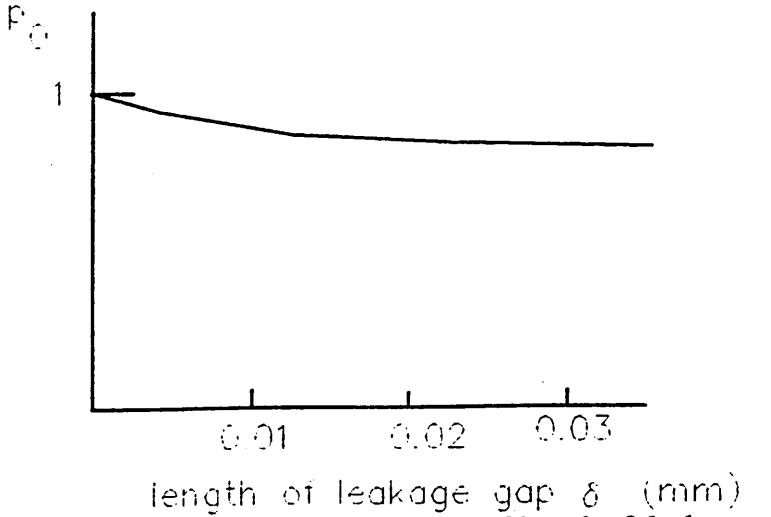

Figure 3.6 Correction factor as function of length of leakage gap

Here a correction factor (p_0) is introduced. The factor can be expressed in terms of the square of a ratio which is the inverse reluctances G_0 to G_δ .

$$p_0=\left(\frac{G_0}{G_0+G_1}\right)^2 \tag{3.33}$$

From equations (3.31),(3.32) and (3.33), the function(p_0) is obtained to the length of leakage gap (δ) as shown in figure 3.6.

The computed results for airgap of 1μm when the control coil carrying currentsare listed in table 3.2. These results take the factor p_0 into account and the values are also presented in the table3.2.

Table 3.2 Comparison of force varying with DC current in 2D transient and 3D static fields for airgap=1μm

Dimensions (mm)			Coil MMF	Force in 2D(N)		Force(N)	
a	d	δ	(AT)	2D	Corrected	3D	Measured
0.9	12	0.01	0.4	0.48	0.44	0.42	0.45
0.9	12	0.01	0.6	0.39	0.36	0.34	0.35
0.9	12	0.01	0.8	0.29	0.26	0.25	0.27

Comparisons between 2D forces and 3D computed forces in tables 3.1 and 3.2 demonstrate that if the dimensions of permanent magnet are classified as a=0.9, d=12mm and leakage gap δ=0.01mm in 2D modelling, the computed forces of attraction in 2D are reasonably close to the forces predicted in 3D for the range of airgaps 1-5μm at non-energised state and energised state for neglecting the eddy current in the iron.

3.4 Transient Analysis of the Actuators

The transient magnetic finite element method was used to compute the 2D electromagnetic field of the actuator. The dimensions of the 2D model were the same as the dimensions used in static computation. The dimensions of the permanent magnet being a=0.9, d=12mm and δ=0.01mm were used. The computed force of attraction in the 2D transient field associated with a sinusoidal tripping current at the frequencies of 10,50 and 100Hz is shown in figure 3.7. The figure shows the comparison between the forces performed in the 2D transient and in the 3D static fields and together with the measured results.

Figure3.7 shows that when higher frequency control current is applied, a higher tripping current is required in order to subtract the attractive force from static value(Fm) to trip force level (Fs). The figure also demonstrates that when the current frequency is less than 100Hz, 3D static predicted results are reasonably close to the results predicted in the 2D transient field. If the control current frequency is over 100Hz the 3D predicted results differ greatly from the 2D transient predictions and measured values. The reason is that at the higher frequency the currents produce higher eddy currents which diminish the effect of control current on the actuator. However, the static computation cannot include this effect. From the computation and simulation, the main conclusions to be drawn are as follows:

(i) the predicted results using the 2D transient magnetic field model are reasonably close to the measured ones

(ii) 3D static computation could be used to predict the characteristics of this type of magnetic actuator for control current frequency less than 100Hz.

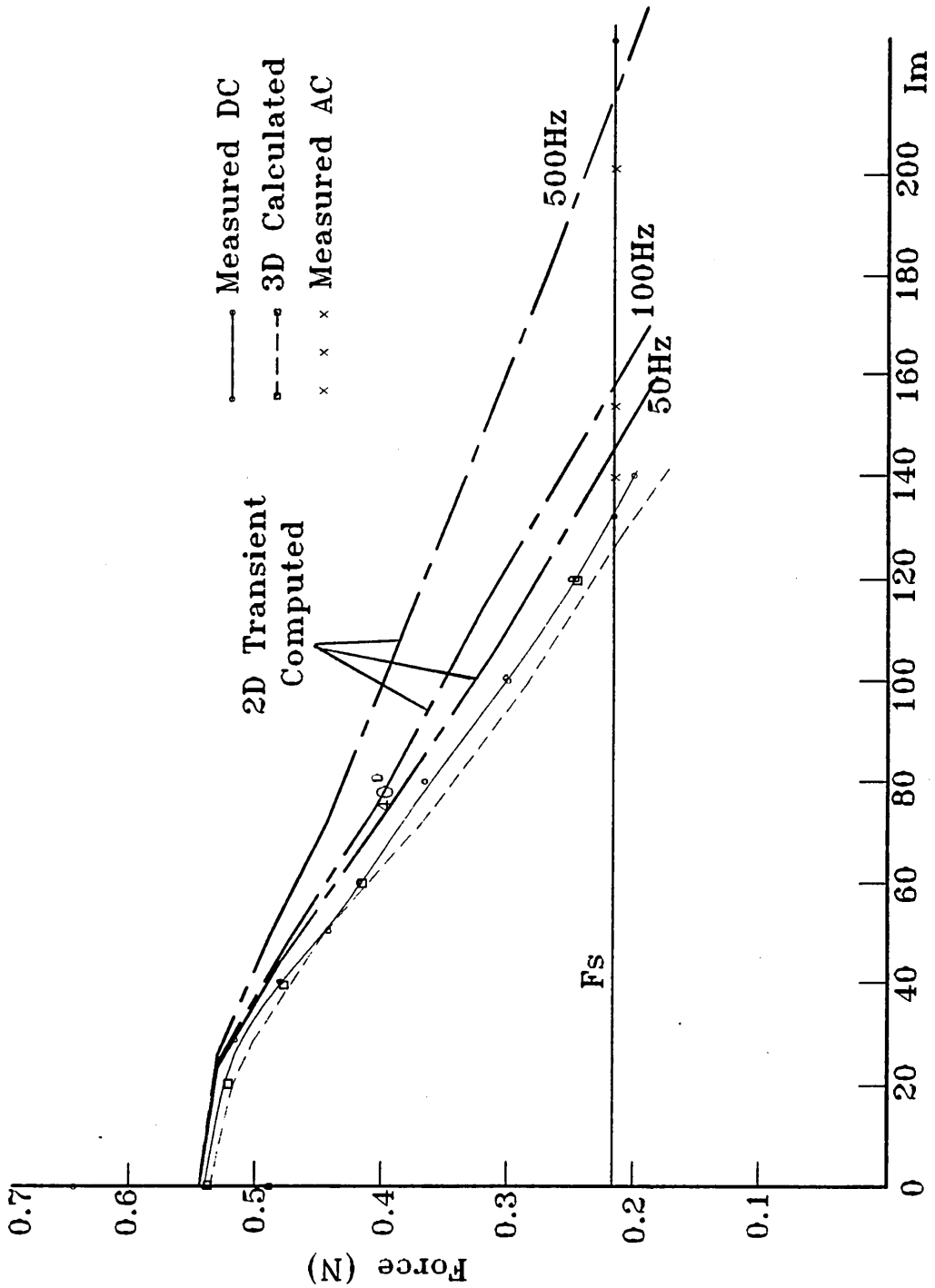

Figure 3.7 Comparison of the computed electromagnetic force between 2D transient and 3D static fields of the clapper actuator

3.5 3D FEM for Determining the Transient Response of Actuator

Based on the study [12] of the time/current zones on the effect of AC current on humans, a range of declared safety current thresholds exist for the duration and amount of the current passing through the human body. For example, when a value of 30mA(RMS) current flows in a human body, the safety duration is limited to 200ms[APPENDIX I] for which usually no harmful physiological effects occur. At increasing current levels the probability of a lethal electrical accident is reduced by reducing the duration of the current flow. The effects of shock current on humans are not relevant, here to say that 30mA is a common trip current level for domestic and many electrical installations.

When a residual current circuit breaker is used to prevent electrical accidents, the duration of the current passing through the human body is defined from the time when the person touches a live part, to the time when the circuit is broken. In other words, from the moment current imbalance occurs to isolation of the current in the circuit by the RCD device.

3.5.1 System Topology

The general circuit diagram is shown in figure 3-8 in which the actuator is used to trip the latch mechanism. If the currents in the live (L) and neutral(N) lines are equal their magnetising effects on the core of the transformer are equal and opposite, and therefore cancel. The actuator does not react. A small difference in the two currents will produce an imbalance current which will magnetise the core. A voltage appears in the output winding and consequently a current flows in the control coil to reduce the electromagnetic force acting on the armature until it trips.

Once the armature leaves its seating, the attractive force dramatically decreases and the armature is drawn away by means of the opposing spring, to release the latch mechanism. It is reasonable to assume that the transfer loss of energy between the two elements and the reluctance of the secondary winding (normally only 1 turn) are negligible.

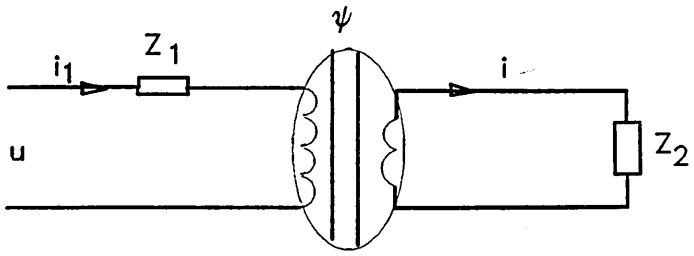

Figure 3.8 General circuit diagram of the actuator

AC current with different frequencies was taken into account in the simulation. The equations of the circuit are:

$$u=Z_1 i_1+\frac{d\psi}{dt} \tag{3.34}$$

$$0=iZ_2+\frac{d\psi}{dt} \tag{3.35}$$

then,

$$i=\frac{i_1 Z_1-u}{Z_2} \tag{3.36}$$

where flux ψ is in the toroidal transformer.

If the input current is a sinusoidal waveform, the output current should be sinusoidal, neglecting the transfer energy losses.

The spring force equations are therefore derived from the force diagram in figure 2.11 as;

$$Fs(y)=[F_{sz}\, l_y - F_{sy}\, lz\ ]\ /l_a \qquad \text{for } 0<y<0.5\text{mm}$$

$$Fs(y) =[F_{sz}\, l_y - F_{sy}\, l_z\ ]\ /l_a - F_c \qquad \text{for } y>=0.5\text{mm}$$

where

$F_{sz} = F_{so} \sin(\beta(y))$

$F_{sy} = F_{so} \cos(\beta(y))$

$\alpha(y) \approx y/l_a$, $\cos(\beta(y)) = l_y / l_s$

The equation for the spring tension force Fsp, acting along the axis of the spring, was determined in equation (2.38)

3.5.2 Decoupled integral-3D-FE method

3.5.2.1 Dynamic equations

From the force diagram and magnetic circuit systems, the dynamic equation of the moving armature is solved by reducing the second order differential equation to two first order equation;

$$Fs(y)-Fe(i,y)=m\, dv/dy \qquad (3.37)$$

$$v=dy/dt \qquad (3.38)$$

where m is the mass of the moving part,

y the airgap spacing and v is the velocity,

Fe(i,y) is the electromagnetic force acting on the armature in function of control current(i) and airgap displacement.

The initial conditions are determined by measurement and computation and prescribed as follows;

$$y|_{t=0} = y_0 = 0.5\mu m, \quad v|_{t=0} = 0, \quad i|_{t=0} = 0$$

$$Fs(y_0)\,|_{t=0} = F_{so},\ Fe(0,y_0)|_{t=0} = F_0$$

where Fo is the magnetic force acting on the armature produced only by the permanent magnet, and Fso the initial force of the spring acting on the armature in y direction.

From measurements the armature was found to strike the trip mechanism when y=0.5mm, whereupon the spring force is suddenly opposed by the trip mechanism force Fc.

3.5.2.2 Decoupled Integral - 3D FEM method

The Decoupled method is based on predetermining the electromagnetic force Fe(i,y) for a range of currents and displacement values, using 3D finite element solution such as TOSCA, and to then store the values in the form of look-up data tables. The solution of the dynamic equation then progresses in incremental time steps Δt by substituting the latest computed values of Fe(i,y) and Fs(y) into the difference equation (3.37) corresponding to the respective values of the instantaneous current and displacement at the instant $t=n\Delta t$. The latest calculated value of the velocity is obtained from

$$v_{n+1} = v_n + \frac{F_s(y) - F_e(i,y)}{m}\Delta t \qquad (3.39)$$

where n is the current number of time increment.

The latest value of armature displacement is subsequently determined by substitution of the calculated values Vn , Vn+1 into the corresponding weighted difference equation

$$y_{n+1}=y_n+\frac{\Delta t}{2}(v_n+v_{n+1}) \tag{3.40}$$

3.5.3 Dynamic Characteristics For 50Hz Sinusoidal Current

The proposed Decoupled integral 3D-FE method was used to predict the dynamic performance of the current sensitive actuator. Figure 3-9 shows the characteristics of the electromagnetic force Fe(i,y) before and after the armature moving for a 50 Hz sinusoidal control current (3 primary coil turns and 1 secondary turn in the toroid transformer). The results indicate that for 50Hz current the delay, before the armature commences movement, is of the order of 3ms. Figure 3-10 shows the characteristics of the dynamic response of the armature, which also shows the vari-

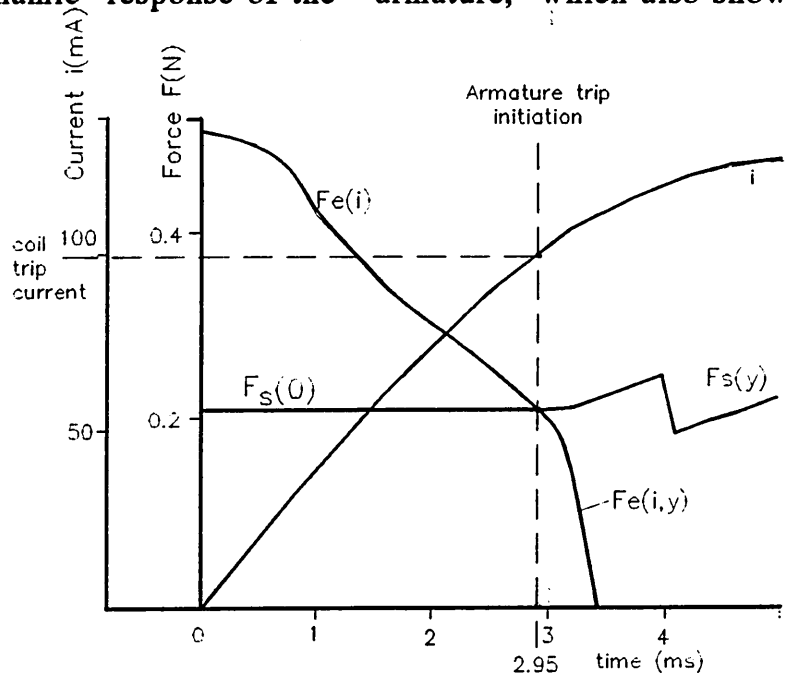

Figure 3.9 Actuator dynamic response characteristics for a 50Hz sinusoidal control current(1)

ations of velocity, displacement and force with the operating time. This figure shows the classical rapid declination of the electromagnetic force acting as the air-gap increases. The figure also clearly exhibits that the opposing spring force Fs(y) increases slightly and suddenly drops when the displacement exceeds the critical value where the 'y' component of the spring force Fs(y) changes sign. This action is of academic interest only since it has little effect on the transient response of the actuator. The measured and calculated response time of the actuator at magnetic displacement angle of 50^0 degrees is given in the Table 3-3.

Table 3-3 Comparison between measured and predicted response time

Calculated (ms)	Measured(ms)	relative error
4.95	5.6	11.6%

The distributions of the magnetic flux at different times were plotted as shown in figure 3-11. The figures demonstrate the diffusion of the flux produced by the tripping coil currents into the magnetic yoke at different times and the corresponding diminution of the flux in airgap. Actually, when the coil flux gradually diffuses into the iron yoke around the window with increasing control current, the coil flux adding to the permanent magnet flux in one constriction region causes the saturation, which forces the permanent magnet flux to be diverted into shunt path. Consequently, the flux in other path is diminished by the coil flux. It can be seen that when the leakage flux increases, the airgap flux decreases as the control flux increases after the time t=1.5ms. The armature motion does not commence until the resulting force falls below the opposing spring force at the time, t=2.95ms. Almost all the flux passes through shunt

path, after t=3.4ms. The figure shows that the armature moves to the position where the mechanism releases at the time t=5.5ms.

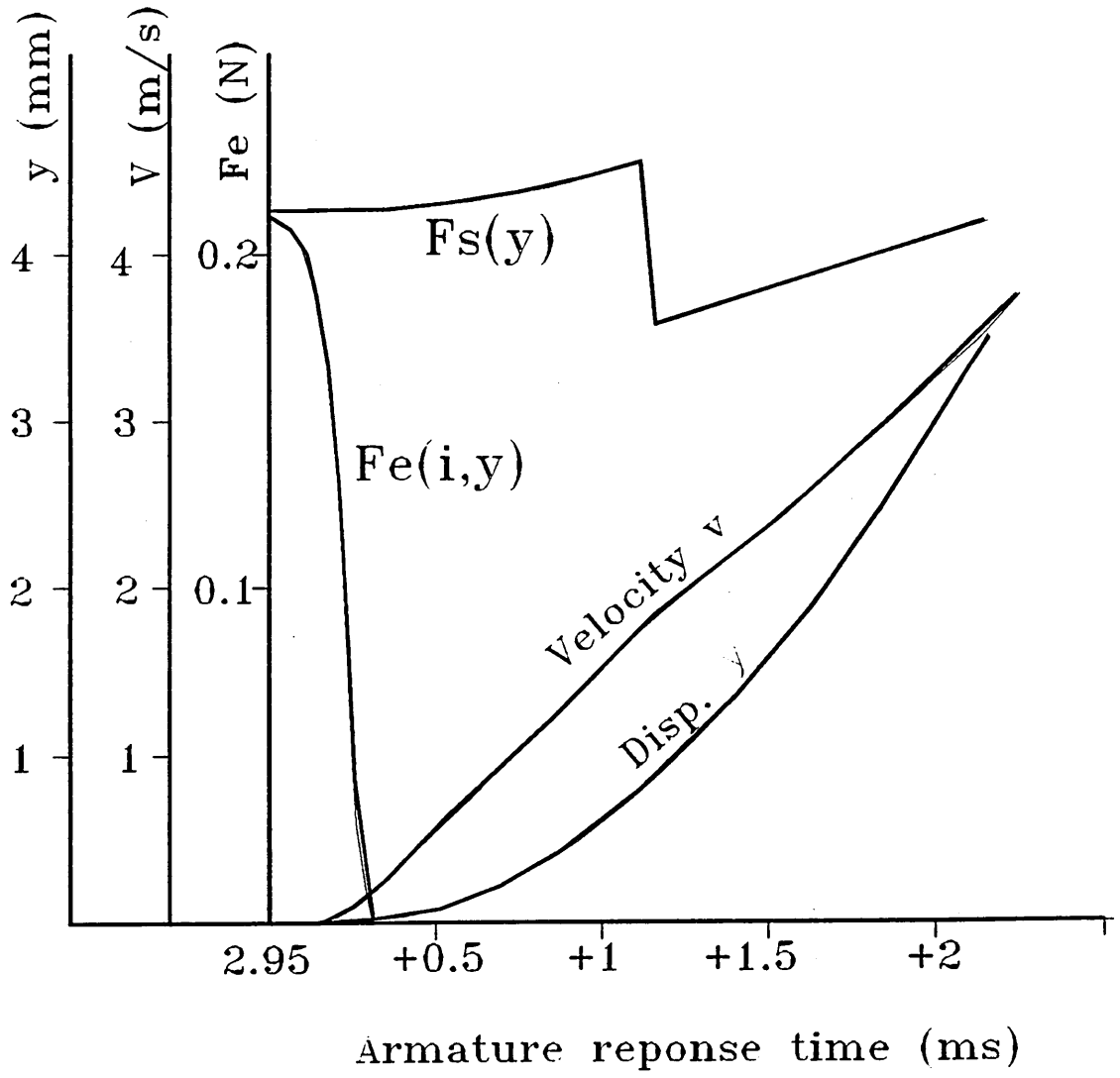

Figure 3.10 Actuator dynamic response characteristics for a 50Hz sinusoidal control current (2)

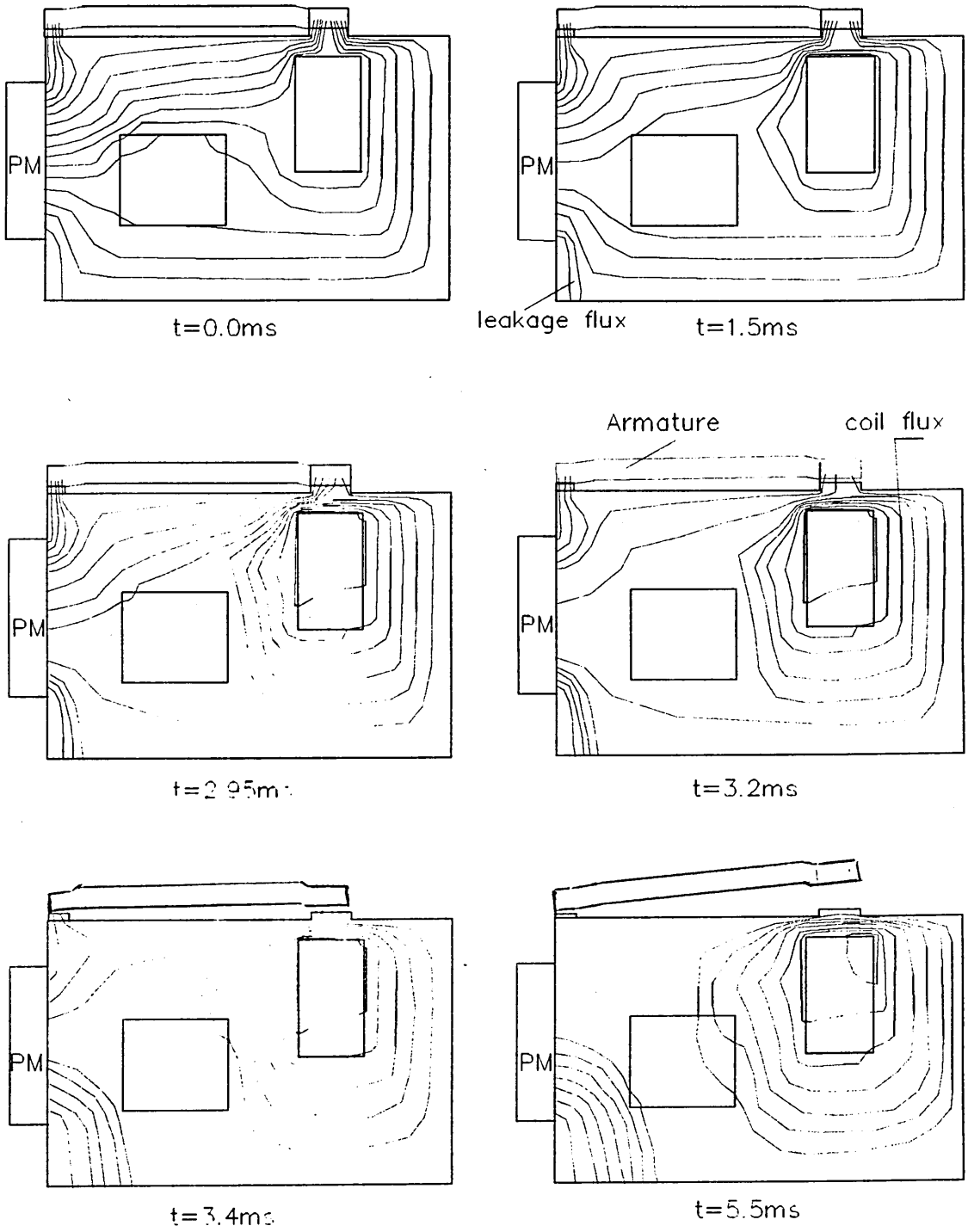

Figure 3.11 Flux distribution in the magnetic actuator at different time

3.5.4 AC Current with High Frequencies

Higher frequency supplies nowadays are increasing in applications, e.g. power tools up to 450Hz and for electromedical purpose, for example in electrotherapy, using mostly 4000Hz to 5000Hz. As it is known from the research of the electrical impedance of the human body[12]. The impedance of the human skin for touch voltages in the order of some tens of volts decreases approximately inversely with frequency. This skin impedance at 500Hz is only about on tenth of the skin impedance at 50Hz. At higher frequencies the impedance of the human body is reduced down to the value of its initial resistance Rb.

The studies indicated that the sensitivity to the effects of higher frequencies on the perception, let-go and ventricular fibrillation of the body is greater than at 50/60Hz. A higher sensitivity quick response residual current operated circuit breaker may now be required to protect electric circuit. Although the effects on ventricular fibrillation humans is inextricably related to the length of heart-beat, this complicates the situation and the applications of RCD devices for protecting humans at higher frequencies.

Figure 3-12 shows the variations of trip current(RMS) against frequencies for a production type actuator.

The tested oscilloscope curves for the current frequencies of 50,100,500 and 800Hz are shown in figure 3.13. In these figures, at time t_0 , the current i=0, at time t_1 , the armature commerces to move and at time t_2 the armature moves to the open position. It can be seen that the tripping current is increased with increase of the current frequency and the response time is decreased as analysed.

The response time of the clapper type current sensitive actuator for a range of frequencies from 20Hz to 1000Hz are computed and together with the measured results are given in Table 3.4

Table 3.4 Measured and calculated response time for different frequencies at magnetic angle of 65^0

Current frequencies (Hz)	20	50	100	500	1000
instantaneous trip current (mA)	36.8	40.1	50.9	84.3	126.0
3D calculated response time(ms)	5.2	4.0	2.8	2.0	1.9
Calculated response time in 2D transient	-	4.7	3.6	3.2	
Measured time(ms)	-	4.3	3.3	2.8	-

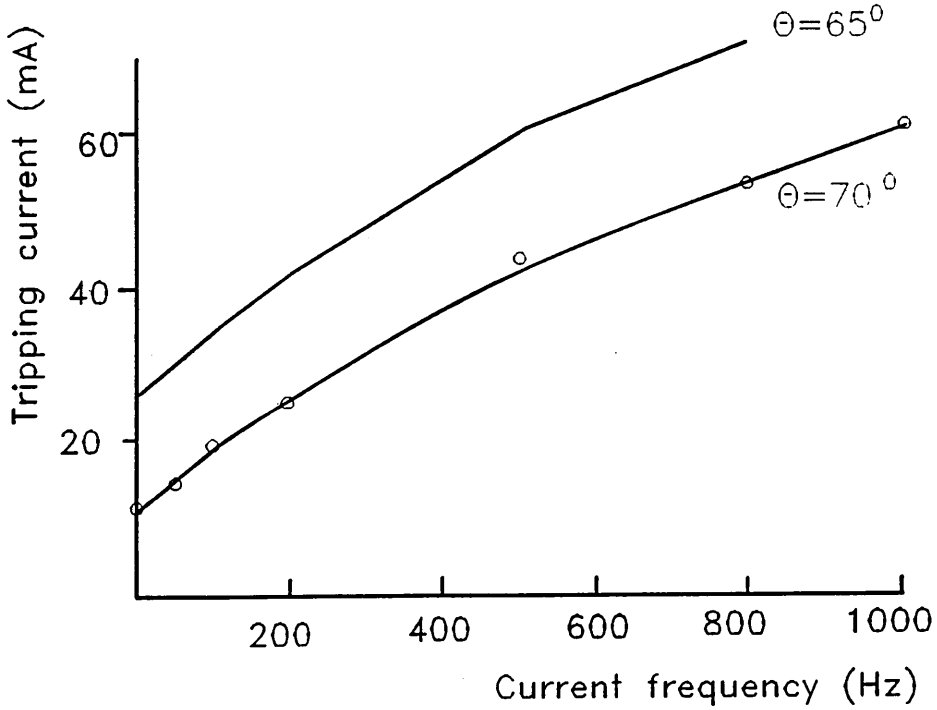

Figure 3.12 Trip current against control current frequencies at an opposing force of 0.21N

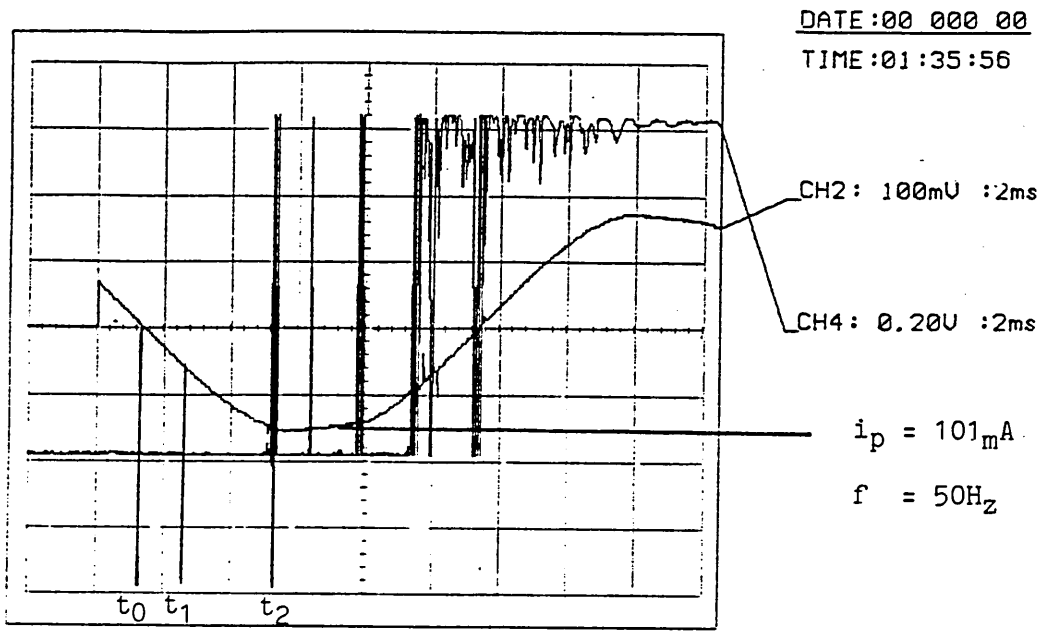

(a) trip current for 50Hz

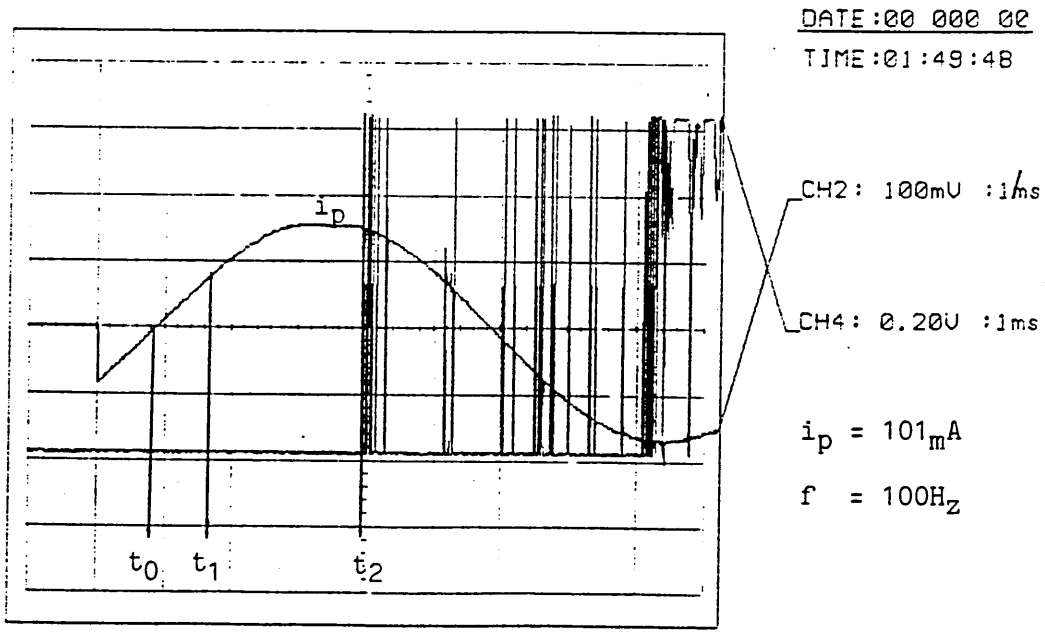

(b) trip current for 100Hz

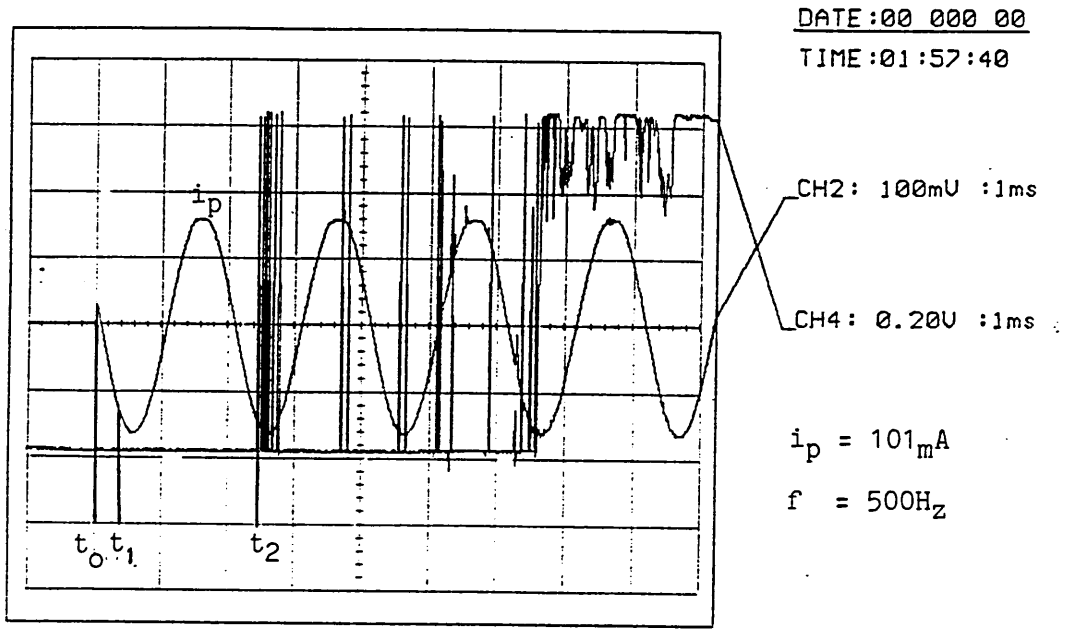

(c) trip current frequency 500Hz

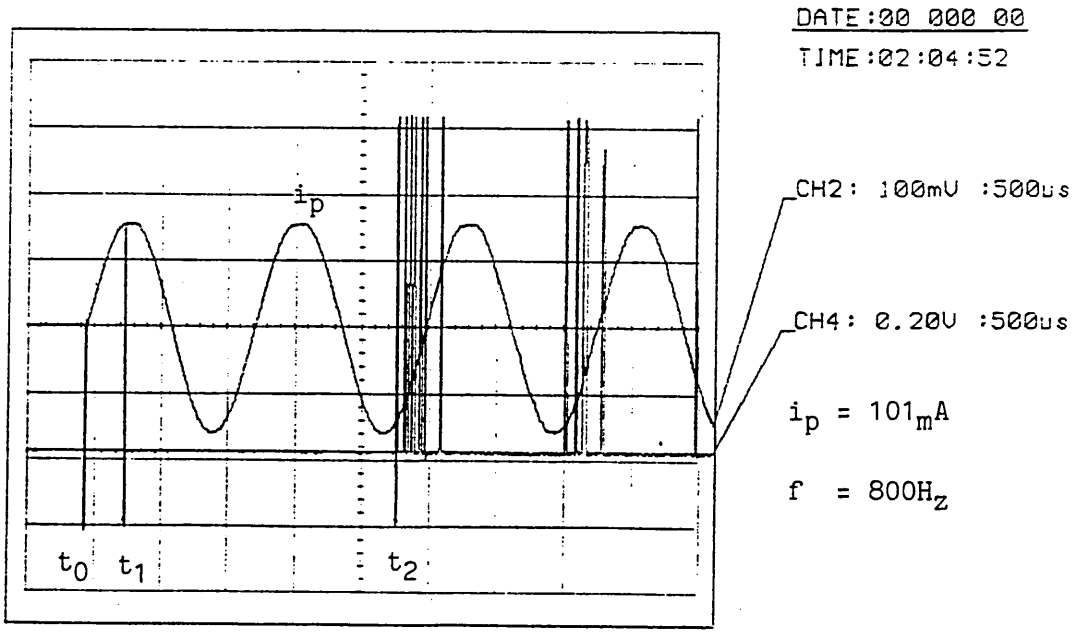

Figure 3.13 Oscillograms of the tripping for different current frequencies 50,100,500 and 800Hz

3.6 Conclusions

The three dimensional magnetic field of the actuator was modelled as a two dimensional transient field. The 2D transient magnetic finite element method, which took account of the 3rd dimension by means of a correction factor, was developed and used to evaluate the characteristics of the actuator with time-varying current. It was found that the three dimensional static computation is highly suitable for analysing actuator design for control current frequencies less than 100Hz, but beyond 100Hz the use may lead to unacceptable errors.

A decoupled 3D-FEM integral method was proposed to enable the solution of the dynamic response of a current sensitive electromagnetic actuator to a time-varying current. The method took account of the complete magnetic circuit and mechanical design of the actuator and therefore permitted the actuator response and design to be optimized for any current waveform. Given that the travel time of the armature to actuate the mechanism was of the order of 4-5ms, the analysis indicates that initiation would occur within 2.5ms. This result compared very favourably with measurements.

Chapter 4

Optimisation Design of the Clapper Type Actuators

4.1 Introduction

It is most important to minimise the source MMFs and size of magnetic circuit for improving the actuator sensitivity. The investigations are made into the effects on the actuator operating characteristics of changes to some key dimensions and to control coil and magnetic material properties using FE-CAD technology by reference to those for a typical actuator whose details are illustrated in the figure 2.3. Finally, an improvement to actuator design is given.

4.2 Optimisation of Shunt Reluctance

The dependency of the actuator sensitivity upon the length of airgap has been demonstrated above. The rest of the design parameters such as shunt reluctance, dimensions of constriction regions, contact surface and material properties also have significant effects on the actuator characteristics. This section gives consideration to these dependencies and also to their optimization.

The intermediate layer between the yoke plates (see fig. 2.3) provides a relatively high reluctance to flux, namely, the leakage shunt path, for the permanent magnet as described. The value of the leakage shunt reluctance greatly influences the diversion of the flux away from airgap into the shunt path during energisation, which consequently significantly affects the sensitivity of the actuator to control current. The shunt reluctance can be expressed in terms of a factor Ks, which is the ratio of the distance(δ) between the two yoke plates to the face-to-face area(S) of plates, $Ks=\delta/S(\mu m/mm^2)$. Figure 4.1 shows the armature force as a function of the shunt factor(Ks) for different airgaps. Figure 4.2 shows the relationship between the shunt factor (Ks) and the force reduction(Fi), which is expressed as the difference

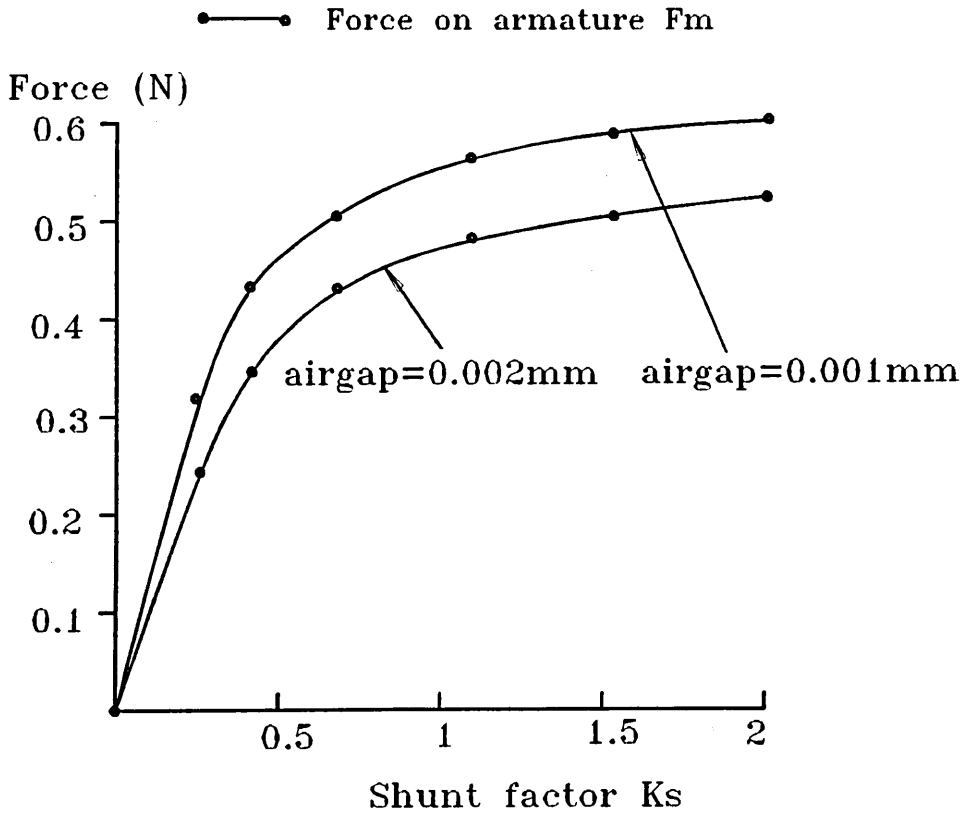

Figure 4.1 Electromagnetic force acting on the armature against the shunt factor(Ks)

between the non-energised armature force (Fm) and the energised force (Fe). This figure also indicates the variation of actuator sensitivity, Fi/AT, which is the ratio of force reduction(Fi) to the control ampere turns(AT), to the shunt factor(Ks). It is observed from figure 4.1 that the armature force increases as the shunt reluctance increases, since a large shunt reluctance leads to less flux through the leakage path. However, it also can be seen(fig 4.2) that the highest sensitivity occurs between, Ks=0.5-1. The reason is that a small shunt reluctance leads to most flux of the permanent magnet having to pass through the shunt path and consequently less flux passing through the airgap. In contrast, a large shunt reluctance leads to most of the flux passing through the airgaps rather than the shunt path. Both of these

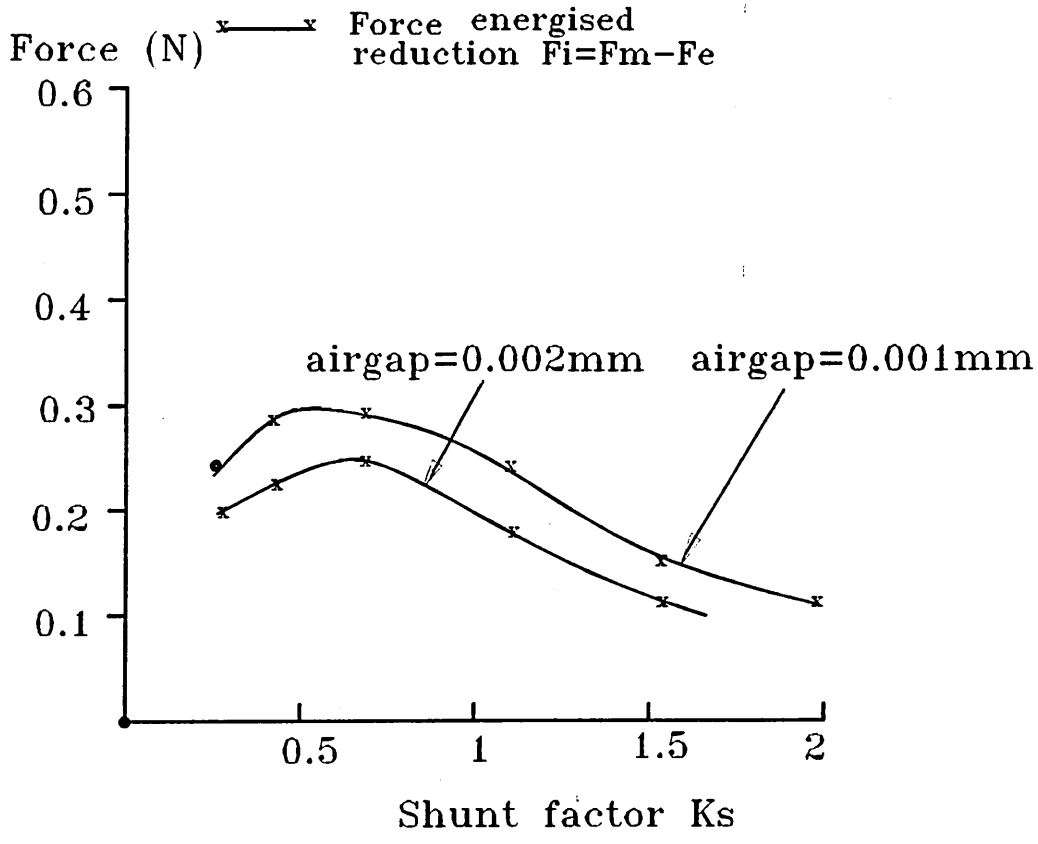

Figure 4.2 Reduction of armature force versus shunt factor(Ks) for different airgaps

contrary effects reduce the sensitivity for which a maximum exists The figure also gives the optimum design point of the shunt reluctance. These characteristics also can be seen to be highly dependent on the airgap dimensions.

4.3 Optimization of Constriction Slot

As described earlier, the area of the constricted section considerably affects the force on the armature due to slot saturation, when the coil carries current. This effect is shown in figure 4.3 where the constricted section is expressed in terms of a factor, Ko, which is the ratio of the slot area to its length. The magnetic force of attraction on the armature increases with increase of the slot factor, whereupon it approximates to a constant value, since a large area of slot diverts more flux to the airgap. It can be seen that when the slot factor(Ko) is greater than 0.6, the force reduction(Fi) decreases, since less saturation occurs in the constriction region. In contrast, for a small constriction area, for example, the slot contains a high flux and therefore is already heavily saturated and as a consequence no further reduction of force is possible. An optimum value of the force(figure 4.3) occurs at the value of slot factor, Ko=0.6, since the over-saturation occurs at small slot factors and non-saturation occurs for large slot factors, both of which lead to reducing sensitivity. It, therefore, can be concluded that for a given value of armature force, the flux density design in the constriction slot should be around the knee point on the material magnetising curve for maximum sensitivity to control current.

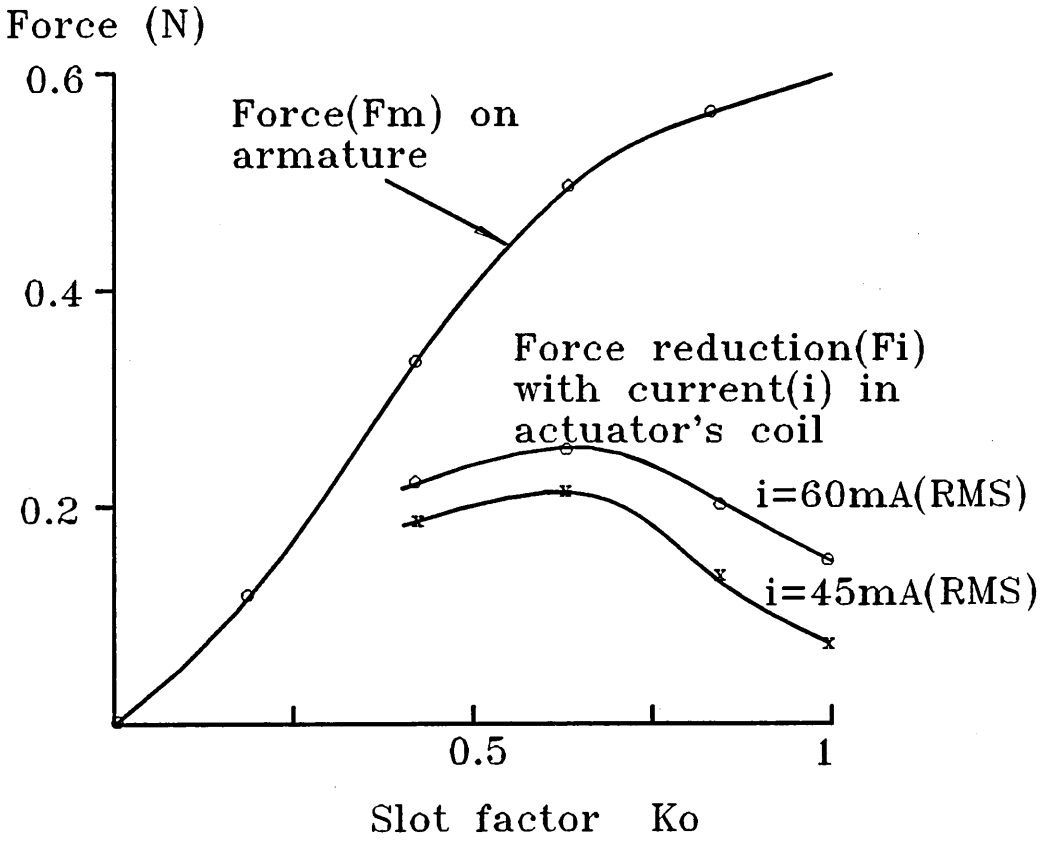

Figure 4.3 Armature force and its reduction as a function of constriction slot factor

4.4 Optimization of Contact Surfaces

The sensitivity of the actuator is significantly affected by the excitation MMF of the permanent magnet. Generally, the smaller the MMF the higher is the sensitivity. In the design, therefore, the lowest MMF is to be desired. Figure 4.4 shows the relationship between the source MMFs required to produce the force of attraction on the armature(typically, 0.5N). The greater source MMF is required to produce a force of 0.5N with smaller contact surface for airgaps larger than 2μm as is to be expected. However, an inverse relationship is obtained for airgaps of length less than 1μm and the contact areas larger than $1mm^2$. The latter

result is mostly applicable in the design of the clapper type of current sensitive actuators.

For large airgaps, the flux in the magnetic circuit mainly depends on the airgap reluctance, for which the analytical expression of the electromagnetic force is given by,

$$Fm=\frac{1}{2}u_{\delta}^{2}\frac{dG_{\delta}}{d\delta} \tag{4.1}$$

The airgap reluctance is expressed as

$$R_{\delta}=\frac{1}{G_{\delta}}=\frac{\delta}{\mu_0 A} \tag{4.2}$$

hence

$$F_m=\frac{1}{4\mu_0}(IN)^2\frac{A}{\delta^2} \tag{4.3}$$

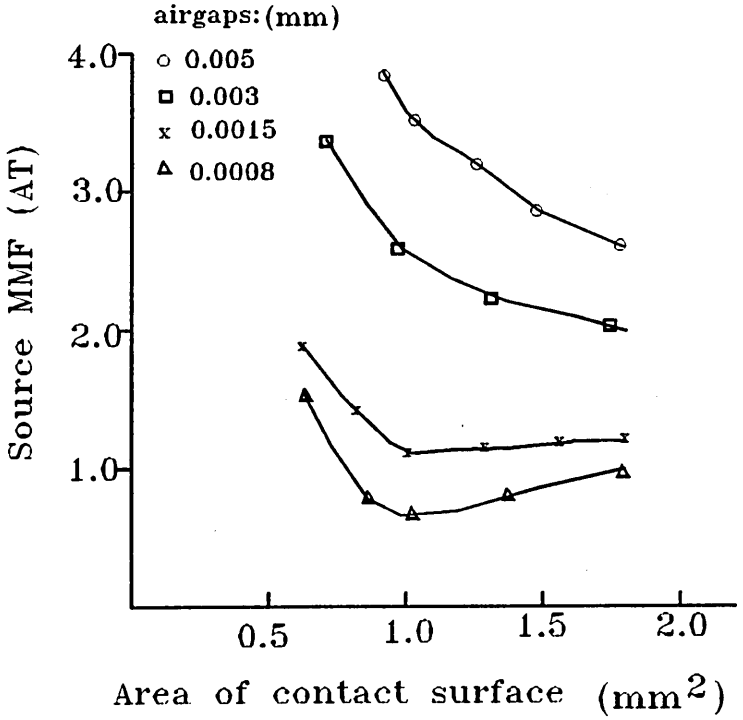

Figure 4.4 Relationship between source MMF required and the area of contact surface for producing an armature force Fm=0.5N

where δ is the length of the airgap;

u_δ is the magnetic potential in the airgap,.

IN is the magnetomotive force of the actuator.

It is obvious that the force is directly proportional to the contact surface area. But for small airgaps the flux(φ) in a magnetic circuit critically depends on the magnetic material properties and not just on the airgap reluctance. The flux density in the airgap is approximately uniform. Therefore, the electromagnetic force acting on the armature can be calculated by equation (2.36) as,

$$F_m = \frac{\varphi_0^2}{2\mu_0 A} \tag{4.4}$$

The critical design postulation emanating from the above formulations is that for a given value of electromagnetic force acting on the armature, the contact surface area (A) should be made as small as possible to allow the operating flux density to be near the saturated point. This will enable the minimisation of the flux in the airgap and consequently the minimisation of the source MMF.

4.5 Optimal Magnetic Material Properties

The electromagnetic force obviously increases with increase in the material permeability for a given actuator as shown in figure 4.5a. The influences of the magnetic permeability on the force reduction can be seen in figure 4.5b, when the coil carries current. It is clear from

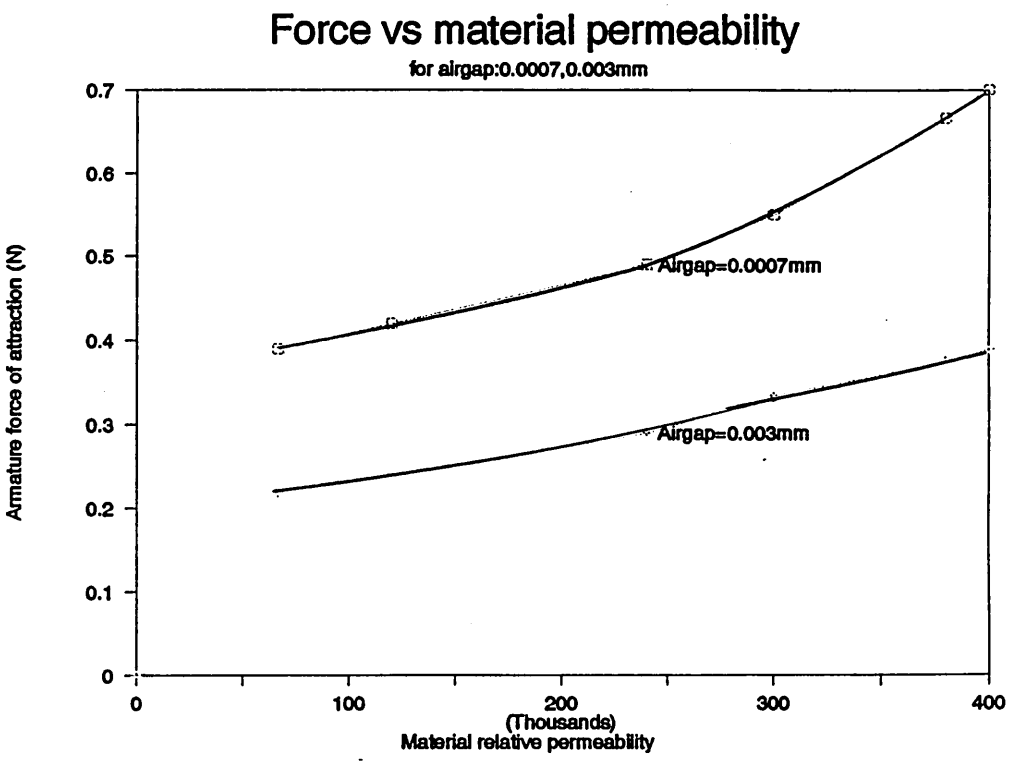

Figure 4.5a Electromagnetic force on armature versus material relative permeability

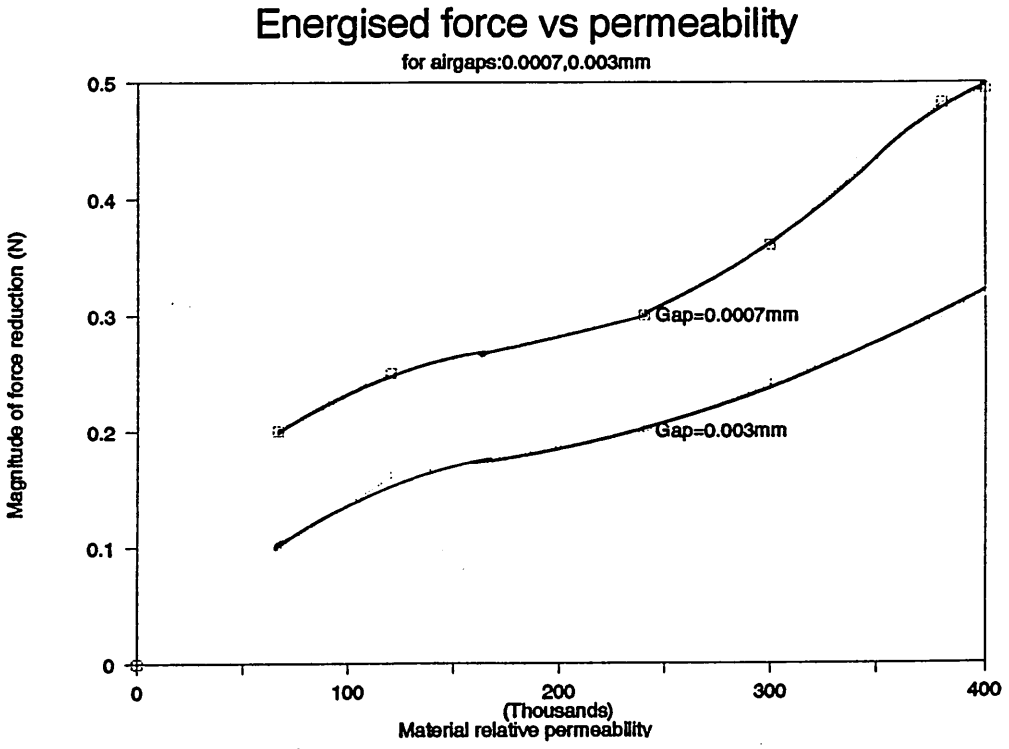

Figure 4.5b Reduction of armature force versus material permeability for trip setting of 1.5AT

figure4.5a that the increasing value of the force for small airgaps(i.e. 0.7μm) is greater than that for large ones (i.e. 3μm). Since the magnetic material reluctance with a permeability over 120,000 compared to the large airgap(i.e. 3μm) reluctance can be neglected. The variations of material permeability therefore significantly affect the magnetic force of small airgaps rather than large airgaps. The results further highlight that the flux in the magnetic circuit considerably depends on the material reluctance rather than the size of the airgap (for airgaps less than 1μm).

The figures 4.5a and 4.5b show that the material properties not only affects the magnetic force but also the sensitivity. These effects are most influenced by the quality of the machined airgap facings.

4.6 Test results

Two clapper type actuators, the type II being based on the optimum design parameters, were tested. The design data for both types are illustrated in table 4.1. The test results are given in table 4.2.

Table 4.1 Design data of two types of actuators

Type	I	II
Dimensions of permanent magnet (mm^3)	$\pi x3^2x3.5$	$\pi x3^2x3.5$
length of leakage gap (mm)	0.12	0.08
Area of contact surface (mm^2)	1.6x0.95=1.52	1.6x0.8=1.28
Cross section area of slot (mm^2)	0.65	0.64
Thickness of yoke plate (mm)	0.95	0.8
coil turns	20	20

* the rest dimensions of both types of actuators are same, the construction is shown in figure 2.3

The two types of actuator are simulated using a 3D magnetostatic finite element technique , together with the calculation of the electromagnetic force and tripping characteristics. The measured and computed results are given in table 4.2.

Table 4.2 Measured and calculated electromagnetic force and trip current(D.C.) at different magnetic displacement angles for two type actuator

Type I		Magnetic displacement angles (θ^0)							
	No.	0	10	20	30	40	50	60	65
Measured force Fm(N)	1	0.620	0.600	0.586	0.545	0.439	0.430	0.290	-
	2	0.550	0.540	0.530	0.512	0.488	0.443	0.295	-
	3	0.610	0.606	0.594	0.577	0.540	0.490	0.378	-
	4	0.610	0.590	0.580	0.550	0.470	0.450	0.310	-
Average Fm(N)		0.597	0.583	0.573	0.545	0.484	0.453	0.317	-
Calculated Fm(N)		0.58	0.571	0.560	0.540	0.510	0.440	0.350	0.220
Measured tripping current (mA)	1	-	194.1	174.0	138.4	130.0	90		
	2	223.0	215.0	192.0	141.0	121.0	62.0	42.0	
	3	237.0	221.0	201	169.2	135.0	86.1	44.6	
	4	209	198.5	180.0	151.5	126.6	78.0	30	
Average i_t (mA)		223.0	207.2	186.7	150.1	128.0	79.0	38.7	-
Calculated i_t(mA)		-	-	-	171.0	139.0	76.0	32.0	-

continued from table 4.2

Type II	Serial No.	magnetic displacement angles (θ^0)							
		0	10	20	30	40	50	60	65
Measured force Fm(N)	1	0.690	0.640	0611	0.590	0.550	0.49	0.390	0.310
	2	0.711	0.650	0.630	0.612	0.56	0.500	0.420	0.320
	3	0.670	0.633	0.606	0.592	0.544	0.483	0.403	0.318
	4	0.590	0.585	0.560	0.550	0.530	0.460	0.380	0.27
Average Fm(N)		0.665	0.627	0.601	0.586	0.546	0.483	0.398	0.304
Calculated Fm(N)		0.625	0.606	0.590	0.572	0.530	0.476	0.410	0.320
Measured tripping current (mA)	1	168	167.5	163.5	140.0	119.0	81.5	53.5	-
	2	169.0	166.0	157.5	-	121.0	78.5	46.8	36.7
	3	166.0	161.5	155.5	140.0	124.0	75.5	46.7	28.4
	4	-	157	149.0	137.0	118.0	66.8	34.5	16
Average i_t(mA)		167.7	162.9	156.4	139.0	120.5	75.6	45.4	29.1
Calculated i_t(mA)		-	-	-	151.0	131.0	92.0	47.0	30.0

The measured and calculated electromagnetic forces acting on the armature against the permanent magnet displacement angle are shown in figure 4.6 for the two types of actuator. Both type actuators have the same frame size, airgap lengths and magnetic material properties and were excited by same (magnet)MMF. The dimensions which were made different are: the area of contact surface, shunt reluctance and cross section area of slot of type II all of which are smaller than that of type I. From the results, it is clear that the higher magnetic force is produced in type II for each corresponding magnetic angle. To produce a specific force, the excitation (magnet)MMF for type II is required less than that of type I, and consequently a smaller control current would be required. In other words, the optimised type II actuator is more sensitive to the current.

A comparison of the tripping characteristics was made for the two types of actuators. The key design dimensions are given in table 4.1, and the construction being as shown in figure 2.3. Figure 4.7 shows the electromagnetic force acting on the armature when energised to both types actuators. It is observed that the decline in the force for type II is greater than that of type I for the same value of tripping current. As a consequence the type II actuator requires a lower tripping current. The reason is that the smaller shunt reluctance in type II leads to more flux being diverted into the shunt path following saturation and consequently a greater declination in the type II. These results demonstrate that the type II actuator is more sensitive to control current than type I, and therefore is a more effective current sensitive magnetic actuator. The characteristics also indicate that an optimization method for designing this type of actuator is feasible.

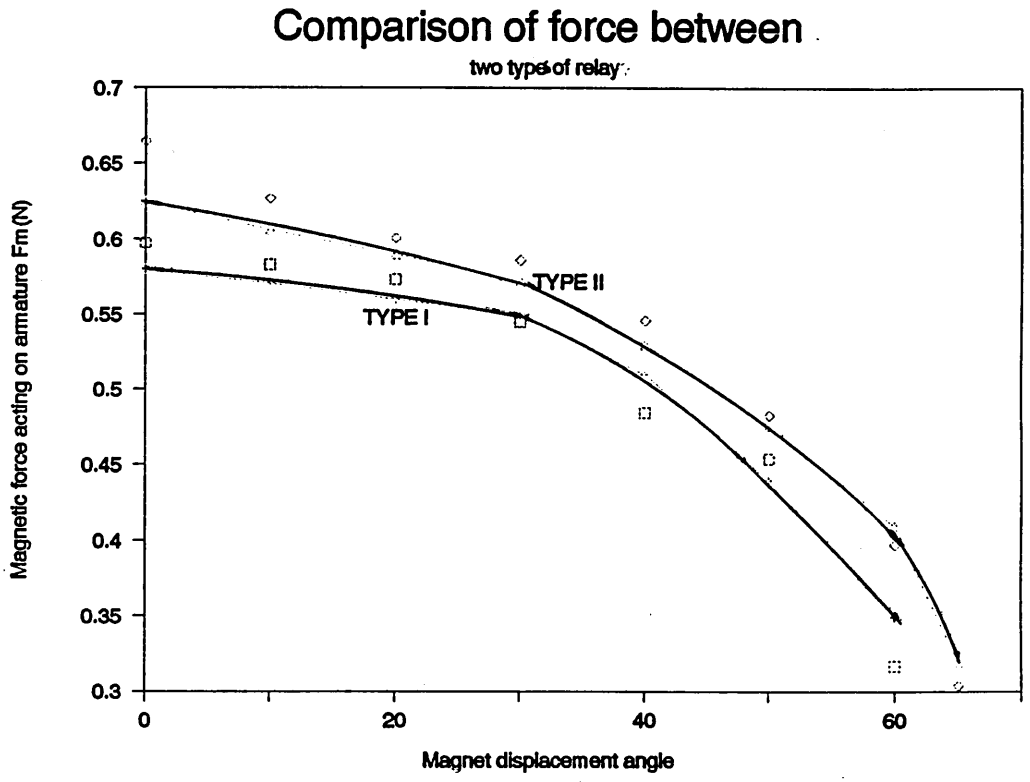

Figure 4.6 Electromagnetic force against the magnetic displacement angles for two type s of actuator

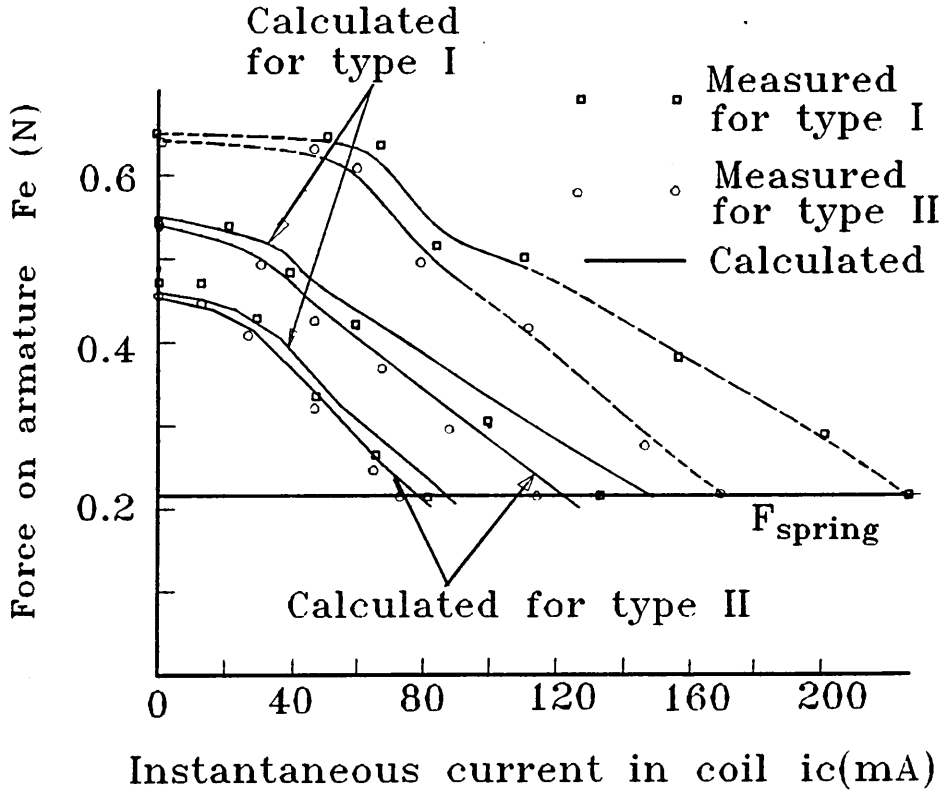

Figure 4.7 Computed and measured armature force for two types of actuator varying with coil current

4.7 Optimal Design Specification

The study of the optimisation of clapper type actuators has demonstrated that certain design parameters, shunt reluctance, magnetic properties, control current, contact surface and constriction regions, have a significant effect on the actuator performance. It was observed that the shunt reluctance and constriction slot have a greater influence on the current sensitivity or force reduction for same magnetic material property and airgap length, when energised, than the electromagnetic force acting on the armature. The property of the magnetic material has, however, an effect on the overall performances. CAD technique enables realization of these optimised designs.

Minimising the size and weight in the current sensitive actuator design is desirable but is not critical. However, in many applications, the actuator will be required to operate with great precision at very low current(less than 30ma) and will need to be able to produce relatively higher mechanical forces to oppose the mechanical shock, so it is mostly desired to minimise the control current and to improve the force sensitivity if possible.

The details of an optimised design are considered. The most suitable of the available magnetic materials was found to be permalloy 65 with maximum permeability(μ) of 450,000 and saturated flux density of 1.3Tesla and consequently was chosen as the actuator material. An electromagnetic force(typical 0.5N) is required to hold the armature closed on to the yoke. For the flux density in the contact surface to operate near the knee on the BH magnetising curve (B_k=1.1T), the contact surface area (A) evaluated from the basic equation (4.4) yields,

$A=2\mu_0 F_m / B_k^2 = 1.04mm^2$

Given a thickness(0.7mm) of the material plate, the constriction region was determined by, cross section area=thickness (a) x width(f) =A/2=0.502mm^2, if a=0.7mm, then f=0.72mm. Referring to the studied results shown in figure 4.1, the distance between the two yoke plates is defined as 0.06mm. The dimensions of permanent magnet is reduced to diameter, 6mm, and thickness, 3mm. Other dimensions are similar as in figure 2.3. The physical parameters of theoptimised actuator design are given in Table 4.3 .

Table 4.3 Dimensions of the optimised actuator design

Area of contact surface(mm^2)	1.7x0.7=1.05	
Length of leakage airgap (mm)	0.06	
Cross section area of constriction slot (mm^2)	0.51	
Thickness of iron yoke plate (mm)	0.7	65 permalloy
Permanent magnet (mm^3)	$\pi 3^2 x3$	
Airgap	0-1μm	
Coil turns	25	

The performance of the optimised actuator was analysed using TOSCA and previously described analytical methods. The results are illustrated in Table 4.4 and compared to those obtained from production actuators .

Table 4.4 Comparison between the conventional actuator and the optimised design

Parameters	type I	Type II	Optimised Design	
length of airgap μm	0-1	0-1	0-1	
Maximum permeability μ_{Max}	240,000 300,000	240,000 350,000	300,000 400,000	
Dimensions of permanent magnet(mm^3)	$\pi x3^2$ x3.5	$\pi x3^2$ x3.5	$\pi x3^2$ x3.	same material
Maximum force Fm(N) (θ=0)	0.6	0.665	0.62	
Fm/PM (N/mm^3)	3.2-6.05	4.0-6.7	4.5-7.2	
Sensitivity (N/AT)	0.08-0.16	0.12-0.18	0.14-0.21	
Tripping ampere turns required to trip force 0.48N	1.84	1.2	0.75	Fs=0.21N
Coil turns	20	20	25	
Coil current RMS (mA)	92	60	30	
Toroid diameter (mm)	26	20	13	
Weight of toroid (g)	38.6	29	8.6	

4.8 Conclusions

The dependency of the actuator sensitivity on the critical design parameters has been investigated, from which the optimum design of the clapper type actuator was found. It was demonstrated that a smaller shunt reluctance could lead to a higher sensitivity, however, too small a shunt reluctance causes the force to dramatically decrease. Therefore a range of optimum values were obtained for the shunt factor between 0.5 and1.

The design of constriction slot is determined by the force of attraction required, which fixes the flux in the airgap. The optimum flux density in the constriction slot should be on the knee point of the material magnetising curve. The size of contact surface should be made as small as possible to allow the operating flux density to be near the saturated value. This will enable minimisation of the flux in the airgap and consequently minimisation of the source MMF. Design and performance data for an optimally designed actuator have been discussed and compared with summary data for current production actuators. This optimal design can also reduce the size of toroidal transformer required as an alternative to increasing the sensitivity.

Chapter 5

Design of Current-Sensitive Stepper Motor Actuators

5.1 Introduction

5.1.1 Introduction to the Proposition of a Stepper Motor Actuator

As described earlier, the clapper type actuator requires very fine machined surfaces and also requires a separate toroid transformer with actuator winding to operate it and to detect a 30mA trip setting. These suffer from the following disadvantages: (i) Producing the high quality machined surfaces is expensive and difficult. (ii) In the system, the energy transfer (toroid and actuator winding) is from electrical to magnetic, back to electrical and then to magnetic again, and finally to mechanical. Each time energy is converted from one form to another losses occur. Thus the transfer of energy is inefficient. (iii) In conventional RCDs where a wound toroid drives an eletromechanical release, the current monitoring device is inherently sensitive only to alternating currents and special measures have to be taken to produce a satisfactory response to any form of direct current such as smooth d.c. or pulsating d.c. obtained from rectification circuits.

An alternative actuator design was considered The ideal actuator should have the highest possible tripping sensitivity, great precision, minimum value of trip current and satisfy the full performance specification.

This chapter describes such a magnetic actuator. The actuator combines a current monitoring system and an electro-mechanism together and is actuated upon current imbalance. The electro-mechanism is based on a stepper motor, where the rotary output shaft is provided with a cam or ramp surface to engage with a release flag which releases the switch mechanism of the RCD.

5.1.2 Introduction to the Work

An equivalent magnetic circuit technique was developed and used to obtain the stepper motor magnetic actuator preliminary design. The equivalent circuit technique was also adopted for the initial analysis of both the permanent magnet and an assumed pure iron field of the actuator. The permanent magnet in the actuator is treated as a source of fixed MMF in series with a constant reluctance. The iron reluctance was neglected initially but later taken as a constant value in a second approach which used the concept of lumped magnetic circuits comprising elements corresponding to discrete physical sections of the actuator.

The proposed technique is appropriate for the preliminary design and analysis of the actuator. The investigations were made into the effects of the key dimensions and magnet data on the actuator's performance. The preliminary design specification of the proposed stepper motor actuator was covered in this chapter and discussed. The 3D finite element CAD technique is used to obtain the solutions for the actuator to be covered in a later chapter.

5.2 Study of a Disc Magnet Stepper Motor

The disc magnet stepper motor was developed based on the requirement of a very small and very efficient stepper motor, for example, as used for driving the hand watches. The high magnetic energy made it possible to magnetize a relatively long airgap using a magnet which was actually shorter than the airgap. A basic construction of the disc magnet stepper motor is shown in fig.5.1. If a given discrete magnet had its north pole on the top of the rotor disc and its south pole on the bottom then the adjacent magnet would have its south pole on top and the north pole on the bottom. The magnetic circuit of such a motor is shown schematically in figure 5.1. The rotor consists mainly of a thin disc made of samarium-cobalt. A particular technique of axial magnetization allows a large number of evenly spaced magnetic poles of alternating polarity to be achieved. The disc is placed in the airgap between the two stator halves. The stator of the stepper motor is composed of two symmetrical stator halves. Each stator halve has 6 iron segments. One phase coil is wound between the two stator halves to produce a flux axially through the disc magnet. This iron circuit is shorter than with any other kind of stepper motor. The advantages for this are that the power supply may be smaller, with a much smaller

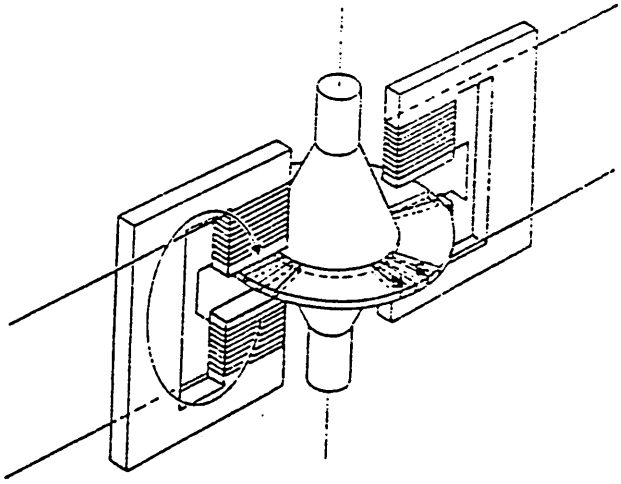

Figure 5.1 Basic disc magnet stepper motor

drop in torque at high step rates.

The working process is shown in figure 5.2. which illustrates part of the rotor disc with alternate magnetization and one segment of each phase which in reality would be at opposite sides of the rotor. If positive current in A magnetizes the iron as shown in (a), the rotor will take the position indicated. The phase B segment overlaps magnets of opposite polarity. With negative current in phase B and phase A switched off, the rotor will move one step to the right(b). Positive current in phase B would create a north pole in the upper half and a south pole in the lower half of the segment, and the rotor would move to the left. If B is switched off and A receives negative current, the rotor makes a second step to the right(c). The third step is initiated by commutating positive current into phase B (d), and positive current in A completes the sequence(a'): a full rotation of the stator field vector and a move of the rotor of 4 steps.

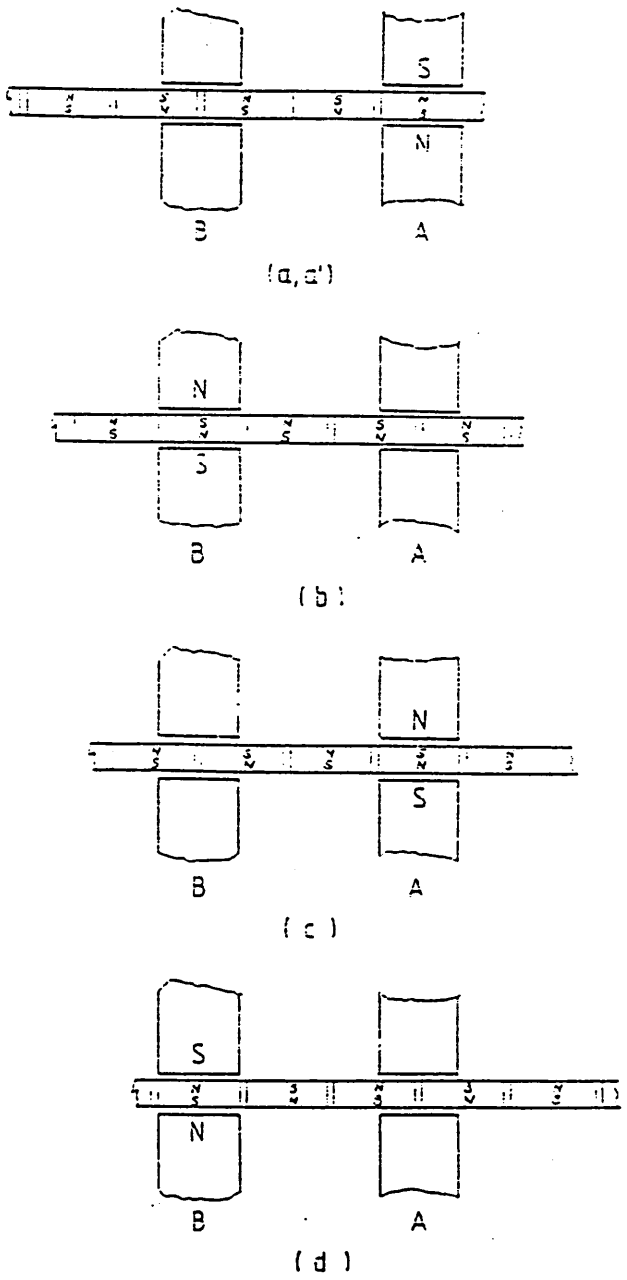

Figure 5.2 Working process of the stepper motor

The torque function of a stepper motor describes the variation of torque output for one fixed rotor position and a full rotation of the stator field vector, or also for one fixed state of phase excitation and rotor movement of 4 steps. This is illustrated in figure 5.3 where positive current is maintained in phase A. initially, the rotor is in a position of stable equilibrium(5.3a). This means, whenever an external force would move the rotor to the right or to the left, the motor would develop a opposing torque to drive the rotor back to its target position. As the rotor is forced to move from (a) to (b) there is an increasing torque opposed to the movement. This torque will diminish as one continues to move the rotor from (b) to (c). In (c) it is

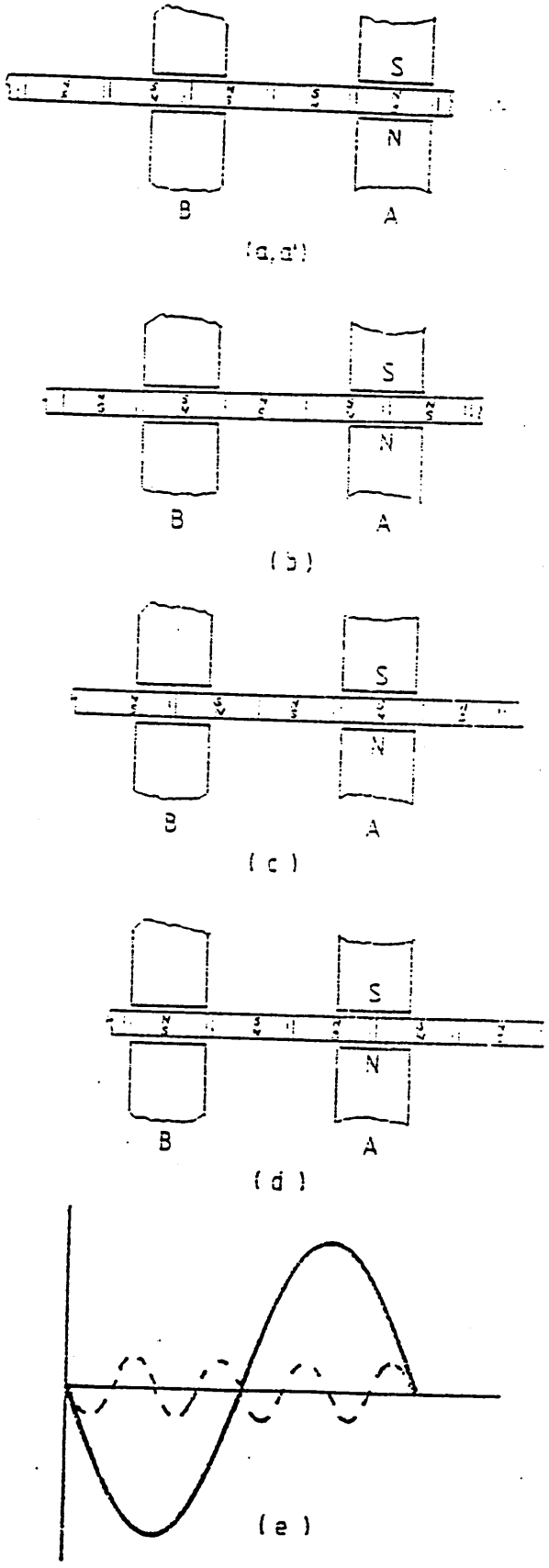

Figure 5.3 Function of holding torque versus angular displacement.

zero but the rotor is clearly in a position of unstable equilibrium, which means if it is allowed to move slightly to the left, the negative torque will drive it back to (a); and if it moves to the right then there will be positive torque driving it forward to (a'). this positive torque is highest in position(d). The angular movement from (a) to (a') corresponds to one complete sequence which, with 2-phase motor, gives 4 steps. The resulting motor torque curve over one sequence is shown in fig.5.3e. The detent torque curve is obtained by repeating the movement (a...a') with the motor non-energized.

5.3 Description of the Proposed Stepper Motor Magnetic Actuator

The proposed magnetic actuator must operate within 5-10ms from the moment the circuit fault occurs to the time the release mechanism lever moves to an open position for an operating current less than 30mA (RMS). The actuator is also required to provide a sufficient mechanical torque to actuate the latch mechanism system.

Figure 5.4 shows the physical arrangement of the proposed stepper motor magnetic actuator. The actuator comprises a current detecting system including an electromechanical release which is formed by a stepper motor. The stationary poles(25) of the stepper motor are spaced axially along the stepper motor shaft(22) on which is mounted a rotor disc(20) of permanent magnet material having alternate magnetic poles,N,S,N,S. Each N is opposite an S on the other face of the rotor disc. The axial magnetic flux provided by the permanent magnet(27) between the stationary poles causes the disc to align with the stationary poles. The permanent magnet bridges the two yoke plates(24) which are separated by an intermediate layer(23) of non-magnetic material to provide a leakage reluctance. The permanent magnet and

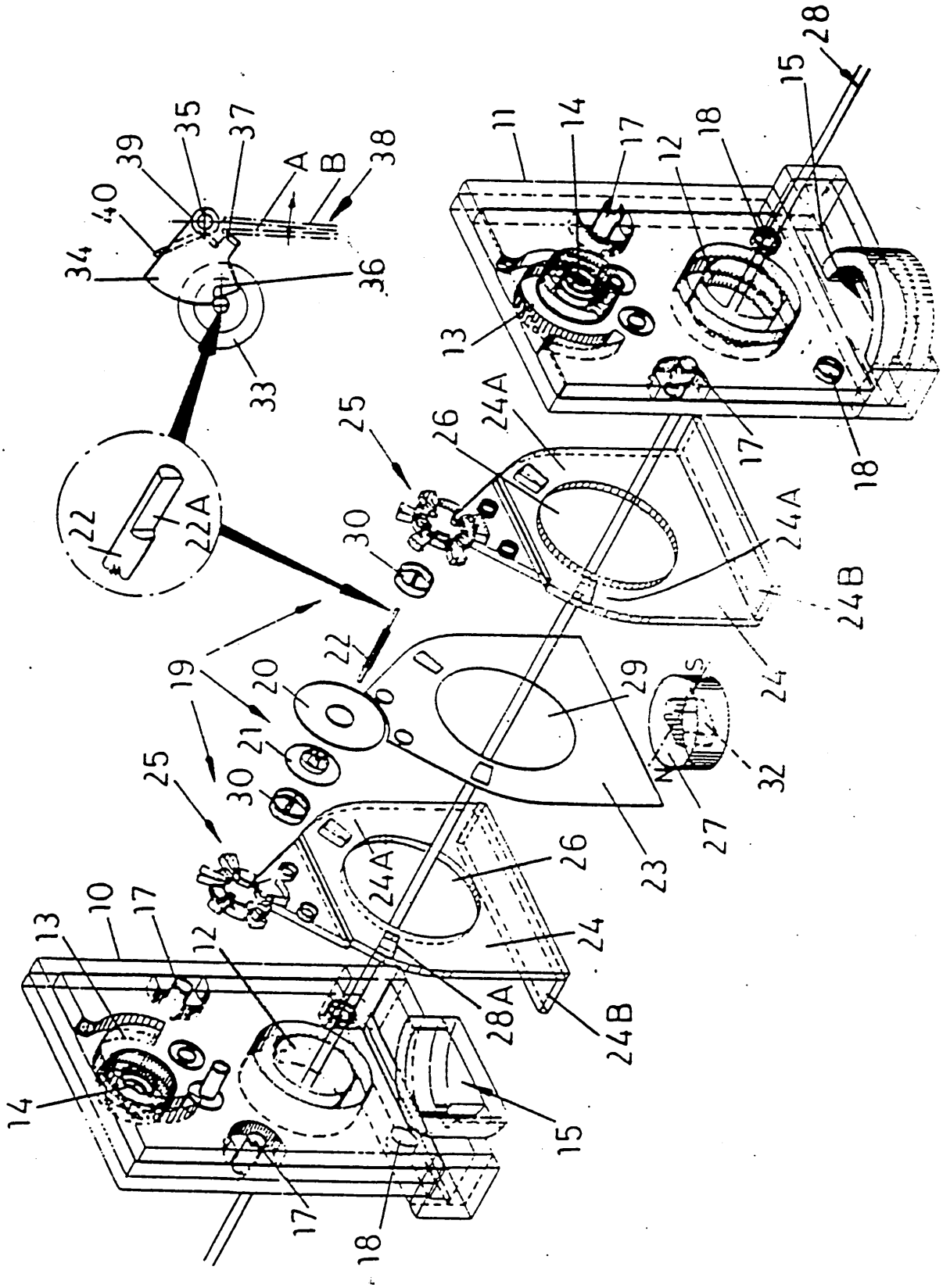

Figure 5.4 General arrangement of proposed current sensitive stepper motor actuator

yoke plates are all located in two moulded insulated casing apertures[10,11]. Each yoke plate provides two constricted cross sections(28A), one of which will be saturated by the summation of the magnetic flux due to a permanent magnet and the imbalance current provided by the conductors(28) which pass through the apertures(26). The flux in the other constriction will be diminished by the imbalance current. When a signal from the current monitoring system exceeds a predetermined level, the flux from the magnet through the rotor disc(20) will be effectively cut off which will cause the disc to rotate in order to align the ramp or cam face(22A) of the shaft(22) with the release detent(36). The movement allows the release flag(34) to pivot, under spring(39) action, against the cam or ramp face (22). This in turn causes the actuating and reset surface(37) to urge the release lever (38) from position A to position B. The movement of the release lever must be sufficient to cause the contacts(not shown) of the RCD to open and to clear the circuit fault usually by disturbing a latch mechanism.

As the actuator design is a stepper motor. It does not need a very small airgap. This design also combines the toroid with the actuator winding in one assembly, so that it is simple to construct and assemble. The design is responsive to alternative current and direct current supplies.

5.4 Analytical Method-Equivalent Magnetic Circuit

5.4.1 Basic Torque Expression

Figure 5.5 shows the simple construction of the proposed stepper motor actuator. The simplifying assumptions in this section for the actuator are (a) leakage and fringing flux are neglected,

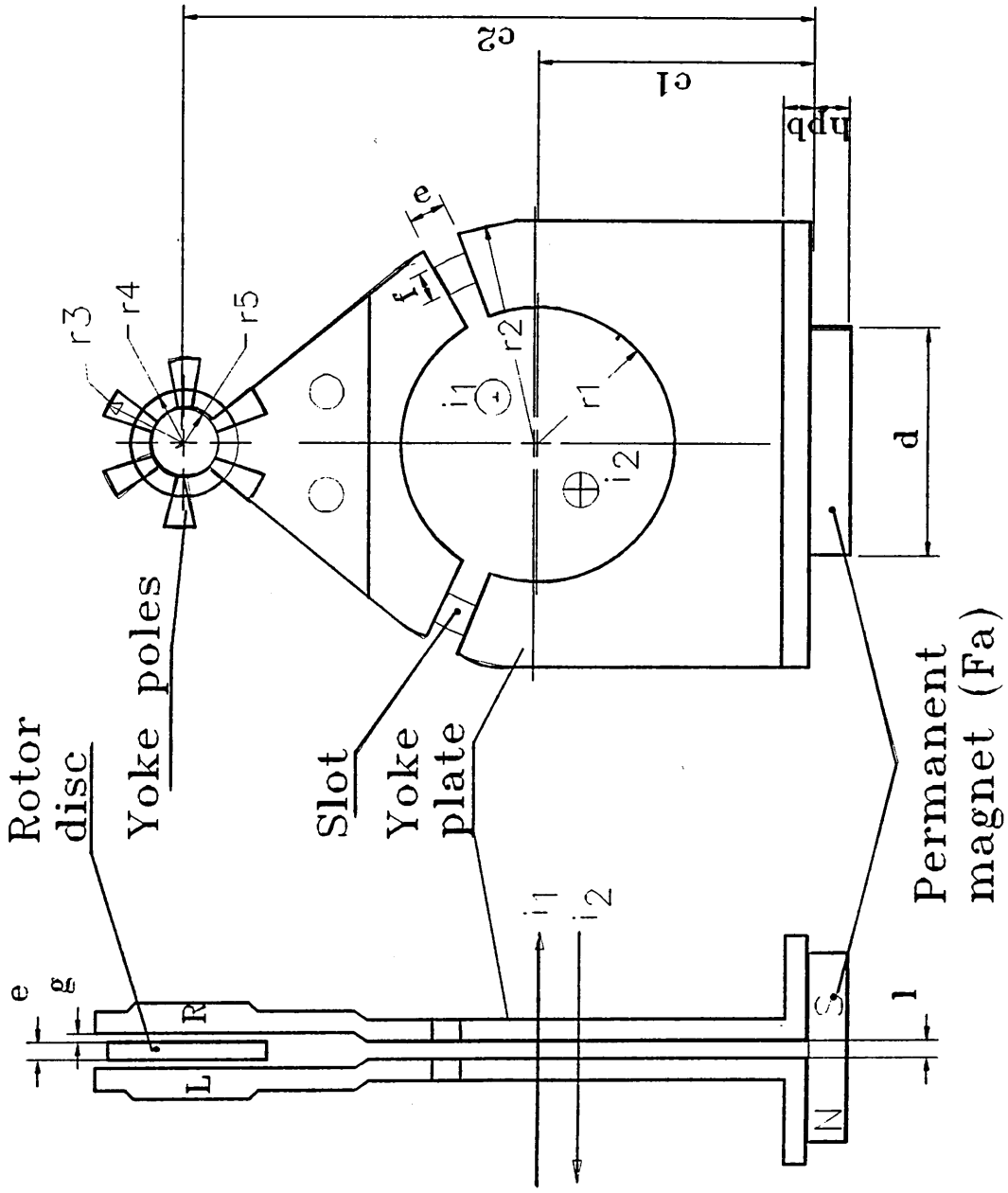

Figure 5.5a Proposed stepper motor actuator shematic diagram

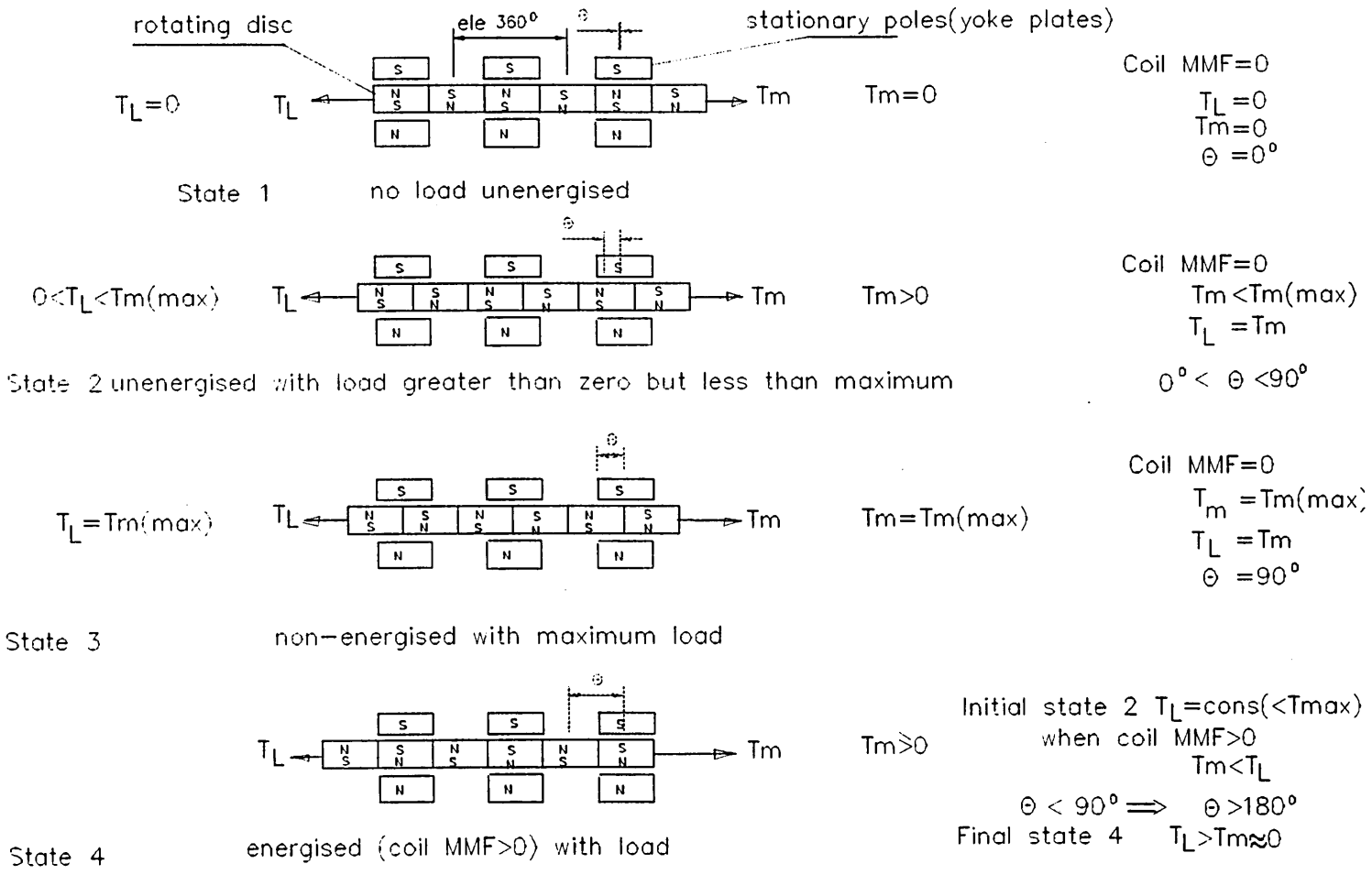

T_L: load torque Θ: displacement angle between the poles of disc and stator
Tm: torque produced by permanent magnet interacting with rotating disc poles and coil MMF

Figure 5.5b Stepper motor actuator working process

Pink : *Rotor Magnet Disc*

Red: *Coils*

Bottom: *Permanent Magnet*

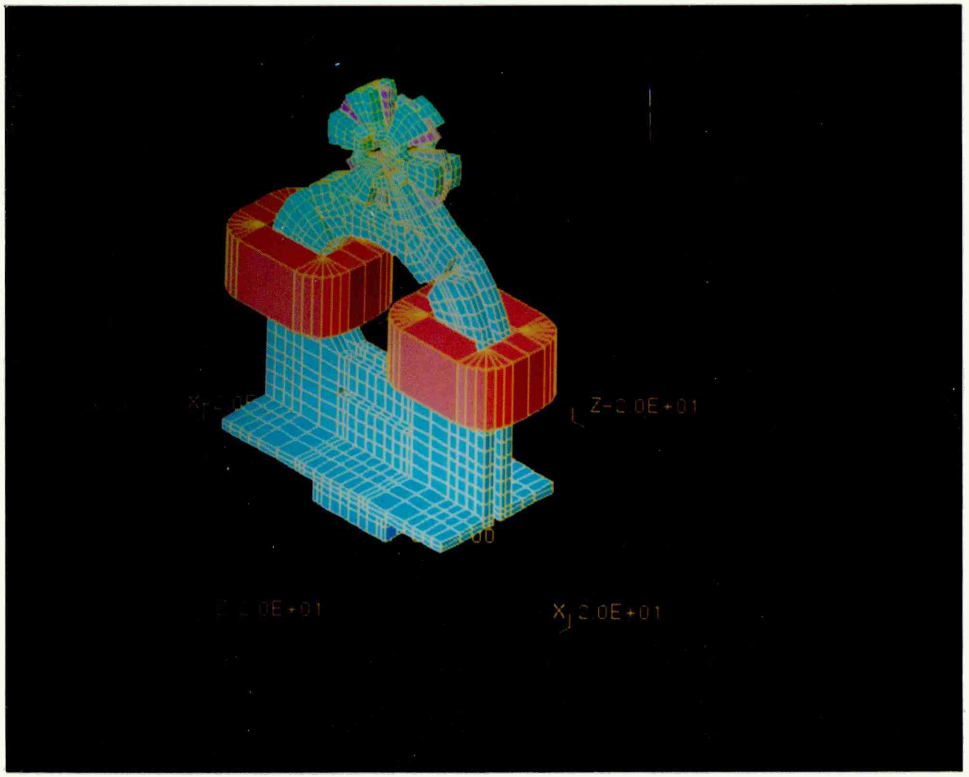

Figure 5.5c FEM model of the proposed stepper motor actuator

(b) the iron magnetic reluctance is negligible compared to the airgap reluctance. The flux density Ba in the airgap is given below,

$$B_a=\frac{\mu_0(F_a+F_b)}{2g} \tag{5.1}$$

where Fa is the magnetomotive force(MMF) produced in the source permanent magnet,

Fb is the equivalent MMF produced in the magnet disc,

g is the length of airgap .

and the stored magnetic energy in the airgap is

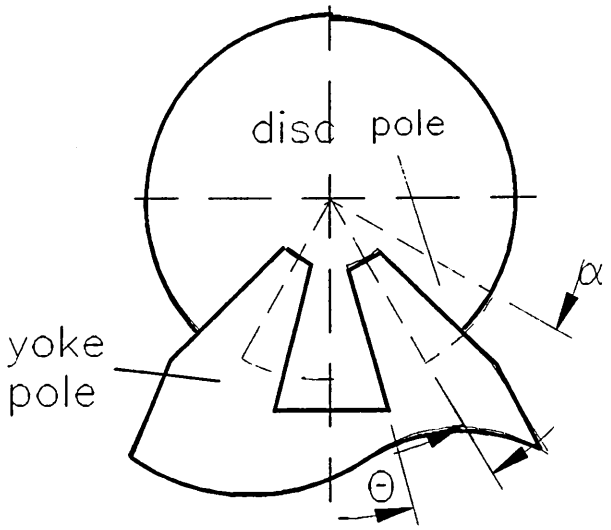

Figure 5.6 Disc over lap area

$$E=\frac{1}{2}\iiint HBdv \tag{5.2}$$

When B is taken as uniform over the gap volume Vg,

$$E=\frac{B_a^2 g}{2\mu_0}=\frac{\mu_0 r_3^2}{8g}(F_a+F_b)^2(\alpha-\theta)n \tag{5.3}$$

where α is angle of each magnet disc pole;

θ is the rotor orientation from zero position.

The torque is given as the change of the stored energy with respect to rotor disc orientation.

$$T=\frac{\partial E}{\partial \theta}=-\frac{\mu_0 r_3^2 n}{8g}(F_a+F_b)^2 \tag{5.4}$$

This expression shows that the dependency of torque on the magnetic disc size (in particular to the radius of disc) and number of the pole-pairs,n, at a constant excitation. For a given disc size the torque is proportional to the square of the sum of the two excitation levels. This formula can be helpful when initial trial design values are required.

5.4.2 Non-energised Equivalent Magnetic Circuit

Neglecting the iron reluctance generally leads to appreciable errors. A better solution can be done by assuming that the iron reluctance is constant.

The operating locus of a permanent magnet on the B/H plane can usually be approximated by a straight line(recoil) as shown in figure 5.7a near to the demagnetisation curve of the permanent magnet. Fig. 5.7b shows the lumped equivalent circuit of a permanent magnet. It is represented as a

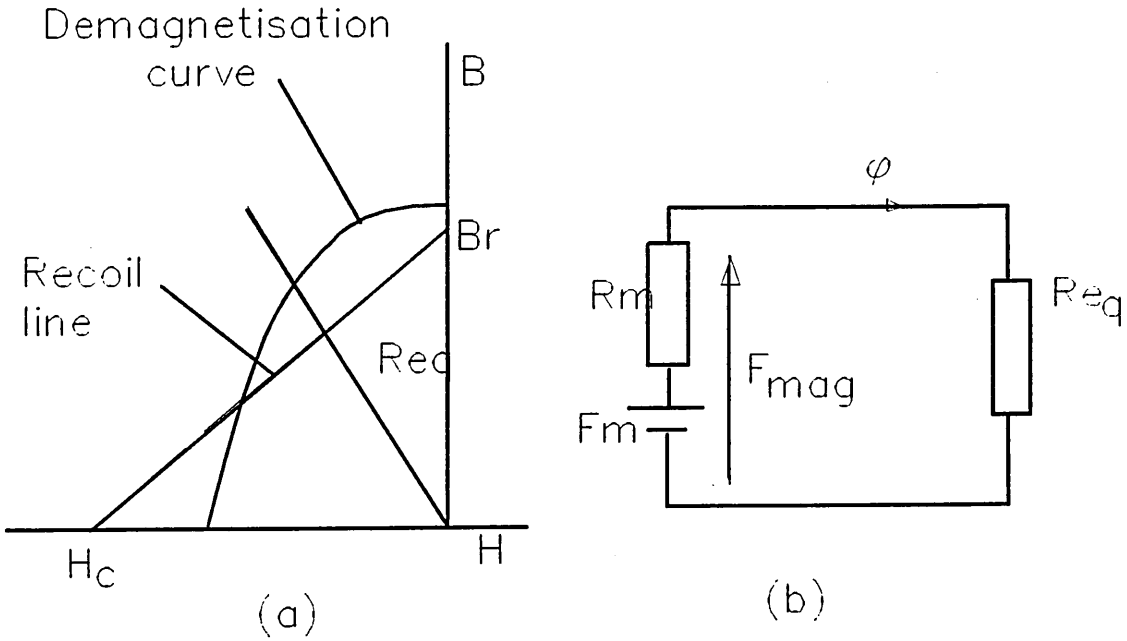

Figure 5.7 Derivation of a simple magnetic equivalent circuit

a. linearised characteristics of magnet

source of MMF Fm in series with a reluctance Rm. The MMF Fmag and flux ,ϕ, produced by the magnet are related by

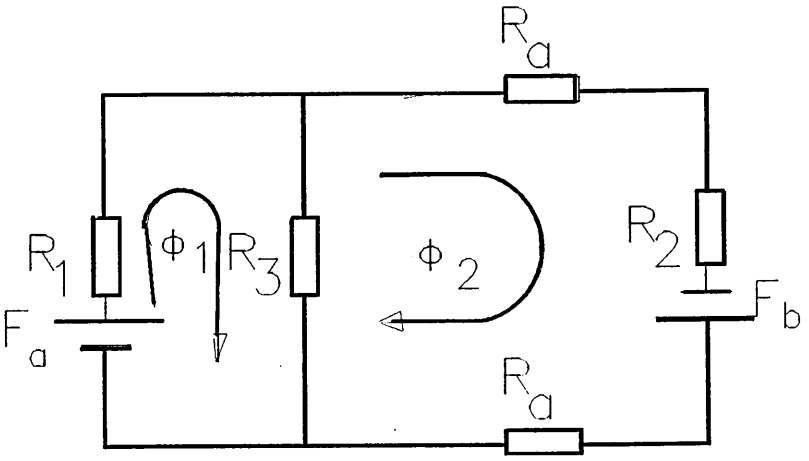

Figure 5.8 Magnetic equivalent circuit for static state

$$Fmag=Fm-Rm\,\phi \tag{5.5}$$

Fig. 5.8 presents the proposed actuator's magnetic equivalent circuit in which each reluctance is lumped corresponding to a physical section of the actuator. Fa in the circuit is the equivalent MMF of permanent magnet which bridges the two yoke plates and Fb is the equivalent MMF of the permanent magnet rotor disc. The air-gap reluctance is given as

$$R_a=\frac{g}{\mu_0 r_3^2(\alpha-\theta)n} \tag{5.6}$$

where $(\alpha-\theta)$ is the rotor orientation

The following equations are used to express the circuit system

$$F_a=(R_1+R_3)\varphi_1-R_3\varphi_2 \tag{5.7}$$

$$F_b=-R_3\varphi_1+(2R_a+R_2+R_3)\varphi_2 \tag{5.8}$$

Solving the two equations (5.7) and (5.8) yields

$$\varphi_1=\frac{(2R_a+R_2+R_3)F_a+R_3F_b}{(2R_a+R_2)(R_1+R_3)+R_1R_3} \tag{5.9}$$

$$\varphi_2=\frac{R_3F_a+(R_1+R_3)F_b}{(2R_a+R_2)(R_1+R_3)+R_1R_3} \tag{5.10}$$

The total energy is given as function of flux as follows

$$E=\frac{g\varphi_2^2}{\mu_0 r_3^2(\alpha-\theta)n}=Ra\varphi_2^2 \tag{5.11}$$

where $R=\frac{g}{\mu_0 r_3^2 n}$ and $a=\frac{1}{\alpha-\theta}$

The torque expression as function of fluxes can be derived from the total electrical energy, stored in the airgap, as functions of orientation

$$T=\frac{\partial E}{\partial\theta}$$

$$=Ra^2\frac{[(R_2-2Ra)(R_1+R_3)+R_1R_3)][R_3F_a+(R_1+R_3)F_b]^2}{[2Ra(R_1+R_3)+R_2(R_1+R_3)+R_1R_3]^3} \tag{5.12}$$

Letting $R_1=R_2=0$, $R_3=\infty$, the equation(5.12) corresponds to equation(5.4).

5.4.3 Energised Equivalent Magnetic Circuit

When a leakage current to earth occurs in an electric circuit protected by the device, the imbalance current in the conductors causes the flux to be produced in the iron core which reduces the flux in the air-gap of an actuator, and consequently the holding torque. Figure 5.9 shows the lumped magnetic equivalent circuit of the proposed actuator with energised MMF,Fc, which is the current in the coil multiplied by the coil turns.

The reluctance R_5 and the saturation reluctance R_4 are calculated from

$$\frac{(iron\ length)}{\mu(cross\ sectional\ area)}$$

using value of μ at the relevant operating point on the iron B/H curve.

Flux cancelling occurs in one constricted section and saturation occurs in the other. It is obvious that the reluctance of the unsaturated constricted section is very small compared to the reluctance of the other saturated section. Thus this assumption leads to the following simplified equations. The equations describing the magnetic circuit system Fig.5.9 reduce to those given below

$$F_a=(R_1+R_3)\,\varphi_1-2R_3\,\varphi_3 \tag{5.13}$$

$$F_c=R_4\,\varphi_2+R_4\,\varphi_3 \tag{5.14}$$

$$F_b-F_c=R_4\,\varphi_2-R_3\,\varphi_1+(4R_a+2R_2+2R_3+R_4)\,\varphi_3 \tag{5.15}$$

where the saturated reluctance, R_4, is in function of control MMF, Fc, and the size of the constriction, as $R_4=f(Fc,e,f)$.

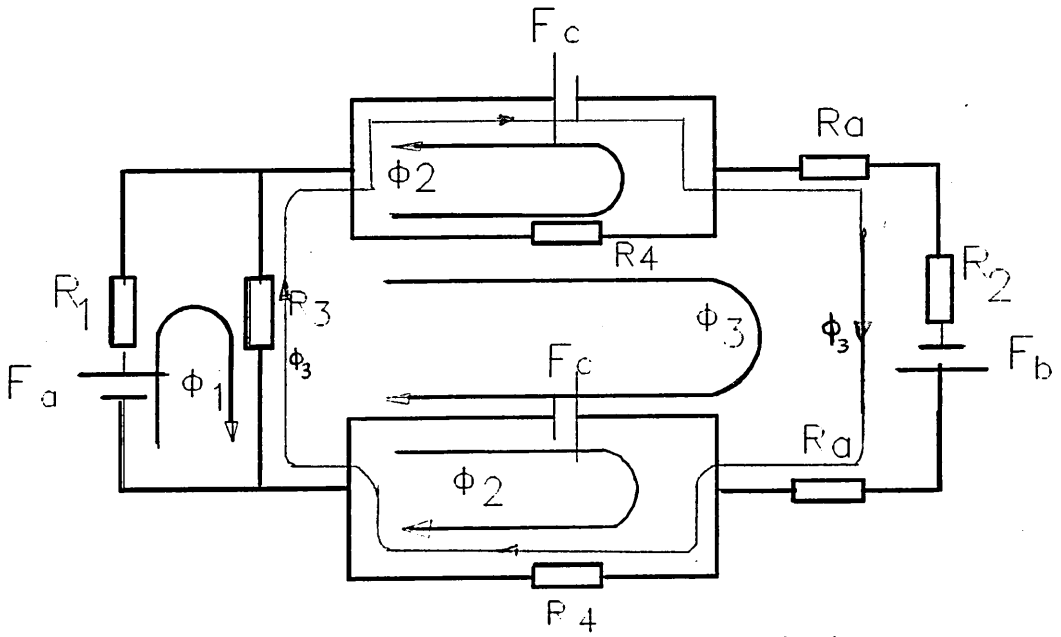

Figure 5.9 Energised magnetic equivalent circuit

Solving equation (5.13) and (5.14) yields

$$\varphi_1=\frac{F_a+2R_3\,\varphi_3}{R_1+R_3} \tag{5.16}$$

$$\varphi_2=\frac{F_c-R_4\,\varphi_3}{R_4} \tag{5.17}$$

Substituting equation (5.16) and (5.17) into (5.15) yields

$$(4R_4+2R_2+2R_3-\frac{2R_3^2}{R_1+R_3})\,\varphi_3=F_b-2F_c+\frac{R_3F_a}{R_1+R_3} \tag{5.18}$$

then,

$$\varphi_3=\frac{(R_1+R_3)F_b-2(R_1+R_3)F_c+R_3F_a}{(2R_a+R_2)(R_1+R_3)+R_1R_3} \tag{5.19}$$

Substituting equation (5.19) to (5.16) and (5.17) yields

$$\varphi_1=\frac{(2R_a+R_2+R_3)F_a+R_3F_b-2R_3F_c}{(2R_a+R_2)(R_1+R_3)+R_1R_3} \tag{5.20}$$

$$\varphi_2=-\frac{R_3\,R_4\,F_a-R_4(R_1+R_3)F_b+[4(R_a+R_4)(R_1+R_3)+R_1R_3]F_c}{2R_4[(2R_a+R_2)(R_1+R_3)+R_1R_3]} \tag{5.21}$$

Simplifying the equations (5.19)-(5.21),for $R_1=R_2=0$,they are

$$\varphi_1=\frac{(2R_a+R_3)F_a+R_3F_b-2R_3F_c}{2R_3\,R_a} \tag{5.22}$$

$$\varphi_2=-\frac{R_4(F_a+F_b)+4(R_a+R_4)F_c}{4R_4\,R_a} \tag{5.23}$$

$$\varphi_3=\frac{F_a+F_b-2F_c}{2R_a} \tag{5.24}$$

The energised torque expression as a function of control MMF Fc can be derived from the total electrical energy stored in the airgap as a function of orientation,

$$E=\sum E_i=\sum V_i\int BdH_i \tag{5.25}$$

where $B=\mu H=\phi_3/s$ and s is the area of the airgap.

The energised torque expression as a function of MMF Fc is thus,

$$T_i=Ra^2\frac{[(R_2-2Ra)(R_1+R_3)+R_1R_3][R_3F_a+(R_1+R_3)F_b-2(R_1+R_3)F_c]^2}{[2Ra(R_1+R_3)+R_2(R_1+R_3)+R_1R_3]^3} \tag{5.26}$$

It is obvious that the simplest expression of energised torque T_i can be written as a function of source MMFs, Fa and F_b, control Fc and airgap reluctance Ra, as follows,

$$T_i=f(\phi_i)=f(F_a,F_b,Fc,R_a) \tag{5.27}$$

This function indicates the dependency of the torque on the excitation MMFs in terms of Fa,F_b and Fc as well as airgap reluctance Ra. If a typical static holding torque is required, either increasing excitation MMF or decreasing airgap can achieve the aim. However for such a stepper motor actuator the airgap must be designed big enough to allow the rotor movement i.e.the airgap≥ 0.1mm. The deduction of energised torque thus significantly depends on the magnitude of control MMF, Fc.

5.4.4 Theoretical Analysis of Eddy Current in Iron

In the proposed actuator, the current-detection system monitors the current passing through the live and neutral conductors connecting a power supply to a load. The current generally is sinusoidal . The conductors are wound on the toroid as shown in Figure 5.10

Assuming for a single-phase system that the two conductors are wound on top of each other distributed around the toroid and have the same ampere turns.

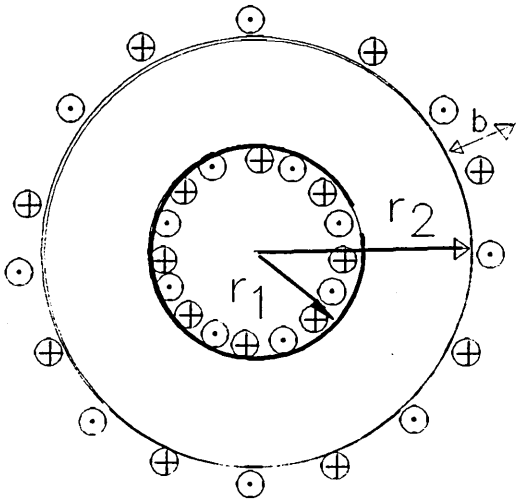

Figure 5.10 Coil window

$$i_1N=i_2N=NI_m\sin(\omega t) \tag{5.28}$$

From Ampere's Law, the flux density in the iron core is given below

$$B=\frac{\mu I_m N \sin(\omega t)}{\pi(r_1+r_2)} \tag{5.29}$$

The eddy current density in the iron produced by one conductor, from $J=-\Sigma\ {}^{dB}/_{dt}$,follows as

$$J_1=-\sum\frac{\mu I_m N\omega\cos(\omega t)}{\pi(r_1+r_2)} \tag{5.30}$$

Assuming a uniform eddy current in an iron core, the total eddy current produced by one conductor becomes

$$\Sigma J_1 = -\sum \frac{\mu I_m N \omega \cos(\omega t)}{\pi(r_1+r_2)}(r_2-r_1)b \tag{5.31}$$

and the eddy current produced by another conductor is

$$\Sigma J_2 = -\Sigma J_1 \tag{5.32}$$

where μ is the permeability of iron,

b is the thickness of the yoke plate.

So that the total eddy current in the iron core is

$$SJ_1+\Sigma J_2 = 0$$

5.4.5 Influence of Leakage Reluctance on Torque Sensitivity

The intermediate layer between the two yoke plates,which forms the shunt of the permanent magnet flux, must not be too high, in order that flux through the airgap can be sharply reduced, but it can not be too small so as to cause most of flux through the leakage path rather than airgap. Therefore a optimal value should exist for a design specification. The difference between the static torque expressed in equation (5.12) and energised torque equation (5.26) is given:

$$\Delta T = T - T_i$$

$$= 4Ra^2 \frac{[(R_2-2R_a)(R_1+R_3)+R_1R_3](R_1+R_3)[R_3F_a+(R_1+R_3)(F_b-F_c)]F_c}{[(R_1+R_3)(R_2+2R_a)+R_1R_3]^3} \tag{5.33}$$

Approximate estimation of the optimal leakage reluctance in terms of the distance between the two yoke plates is possible by differentiating equation 5.33 with respect to R_3, thus

$$\frac{\partial \Delta T}{\partial R_3} = 4Ra^2(\alpha_1+\alpha_2+\alpha_3) \tag{5.34}$$

where

$$\alpha_1 = \frac{3(R_1+R_2+2R_a)(R_1+R_3)\,[(R_1+R_3)(R_2-2R_a)+R_1R_3)]\,[R_3F_a+(R_1+R_3)(F_b-F_c)]F_c}{[(R_1+R_3)(R_2+2R_a)+R_1R_3]^4}$$

$$\alpha_2 = \frac{[(R_1+R_3)(R_2-2R_a)+R_1R_3)]\,(R_1+3R_3)+R_1^2 R_3}{[(R_1+R_3)(R_2+2R_a)+R_1 R_3]^3} F_aF_c$$

$$\alpha_3 = \frac{(R_1+R_3)[R_1R_3+(R_1+R_3)(R_1+2R_2-4R_a)]}{[(R_1+R_3)(R_2+2R_a)+R_1 R_3]^3} (F_b-F_c)F_c$$

and letting function 5.34 be zero yields

$$\frac{\partial \Delta T}{\partial R_3} = 0 \tag{5.35}$$

Hence the optimum leakage reluctance R_3 can be obtained from the equation (5.35), and consequently can be used to evaluate the shunt path dimension of the initial design.

5.5 Demagnetisation

The permanent magnetic materials are usually classified into two main groups , as shown in Fig 5.11

One group includes the ferrite rare-earth and banded-polymer-rare-earth materials, characterised by linear or near-linear demagnetisation curves. The second group, containing metallic alloy materials of the Al-Ni-Co type, is characterised by a non-linear demagnetisation curve. As is well known, the alloy materials generally offer better remnant flux density values, lower costs per unit volume of material, but poor coercive force values than the materials in the first group.

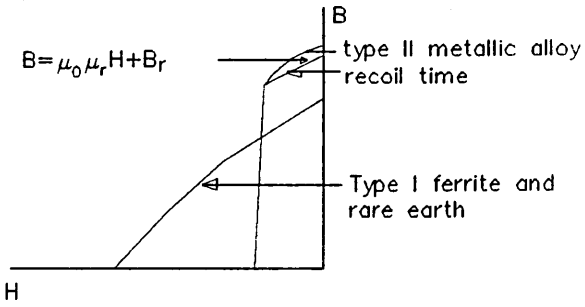

Fig. 5.11 Typical demagnetisation curves for permanent magnet materials

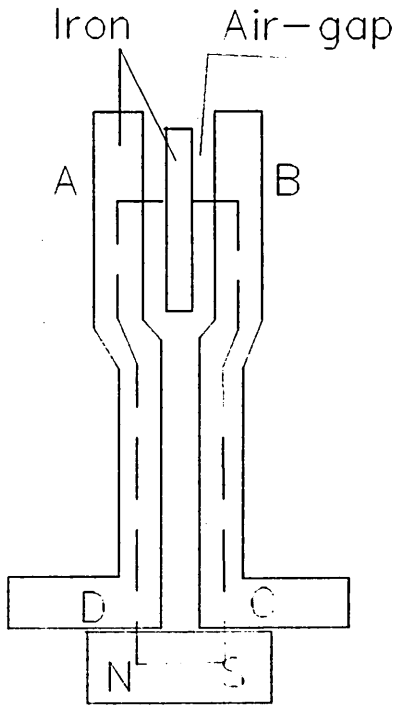

Figure 5.12 Integration path circuit of this actuator for demagnetisation

Considering the effects of the permanent magnet MMF on the flux density in the air-gap and assuming the replacement of the the magnetic disc by an iron disc, as shown in Figure 5.12, the magnetising force may be integrated along the path ABCDA, assuming MMF drops in the iron to be negligible. If the values of magnetising force in the air-gap Ha and the magnetic material Hm are assumed constant over their respective distances, g and lm, then

$$H_m.l_m+2g.H_g=0 \qquad (5.36)$$

The Flux density in the magnetic material, Bm, is related to the magnetising force by equation 5.37 (see Fig. 5.11),

$$Bm=\mu_0 \mu_r Hm + B_r \tag{5.37}$$

Additionally

$$Ha = Ba / \mu_0 \tag{5.38}$$

and

$$B_m = k k_1 B_a \tag{5.39}$$

Combining equations 5.36,5.37,5.38 and 5.39 yields the following expression for the air-gap flux density, in the absence of rotor disc,

$$B_a = \frac{B_r}{k k_1 + 2\mu_r g / l_m} \tag{5.40}$$

where k is the leakage factor and k_1 is the ratio of the air-gap area to the magnetic area.

Alloy magnets have appeal because of their low costs and generally high flux densities. The torque on the disc is a function of its position and the size of disc, but it depends essentially on the flux density in the air-gap. From equation 5.40 the use of alloy magnets will also be influenced by the need to magnetise the material to high values of flux density and also by the poor values of the ratio of the peak torque to the continuous torque,Tp:Tc, which is inevitably affected by the coercive force. The bonded-polymer rare-earth material costs significantly more than alloy material, but is readily machinable with conventional machine tools. It also possess a high Tp:Tc ratio due to the large coercive force.

5.6 Analytical Method in the Design of Stepper Motor Actuator

5.6.1 Introduction to the Design

The design of the proposed stepper motor actuator is orientated towards the production of a set of characteristics possessing high current sensitivity consistent with a torque sensitivity up to 0.5N.mm/20mA. For this proposed actuator , it is questionable whether this performance is feasible and thus whether it immediately can be made to operate without a toroid transformer and whether there is no need for high precision machined surfaces. There are two permanent magnet excitation sources in the proposed actuator, one of them being the multi-pole permanent magnet rotor disc.

The analytical approach was described in the last section and used for the preliminary design and analysis of the actuator. The investigations were made into the effects of the key dimensions and magnet data on the actuator performance. The preliminary design specification of the proposed stepper motor actuator was given and its characteristics were discussed

5.6.2 Determination of Excitation MMFs

An approximate torque expression(5.4) is used to find the variations of the torque with the required excitation MMFs in order to determine the preliminary design dimensions and excitation levels for the proposed stepper motor actuator at a given holding torque value of 0.15N.mm. Figure 5.13 shows the source excitation MMF(equivalent) as a function of the holding torque for different rotor disc sizes. The required excitation MMF is seen to considerably increase with the electrical torque. An approximate linear relation between electrical torque and MMF appears after a specified

value of torque,says, 0.04N.mm(Fig 5.13). The projected value of holding torque, 0.15N.mm, is seen to require an equivalent MMF,i.e. 18AT, corresponding to the disc diameter of 6mm. Fig 5.14 shows the excitation MMF as a function of the rotor disc diameters for producing different holding torques. The conclusion is that the smaller excitation MMF to produce a value of electrical torque requires a larger diameter disc.

These results can be used to estimate the value of the excitation MMF required for a given holding torque. The design of permanent magnet dimensions and magnetisation were carried out by reference to the design approach described in section 5.4 based on the above estimated value of MMF and some parameters such as disc inertia, material properties. Furthermore, the flux in the airgap is calculated using the equation (5.1), and the results are illustrated in the Table5.1

Table 5.1 Predicted flux in airgap for different torque

and rotor disc diameter pole-pairs n=6

disc diameter	Flux in the airgap x10^{-6} WB					
mm	Torque (N.mm)	0.01	0.02	0.05	0.1	0.2
8	2.51		3.53	5.57	7.88	5.2
10	3.11		4.38	6.97	9.85	13.94
12	3.74		5.29	8.36	11.78	16.73
13	4.05		5.73	9.05	12.83	18.12
7	4.36		6.17	9.76	13.79	19.52

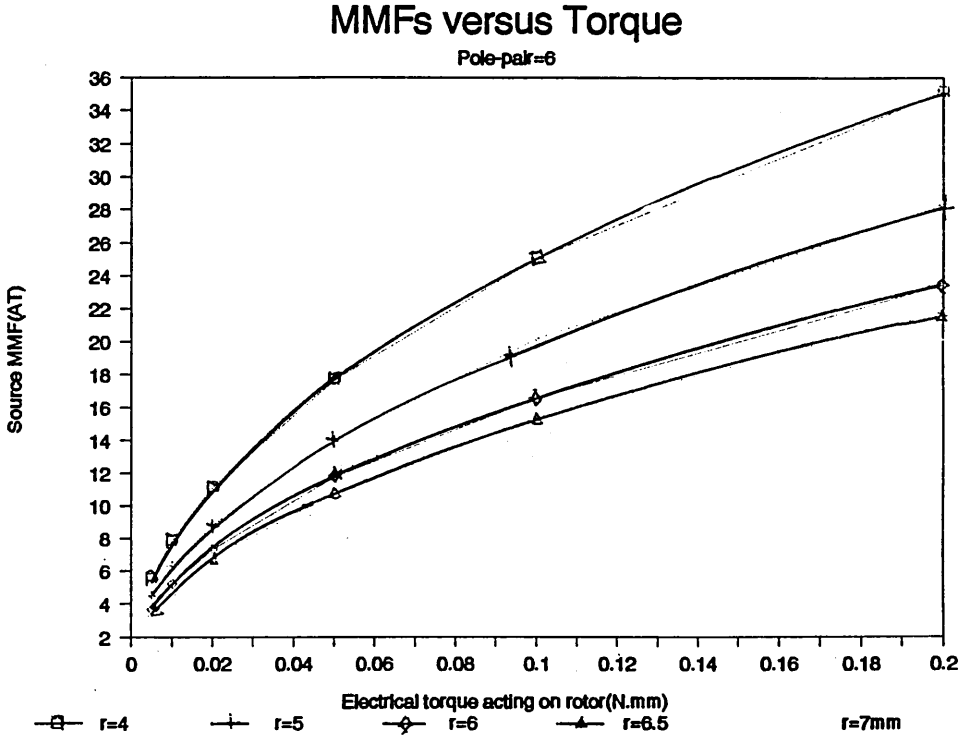

Figure 5.13 Predicted excitation MMF versus the electromagnetic torque

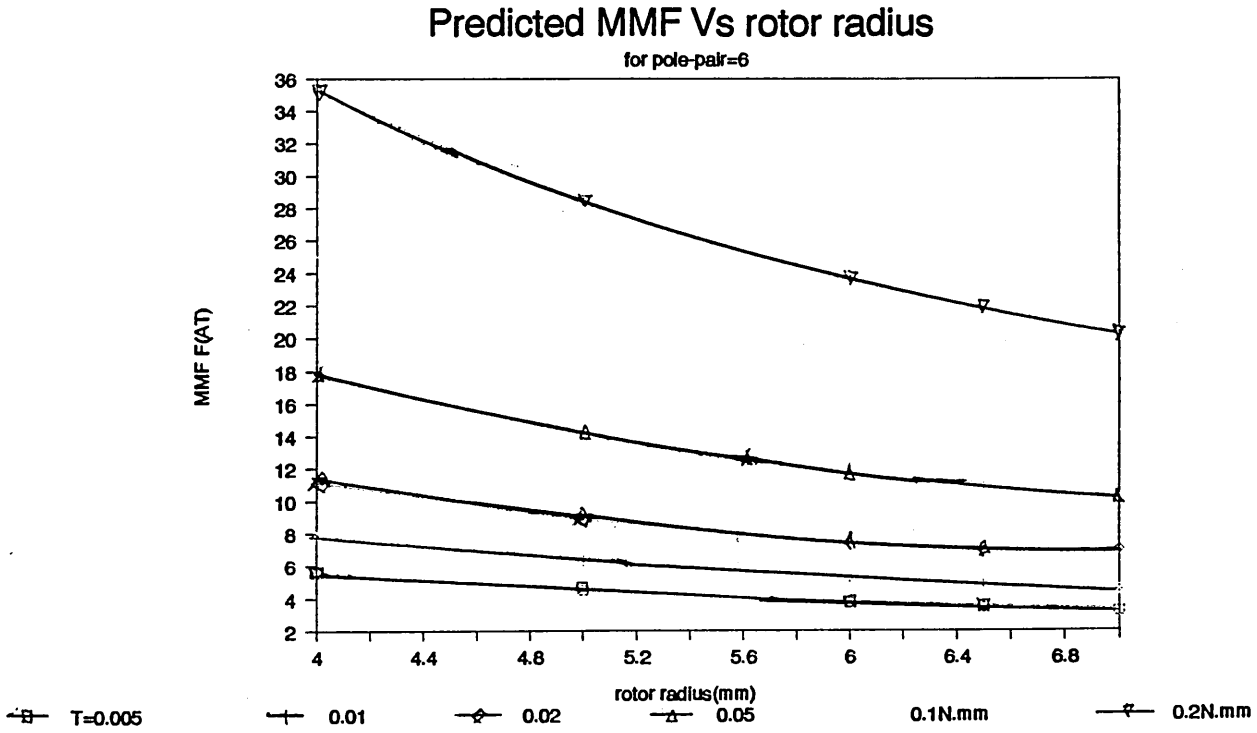

Figure 5.14 Predicted Excitation MMF versus disc rotor size

5.6.3 Prediction Of Dynamic Response Time

The actuator sensitivity not only depends on the magnitude of control current but also on the actuator response time which plays a significant role in the actuator operation. The governing dynamic equation of the rotor disc is given by

$$\Delta T = J\frac{d^2\theta}{dt^2} \tag{5.41}$$

where $\Delta T = To - Tm(i,\theta)$ (5.42)

To is the opposing torque produced by the acting spring;

Tm(i,θ) is the electrical torque in function of control current and rotating angular displacement as shown in figure 5.15;

J is the inertia of the rotor;

θ is the angular displacement.

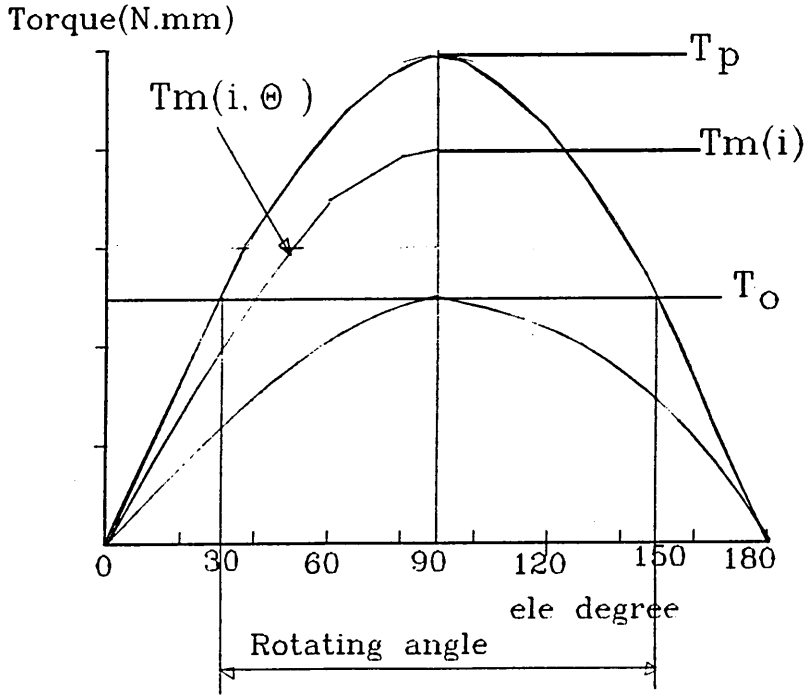

Figure 5.15 Basic torque as a function of current and angular displacement

The shape of the torque curve depends on the actuator magnetic poles construction and generally follows a rather complex mathematical expression. Here, we suppose the disc magnet stepper motor may produce a purely sinusoidal torque function. The relation between electrical angle, α, and mechanical angle,θ, and the number of rotor pole pairs,n, is then

$$\alpha=n\theta$$

The electrical torque,$T(i,\alpha)$, is expressed in a sinusoidal function of the electrical angular displacement(α) , as follows,

$$T_m(i,\alpha)=T_m(i)\sin(\alpha) \tag{5.43}$$

where Tm(i) is α function of control current at electrical angle ($\alpha=90^0$), and expressed as follows:

$$T_m(i)=T_p-A\,I_m^2\sin^2\omega t \tag{5.44}$$

where T_p is the peak electrical torque for electrical angle $\alpha=90^0$ at time(t=0).

For a typical 50Hz sinsoidal operating current, when the disc rotating time is a quarter of one cycle(5ms), the peak electrical torque Tm(i) has to be reduced to the opposing force level,thus, $Tm(i)=T_0|_{t=5ms}$. From equation(5.44), we obtain

$$A=(T_p-To)/I_m^2$$

Hence the peak electrical torque can be given by

$$T_m(i)=Tp-(Tp-T_0)\,Sin^2\omega t \tag{5.45}$$

Substituting (5.45) into equation (5.43) then into (5.42)

$$\Delta T=To-[T_p-(T_p-To)\sin^2\omega t\ ]\sin(\alpha) \qquad (5.46)$$

thus the governing dynamic equation of the rotor disc is represented as

$$Jd^2\theta/dt^2=To-[Tp-(Tp-To)\sin^2\omega t]\ \sin\ \alpha \qquad (5.47)$$

The equation (5.47) is a non-linear differential equation. A numerical computation method was used to solve this equation for which a maximum step rotating angle(θ) was set to 30^0 for a12 pole-pairs disc rotor. The peak value of the torque was set to 0.1 to 0.15N.mm, and the inertia of the rotor disc set at 0.01 to 0.05g.cm^2. The predicted results for these values are shown in figure 5.16

From figure 5.16 the dynamic response time of the current sensitive stepper motor actuator must be limited to 10ms, since when the current decreases from the peak value to a smaller value, the torque will rise again, which may cause the disc to roll back. The actuator must also be stable for a range of mechanical shock which can be expressed in terms of a torque difference between the peak value of static torque (Tp) and the opposing torque (To) being $\Delta T=Tp-To$. Figure 5.16 shows the range of design parameters. The maximum operating time is limited to 10ms based on the appropriate choice of disc inertia and the acting torque.

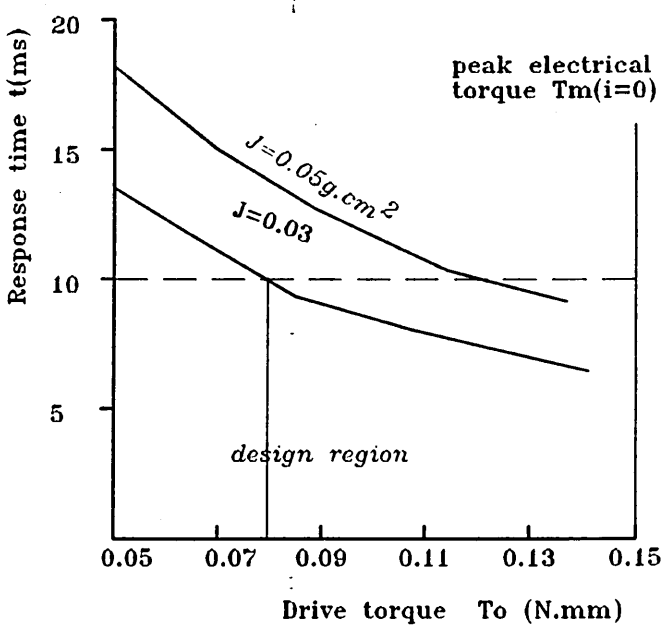

Figure 5.16 Predicted response time versus opposing torque for different rotor disc inertia

5.6.4 Determination of the Minimum Torque Required

The detailed view of the release system for the proposed system is represented in figure 5.17. The figure shows the output shaft 22 of the stepper motor with a cam surface at 22A. The cammed end of 22A of the output shaft 22 cooperates with a release flag 34 of quadrant shape which is pivoted on a spindle 35 secured to a support plate(not shown). The release flag 34 at its pivot end has an actuating and release surface 37 for co-acting with a release lever 38. A spring 39 supported by the spindle 34 has an active arm 40 engaging the release flag 34 to urge the latter against the end 28 of the output shaft 22. The mechanical release system is described as , when the rotor disc rotates to align the

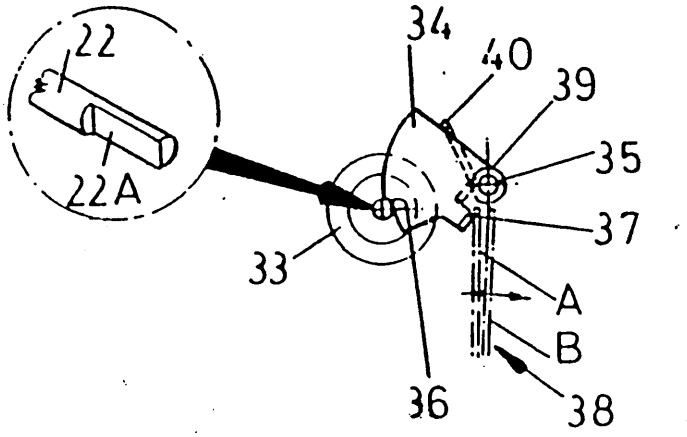

Figure 5.17 Mechanical diagram of the release system

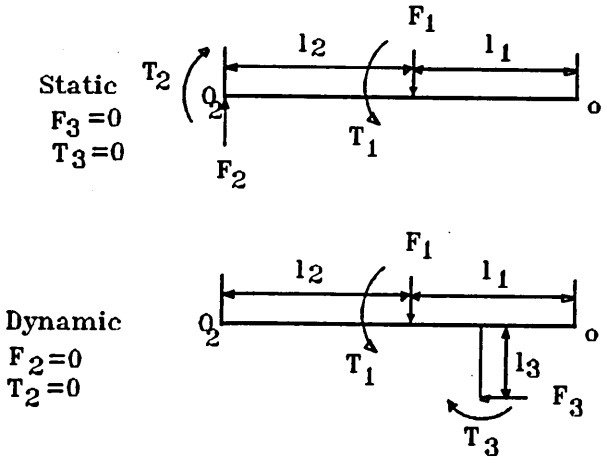

Figure 5.18 Force diagram of the release system

ramp or cam face 22A of the shaft 22 with the release detent 36 which allows the release flag 34 to pivot, under the spring action, against the cam face 28. It thus causes the actuating and reset surface 37 to urge the release lever 38 from position A to position B which, to be expected, causes the contacts of the RCD to be thrown to the off position. The determination of the opposing force relies on the dynamic response time and the effect of permitted mechanical shock which is concerned to the mechanical vibration of the release system.

The mechanism release lever system is divided into two stages, stationary and dynamic. Figure 5.18a shows the force diagram for stationary release system in which the release flag(34) is disconnected from the release lever(38), thus $F_3=0$. In this figure force F_2 acts on on the cam face 22A of the shaft 22, force F_1 acts on the flag provided by the opposing spring,thus $T_1=T_2$. Figure 5.18b shows the force diagram for the release moving system in which the magnetic torque (T_m) acting on the disc (or shaft) is supposed to be zero, and the force F_3 acting on the release lever(38) typically requires 25gf-30gf to urge the lever 38 from position A to B, thus $T_1=T_3$. The movement displacement of the release lever from A to B, typically, is required to be $d_1=2mm$. Assuming the flag needs to rotate an angle of $\pi/3$ around the acting point O to release the lever, then the length of lever l_3 is required to be,

$$l_3=d_1/\pi/3=1.9mm$$

Hence the torque T_3 is given by

$$T_1=T_3=F_3*l_3=25*1.9=47.5gf.mm=0.46N.mm$$

Setting the friction coefficient c=0.1, the torque T_2 is given by

$$T_2=(1+c)T_1=0.506N.mm$$

Assuming the length of lever l=12mm, the force F_2 is

$$F_2=T_2/l=0.042N$$

Setting the force (F_2)acting distance(r) from point (o_2) to axis of the shaft to be 1.5mm, then the minimum magnetic torque acting on the rotor disc is required

$$Tm=F_2*r=0.063N.mm$$

5.6.5 Mechanical Vibration Of the Release Beam

In the design, the release system is simplified as a release beam supported by the two points (O,O_2) with forces (F_1,F_2) as shown in figure(5.19). The following assumptions are made that the mass of the beam itself is negligible in comparison with force F_1 and y is the dynamic instantaneous displacement. The inertia force is $\frac{F_1}{g}\frac{d^2y}{dt^2}$, the restoring force in the beam is ky, where k depends on the position of the load and the material being used. From the strength of materials, we find that the static deflection of the beam under the static load F_1 is

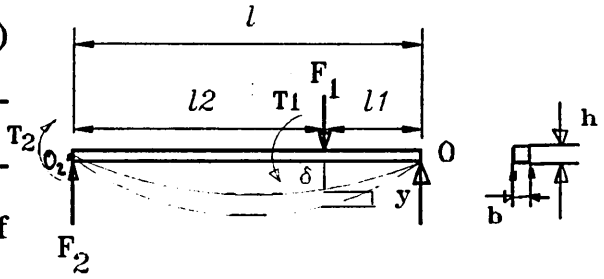

Figure 5.19 release beam

$$\delta=\frac{F_1 l_1^2 l_2^2}{3EI\,l} \tag{5.48}$$

and

$$k=\frac{F_1}{\delta}=\frac{3EI\,l}{l_1^2 l_2^2}$$

The acceleration equation is therefore;

$$\frac{3EI\,l}{l_1^2 l_2^2}y=-\frac{F_1}{g}\frac{d^2y}{dt^2} \tag{5.49}$$

The equation (5.49) can be written as

$$my''+ky=0 \tag{5.50}$$

where E is the modulus of elasticity, here $E=200kN/mm^2$

$m=F_1/g$

I is the moment of inertia, for this rectangular cross section $I=Sbh^3/12$

The solution for equation(5.50) is

$$y=A\cos\omega t+B\sin\omega t$$

Let us assume $y=0, y'=v_0$, when t=0, thus we have

$$y=v_0/\omega\sin\omega t \tag{5.51}$$

The natural frequency of this beam is known as

$$\omega=\sqrt{\frac{k}{m}}=\sqrt{\frac{g}{\delta}} \tag{5.52}$$

Hence the dynamic force acting on the point O_1 is

$$F_{1d}=ky=\frac{3EI\,l}{l_1^2 l_2^2}\frac{v_0}{\omega}\sin\omega t$$

The dynamic force acting on the point O_2 is therefore

$$F_{2d}=\frac{3EI}{l_1 l_2^2}\frac{v_0}{\omega}\sin\omega t \tag{5.53}$$

It can be seen that the dynamic force produced by the mechanical vibration depends on the external vibration velocity, the acting position of the load and the material used.

For a typical release weight F_1=25gf=0.245N, l_1 =3mm ,

the required section modulus of the cross section area can be obtained from the equation :

$$S=\frac{M_{Max}}{\sigma_w} \tag{5.54}$$

where σ_W is the allowable normal stress, for steel 165N/mm^2;

M_{Max} is the maximum bending moment;

S is the section modulus of the cross section=$bh^2/6$

hence

$$bh^2=\frac{6F_1l_1}{\sigma_w}=\frac{6x0.245x3}{165}=0.0267mm^3$$

Set maximum length of lever l=13mm, b=0.3mm, then h~2 mm and F_2=0.0565N

The static deflection of the beam is:

$$\delta=\frac{F_1l_1^2 l_2^2}{3EIl}$$

$$=\frac{0.245x3^2\,10^2x12}{3x200x0.3x2^3x13}10^{-6}=0.14\mu m$$

The natural frequency of the beam is:

$$\omega=\sqrt{\frac{g}{\delta}}=\sqrt{\frac{9.8}{0.14x10^{-6}}}=8.3x10^{3}\ rad/sec$$

$$T_{2d}=r\frac{3EI}{l_1 l_2^2}\frac{v_0}{\omega}=0.12v_0$$

Assuming the external vibration velocity V_0 is less than 0.4m/s, r=2.5mm, the maximum dynamic torque acting on the shaft from equation (5.53) is therefore:

$$T_{2d}=r\frac{3EI}{l_1 l_2^2}\frac{v_0}{\omega}=0.12v_0$$

$$=0.048\text{N.mm} \quad \text{for initial velocity } v_0=0.4\text{m/s}$$

Considering the dynamic response time in figure 5.16 , if the inertia of the moving part is chosen as 0.03g.cm^2 and the response time is limited in 10ms. The opposing torque must exceed 0.09N.mm. Considering the mechanical shock (producing a torque of 0.048N.mm), the peak electrical torque(Tp) has to be greater than 0.09+0.048=0.138N.mm.

5.6.6 Preliminary Determination of the Permanent Magnet Disc

The preliminary determination of the magnet disc is associated with the size and material. The study made in section 5.4 has demonstrated that the higher permanent magnet remanent flux density can produce a higher flux density in the airgap(equation 5.40) and consequently a higher electrical torque. The energised actuator dynamic response time depends on the inertia of the rotor disc for a given value of acting torque. The prediction of dynamic response (Fig 5.16) demonstrates that the inertia of the disc should be made as small as possible to reduce the operating time.

From Figure 5.20 the inertia of cell V is,

$$dJ=2\pi\, dh\, r^2 dr$$

from which the inertia of the disc is

$$J=\int_0^{r_3} 2\pi d h r^3 dr=\frac{1}{2}\pi d h r_3^4 \qquad (5.55)$$

where d is the density of the material;

h is the thickness of the disc;

r_3 is the disc radius.

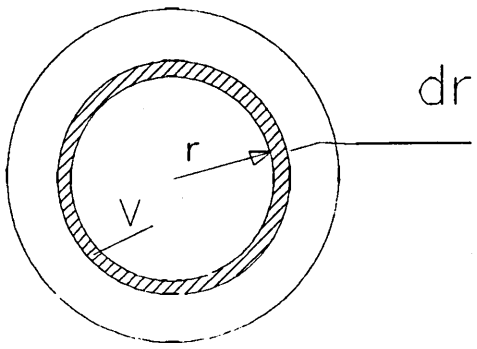

Figure 5.20 Disc dimension

The approximate relationships between the inertia of the rotor disc and disc size for several material properties are illustrated in the Table 5.2.

Table 5.2 Disc material and Inertia

Material	Br(T)	Hc	Density	r(cm)	Inertia g.cm^2			
		kA/m	g/cm^3	h(cm)	0.5	0.6	0.65	0.7
AlNiCo				0.02	0.014	0.029	0.04	0.055
	0.7-1.3	56-130	7.3	0.03	0.0215	0.044	0.0614	0.0826
				0.04	0.0287	0.0595	0.0819	0.1101
Rare-earth				0.02	0.016	0.033	0.045	0.0618
	0.7-1.2	230-800	8.2	0.03	0.0241	0.05	0.0689	0.0927
				0.04	0.0322	0.0667	0.0919	0.1236
Ferrite				0.02	0.009	0.0195	0.0268	0.0362
	0.1-0.4	120-290	4.8	0.03	0.0141	0.0293	0.0403	0.0543
				0.04	0.0188	0.0391	0.0537	0.0723

The actuator operating response time must be taken into account in the design of the rotor disc. From the evaluation in the last section, if the operating response time is limited to 10ms, the inertia of the disc has to be a value of 0.03g.cm^2 under the action of the opposing torque,0.09N.mm from figure 5.16. The permanent magnet material was chosen as the rare-earth material with high remanent flux density and high energy. The approximate calculation of the magnet parameters were carried out by reference to the formula of equation (5.5) as illustrated in Table 5.3.

Table 5.3 Initial Design parameters of permanent magnet disc

h(mm)	dia.(mm)	pole-pair	Br(T)	Hc(KA/m)
0.4	12	6	1	450
Angle of each slot	25^0	Angle of pole	25^0	

5.5.7 Relationship between Conductor Turns and Yoke Size

The inner and outer radius of the yoke plate are r_1 and r_2. Assuming N conductor turns through the core as shown in Figure 5.21, the relationship between the hole area and the conductor cross section area is given below

$$\pi r_1^2 = 2\pi k_2 N r_0^2 \qquad 5.56$$

where

k_2 is the coil fill factor,=1.2-1.3;

r_0 is the radius of conductor,=2.5mm.

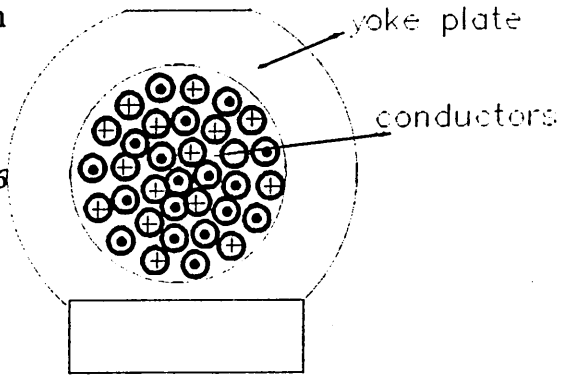

Figure 5.21 Coil window

From equation(5.56), the data of the ampere turns and the inner radius of the yoke plates were calculated and given in Table 5.4

Table 5.4 Conductor turns with yoke size

Turns (N)	iN=30mA XN(AT)	$d_1=2r_1$
2	60	11
3	90	13.4
4	120	15.5
5	150	17.3
6	180	18.9
7	210	20.5

5.5.8 Determination of the Distance Between Two Yoke Plates

The distance between the two yoke plates can be approximately determined using the analytical formulae and experience. The simplest formulae 5.57 and 5.58 were used in the preliminary determination of the leakage reluctance. The airgap flux for non-energised state is

$$\varphi_a=\frac{R_3\varphi_1}{R_a+R_3} \tag{5.57}$$

Flux in airgap for the energised state is given by ,

$$\varphi_i=\frac{R_3\varphi_1}{R_4+R_a+R_3} \tag{5.58}$$

where R_3 is the leakage reluctance between the two yoke plates;

R_4 is the saturated reluctance in the slot section;

φ_a ,φ_i are the fluxes passing through the main circuit and the air-gap respectively.

Assuming Ra=constant, the ratio function, which is the equation 5.58 divided by the equation 5.57, is expressed as

$$f(\varphi)=\frac{1+\beta}{\alpha+1+\beta} \tag{5.59}$$

where $\alpha=R_4/R_a$

β is the ratio of the leakage reluctance to the airgap reluctance $=R_3/R_a$

The ratio function 5.59 is roughly plotted against the saturated reluctance factor α for different reluctance ratios β.

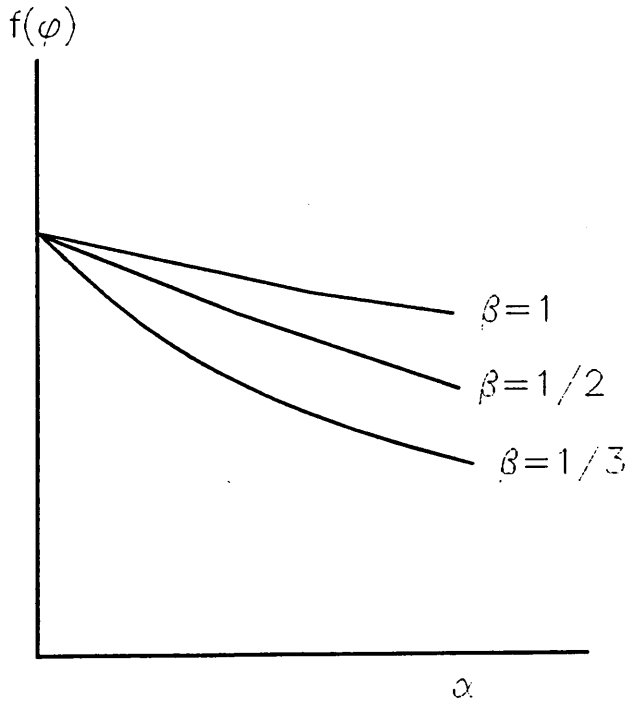

Figure 5.22 f(ϕ) as a function of saturated reluctance factor α for different leakage reluctance levels

This figure shows the smaller leakage reluctance can lead to a greater reduction of the energised flux in the airgap. The leakage reluctance can be determined based on previous design experience data and the evaluation in which the leakage reluctance is represented as $R_3=\beta Ra$. If the minimum length of the air-gap between the disc and yoke plate is assumed 0.1mm, therefore the approximate airgap reluctance is ,

$$R_a=2\frac{0.1}{\mu_0 S_{disc}}$$

Assuming that the area of the face-to-face surface of the two yoke plates is 3 times that of the disc, the width between the two yoke plates is given by

$$\delta=0.6\beta$$

Values of δ are given in Table 5.5 for $\frac{1}{4}\leq\beta\leq\frac{1}{2}$

Table 5.5 Range of the intermediate width (δ)

β	1/4	1/3	1/2
δ(mm)	0.15	0.2	0.3

5.7 Magnetic Material Properties

The magnetic material with high permeability(μ) is proposed to employ in the stepper motor actuator for producing high flux in the magnetic circuit. The parameters and magnetisation BH data of a high (μ) alloy magnetic material (Supermumetal) are illustrated in Table 5.6 and 5.7 respectively.

Table 5.6 Parameters of Supermumetal alloy

Parameters		Magnetic Material	
		Supermumetal	
Remanence Br (Tesla)		0.5	
Saturation Bsat(Tesla)		0.77	
Coercivity, Hc d.c. (A/m)		0.55	
Hysteresis loss at B_{sat} (J/m^3)		0.9	
Initial permeability d.c μ_4		140,000	
Maximum permeability D.C.		350,000	
Curie temperature(^{0}C)		350	
Physical properties		**Mechanical Properties**	
Coefficient of linear expansion (per ^{0}C)	13x10-6	Modulus of Elasticity (GN/m^2)	185
Resistivity (microohm m)	0.6	Vickers Hardness (HV)	290
Thermal conductivity (W/m ^{0}C)	33	Ultimate Tensile Strength (MN/m^2)	910

Table 5.7 DC Magnetisation BH Data of Supermumetal alloy

H		B
OE	A/M	Tesla
0.005	0.4	0.086
0.01	0.8	0.322
0.0125	1.	0.48
0.0188	1.5	0.583
0.025	2	0.614
0.0375	3	0.64
0.05	4.	0.66
0.075	6.	0.69
0.1	8	0.708
0.125	10	0.725
0.25	20	0.755
0.375	30	0.766
0.5	40	0.77
0.625	50	0.773
0.75	60	0.775
1	80	0.77

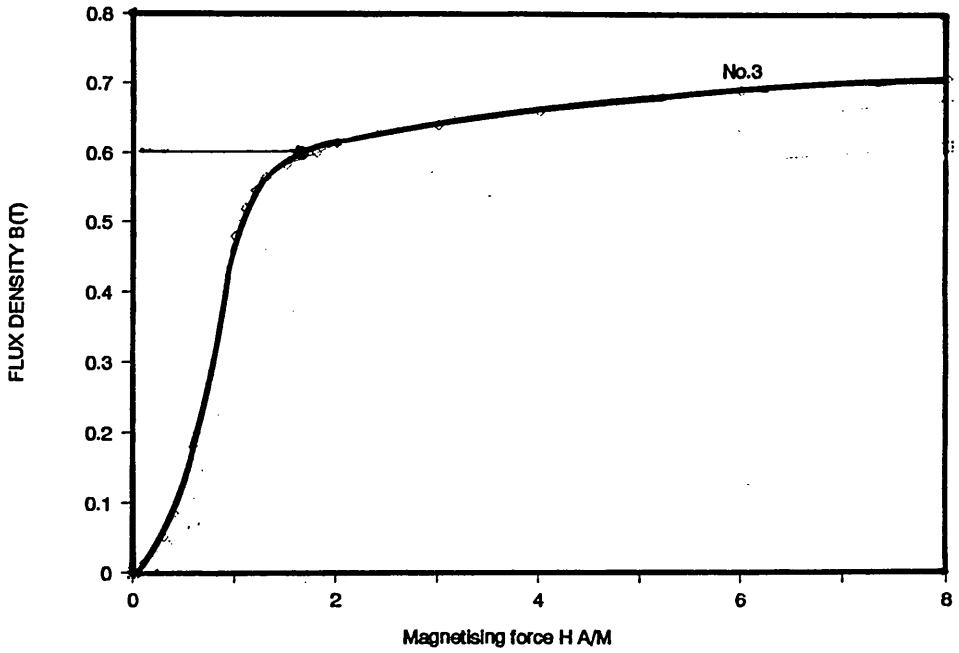

Figure 5.23 DC magnetisation BH curve of Supermumetal

5.8 Preliminary Design Specification of the Stepper Motor Actuator

An electrical torque of 0.15N.mm, acting on the disc is required as described, corresponding to an excitation MMF of 13AT. The design was carried out using the method described in section 5.4. The design used the material,SUPERMUMETAL, which possesses very high permeability and the thickness of 0.8mm plate. The design value of flux in the airgap was calculated (see table 5.1) $9.3\text{x}10^{-6}$WB, and the flux through the yoke plate was designed to $5\text{x}10^{-6}$WB due to the division of the leakage flux. The flux density in the yoke is designd to be lower than the knee point,see Fig 5.23 says, Bw=0.6T, then the cross section area of the yoke plate is required

$$S=0.5\phi_{\delta}/B_w = 0.5 * 9.3\text{x}10^{-6}/(0.65)=7.2\text{mm}^2$$

From the evaluated values in table 5.4, if inserting 4 coil turns through the actuator's yoke plates, the inner diameter of the window in the yoke plate is required 15.5mm and the outside diameter of the window is,

$d_2=2xr_2=2(r_1+7.2/0.8)=33.5mm$

The flux density in the constriction slot is designed to be just over the knee point(0.7T), (saturated flux density 0.79T), then the cross section area of the slot is obtained as,

$$A_{slot}=\frac{0.5*9.3X10^{-6}}{2*0.75}=2.98mm^2$$

Hence the width of the slot is , f=A/b=2.98/0.8=3mm

The distance between the two yoke plates is chosen as δ=0.12mm reference to table 5.5. The dimensions of the excitation permanent magnet(MMF 13AT) at the bottom of the actuator was initially designed as diameter(7mm) and thickness(4mm) using Al-Ni-Co material with Br=0.8T and Hc=1600 OE. The design parameters of the rotor disc is listed in table 5.3.

The preliminary design dimensions of the proposed stepper motor actuator are illustrated in the table 5.8.

Table 5.8 Preliminary design dimensions of the proposed stepper motor actuator

Unit: mm

a	b	c_1	c_2	e	f	g
0.8	0.8	14	29	1.5	2.5	0.1
h	l	n	r_1	r_2	r_3	r_4
0.4	0.12	6	7.5	13	6	3.5
r_5	N	d	h_p			
2	4	7	4			

5.9 Prediction of Torque Characteristics

The predicted torque characteristic of the preliminary design using the lumped equivalent magnetic circuit approach is shown in figure 5.24. The peak value of torque versus the control current is plotted in figure 5.25.

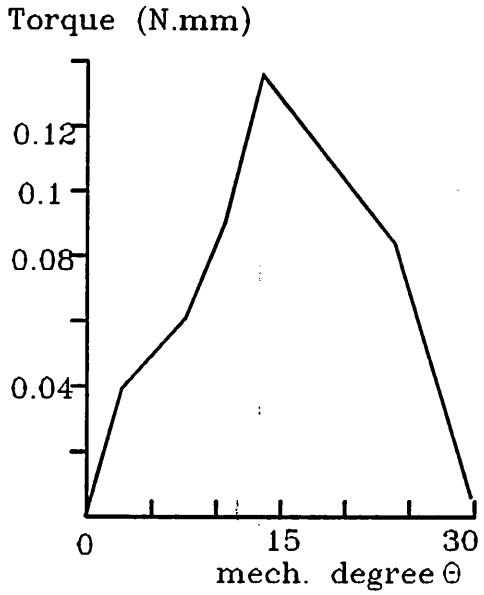

Figure 5.24 Predicted torque as a function of angular displacement

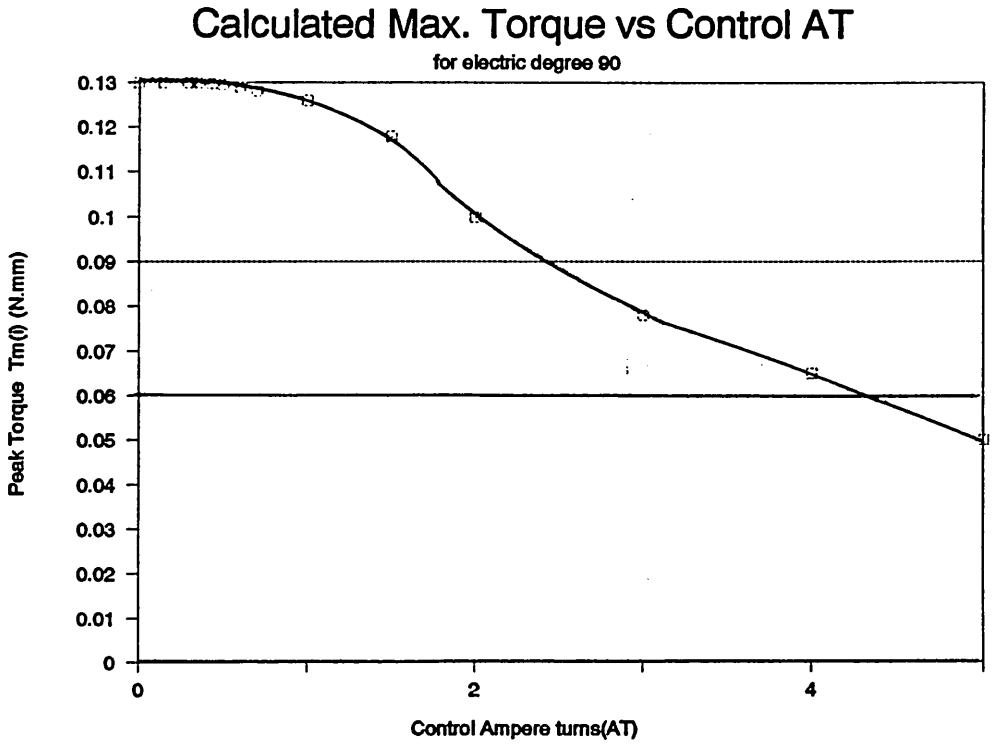

Figure 5.25 Electrical torque at 90^0 electrical degrees against the control current in a 20 turn coil

5.10 Conclusions

A stepper motor actuator was postulated, which possessed high sensitivity to control current and combined the toroid transformer and electromechanical release system. It furthermore utilized 4 or 5 coil turns for an excitation RMS current 30mA to actuate the release system. A miniature disc magnet stepper motor was proposed to employ as the release means to obviate the need of very small airgaps. An analytical approach equivalent magnetic circuit was described in this chapter and used to evaluate the proposed actuator.

The analytical approach is easy to use and gives a good approximation of the performance for low level of saturation. The design highlighted that this approach is suitable for the preliminary design evaluation of the stepper motor actuator.

Chapter 6

Optimisation Design of the Stepper Motor Actuators

6.1 Introduction

For a stepper motor type actuator to detect a small residual current (typically, 10mA-30mA), it is necessary to minimise the excitation MMFs of the actuator. Ideally, it is desirable to insert the smallest possible current into the coil to reduce the electrical torque from its holding level to its release level. However, the dependency of the energised torque reduction not only relies on the control current, but also relies significantly on the geometry of the actuator, particularly, the size of shunt path, slot and airgap. It, therefore, is most important to investigate the effects of the key dimensions and parameters on the actuator performance, in order to minimise the source MMFs, control MMF and to optimise the dimensions, and consequently to reduce the manufacturing cost.

The actuator was designed to operate in a highly saturated mode. A good prediction accuracy is required at a high flux level over part of the working range. The comparison between the two approaches, magnetic equivalent circuit(LEMC) and finite element method(FEM), was made for the same design specification as shown in figure 6.1. The curve labelled LMC is

obtained using the LEMC approach and curve labelled '4' is obtained using FEM, with 4 mesh layers . It is noticed that the results computed by the two approaches are quite different. The main causes are: larger nonuniformities in the flux density distribution within each lumped element of the magnetic circuit and the greater significance of the increased flux levels in the constriction slots. Hence, full magnetostatic field prediction is desirable, together with the simulation of the magnetic poles and shapes as well as the corresponding torque.

In this chapter a set of calculate-and-modify iterations are embarked on with the aid of the Finite Element CAD technique and lumped equivalent magnetic circuit method(LEMC) . The FEM CAD technique can be used for the optimisation and prediction when good accuracy is required. The LEMC method is valuable for the preliminary design since it gives a quick and ready solution.

An evaluation of the dependencies of the torque and sensitivity on the actuator key design parameters was performed. The analysis demonstrates the optimum values for the design. Finally, a design specification is obtained and evaluated.

6.2 3D Finite Element CAD in Stepper Motor Actuator Design

Before using the finite element CAD in this study, it is necessary to check the accuracy of the finite element CAD, TOSCA in the computation of a rotating magnetic field in the stepper motor actuator, although the application in the design of clapper actuator has demonstrated its precise

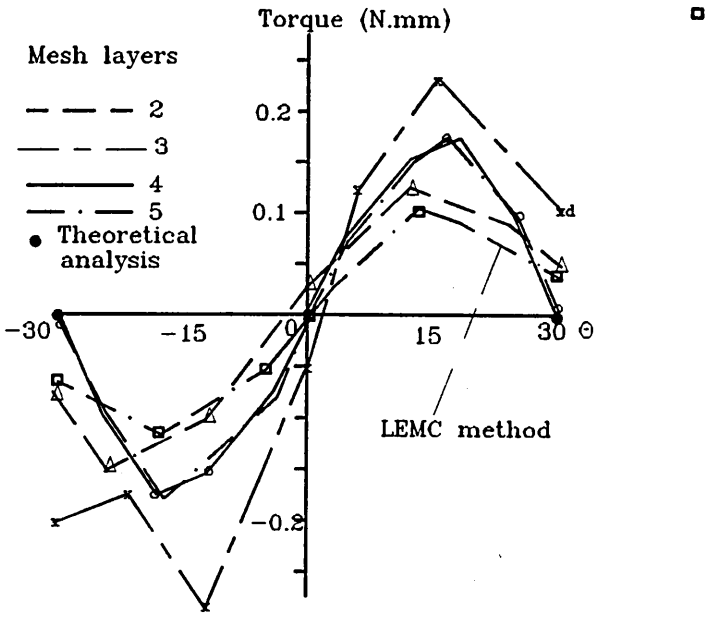

Fig. 6.1 Comparison between the computed results using the two methods: FEM and LEMC

computation. Figure 6.1 shows the electrical torque against the angular displacement for different mesh layers in the airgap performed in TOSCA. Table 6.1 gives the comparison between the theoretically analysed and 3D FEM computed electromagnetic torque at two typical points.

Table 6.1 Comparison between theoretically analysed and 3D FEM computed results

Electric degree		0^0	180^0
Theoretical torque		0.0	0.0
FEM result Peak torque (Tm=0.16N.mm)	Layers=2	-0.05	0.2
	3	0.04	0.08
	4	$1.5x10^{-5}$	0.003
	5	$2x10^{-5}$	0.001
LEMC		0.02	0.1

It is obvious from Fig. 6.1 and table 6.1 that the increase of the division mesh layers in the airgap can obtain better results. The solution also indicates that at least four layers have to be used for the airgap to obtain reasonable accuracy . The optimization for the stepper motor actuator was carried out based on the initial design whose details as illustrated in the table 5.8 for the pole position of 90^0 electrical degree as shown in figure 6.2.

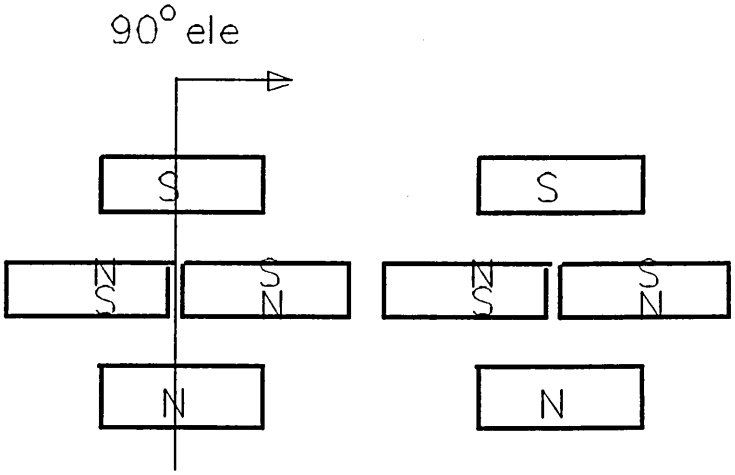

Figure 6.2 Magnetic poles arrangement

6.3 Optimisation

6.3.1 Torque Versus the Airgaps

The electrical torque, generally, is inversely proportional to the airgap length as shown in figure 6.3 which gives the electrical torque as a function of airgap for two typical excitation MMFs,Fa and Fb, for a given size of actuator.

It is obvious that a considerable increase of torque occurs for smaller air gap, particularly for gap less than 0.05mm, where the air gap reluctance is equal or less than the iron part reluctance. However, in this design the minimum design airgap is limited to 2x0.1mm, to permit a restricted disc movement. Therefore the computations are based on the minimum airgap of 2x0.1mm.

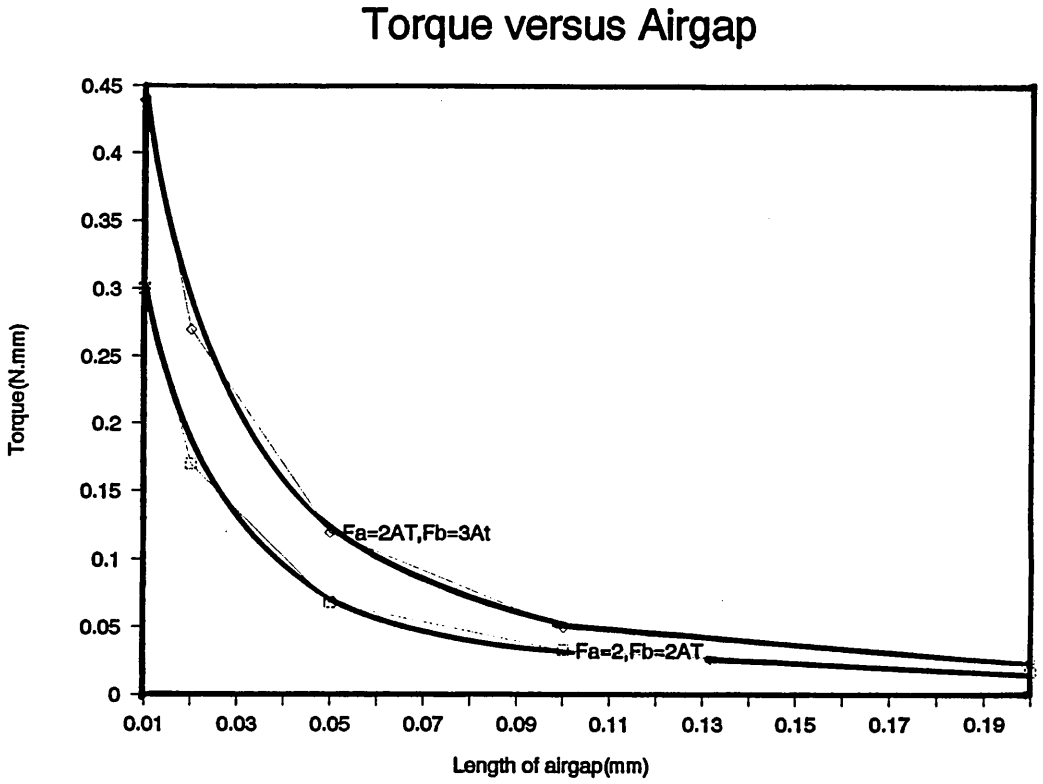

Figure 6.3 Electromagnetic torque acting on disc veresus length of airgap

6.3.2 Optimisation to Leakage Shunt Reluctance

The shunt reluctance can be expressed in terms of a factor, Ks, which is the ratio of the distance(δ) between the two yoke plates to the face to face area of the plate, $Ks=\delta/s(\mu m/mm^2)$. Figure 6.4a shows the variations of torque with the factor Ks and Figure 6.4(b) shows the torque sensitivity($\Delta T/AT=[T_m(i=0)-T_m(i>0)]/AT$, which is the torque reduction to the energised ampere turns) to the factor Ks. Figure 6.4a shows that when the factor Ks increases, the torque increases slightly and then becomes constant. It is also observed from Fig 6.4b that the maximum torque sensitivity occurs to the factor ,Ks ,for the range of 0.3-0.4. The reason for this is that after injecting current into the coil one of the

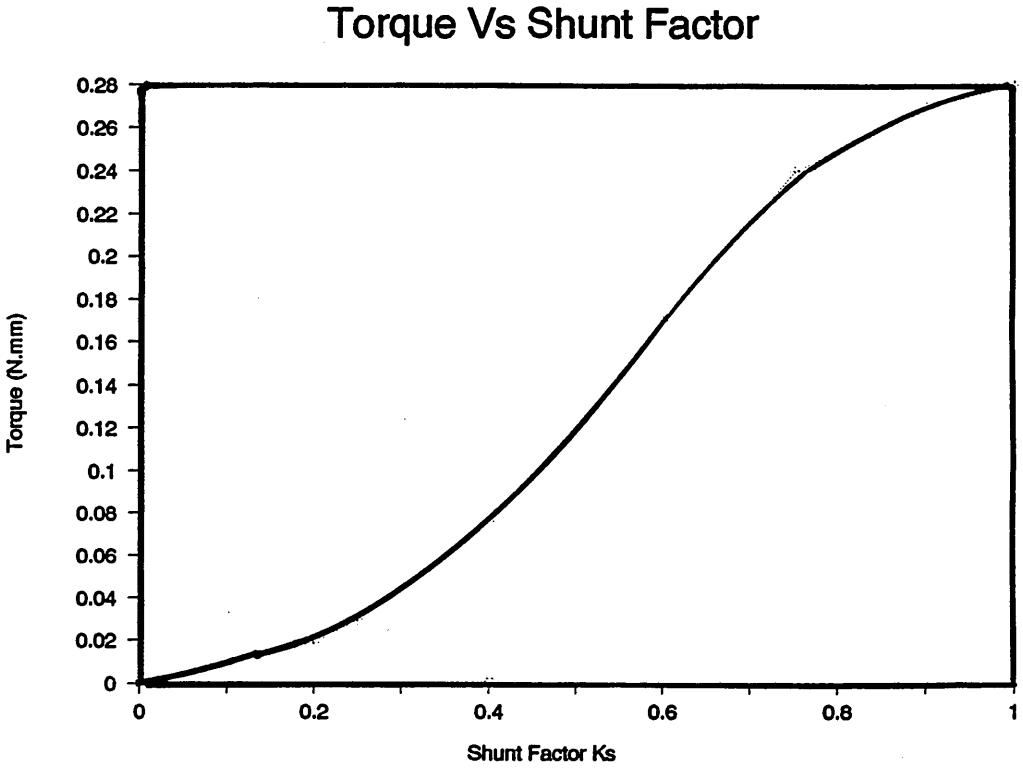

Figure 6.4a Torque against shunt factor

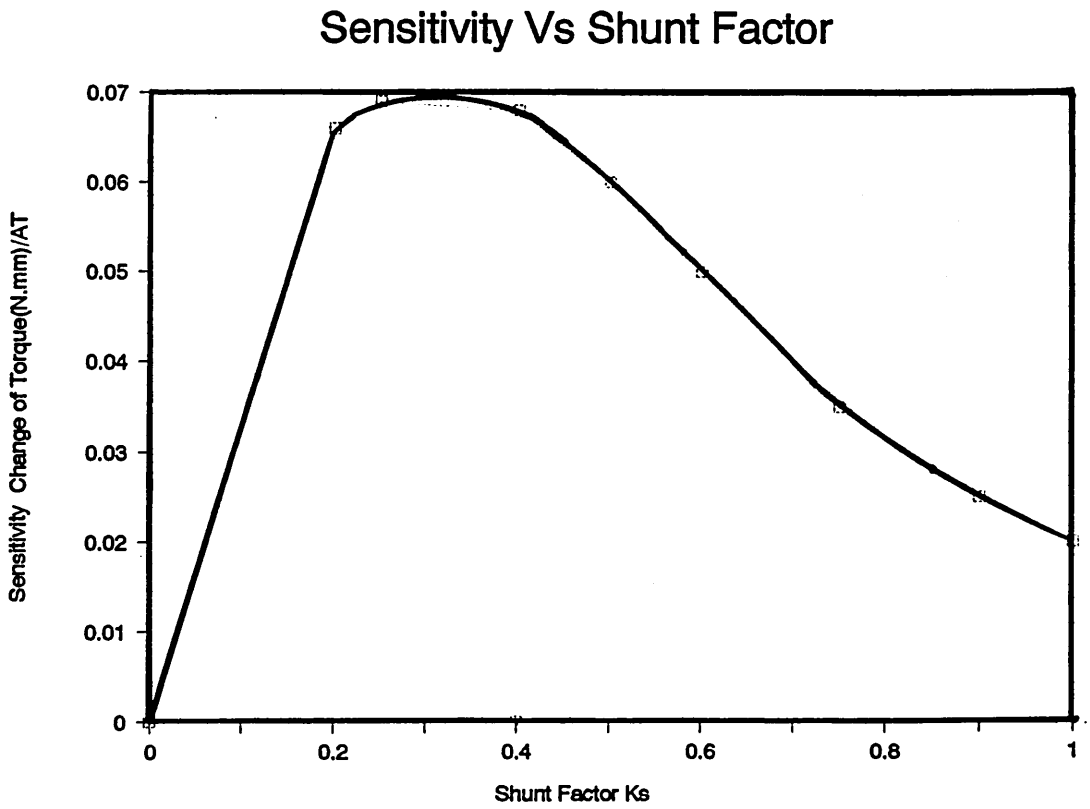

Figure 6.4b Torque sensitivity versus shunt factor

constriction slots is saturated, consequently, the flux produced by the source permanent magnet is diverted into the shunt path rather than airgap. Obviously, a smaller shunt reluctance can lead to more flux being diverted into the shunt path, which consequently leads to more torque reduction when energised. In contrast, a higher shunt reluctance produces a lower torque sensitivity. The chosen design points, which lie between Ks=0.3-0.4 on the curves are shown in figure 6.4a,b.

6.3.3 Optimisation to Constriction Slot

The investigation is made into the effects of the constriction slot cross section area on torque sensitivity. The slot factor(Ko) is expressed in terms of a factor, Ko, which is the ratio of the cross section area to the length of the slot. The study is based on the above optimal solution of airgap and shunt reluctance. Figure 6.5 shows the variations of torque and torque reductions with slot factor Ko for the length of the airgap of 2x0.1mm and the shunt factor Ks=0.3. From the figure it is observed that increasing the slot factor leads to an increase in torque over a limited range of Ko, whereupon the torque is constant. In particular interest is that the torque reduction,$\Delta T(i)$, does not follow the torque variations. Moreover it appears that the peak value occurs for K_0 values between 1 and 1.4, which is caused by the over-saturation in a small slot and non-saturation in a large slot. Neither of these effects can,however, efficiently control this type saturated actuator.

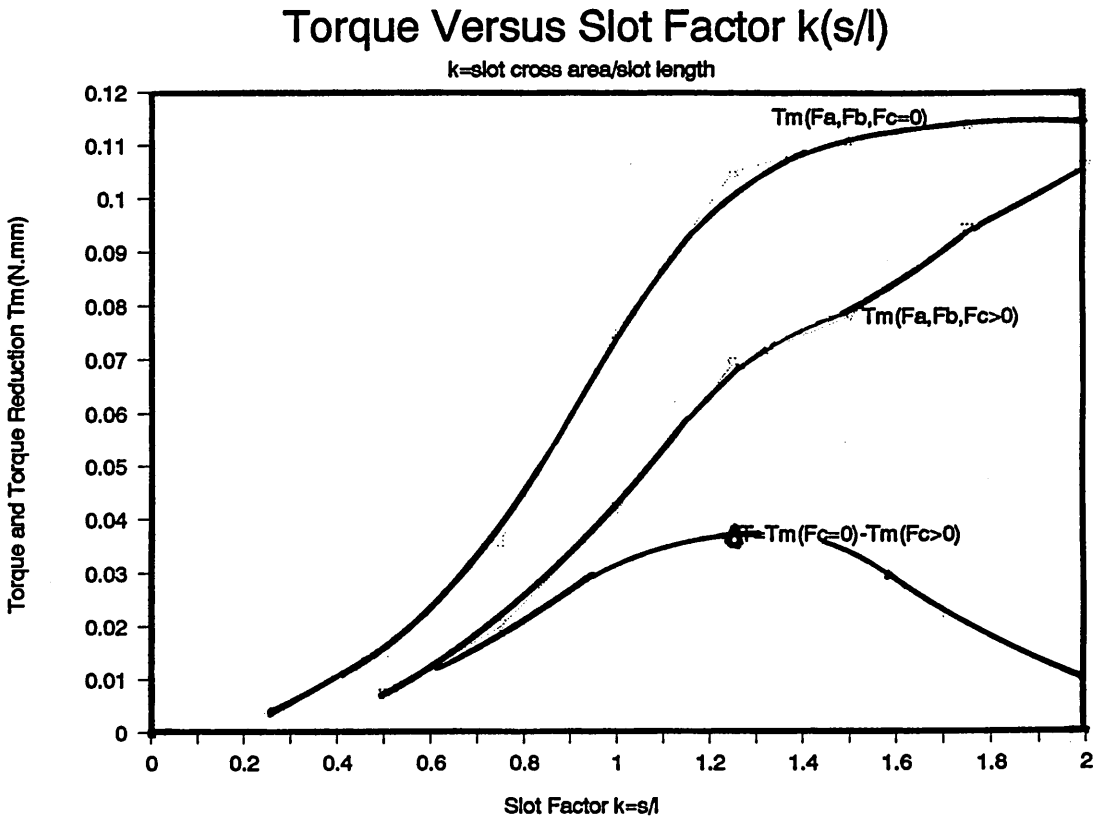

Figure 6.5 Torque and torque reduction against the constriction slot factor

6.3.4 Influence of Material Properties on Torque Sensitivity

The material property, particularly the permeability, μ, has a significant effect either on the torque or torque sensitivity. Figure 6.6 shows the torque and torque reduction against the relative permeability ,μ_r. It can be seen from figure6.6,however, that the change of permeability does not make a great difference to the electromaginetic torque, but does cause a large variations in the torque reduction. The explanation for this behaviour is that the iron reluctance is negligible compared to the airgap reluctance in the whole magnetic circuit, so that the high magnetic ma-

terials permeability does not produce major change in the static torque. On the other hand, the reluctance of the magnetic circuit around the winding greatly depends on the material permeability. Therefore a high material permeability can cause a big cancellation of the flux in the airgap, and consequently the electrical torque. The conclusion is that for the design the magnetic material with highest permeability should be chosen for the iron yoke.

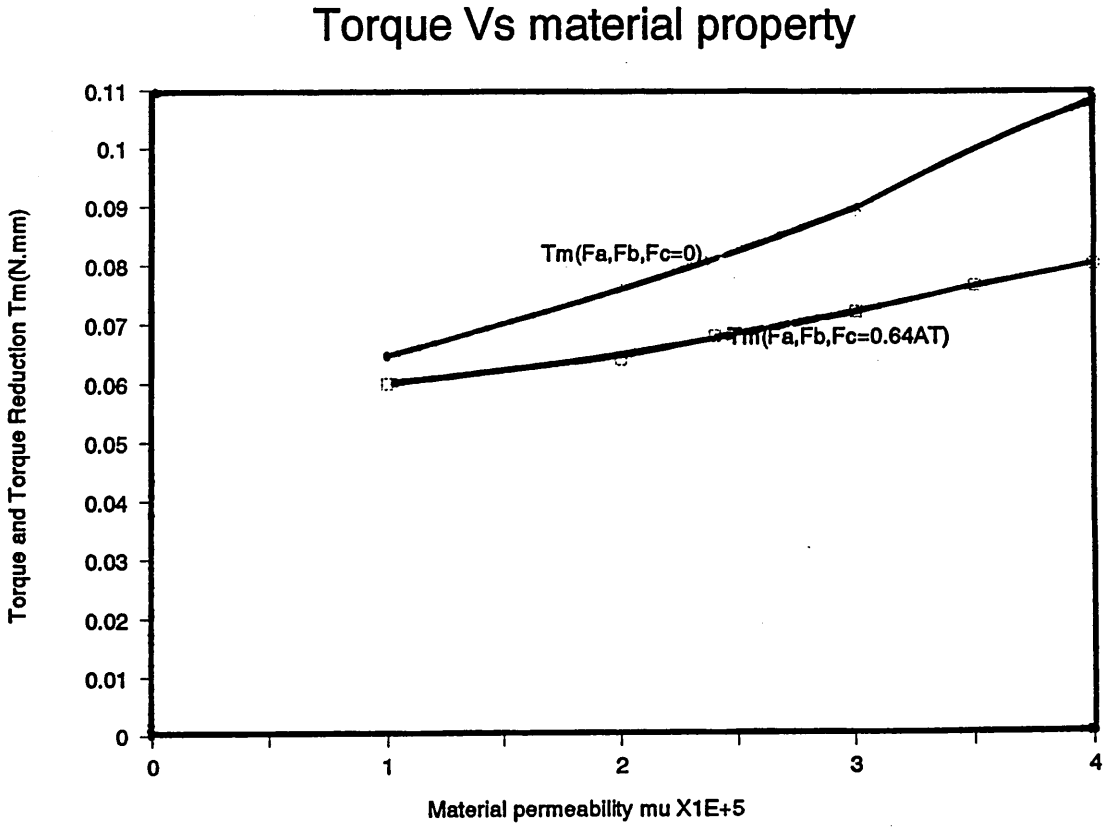

Figure 6.6 Statictorque and energised torque versus magnetic material permeability

6.3.5 Torque and Sensitivity - Source MMFs(Fa,Fb)

Based on the actuator dimension determined by above investigations, the relationships between electrical torque and excitation MMFs, Fa and Fb, were obtained as shown in Figure 6.7. From this figure it can be found that the increase of electrical torque with increasing Fb is higher than that for a corresponding to increasing Fa. The reason is that the electro-magnetic torque depends on the change of stored energy in the airgap and therefore any increase for excitation Fa leads to a relatively small change in airgaps energy. A greater change occurs in the leakage path, a smaller increase to the co-energy in the airgap is compared to increasing the Fb in the magnetic circuit.

From the studies, it was found that for a given actuator there is a permanent-magnet magnetisation level beyond which the torque sensitivity will actually decrease. This phenomena is seen in figure 6.8, which shows the relation between torque and equivalent magnetisation Fb for several constant excitation levels Fa. The choice of design Fb is seen to require a compromise. At different value of Fa, a required value of Fb to produce the maximum torque sensitivity is different. Any higher value is seen to lead to a reduction in sensitivity.

Figure 6.9 shows the relationship between the energised electrical torque and control MMF,Fc, for different excitation MMFs,Fa and constant value of Fb. It is apparent from the sets of curves in figure 6.9 that if the electrical torque from static level is to be reduced to a release level, the higher control Fc is required to reach this level for the torque produced by high MMF,Fa, than that produced by lower Fa, since the saturation to the actuator slots leads to most of the flux from Fa through leakage path rather than the airgap, and the poles of the yoke plate will appear neutral, whereupon no

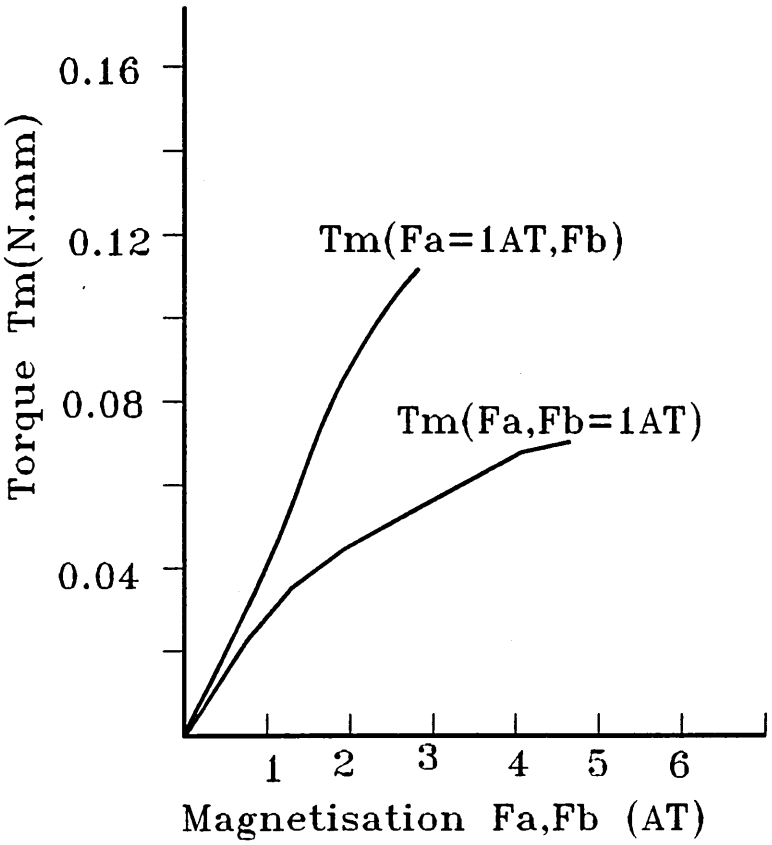

Figure 6.7 Electromagnetic torque versus the source MMFs (Fa,Fb)

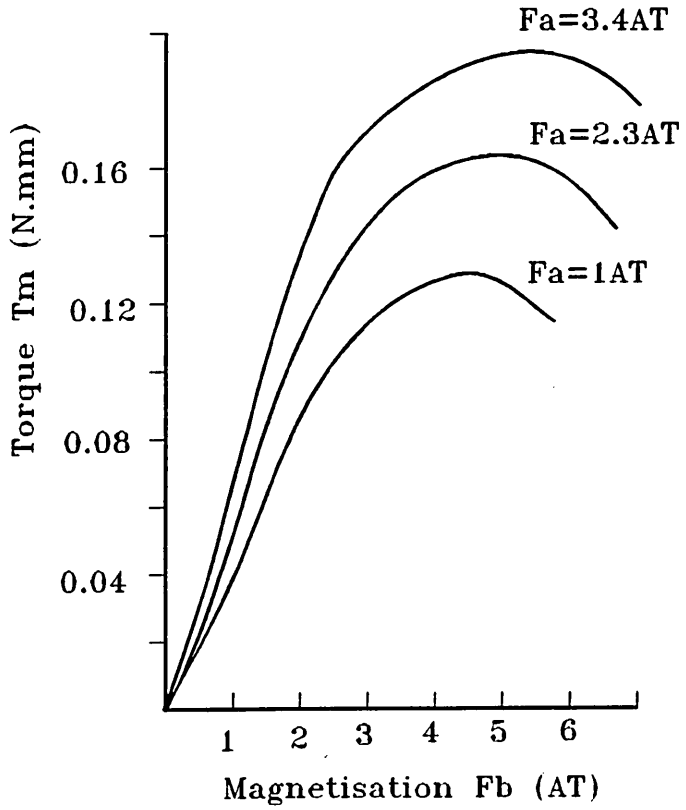

Figure 6.8 Electromagnetic torque versus the source MMF(Fb) at fixed Fa

torque is produced. Naturally, smaller values of Fa have higher torque sensitivity, and consequently higher sensitivity of the actuator.

The analysed solutions indicate that the dependency of electrical torque on the excitation MMFs ,Fa and Fb is regarded as increasing a small value of Fb leads to a large increase in torque rather than Fa. The smaller value of Fa is easily controlled than higher Fa, which leads to a higher actuator sensitivity as shown in figure 6.10.

However, the increase of Fb is limited by the volume of the disc, because increase of Fb is obtained by means of either using the high energy of permanent magnet or increasing the volume of magnet disc. But if the highest energy permanent magnet material is used and still does not achieve the required value, it would be necessary to increase the volume of the disc. The volume of disc Fb can not, of course, be made too large, since the volume has a bearing on the inertia, the operating response time, and also on the optimal magnetising level. Therefore there exists a optimal design points for Fa and Fb which lie on the knees of the curves in figure 6.7 and 6.8.

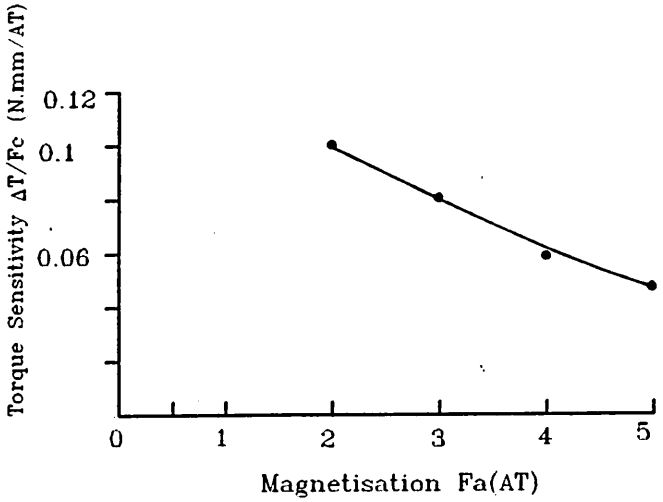

Figure 6.10 Torque sensitivity versus MMF(Fa)

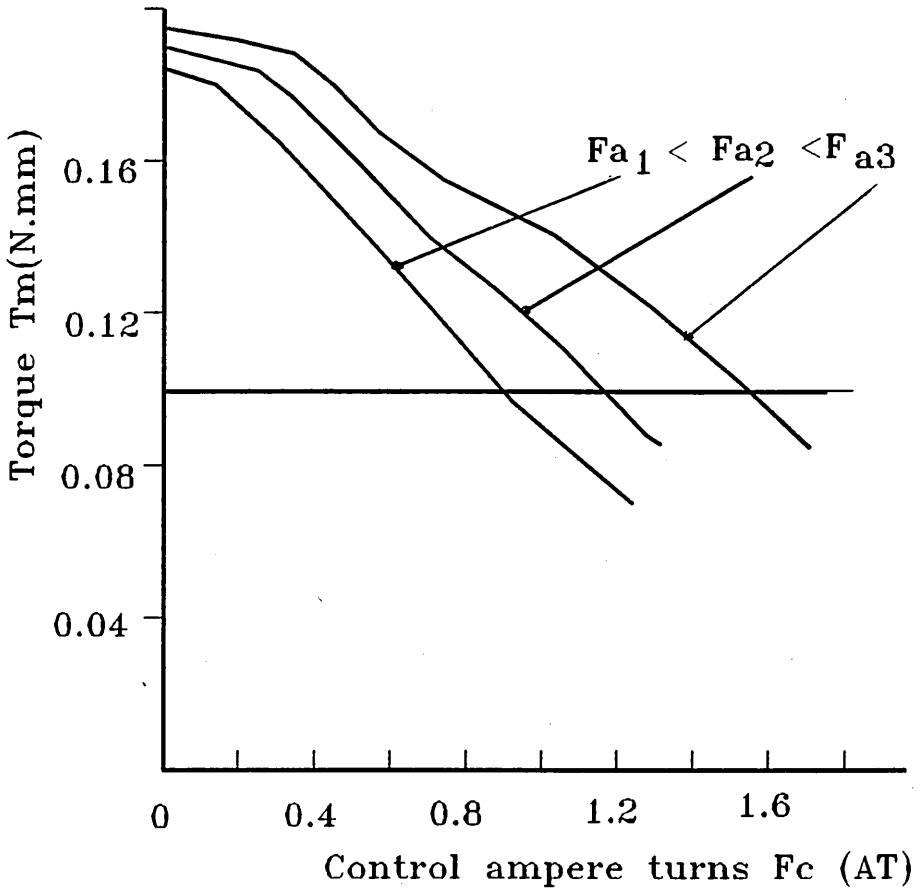

Figure 6.9 Torque as a function of control MMF(Fc) for different values of Fa

6.3.6 Optimisation of Window Path

The path around the coil window forms the magnetic circuit for the control flux . The influences of the length of the window path on the torque sensitivity is shown in figure 6.11 for the given actuator geometry and magnetic material property. It is observed that the length of the window path has a little effect on the static torque but it has a relatively large effect on the torque reduction, since the iron reluctance is proportional to the length of the magnetic circuit. The conclusion here is that the window should be made as small as possible to obtain low reluctance and higher torque sensitivity.

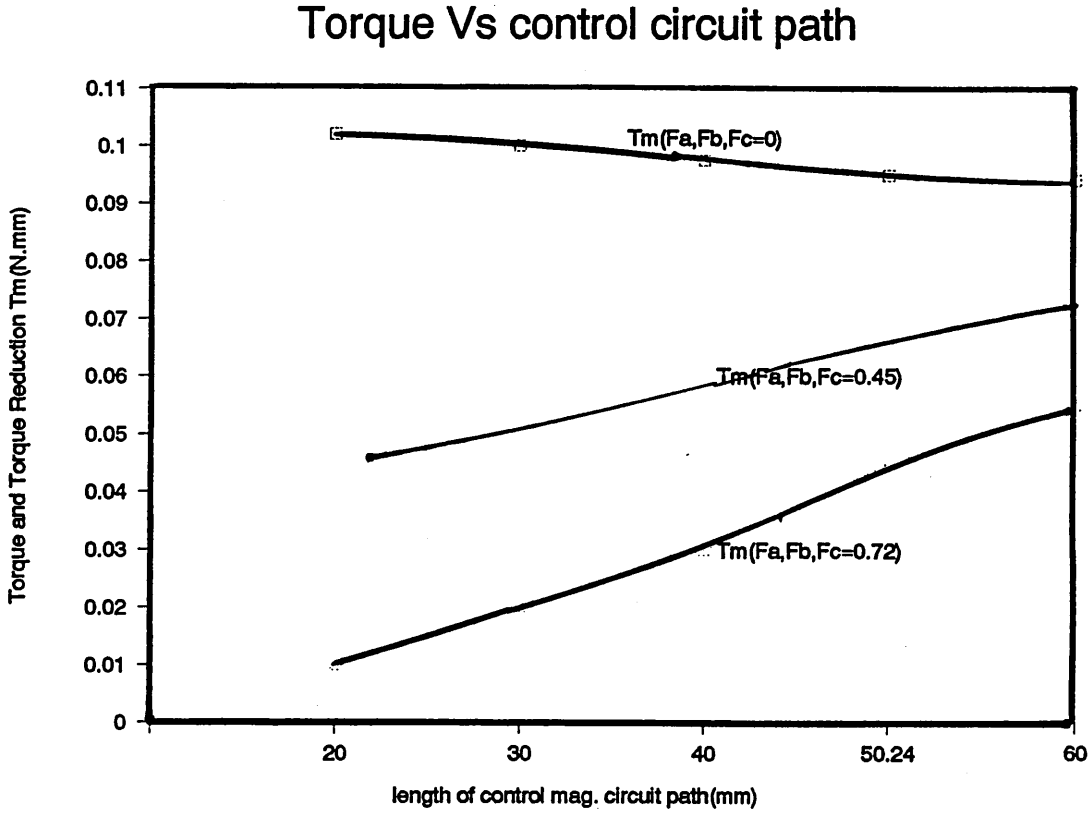

Figure 6.11 Torque sensitivity versus window path

6.3.7 Torque versus Number of Magnetic Poles

Since the torque components are produced by the two sides of the magnet, increasing the poles number can produce higher output torque. The simple formula(5.4) has shown the linear relationship between the torque and number of magnet poles. The relationship between the holding torque and the number of magnetic disc poles performed in TOSCA is shown in Figure 6.12. It is obvious that increasing number of poles increases the holding torque. However, the number of magnetic poles is limited by the step rotating angle.

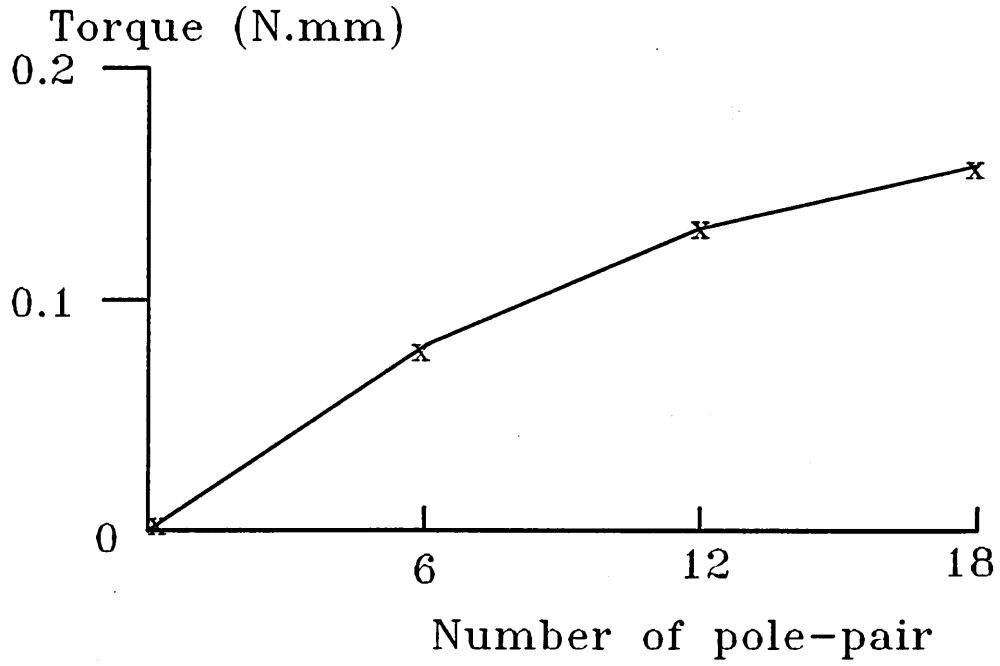

Figure 6.12 Predicted torque versus number of magnetic disc poles

6.4 Optimal Design and Evaluation

6.4.1 Optimal design Specification

The comments from the above analysis are epitomized, as follows: (a) the airgap between the yoke plate and disc needs to be at least, 2x0.1mm, to allow disc movement and the smallest airgap reluctance possible; (b) the shunt reluctance greatly affects the actuator sensitivity, the optimal design point occurs for the design shunt factor ,Ks, between 0.2-0.4 $\mu m/mm^2$; (c) the slot cross section area is a critical design parameter in relation to the actuator sensitivity. The area should be determined so as the flux density is just below the knee point value on the material magnetisation BH curve; (d) The material property, particularly the permeability, significantly affects the torque reduction sensitivity rather than the holding torque, therefore the material with highest permeability ,e.g. SUPERMUMETAL, should be used , subjected to cost; (e) for a given actuator geometry there is a permanent-magnet magneti-

sation level for either, Fa or Fb, beyond which the torque sensitivity will actually decrease. The control MMF,Fc, related to the torque sensitivity was found to rely on the value of MMF, Fa, rather than Fb,which means less Fa will lead to a higher torque sensitivity. It was also found that the torque produced by Fb is higher than that by the same value of Fa. Both of the two phenomena are most expected , hence there exists optimal points for both MMFs, Fa and Fb, in this type actuator.

From the above prediction the design dimensions for the proposed stepper motor actuator were modified as listed in table 6.2.

Table 6.2 Optimised actuator dimensions Unit :mm

a	b	c_1	c_2	e	f	g
0.8	0.8	14	28	0.8	0.7	0.1
h	l	n	r_1	r_2	r_3	r_4
0.3	0.06	18	7.5	10.5	6	3.5
r_5	d	h_p				
2	6	3.5				

Magnetic material: SUPERMUMETAL

Permanent magnet materials: Al-Ni-Co, B_r=0.8T μ_r=3

The torque characteristics of this actuator are evaluated based on the set of design dimensions in table6.2. Figure 6.13 shows the electromagnetic torque at 90^0 electrical degree as function of the control current. The electrical torque varying with the rotating angular displacement is shown in figure 6.14.

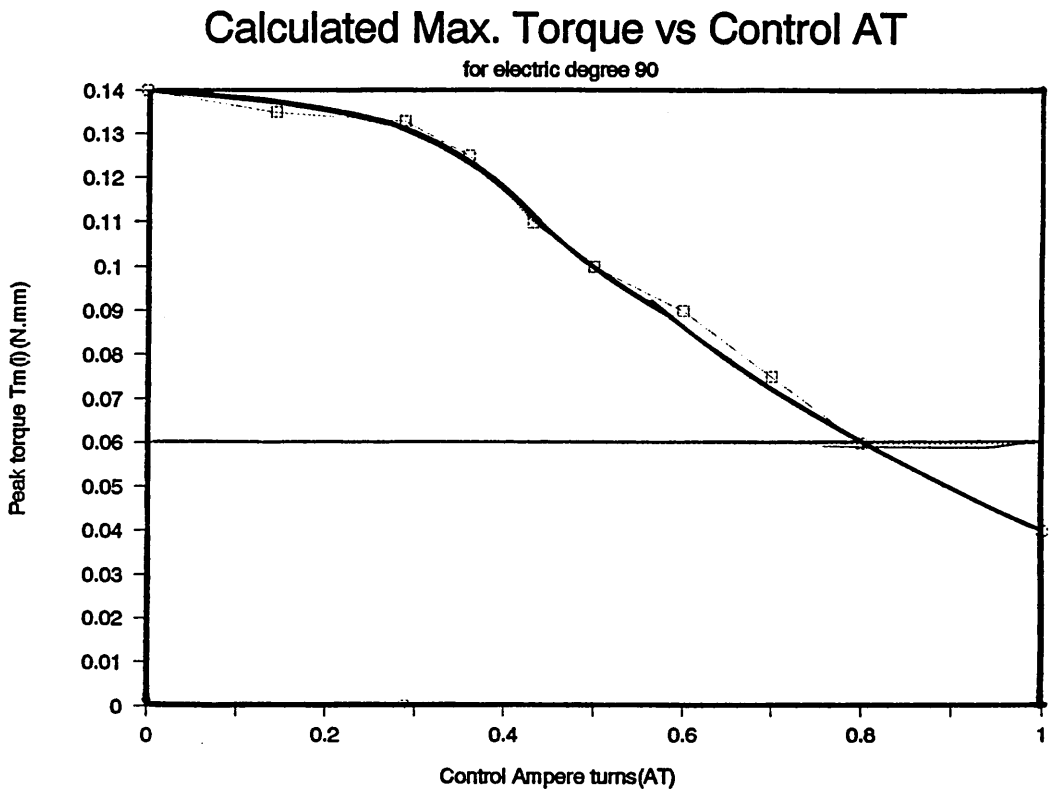

Figure 6.13 Predicted torque at 90^0 electrical degrees versus control ampere turns

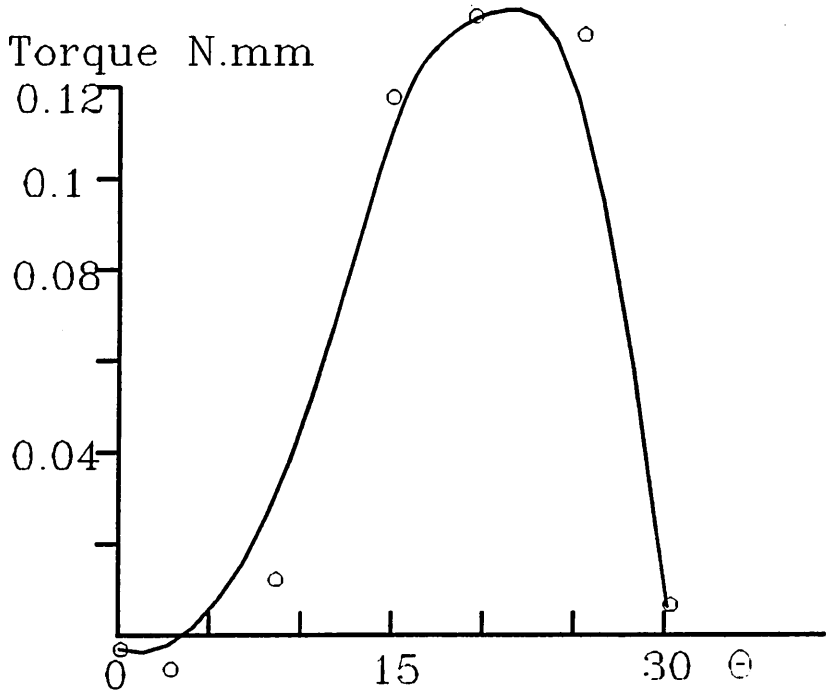

Figure 6.14 Predicted torque versus disc angular displacement

6.4.2 Recommendations for the Proposed Stepper Motor Actuator

The studies have demonstrated the effects of the critical design parameters and key dimensions, which are mainly associated with the permeability of magnetic material, airgap, shunt path and constriction slot, on the actuator sensitivity to control current. The investigation resulted in an optimum design for the proposed actuator based on an equivalent magnetic circuit technique and three dimensional finite element method.

The design parameters and dimensions were taken for the optimum values from the above investigations, the magnetic material with highest permeability such as SUPERMUMETAL was chosen . The characteristics of the optimal design have been evaluated as shown in figures 6.13 and6.14. The characteristics indicate that control ampere turns of 0.6AT is required to diminish the electrical torque from 0.15N.mm to 0.07N.mm at 90^0 electrical degrees, for which the flux in the magnetic circuit is minimum. In conclusion, for an airgap of 2x0.1mm a minimum holding torque of 0.15N.mm is required for the stepper motor type actuator, which would necessitate the use of a toroid transformer to provide sufficient tripping current (or control MMF) . It therefore cannot be operated at 30mA trip current, without a toroid transformer.

The relative position of the magnetic disc pole and yoke poles may be rearranged to produce the highest torque at the lowest flux in the magnetic circuit, and also to produce a ideal sinsoidal electrical torque with the rotating angle. It therefore should reduce the detent torque existing in the proposed designed actuator by means of changing the pole shape, position and design. The magnetic circuit providing the control flux should be as short as possible to produce a highest control flux.

6.5 Combination of Clapper Actuator and Stepper Motor

6.5.1 Combination of Clapper Actuator and Stepper Motor

The studies indicate that the proposed stepper motor actuator(fig.5.4) can not be operated by the standard residual current, up to 30mA, without a toroid transformer. The modification of the proposed stepper motor actuator may need to adopt some optimum solution discussed in last section. The magnetic circuit and winding should be made shortest possible to produce a highest control flux. The winding is designed to accommodate a coil with 20 to 30 turns and possibly to be put nearest to the yoke poles for sensitivly controlling. The choice of shunt reluctance and constriction slot are based on the optimum solutions in terms of shunt factor and slot factor.

The general arrangement of modified stepper motor actuator is shown in figure 6.15. The optimum pole's shape and position will be obtained in the latter studies.

6.5.2 Design of Mechanical Release System

The rotor disc rotating from its static position to release position is shown in figure 6.16. The relationship between the rotating angle and the diameter of the shaft is given by:

$$\beta=cos^{-1}(1-\frac{\Delta x}{r+cl})$$

Supposing the lever l =13mm , r=1 -4mm and Δx=0.3mm, the coefficient c is given 0.1, thus the rotor disc rotating angle is obtained from the above equation as listed in table 6.3

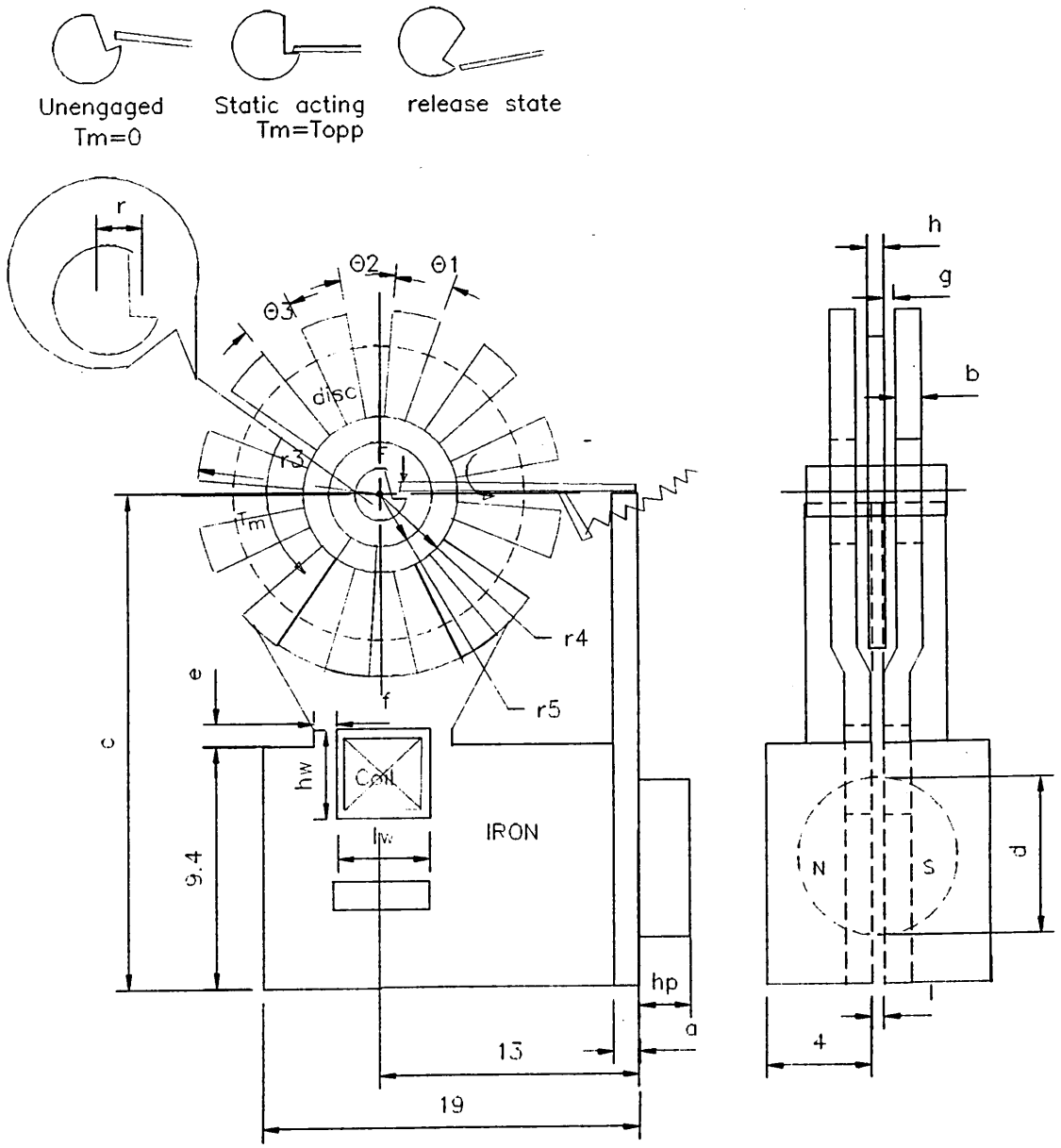

Figure 6.15 Combined electromagnetic actuator

Rotor Magnet Disc(Pink) among the Yoke Poles

Permanent Magnet bridges the Two Yoke at the End of the Yoke

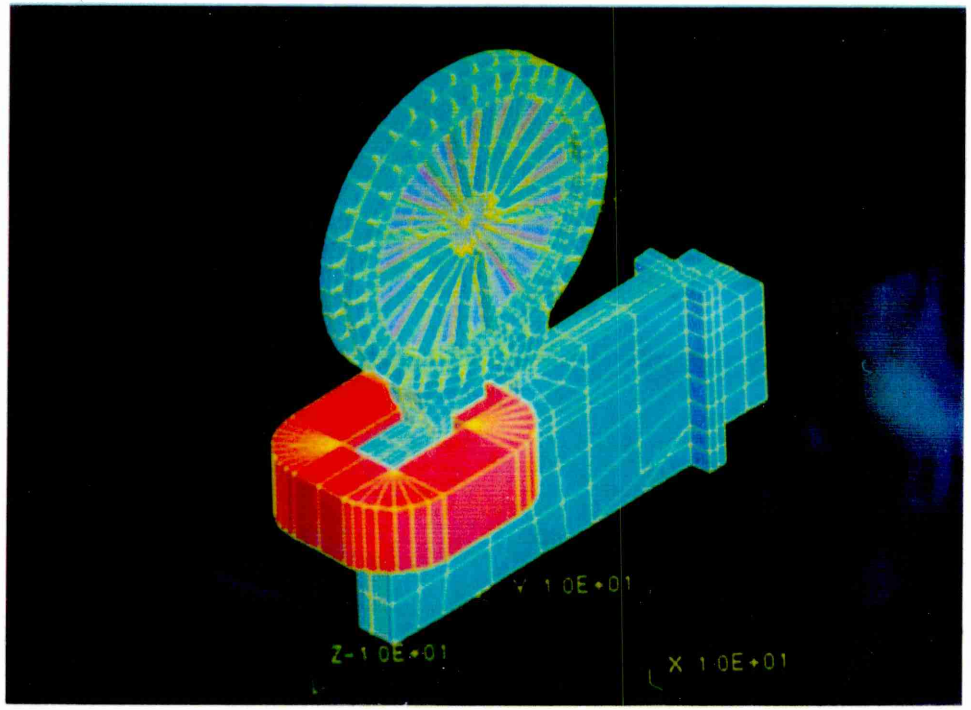

Figure 6.15b FEM model of combined electromagnetic actuator

Table 6.3 Rotating angle varying with shaft diameter

r(mm)	1	1.5	2	2.5	3
β^0	34	31	22	20	18

If the diameter of the shaft is given 4mm , the maximum number of pole-pairs of the magnet disc is determined as 20.

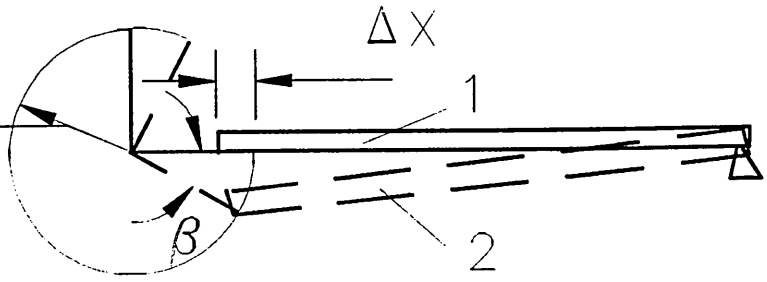

Figure 6.16

The weight of the release lever is necessary to be minimised at lowest level to reduce the moving inertia. Therefore a thin beam is chosen as the release lever. The cross section of the beam depends on the loads and the material being used. The force diagram of the release lever is shown in figure 6.17. The required section modulus of the cross section area can be obtained from the equation (5.54).

The parts of the beam between the supports is in pure bending with Mmax=$F_1.l_1$, for a typical release F_1=25gf=0.245N,

F_1=25gf=0.245N,

l_1 =2mm

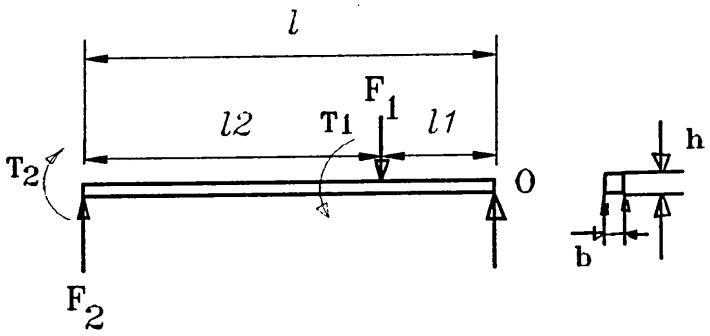

Fig. 6.17 Force diagram of release mechanism

$$bh^2=\frac{6F_1l_1}{\sigma_w}=\frac{6x0.245x2}{165}=0.0178\ mm^3$$

Set maximum length of lever l=13mm, b=0.3mm, then h~0.5 mm and

$$F_2=F_1l_1/\ l=0.0376N$$

The static deflection of the beam from equation (5.48) is given by:

$$\delta=\frac{F_1l_1^2\ l_2^2}{3EI\ l}$$

$$=\frac{0.245x2^2\ 11^2x12}{3x200x0.3x0.5^3x13}10^{-6}=6.86\mu m$$

The natural frequency of the beam in equation (6.52) is:

$$\omega=\sqrt{\frac{g}{\delta}}=\sqrt{\frac{9.8}{4.86x10^{-6}}}=1.4x10^3\ rad/sec$$

Assuming the external vibration velocity V_0 is less than 0.2m/s, r=2.5mm, the maximum dynamic torque acting the shaft from equation (5.53) is therefore:

$$T_{2d}=r\frac{3EI}{l_1\ l_2^2}\frac{v_0}{\omega}=0.108v_0$$

=0.0504N.mm for initial velocity v_0=0.4m/s

From figure 5.15, the inertia of the moving part is chosen as 0.03g.cm^2 and the response time is limited to 10ms. The opposing torque must exceed 0.09N.mm as before. Considering the mechanical shock of 0.0504N.mm, the peak value electrical torque required must exceed 0.15N.mm .

6.5.3 Reduction of Detent Torque

A problem found for this type of permanent magnet actuator is existence of a high detent torque which arises from the interaction of the rotor magnets with the steel yoke poles due to the relatively higher Fb.

The electrical torque was evaluated by reference to the structure in figure 6.15. The electrical torque(Tm) acting on the rotor disc is shown in figure 6.18 for which the MMF,Fa, can be controlled by a reasonable value of control MMF,Fc=2AT. The electrical torque in figure 6.19 is non-sinusoidal function of angle(θ) due to the existence of detent torque. The detent torque for this construction however is higher than the value of holding torque at 90^0 electrical degree. This torque characteristic is not suitable for the

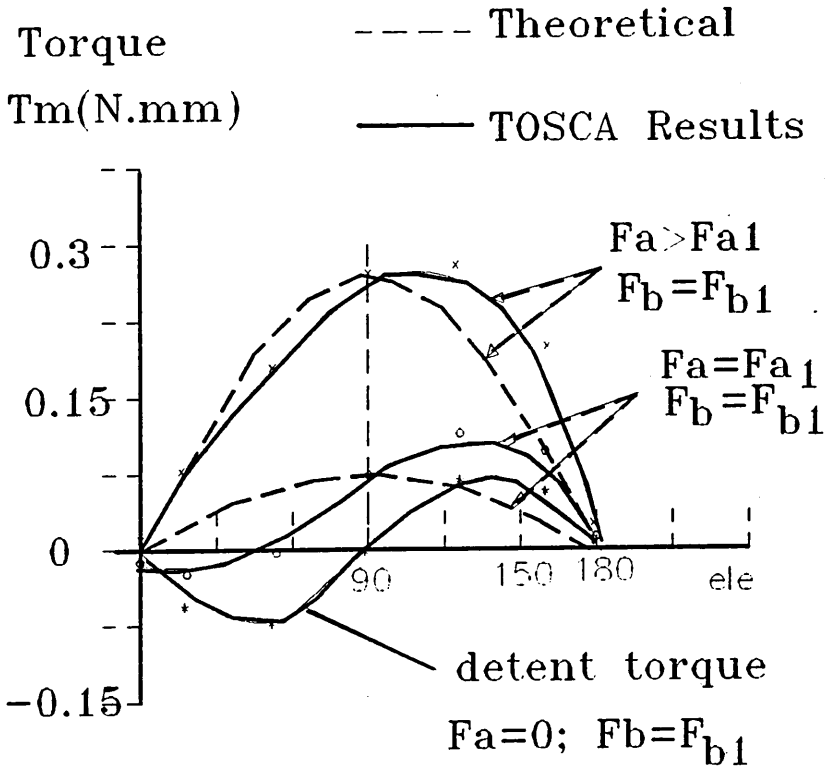

Figure 6.18 Predicted torque and detent torque as a function of angular displacement of the disc stepper motor for non-reduction of detent torque state

actuator operation. Considering on increasing in the magnetisation of Fa, the electrical torque can be made approximately as a sinusoidal function, however this causes a lessening in the torque sensitivity. In contrast, increasing Fb and decreasing Fa leads high torque sensitivity, but a higher detent torque appears. The aim here therefore is to develop a technique to reduce the detent torque to a reasonable value, for example, by appropriate choice of number of magnetic poles , pole shape, arrangement between the rotor disc and yoke poles and the dimensions.

6.5.3.1 Effects of Poles Spacing

The detent torque is dominated by the fundamental component of the magnet poles and yoke poles design having a repetition period of 10 mechanical degrees. For rotor magnet disc containing 18 pair-poles, the relative arrangement between the magnet poles and yoke poles can change the frequency of the Detent torque, and consequently change the magnitude of detent torque. If the frequency of the detent torque increases by one time, the value of detent torque will be reduced by 30%. Figure 6.19 shows two types of magnetic poles arrangements, where one in every two teeth are spaced about half a pole pitch(about 5^0) around the disc . The peak value of the detent torque produced in figure 6.19b pole arrangement is 60% of the torque produced in fig 6.19a. The frequency of detent torque in figure 6.19b is twice as that in figure 6.19a. However, it is expected that the holding torque is only slightly reduced for pole design from(a) to (b).

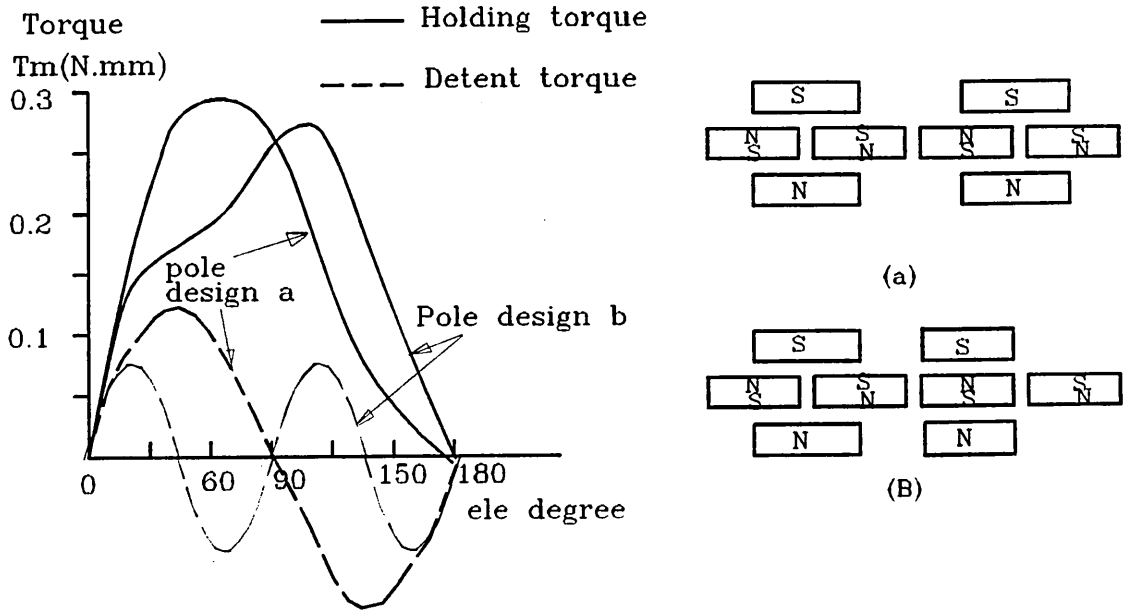

Figure 6.19 Effects of poles spacing on holding torque and detent torque

6.5.3.2 Effects of Magnet Pole Width

As the electrical torque components are produced by the ends of the magnet, it follows that the fundamental sinusoidal component of detent torque can be eliminated by appropriate choice of the magnet width. The holding torque and detent torque varying with angular displacement are shown in figures 6.20 and 6.21 respectively with the magnet disc poles ratio w/w_0,0.8,0.5,0.3 where the full pole width w_0 is 10^0 mechanical.

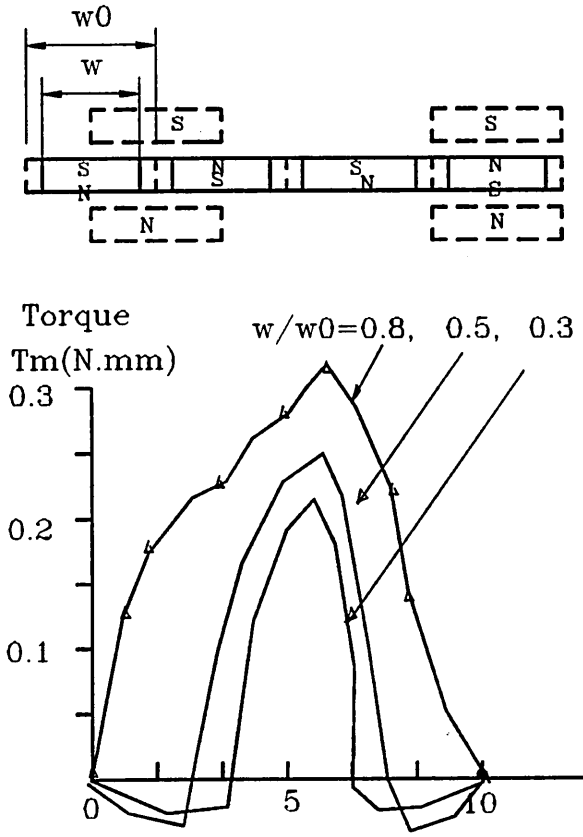

Figure 6.20 Holding torque as a function of angular displacement for w/w_0=0.8,0.5,0.3

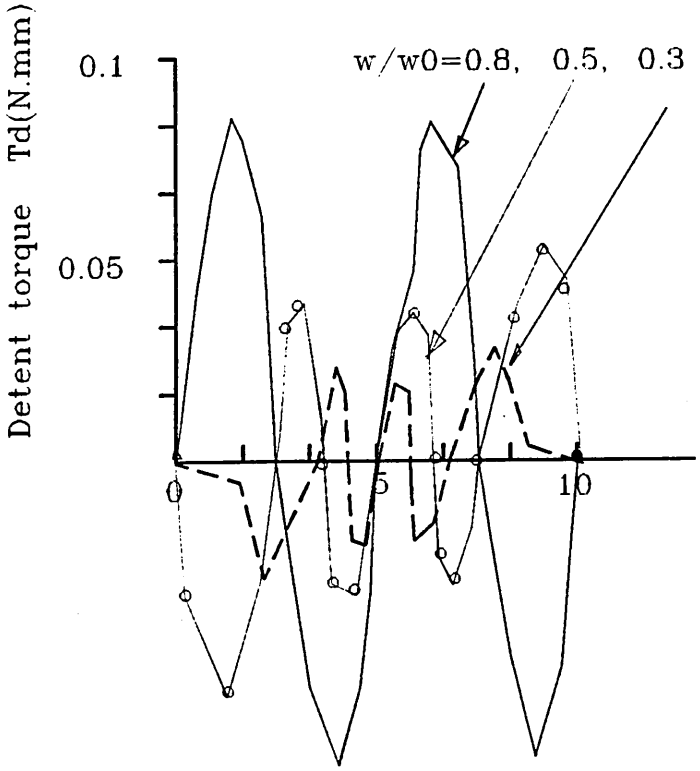

Figure 6.21 Detent torque as a function of angular displacement for w/w_o=0.8,0.5,0.3

It is expected that the decreasing of the magnet width leads to much greater reduction of detent torque rather than holding torque. For example, the detent torque is decreased by 70 %, and only a 25% reduction of holding torque by reducing the magnet width ratio w/w_0 from 0.8 to 0.3. However, the magnet width cannot be further reduced for keeping the rated output torque. The small angle will also result in manufacturing problems.

The Detent torque reduced to 60% of the output rated torque is still not acceptable in this actuator design. It was found that the increasing the thickness of the permanent magnet disc and further reducing the magnet width can obtain a better solution for this actuator as shown in Figure 6.22.

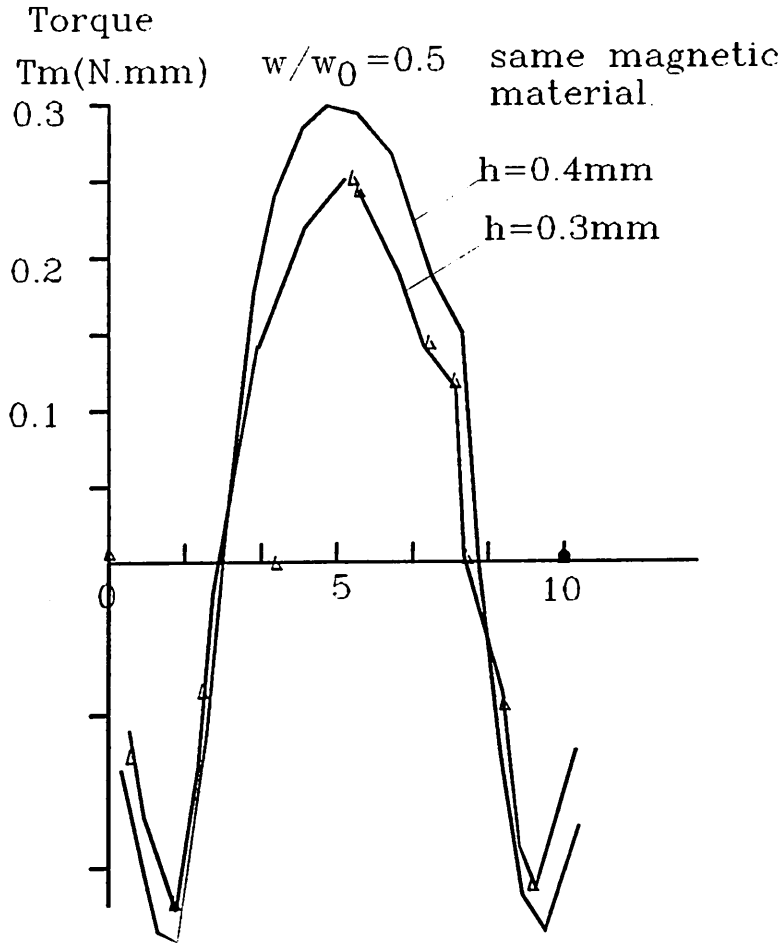

Figure 6.22 Effect of magnet disc thickness on the holding torque

6.5.3.3 Effects of Magnetic Pole-pairs

From figure 6.21 the detent torque for magnet pole ratios of 0.3 and 0.5 on both sides of the angle of rotation appears a sinusoidal function. The reason for this is that, for the magnet pole ratio w/w_0 of 0.5 , when the disc rotates over 5^0 only one side of the magnet pole acts on the yoke poles, which produces a considerable imbalance torque on the disc. Therefore the magnet disc is designed as 36 pole-pairs and 18 poles on the yoke as shown in figure 6.23 (b). The elimination of the torque characteristics was carried out by choosing the magnet ratio $w/w_0=0.5$ as shown in figures 6.23 and 6.24. Obviously, the holding torque produced in the construction (b) in figure 6.23 appears as a sinusoidal function of the angle. This design produced a higher negative peak torque . The detent torque is therefore also as sinusoidal function of the angle and consequently the peak value of the Detent torque is reduced in figure 6.24. This magnet disc design provides a large reduction in the Detent torque and also the higher dynamic response.

6.5.3.4 Effects of Yoke Pole Ratio

The effects of the yoke pole size, which can be expressed in terms of a ratio p/w_0, on the holding torque and Detent torque were made based on the optimum solution of the magnet pole size as shown in Figures 6.25 and 6.26. The variation of the yoke pole however made only a small difference to the holding torque, since the electrical torque is produced by the ends of magnet. It can be seen for this design the peak value of the Detent torque is reduced from 35% to 20 % of its rated output torque in figure 6.26.

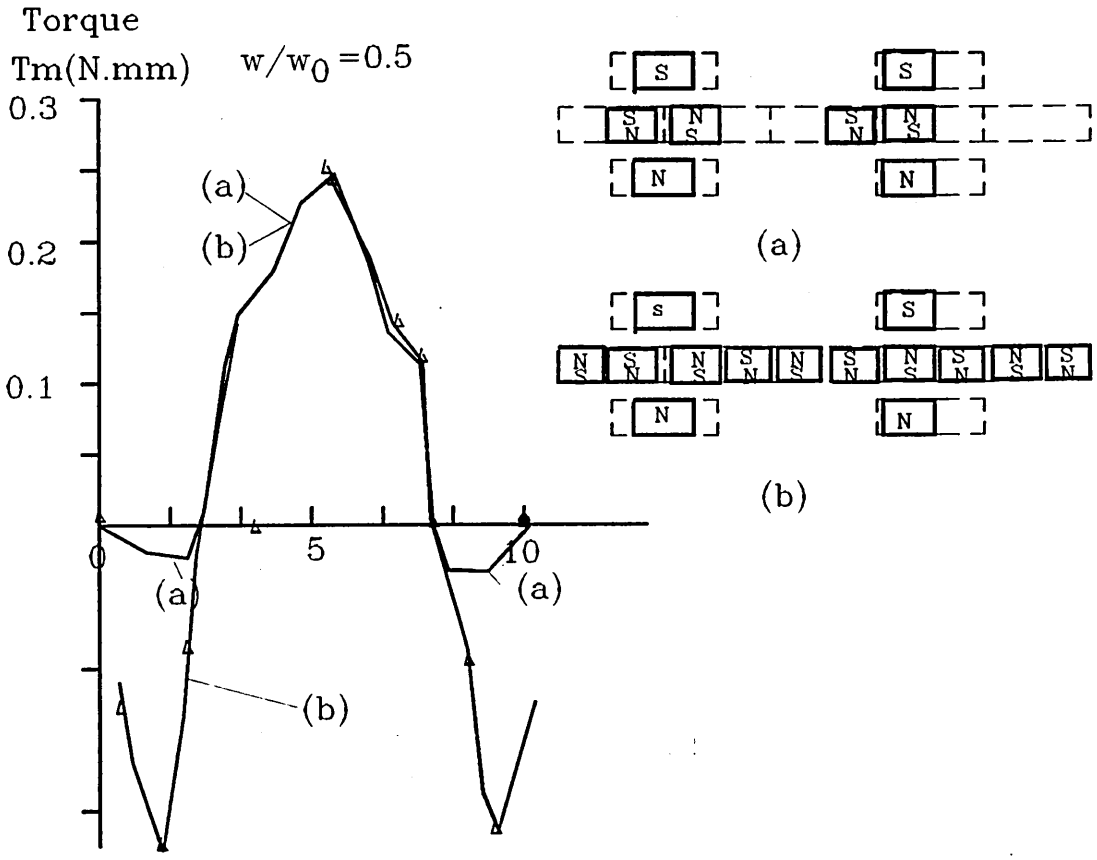

Figure 6.23 Influence of number of pole-pairs on holding torque

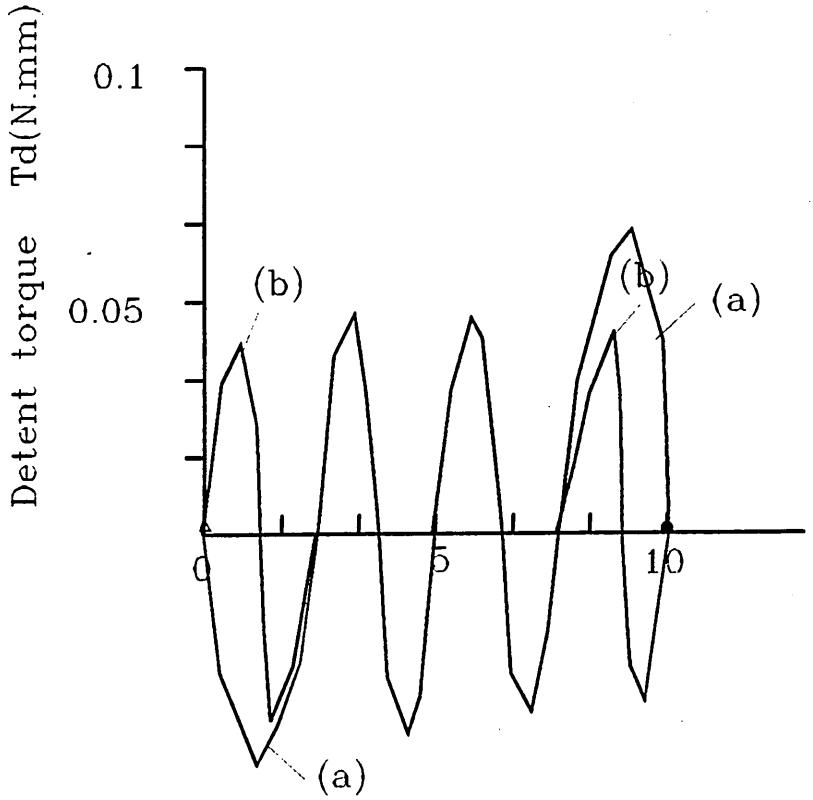

Figure 6.24 Influence of number of pole-pairs on detent torque

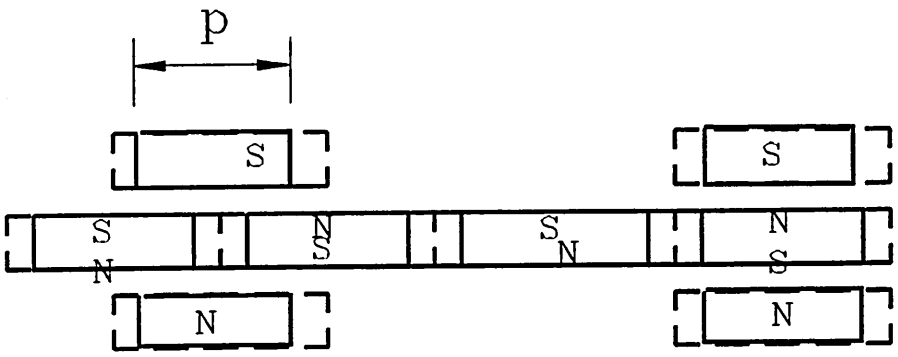

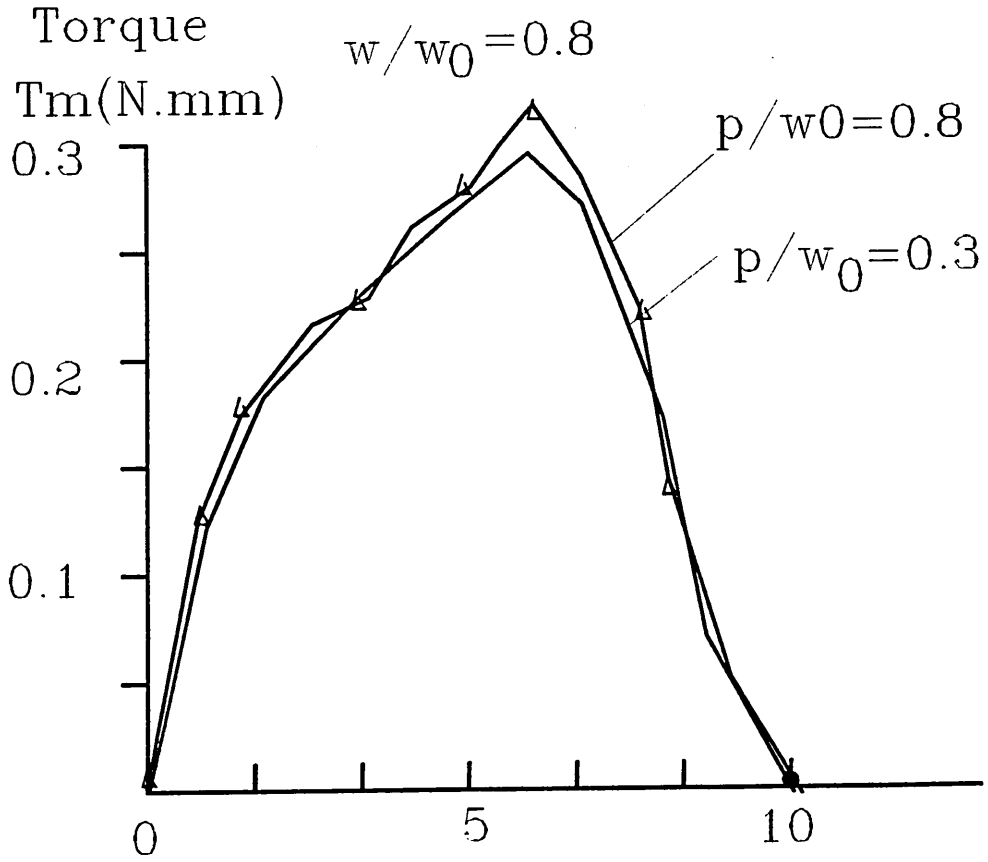

Figure 6.25 Holding torque as a function of angular displacement for different yoke pole ratios

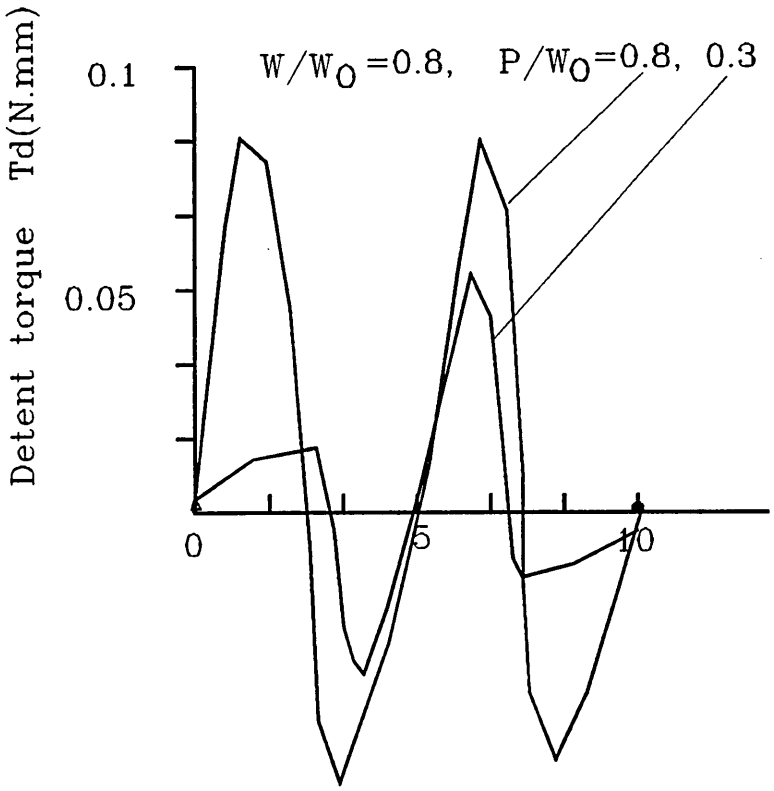

Figure 6.26 Detent torque as a function of angular displacement for different yoke pole ratios

6.6 Design Specification

The investigation of the combination type actuator exhibits that the performance is significantly affected by the key dimensions such as airgap, shunt path, constriction slot size, window, magnet pole and yoke pole size, and also the critical design parameters of magnetisation MMFs and material properties on the output torque characteristics and actuator sensitivity. The sensitivity of the actuator for a proposed smaller airgap,i.e. less than 0.05mm is obviously higher than a larger airgap. However the aim of the actuator design is to set a reasonably large airgap to reduce the manufacture cost. Hence, for this design an airgap of

0.1mm is preferable to allow for the disc movement and to minimize the reluctance in the magnetic circuit.

In the studies of the effects of shunt factor on the actuator sensitivity, it was observed that too small a shunt reluctance could lead low output torque and consequently less torque sensitivity due to more flux being diverted into shunt path. In contrast, a higher shunt reluctance can yield higher output torque, but it produces a lower sensitivity. The preferable solution for the shunt path is to set the distance between the two yoke plates to be between 0.05mm to 0.12mm for the face to face surface area of 250-330mm^2. The ideal size of the slot is that the static flux density (B) lies on the knee of the material magnetisation BH curve. For a value of 0.15N.mm holding torque to be provided, the constriction slot area is designed to be the range 0.8-1.2mm^2 with a slot length between 0.7-1mm.

The studies have concluded that this type of actuator cannot be operated by less than 0.6 ampere turns for an airgap of 0.1mm. This conclusion indicates that the actuator would have to use a toroid transformer to amplify the residual current of the protecting circuit. It follows that the coil window could be designed as smaller as possible to produce the highest control flux. A ferromagnetic material with highest permeability such as SUPERMUME-TAL was proposed to use for the yoke plates, within reasonable material cost. Figures 6.7-6.10 show the torque varying with MMFs(Fa,Fb) and the torque sensitivity with source MMF,Fa. It is expected that source MMF Fb can make a larger contribution to the co-energy in the airgap than Fa, and less MMF Fa can lead a higher torque sensitivity. Thus in this design the Fa is made as smaller as possible and Fb is made as large as possible . However, the magnetisation Fb is limited by its inertia and the detent

torque produced. The optimization of the torque and torque sensitivity with Fa and Fb resulted in optimum values for Fa and Fb.

The investigation for reduction of Detent torque demonstrated that the relative poles arrangement between the yoke poles and magnet disc poles have a considerable influence on the torque characteristics. Figure 6.24 shows the poles arrangement where there are 36 pole-pairs spaced 5^0 mechanical degrees apart and the yoke has 18 poles also spaced 5^0 mechanical degrees apart in magnet disc. The design for this type of actuator would require the magnet disc to have 36 pole-pairs, each of 3^0 mechanical degrees and a yoke with 18 poles each of 3^0 mechanical degrees spacing. The rotor disc would consist mainly of a thin disc made of Samarium-cobalt with axial magnetization. The magnetic disc has 36 evenly spaced magnetic pole-pairs with alternating polarity ,e.g. N S N on one side and S N S on the opposite side.

Based on the optimising procedure and characteristic evaluation, the design dimensions of the actuator whose construction is shown in figure6.15 are illustrated in the Table 6.4 for three length of airgaps,0.01,0.1 and 0.15mm

Table 6.4 Design dimensions for airgaps 2x0.1mm Unit=mm

a	b	c	e	f	g	h
0.8	0.8	18	1	0.7	0.1	0.25
n	r	r_3	r_4	r_5	d	hp
36	2.	6	3	2	5	2.5
l_w	h_w					
3	4.2					

The predicted electrical static torque and its energised torque is shown in figure 6.27 for which the control current is 30mA with 60 coil turns. The electrical torque observed was not purely sinusoidal in function of angular displacement due to the detent torque. But a peak torque apperas near the 90 electrical degrees, which is satisfactory for this type of actuator design.

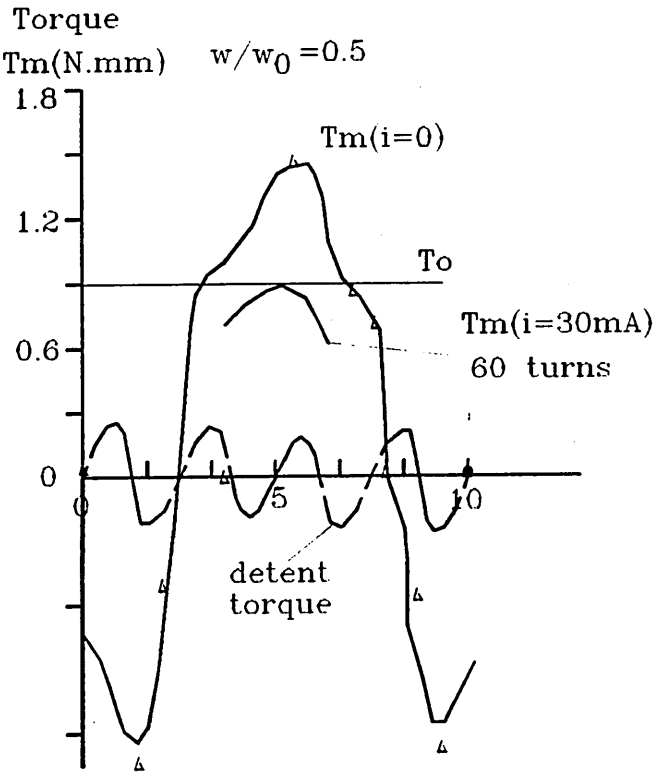

Figure 6.27 Static and energised torque versus angular displacement for airgaps 2x0.1mm

The design for a smaller airgap of 2x0.01mm here is presented, which may be impracticable but which is instructive for testing the optimal design approach. The dimensions are listed in the Table 6.5

Table 6.5 Design dimensions for airgaps of 2x0.01mm unit: mm

e	f	h	d	hp
0.7	0.5	0.12	4	2

The rest dimensions are the same as listed in table 6.4. The torque characteristics for this design were evaluated as shown in figure 6.28, from which it is seen that the peak value of static torque of 0.15N.mm can be diminished

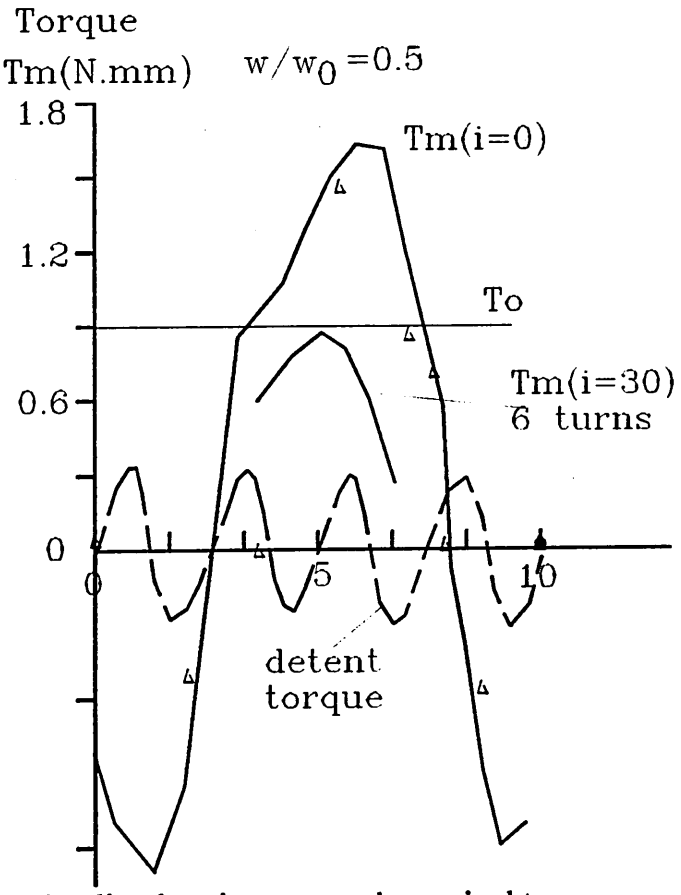

Figure 6.28 Predicted static torque and energised torque versus angular displacement for an airgaps of 2x0.01mm

to a opposing torque level of 0.07N.mm by a smaller control ampere turns (30mA and 4 turns). Neglecting the airgap size, this design is theoretical possible to operate without the need of a toroid transformer. Clearly, since it is impossible to make practical magnet disc rotate in a gap of 0.01mm between two surfaces without some friction, this design can only be considered as theoretical design.

Given the need for a larger airgap, a practical design example is given in table 6.6.

Table 6.6 Design dimensions for airgaps of 2x0.15mm unit: mm

e	f	h	d	hp
1.2	0.8	0.45	7	4

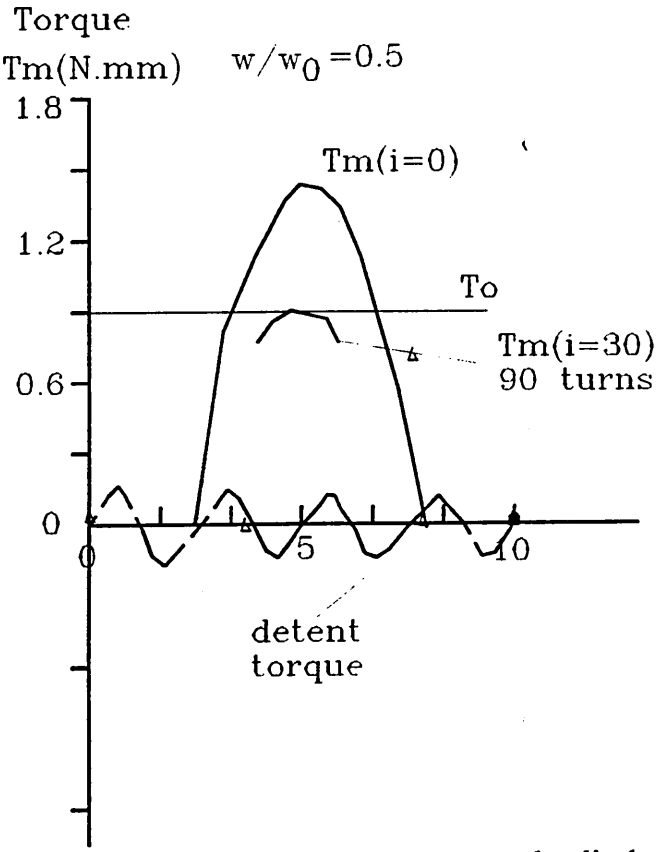

Figure 6.29 Predicted electrical torque versus angular displacement for airgaps of 2x0.15mm

Figure 6.29 shows the evaluated torque characteristics for this design. Given the peak torque value of 0.14N.mm, it is shown that a reasonable release level torque,say To=0.07N.mm requires an operating ampere turns approximately more than 2.7AT (30mAX90N=2.7AT). The evaluations of the torque characteristics have demonstrated that keeping the same torque sensitivity would require higher control ampere turns for larger airgap than smaller airgap.

6.7 Evaluation of Dynamic Characteristics

The movement of the stepper motor actuator is different from the clapper actuator movement, since when the current is injected into the coil, the rotor disc starts to move until the lever is released , providing the trip current is enough to reduce the static torque below the release level. The release torque, To , is set as 0.07N.mm and the inertia of the rotor disc is 0.03g.cm^2 using samarium-cobalt material , the predicted dynamic characteristics of this design specification are good as shown in figure 6.30 for the design dimensions listed in table6.4 with 60 coil turns. From this figure it is noticed that the predicted response time is approximately 8 ms which is within the maximum permitted response time of 10ms.

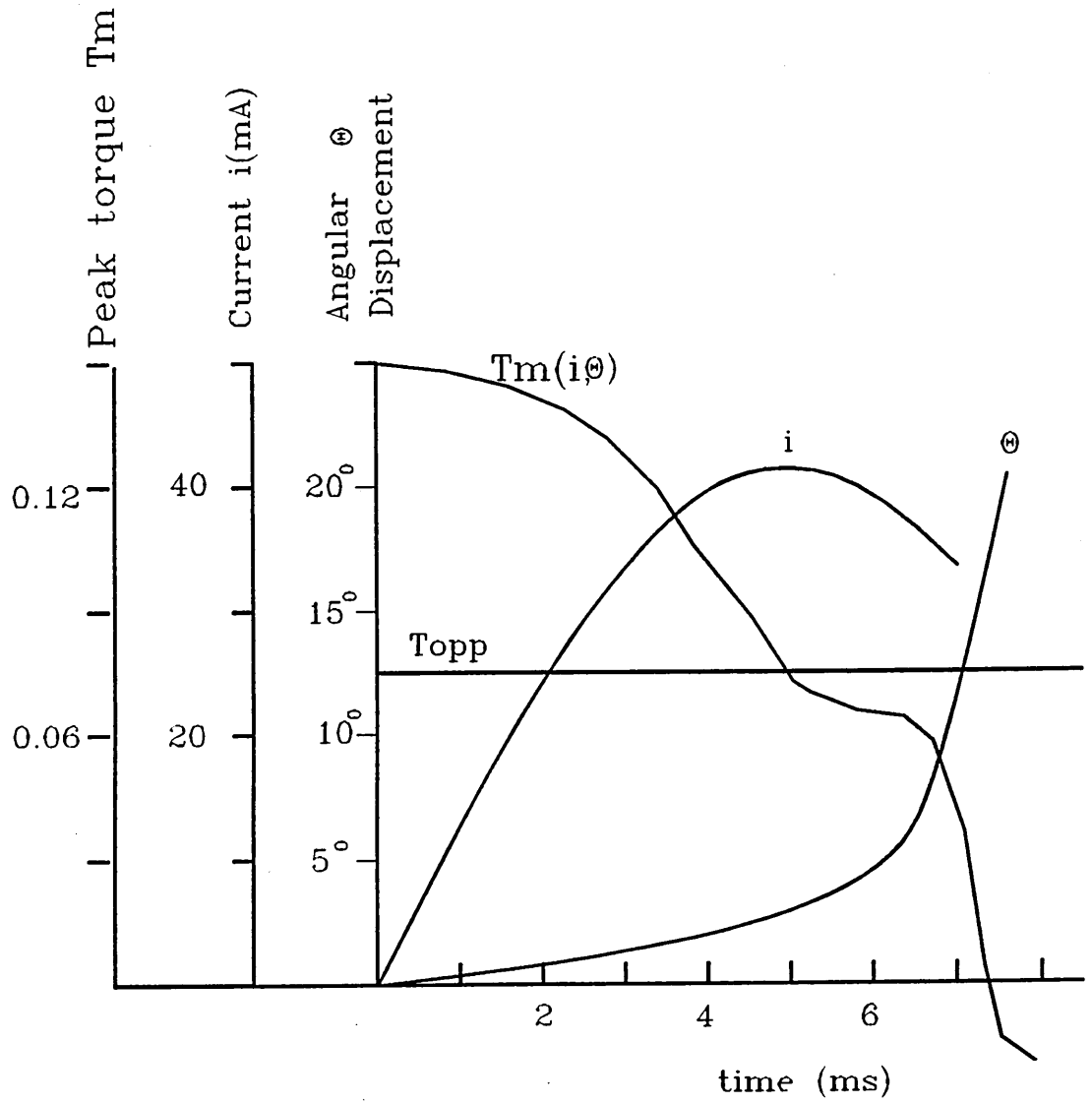

Figure 6.30 Predicted dynamic characteristics of the design based on the airgap of 2x0.1mm

Chapter 7

Conclusion and Recommendation for Future Work

7.1 Introduction

This chapter is split into three sections:

- analysis of the success of the work presented
- recommendations for future work
- other potential developments of electromagnetic actuators

7.2 Conclusions

The Computer Aided Design(CAD) technique was successfully employed in the design, analysis and optimisation of high sensitivity cur rent-operated electromagnetic actuators. A numerical computing technique and an analytical approach was developed and used in the performance prediction and design of the actuators. The performance of the actuators was analysed both experimentally and analytically. A new type of actuator was postulated and evaluated. The conclusions drawn from the studies are as follows:

7.2.1 Application of Computer Aided Design in the Electromagnetic Actuators

The thesis presents the development and application of CAD techniques to magnetic actuator design. It should be emphasised that CAD is, in fact, a process to modify and test(analyse) until the specifications are satisfied.

The types of actuator investigated possess very small airgaps and were heavily saturated. These would need a fine mesh generation and a good convergence technique. In order to provide a high accuracy solution, the finite element CAD technique was used in the design.

The work presented successfully demonstrated, through comparisons between the computed and measured results, the range of validity of the prediction tech nique based on the three dimensional nonlinear magneto-static finite element method. The technique provides good performance estimates for high level of saturation and small size of airgaps. The solutions highlighted some peculiar features of the design which were known about but not fully understood. The analysis permitted the characteristics of the actuators to be determined in terms of the key design and control variables, the results of which correlated very close with the results of practical tests and measurements.

The limitations of the technique were found to be:

- computing takes a long time for a large number of elements to provide even one result

- simulation of magnetic saturation can result in non-converging solutions

•simulation of the magnetic fields at high a.c. energised current frequency is not possible, (i.e. f=100Hz).

For example, if the angle of the clapper actuator permanent magnet was set to 40^0 degrees (see fig2.3), the solutions only converge for coil current up to 80mA, beyond which the convergence often fails. This is plotted in figure7.1 where characteristic was based on an airgap of 1μm, and the supermumetal BH magnetisation curve.

In order to solve the three dimensional non-linear time-varying problems, a 2D transient magnetic finite element was developed which took account of the 3rd dimension by means of a correction factor. The solution obtained demonstrated that the method is suitable for estimating actuator time varying current performance. A decoupled 3D-FEM integral approach was also postulated to enable solution of the dynamic response of current sensitive electromagnetic actuators to alternating current.

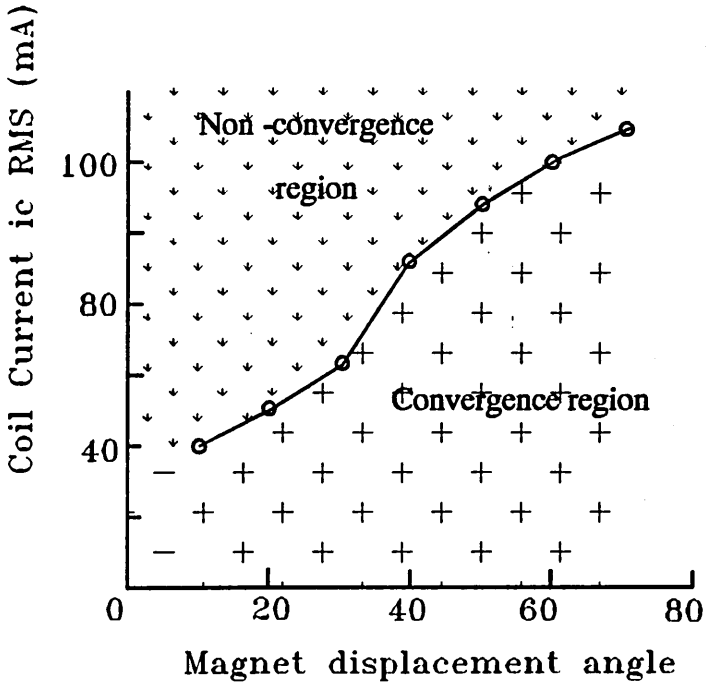

Figure 7.1 3D FEM computing validity of convergence for the Clapper type actuator with 20 turn coil

The analytical approach developed gave good performance estimates of the actuator behaviour. The approach could also be used to estimate the perform ance for high control current with a reasonable degree of accuracy. However, it is unable to deal with transient problems.

The main conclusion is that the developed analytical approach is suitable for accurately solving static field problems with very small airgaps(i.e. less than 1μm) and for estimating the performance for high control current. The finite element method provides accurate transient solutions for airgaps greater than 1μm, at high saturation. Solutions obtained for airgaps less than 1μm took much longer computing time due to a large number of elements required.

7.2.2 Conclusions to the Current Sensitive Magnetic Actuators

The working process of the high sensitivity current-operated magnetic actuators is generally divided into the three distinct steps,

a. static state,

b. energised steady state

c. dynamic movement state.

These steps are now considered.

A. Clapper type actuator

(i) The key design parameters and dimensions for the clapper actuators found are the airgaps,leakage reluctance, constriction slot dimensions, area of the contact surfaces between the armature and keepers, size of coil window,

length of magnetic circuit, inertia of armature, magnetic material properties of soft iron laminations and MMF of excitation permanent magnet.

(ii) The magnetic force and actuator sensitivity rely greatly on the size of airgap especially upon the quality of the facing machined surfaces. It was found that when the airgap was varied from zero to 2μm, the magnetic force reduced by 40% and the sensitivity decreased by 70%. If the size of airgap was increased to 3μm, the actuator did not func tion at all. From test and calculation, the permitted tolerance for the ma chined surfaces were obtained as $(0.5\pm0.5)\mu m$.

The leakage reluctance affects the sensitivity more significantly than the magnetic force on the armature. The optimum design value for this type actua tor was determined over the range of Ks to be between 0.5 and 1.

The dimensions of the slot constriction are critically dependent upon the required armature force and size of the airgaps. The flux density in the slot should be designed to lie on the knee point of the material magnetisation BH curve.

The size of the contact surface is determined by the required magnetic force and the quality of the machined surface. For good quality surfaces, the area of contact surface must be made as small as possible to permit the static flux density to be above the knee point on the BH curve.

(iii) The material properties especially the permeability(μ) are determined by the calculation in relation to the size of the airgap and length of magnetic circuit. Assuming the length of airgap is g, the area is Ag, the total length of the equivalent magnetic circuit is l and the equivalent area is A, the maximum permeability (μ) of the mate rial is given by $\mu = lA_g/g\,A$.

The inertia of the armature should be designed to be smallest possible for quick response under the action of spring. A typical example would be a value of 0.15g.cm^2 or below for an opposing force of 0.2N.

(iv) The dynamic predictions indicated that given the travel time of the armature to actuate the mechanism was of the order of 4-5ms and the actuating would occur within 2.5ms for 50Hz control current. For a higher frequency control current, a greater value of tripping current was required at the same opposing load due to the existence of large eddy currents. However, an analysis demonstrated that the response time did not increase in proportion to increase of the control current frequencies. This is attributed to be a peculiar feature of the type actuator. The investigation concluded that the current sensitive actuators may be used for the high frequency current detection.

(v) The optimisation technique was successfully employed in the design of the magnetic actuators. An optimum design was given based on the evaluations of the performance based on the key design parameters. The performances of the optimal design have been predicted and compared with summary data for current production actuators. The optimal design ap proach showed that the size of toroidal transformer could be reduced with a consequence improvement in the sensitivity.

(vi) The main deficiency of the clapper type actuator was found to be the expense and difficulty in manufacturing high quality machined surfaces.Inef ficient transfer of energy also presented major problem.

B. Stepper motor type actuator

(vii) A novel approach electromagnetic actuator was proposed to obviate the need of very small airgaps and to eliminate the separate use of a toroidal

transformer. This actuator combined the toroid transformer and the electro-mechanical release system by using of a miniature magnet disc stepper motor. It was designed to possess a higher sensitivity than the conventional clapper actuator, and also to provide sufficient force to actuate a latch type mechanism system.

(viii) The simplified analytical technique was developed on the basis of the equivalent magnetic circuit method for analysing and design ing the proposed stepper motor actuator. This technique was found to be suit able for the preliminary design and evaluation of the actuator and also to be adequate for practical engineering design. However, it was found that this method could not obtain a high accuracy solution for the magnetic field of a miniature disc magnet stepper motor. The main reason for the limitation is that large nonuniformities exist in the flux-density distributions for each lump element of the magnetic circuit as well as the greater significance of the increased flux levels in a constriction path. It was also found that the lumped magnetic circuit approach cannot exactly describe the magnetic pole shape influence on the performance.

The three dimensional finite element CAD program was successfully used in the design and evaluation of the stepper motor actuator. The key design factors found are: the number of the magnetic poles; shapes of the poles; relative arrangement of the magnetic poles and slots; magnetic material properties of the disc especially ,the remanence flux density Br and other aforesaid criti cal factors such as airgaps, shunt reluctance and constriction slot.

The dependency of the actuator performance on the key factors were obtained and optimised. The advantage of using the miniature stepper motor is that the permanent magnet disc could energise the relatively longer airgap and

that if the yoke poles appear neutral, then there is no interactive torque between the rotor magnet disc and the iron yoke poles. In order to obtain an efficient control of the stepper motor actuator a small magnet(Fa) is re quired. To provide a high electrical torque, a high value of magnet MMF of the rotor magnet(Fb) is needed. However, a high value of Fb produced a high detent torque between the rotor magnet and the iron yoke poles. A technique to reduce the detent torque was postulated and used in the design of the minia ture stepper motor.

(ix) The relationship between the electrical torque and number of the rotor magnet poles was found to be approximately linear. A large number of magnet poles with small pole width produced high torque and also reduced the detent torque. However, the increase in poles limited the step displacement angle and the maximum number of magnet pole-pairs was determined for a particular disc magnet stepper motor.

If a stepper motor type actuator is designed to be tripped by a residual current of 30mA with 5 coil turns(MMF 0.15AT), and also to provide a torque greater than 0.15N.mm, the detent torque will be unacceptable with value in excess of 0.3N.mm. Hence, the value of Fa has to be increased and Fb has to be decreased. An optimisation of Fa and Fb is necessary in this case. The pro posed optimum solutions demonstrated that the detent torque can be reduced to 20% of the holding torque and the actuator can be controlled by 2 ampere turns. The studies also showed that, in practice, the proposed stepper motor actuator can not be operated by the standard residual current, up to, 30mA, without a toroid transformer. If the airgap size was reduced to be 0.01mm, then the stepper motor actuator could be operated without a toroidal trans former as proposed.

(x) The critical limitation for the proposed actuator is the need for a large airgap to accommodate the rotor disc and to provide the satisfactory clearance. The large airgap requires high excitation MMFs and consequently requires a high control current. The stepper motor has a poor response for high frequency current.

7.3 Future Work

7.3.1 Improvement to Sensitivity of CSEMA Actuators

Improving the sensitivity of the RCD type actuator has constituted a significant area of further work. One method proposed combines the iron and small magnet as the release armature. The magnet is located near the working airgap to magnetise the relatively long airgap. The iron section which directly closes onto the iron yoke could have the advantage that once the armature leaves the keeper, the force could be dramatically reduced and consequently could improve the actuator sensitivity.

The existing clapper actuator suffers not only from the expensive machined surfaces but also from the use of a separate toroidal transformer, and the need for a manually wound the excitation coil. One method to reduce the de pendency on high quality machined surfaces is to use a high saturation flux density magnetic material which consequently requires only a small area of machined surface.

Current designs of the current sensitive electromagnetic actuators have shunt paths which only provide the leakage flux reluctance. A design postulated utilises the leakage flux to produce an opposing force. This gives the

advantage that when the current is injected into the coil, the flux in the working airgap is reduced and consequently the flux in the leakage path is increased. Hence the actuator will have a greater sensitivity than current designs. This method may lead to new future developments of the current sensitive actuator.

A design with two very finely machined surfaces with a long armature clapper type actuator was made. The evaluated results demonstrated that, when providing a typical force up to 0.5N, the highest sensitivity can be obtained e.g. at a tripping current of 30mA with 5 turns. An experimental device was manufactured, however, the test results could not match the design specification. The main reason was that the smoothness of the machined surface did not be manufactured to the design standard $(0.3\pm0.3)\mu m$. The test surface roughness was $(1\pm0.5)\mu m$. It is proposed that this design technique will be successful when the high tolerance smoothness of the surface can be routinely achieved.

7.3.2 Reliability Study of CSEMA Actuators and RCD

A typical application of current sensitive actuators is in the residual current devices as a key tripping element. The RCD mainly per forms a valuable contribution to the safety of installations and protecting humans against hazards caused by electric shock. The reliability of the RCD, particularly, w hen used in the form of protection is most significant. The study of the reliability of tripping system and residual current devices will probably become very important in the future. Investigation of the RCD's

reliability of RCD can exhibit the quality of the product This obviously is a critical factor in the products market.

Reliability engineering is a comprehensive subject based on the theory of probability and statistics. This technique is also associated with systems engineering, value engineering and quality control techniques. Reliability engineering currently plays a significant role in the quality control of products. Reliability studies of electrical contactors and relays have uti lised the multi-functioning test devices and computer aided systems to process data.

The investigation of RCD reliability may be made in three stages:

(i)the reliability of current detecting system;

(ii) the electromechanical tripping system;

(iii) the electrical contact system.

For the first stage, the emphasis should be on the electrical reliability; the second step should be concentrated on the study of mechanical reliability and the third step should be concerned about the electrical contact reliabili ty. A multi-function reliability test system should be undertaken especially for those system with more failures. For example, when failure of contacts occurs, the system then judges whether the failure occurs due to the poor contacting , the electromechanical release system or the current detecting system. The test system should be capable of collecting the test data and processing the critical section, such as, the failure distribution of the products tested and the estimation of the product reliability index.

7.3.3 Potential Development of Electromagnetic Actuators

The techniques used in current sensitive magnetic actuator designs could be applied for other types of electromagnetic actuator. Generally, the magnetic actuator response time from open to closed is much slower than from closed to open. The reason for this is when the actuator is in the open position the airgap requires greater magnetic energy to magnetise the long airgap. This takes a long time to build up. When the airgap becomes short the opposing force increases. Both those effects cause the response time to be longer.

The saturation ,polarisation and the permanent magnet effects could be used in the design of a fast tripping electromagnetic actuator. The response movement could be from closed to open and could be operated by either d.c. or a.c. currents. This could lead to significant reduction in response time as well as saving energy.

The development of an expert system in the design of electromagnetic actuators also has a potential for future work.

7.4 Summary Conclusions

This work will be of value for other applications in the areas

- CAD technique applied to electromagnetic actuator design

- analytical model: the method is easy and convenient to use for analysis and design of actuators which will be useful to the engineers who don't wish to become enmeshed in complex numerical electromagnetic computation.

• The results clearly explored the design of typical RCD actua tors and the magnetic saturation design principle, which will be most helpful for engineers to better understand and to modify designs.

The work has involved a wide range of disciplines from basic electrical engineering to computer expert system design. The work has also involved both experimental and theoretical analysis which demonstrated the import-ance for the modern electromagnetic actuator design manufacturing engineers to be familiar with:

• computer application and design

• new technique applications

• mathematical modelling technique

• commercial implication of all development and design

The project has been successful in that

• Computer aided design has been applied in the design of the magnetic actuators which possess very small airgaps and subject to heavy saturation.

• a commercial problem has been solved and a new type of actuator proposed for industry

• a number of models have been constructed and evaluated which will aid other researches and engineers in developing the new types of actuator

• the work involved implementation of significant computing work on novel magnetic devices and the development of special computing approaches.

- proposes were made for improving the actuator sensitivity, the CSEMA actuator design technique in the design of fast tripping electromagnetic actuators, the development of an expert system in the actuator designs and the investigation on reliability of the RCD systems.

Bibliography

[1] M Ramamoorty, Computer-aided Design of Electrical Equipment, Ellis Horwood Limited,1988

[2] D A Lowther and P P Silvester, Computer-aided Design in Magnetics, Springer-verlag, 1985

[3] A L Kidd, Electrical protection for domestic and small commercial installations, IEE Power Engineering Journal, Vol. 251, pp57-65

[4] Li Erping and P M McEwan, Electromagnetic current sensitive RCD Actuators Research Report No.1, December 1989, Sheffield City Polytechnic

[5] K Yamasawa, Performance of temperature sensitive magnetic actuators, IEEE Tran. Mag. Vol.21, 1985, pp2652-2656

[6] Kiyohito Yamasawa, Shigemitsu, P P Biringer, A proposed for a finite-element force approximation of an automotive magnetic actuator, IEEE Tran. Mag. Vol.26, No.4,1990

[7] C Dawson and H R Bolton, Performance prediction of a wide-angle limited motion rotary actuator, Proc. IEE Vol.125, No.9, 1978

[8] Hydraulic and pneumatic actuators, Automation, 1975.10,pp.19-27

[9] D W Auckland, R Shuttleworth, J R Simms, B R Varlow, Rare-earth permanent magnets in switchgear actuators, Proceedings of 25th UPEC, Aberdeen, Sept. 1990, pp553-554

[10] Li Erping and Chen Degui, Analysis of Transient field for current limiting Electromagnetic mechanism using FEM, Proceedings of Int. Sym. on Electromagnetic Fields Computation, Beijing, China, 1988

[11] P.P. Silvester and R L Ferrari, Finite Elements for electrical engineers, Cambridge University Press,1990

[12] Gottfried Biegelmeier, Effects of current passing through the human body and the electrical impedance of the human body, A guide to IEC-report 479 etz-report 20e, vde-verlag gmbh Berlin und Offenbach, 1987

[13] UK Patent, No.1029314,Improvements in holding magnet release means of high sensitivity

[14] UK Patent, No.1232725,Improvements in or relating to magnetic tripping devices

[15] Austrian Patent, No.337812, Haltemagnetausloser mit einteiligem anker

[16] Austrian Patent, No.337811, Doppeljoch-haltemagnetausloser

[17] UK Patent, No.1159604, Holding magnet with electromagnetic release

[18] A A Winslow, Numerical Solution of the Quasi-linear Poission equation in a non-uniform triangular mesh, Journal of Computer Phys.1, 1971, pp149-172

[19] W Muller, W Tritz and W wolf, New numercal calculation for Large Turbo-Generators ETZ-A Vol.-93, 1972, H7, pp394-399

[20] C W Trowbridge, Electromagnetic computing: The way Ahead? IEEE Tran. Mag. Vol.-24, No.1, 1988, pp13-18

[21] D S Kershaw, The incomplete Cholesky Conjugate gradient method for the interactive solution of the systems of linear equations, Journal of Comp. Phys. 26, 1978, pp43-65

[22] M Fujita and M Yamana, Two dimensional Automatically adoptive finite element mesh generation, IEEE Tran. Mag. Vol.-24 No.1, 1988, pp303-306

[23] F schnoellebeck, H Haas, Three dimensional adoptive FE-preprocesssing using a programmable CAD-system, ibi, pp370-373

[24] A Nicolas and L Nicolas, 3D Automatic mesh generation for boundary integral method, IEEE Tran. Mag. Vol.-26 No.2, 1990, pp767-770

[25] S Ratnajeevan and H Hoole, Finite element electromagnetic field computation on the sequent symmetry 81 parallel computers, IEEE Tran. Mag. Vol.-26 No.2, 1990, pp 837-840

[26] M Barton, J Rattner, Parallel computing and its impact on computational electromagnetics, IEEE 8th COMPUMAG, Italy, July 1991

[27] Yan Weili, Qiu Zhushu, Finite element method for static characteristic of an electromagnetic device, Low Voltage Electrical Apparatus, Shanghai, No.4, 1978.

[28] L Bompa, P Schueller, J.C Sabunadiere, Analysis and synthesis of an electro-magnet used for circuit breaker operation, IEEE Trans. Mag., Vol.21, No.6,1985

[29] Chen Degui, Li Erping and Xie Yunxian, Analysis of an Electromagnetic relay response with coupled magnetic circuit and integral method, Xi'an Jiaotong University, ST-Report 85-448, 1985

[30] Zheng Shiquan and Chendegui, Numerical analysis of the dynamic characteristics of a Basin-conic Solenoidal electromagnet, Journal of Xi'an Jiaotong University, Vol.20, No.3, 1986

[31] Li Erping and Chen Degui, Computer aided optimal design of a lifting electromagnet, Journal of Xi'an Jiaotong University, Vol.-22 No.2, 1988 pp29-37

[32] Li Erping and Chen Degui, Numerical Analysis of Transient process for a current limiting magnetic drive-mechanism, Proceedings of Int. Con. on Ele. Contacts, Arcs, Apparatus and Applications, Xi'an, CHINA, May 1989

[33] A Abri, R Nordgren, S Kjellnas and L Banghammar, Finite element analysis of electromagnets and contact system in low voltage current limiting circuit breakers, IEEE Tran. Mag. Vol.-26, No.2, 1990, pp960-979

[34] Ji Jiaqin and Zhang Lichao, The calculation of the dynamic arcs in transverse magnetic fields, Proceedings of International Conference on Electrical Contacts, Arcs Apparatus and Applications, Xi'an, China,May 1989

[35] W Breer, P Chaudhuri, Prediction of circuit breaker characteristics in the design stage by computer simulation, 4th International Symposium on Short Circuit Currents, Belgium, 1990

[36] Zijad Haznadar, S Berberovic, Electric and magnetic field calculations in vacuum circuit breakers, IEEE Tran. Mag. Vol.-21, 1985, pp2480-2485

[37] A M Pawlak and T W Nehl, Transient finite element modelling of solenoid actuators : the coupled power electronics, mechanical, and magnetic field problem, IEEE Tran. Mag. Vol.-24, No.1, 1988, pp270-273

[38] J Stratton, Electromagnetic Theory, McGraw-hill Book Company, Inc. 1941

[39] L J Segerlind, Applied finite element analysis, John Wiley& Sons Ltd,1976

[40] O.C. Zienkiewicz, Finite element method in engineering science, Mcgraw-hill, London, 1971

[41] R. S Tebble, D J Craik, Magnetic materials, Wiley-interscience, John Wiley &Sons Ltd. 1969

[42] D Hadfield, Permanent magnets and magnetism, London, John Wiley & Sons Inc, 1962

[43] R Parker, R. Studders, Permanent magnets and their application, John Wiley& sons Inc. 1962

[44] J S Waugh, Advanced in magnetic resonance, Academic Press, 1965

[45] Vector Field Ltd: TOSCA Reference manual 1989

[46] AutoCAD Reference manual, Release 10, 1989

[47] Li Erping, A L Kidd and P M McEwan, CAD design of current sensitive electromagnetic actuators, 4th Int. Symp on short Circuit Currents in Power Systems, Belgium, Sep. 1990

[48] Li Erping, A L Kidd, P M McEwan, Application of finite element CAD technique in the design of current sensitive electromagnetic actuators, 8th COMPUMAG, Italy,1991 to be published on IEEE Tran. Magnetics, Vol.28,No2, March 1992

[49] T R Kochler,D R Fredkin, Finite element methods for micromagnetics, IEEE 8th COMPUMAG, Italy, July, 1991

[50] F Pireou and A. Razek, Coupling of saturated electromagnetic systems to non-linear power electronic devices, ibid. pp274-277

[51] Staton David Alan , CAD of permanent magnet p.c. motors for industrial drives, PhD thesis, Sheffield University, 1988

[52] K Hameyer, R Hanitsch, Theoretical and experimental investigation of a rotating actuator with respect to different material, Proceedings of 25th UPEC, Aberdeen, Sept. 1990, pp.555-558

[53] J. Simkin, C. W Trowbridge, Optimising electromagnetic devices combining direct search methods with simulated annealing, IEEE 8th COMPUMAG, Italy, July, 1991

[54] Li Erping, A L Kidd and P M McEwan, A Decoupled Integral-Finite Element CAD method for determining the transient response of current sensitive electromagnetic actuators, 25th University Power Engineering Conference, Aberdeen, UK, 1990

[55] Li Erping, P M McEwan, Analysis of a circuit breaker solenoid actuator system using the decoupled CAD-FE-Integral technique, to be published on, IEEE Tran. Magnetics, Vol.28,No.2, March 1992

[56] C F Bryant, B Dillon, J Simkin, C W Trobridge, Solving high frequency problems using the magnetic vector potential with Lorentz Gauge, IEEE 8th COMPUMAG, Italy, July, 1991

[57] Zheng Shiquan, Transient analysis of a non-linear electromagnetic devices used in electrical apparatus, PhD Thesis Xi'an Jiaotong University, April 1989

[58] S Niikura, A Kameari, Analysis of eddy current and force in conductors with motion, IEEE 8th COMPUMAG, Italy, July, 1991

[59] A. Foggia, N. Burais, L Krahenbuhl, A. Nicolas, Finite element analysis of a fast electromagnetic actuator, IEEE Tran. Mag.-20, No.5, 1984, pp1942-1944

[60] G Asche P K Scattler, Numerical calculation of the dynamic Behaviour of electromagnetic actuators, IEEE Tran. Mag. Vol.-26, No.2, 1990, pp979-982

[61] Li Erping and P M McEwan, Evaluation of a Stepper motor Electromagnetic Current-sensitive Actuator, Research Report No.2, June 1990, Sheffield City Polytechnic,UK

[62] Provisional Patent Specification, Combination toroid and stepper actuator, WYLEX, Limited, 1988

[63] Research Material, Think escape: Stepper Motors, Sheffield City Polytechnic

[64] Albert Leenhouts, The art and practice of stepper motor control, International Communications INc. USA

[65] E P Anderson, Electric motors, Bobbs Merrillic Inc, 1983

[66] P P Acarnley, Stepping motors a guide to modern theory and practice, Peter Percgr Inus Ltd, Institutions of Electrical Engineers

[67] C Dawson, H R Bolton, Design of a class of wide-angle limited-rotation rotary actuators, Proc. IEE Vol.126, No.4, 1979

[68] C Dawson, H R Bolton, Limited motion rotary actuators of the toroidal-stator, permanent rotor type, Proc. IEE, Vol.129, pt.b. No.4, 1982

[69] H R Bolton, Shakweh, Performance predication of Laws's Relay actuator, IEE Pro. Vol.137, pt.B, No.1, 1990,pp1-13

[70] Yost,B.J., Solenoid type rotary actuators, Engineering Dig., 1972,33 pp.49-51

[71] L A Pipes, Applied mathematics for engineers and physicists, McGraw-Hill Book Company,INC, 1958

[72] S P Timoshenko and J M Gere, Mechanics of Materials, Van Nostrand Reinhold Company, 1973

[73] L S Jacobsen, R S Ayre, Engineering Vibrations, McGraw-Hill Book Company, INC ,1958

[74] D Howe, Z Q Zhu, The influence of finite element discretisation on the prediction of cogging torque in permanent magnet excited motors, IEEE 8th Conference on the Computation of Electromagnetic Fields, Italy, 1991

[75] Touzhu Li, Gordon Slemon, Prediction of cogging torque in permanent magnet motors, IEEE Trans. On MAG. Vol.24, No.6, Nov. 1988

[76] M Goto and K Kobayashi, An analysis of the cogging torque of a DC motor and a new technique of reducing the cogging torque, Electrical Engineering in Japan, 1983,103,(5), pp113-120

[77] K Kobayashi and M Goto, A brushless DC motor of a new structure with reduced torque fluctuations, Electrical Engineering in Japan, 1985, 106 No.3, pp104-112

[78] Takashi KEnjo, Stepping motors and their microprocessor control, Clarendon Press, Oxford,1984

[79] DE Patents, No. 2062885, 2503159, 2529221

[80] S J Morrison, Importance of quality and reliability, IEE Proc. Vol.128,Pt.A, No.7,1981

[81] L. Jin, Discussion of residual current circuit breakers reliability, Jounal of Low-voltage Electrical Engineering, Chinese, No.3, 1989,pp26-29

[82] Lu Jianguo, Reliability of Electrical Apparatus, Hebei Institute of technology

[83] Zhu Ruiqi, Mo Feng, A life reliability test system of electric-mechanic relays and contactors with failure analytic function, Proceedings of IC-ECAAA, Xi'an,China,May 1989

[84] Hojjat Adeli, K.V. Balasubramanyam, Expert systems for Structural Design, Prentice-Hall,Inc. Englewood Cliffs, New Jersey 07632, 1988

Appendix I

IEC Publication(479) Curves:

Time/Current Zones of Effects of A.C. Currents(15Hz to 100Hz) on Persons

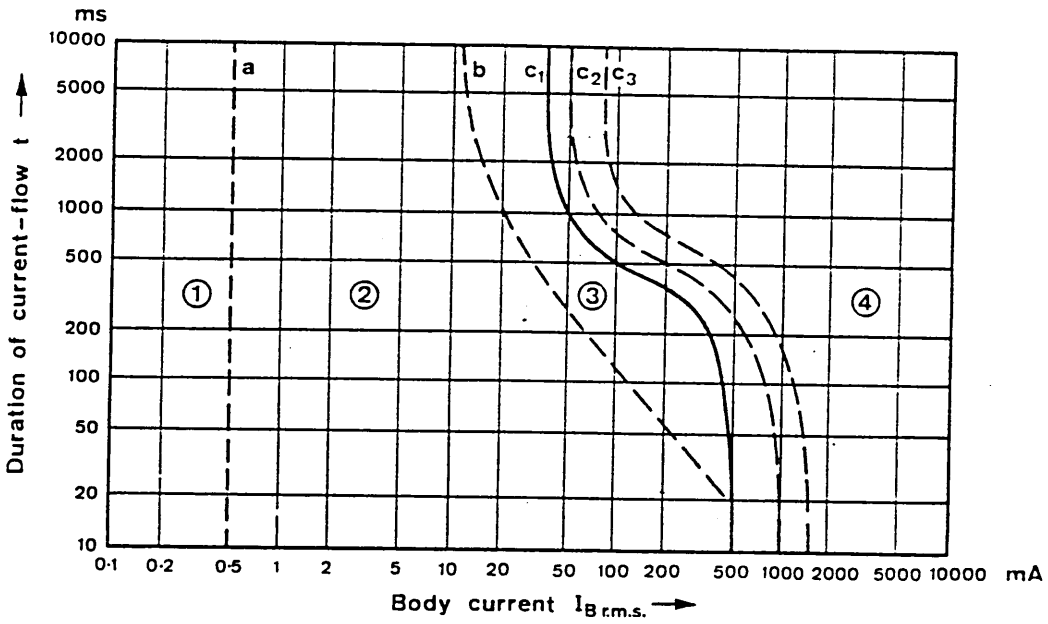

Zones	Physiological effects
Zone 1	Usually no reaction effects
Zone 2	Usually no harmful physiological effects
Zone 3	Usually no organic damage to be expected. Likelihood of muscular contractions and difficulty in breathing, reversible disturbances of formation and conduction of impulses in the heart, including atrial fibrillation and transient cardiac arrest without ventricular fibrillation increasing with current magnitude and time.
Zone 4	In addition to the effects of Zone 3, probability of ventricular fibrillation increasing up to about 5% (Curve C2), up to about 50% (Curve C3) and above 50% beyond Curve C3. Increasing with magnitude and time, pathophysiological effects such as cardiac arrest, breathing arrest and heavy burns may occur.

Appendix II

Parameters Of Surface Roughness And Waviness

THE PARAMETERS

What surface texture is and why it is necessary to measure it are subjects covered in the book "Exploring Surface Texture" supplied with the instrument. The user of Talysurf 5 is advised to read this book to obtain background information on surface texture in general and on stylus-type measuring instruments in particular. It also gives useful information on parameters: their derivation and use.

Surface texture is quantified by parameters which relate to certain characteristics of the texture. These parameters can be classified in three groups, according to the type of characteristic that they measure.

Amplitude parameters are measures of the vertical displacements of the profile

Spacing parameters are measures of irregularity spacings along the surface, irrespective of the amplitude of these irregularities.

Hybrid parameters relate to both the amplitude and spacing of the surface irregularities.

The parameters defined below relate, in general, to the filtered roughness profile, but some corresponding waviness parameters can be determined from the filtered waviness profile. In addition, some parameters can be determined from the unfiltered profile.

When referring to a parameter it is normally assumed that the value quoted is that obtained from the roughness profile. If, however, the value relates to the waviness or unfiltered profile, this should be clearly stated.

1 - Amplitude parameters

Ra See Figure 50.2.
Ra is the universally recognised, and most used, international parameter of roughness. It is the arithmetic mean of the departures of the profile from the mean line. It is normally determined as the mean result over several sampling lengths L (five in 5P, 5L and 5Z, and a number, depending on sampling and assessment length, in 5M).

Rq See Figure 50.2.
Rq is the rms parameter corresponding to Ra.

Rmax See Figure 50.3.
Rmax is the maximum peak-to-valley height of the profile within the *sampling* length L.

Rt See Figure 50.3.
Rt is the maximum peak-to-valley height of the profile within the *assessment* length.

Rtm See Figure 50.3.
Rtm is the average of the Rmax of five consecutive sampling lengths. It is the equivalent of Rz DIN.

Rt1, n Rt_1, Rt_2, Rt_3 etc. are the individual values of Rmax in *n* consecutive sampling lengths.

Rz See Figure 50.4.
Rz is measured on the unfiltered profile only and is numerically the average height difference between the five highest peaks and the five lowest valleys within the assessment length. The parameter is determined over one sampling length only. The definition given above (and used in Talysurf 5) agrees with that for Rz specified in the ISO standard.

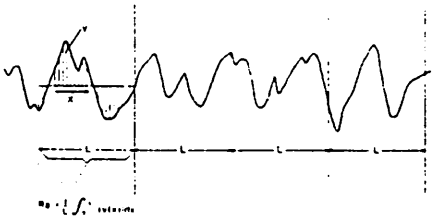

$$Rq = \sqrt{\frac{1}{L}\int_0^L v^2(x)dx}$$

Figure 2 Ra, Rq

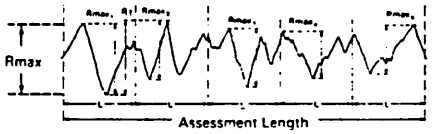

$$Rtm = \frac{Rmax_1 + Rmax_2 + Rmax_3 + Rmax_4 + Rmax_5}{5} = \frac{1}{5}\sum_{i=1}^{5} Rmax_i$$

Figure 3 Rmax, Rt, Rtm

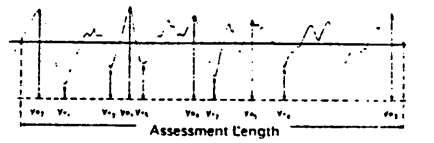

$$Rz = \frac{(y_{p1} + y_{p2} + y_{p3} + y_{p4} + y_{p5}) - (y_{v1} + y_{v2} + y_{v3} + y_{v4} + y_{v5})}{5} = \frac{1}{5}\left(\sum_{i=1}^{5} y_{pi} - \sum_{i=1}^{5} y_{vi}\right)$$

Figure 4 Rz

R3im R_{3i} is the height difference between the third highest peak and the third lowest valley within an assessment length. R_{3im}

Appendix II

Parameters Of Surface Roughness And Waviness

is then the mean R_{3i} determined over several consecutive assessment lengths. R_{3im} is equivalent to R_z JIS provided it is measured on the unfiltered profile.

Rp See Figure 50.5.
Rp is the maximum height of the profile above the mean line within the assessment length.
The processors have a switch for inverting the profile so if it is required, the maximum depth of the surface profile *below* the mean line can be obtained (i.e. the Rp of the inverted profile).

Rpm See Figure 50.5.
Rpm is the mean value of Rp determined over several consecutive sampling lengths.
Like Rp, the Rpm of an inverted profile can be measured.

Rsk See Figure 50.6.
Skewness is a measure of the asymmetry of the amplitude distribution curve about the mean line.

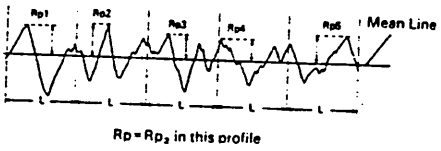

$$Rpm = \frac{Rp_1 + Rp_2 + Rp_3 + Rp_4 + Rp_5}{5} = \frac{1}{5}\sum_{i=1}^{5} Rp$$

Figure 5 Rp, Rpm

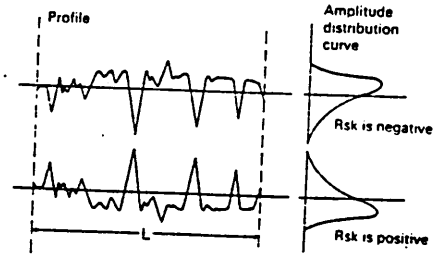

Figure 6 Rsk

2-Spacing parameters

HSC See Figure 50.7.
The high spot count is the number of complete profile peaks projecting above the mean line (in processor 5M), or (in 5P, 5L, 5Z) a line parallel to the mean line and at a preset distance *p* above or below a preset reference (which is normally either the highest peak or the mean line). The count is made over the assessment length and the count displayed is the number within this length.

Sm See Figure 50.8.
Sm is the mean spacing between profile peaks at the mean line, measured over the assessment length.

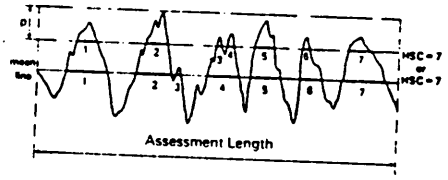

Figure 7 Hsc

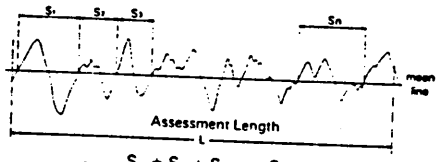

$$Sm = \frac{S_1 + S_2 + S_3 \ldots . Sn}{n} = \frac{1}{n}\sum_{i=1}^{n} S_i$$

Figure 8 Sm

3-Hybrid parameters

Δa This is the arithmetic mean slope of the profile throughout the assessment length; it is a dimensionless ratio, but can also be displayed in degrees.

Δq Similarly, this is the rms slope of the profile throughout the assessment length, again displayed as a ratio.

λa Average wavelength is a measure of the spacings between local peaks and valleys, taking into account their relative amplitudes and individual spatial frequencies.

Numerically $\lambda a = 2\pi \frac{Ra}{\Delta a}$

λq This is the corresponding rms wavelength parameter.

Numerically $\lambda q = 2\pi \frac{Rq}{\Delta q}$

tp See Figure 50.9.
Bearing ratio is the length of bearing line (expressed as a percentage of the assessment length) where the peaks have been cut off at a level *p* below the highest peak or above the mean line. It is measured over the assessment length.

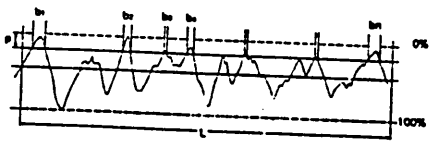

tp (%) is the ratio at a selected depth p.

$$tp = \frac{b_1 + b_2 + b_3 + b_4 \ldots . bn}{L} \times 100 = \frac{100}{L}\sum_{i=1}^{n} b_i$$

Figure 9 tp

Contributed Papers

4.13 CAD Design of Current Sensitive Electromagnetic Actuators

Li Erping[1], A L Kidd[2], P M McEwan[1]

[1] Sheffield City Polytechnic, Sheffield, UK
[2] G H Scholes Ltd, Manchester, UK

ABSTRACT

Non-Linear, three dimensional Finite Element CAD techniques have been successfully applied to the design analysis of a current sensitive electromagnetic actuator. The Finite Element CAD solution permits calculation of forces, sensitivity to current, magnet alignment, together with the evaluation of magnetic material properties, shape and dimensions on the actuator operation. The studies performed correlate closely with measurements and theoretical predictions.

Introduction

Electromagnetic actuators are used in a wide variety of applications. The types of interest in the reported studies were those which are required to operate with great precision at very low current (less than 30ma) and which are able to produce relatively high mechanical actuating forces (typically up to 0.25N). These actuators fall into the class of current-sensitive relays and have applications in accurately detecting leakage current in electrical systems or protecting humans against the effects of electric shock.

The principles of operation are relatively simple, the ingenuity invariably lies in the magnetic circuit design.

Practical current-sensitive actuators require some means for altering the trip-current setting, for tuning purposes and for also overcoming the vagaries of manufacturing tolerances. The critical design influence, however, is the air-gap spacing and consequently the quality of the machined surfaces of armatures and contact surfaces is very important.

The TOSCA non-linear three dimensional finite element electromagnetic field solution CAD package (1) was used to analyse the design of a current sensitive actuator used in a manufactured product. A workstation with added RAM was used to enable realistic modelling and fast solutions. The package enabled precise electromagnetic modelling of the actuator and calculation of the forces acting on the armature.

Actuator Design

The actuator general arrangement is shown in figure 1. The magnetic circuit consists of two yoke plates (4) and (5). The plates are separated by a layer of non-ferromagnetic material (6), which provides a relatively high reluctance path for leakage flux from the permanent magnet (1). The permanent magnet bridges the yoke plates, the polarisation strength and angular direction of which may be adjusted to change the electromagnetic force acting on the armature, by rotating the magnet about its N-S axis. The armature is held against the yoke machined faces by the force of attraction of the permanent magnet against the opposing force of spring 7.

The magnetic circuit has a constricted section, denoted by x and x^1, which contains flux ϕ_1, ϕ_2 from the permanent magnet and flux ϕ_i. The coil produces the control flux ϕ_i, when carrying current, supplied from a toroid winding (not shown). This flux produces saturation of one of the constricted sections when the current exceeds a specified value whereupon the net flux in the armature air-gap is reduced which consequently reduces the force of attraction on the armature. The electromagnetic force therefore decreases as the coil current is increased until the armature opens under the action of the spring. The actuator is then deemed for the purpose of the analysis to have operated.

Calculation of Armature Attraction Force

It is necessary to solve the electromagnetic field distribution in the magnetic circuit and air-gap for different angular displacements of the permanent magnet to enable calculation of the force acting on the armature. A finite element analysis package of the type referred to (1) was the chosen means of solving this class

of non-linear problem.

From Maxwells field equations

$$\nabla\cdot\bar{B} = 0,\ \nabla\times\bar{H} = \bar{J}$$

and material constituent relationship $B = \mu H$, it may be shown that the equation for the two scalar potentials in all the electromagnetic regions is

$$-\nabla\cdot\mu\nabla\phi + \nabla\cdot\mu H_s = 0 \qquad (1)$$

and

$$-\nabla^2\mu\nabla\psi - \nabla\cdot\mu H_c = 0 \qquad (2)$$

given that in regions where no currents exist

$\bar{H} = -\nabla\psi$ where ψ is the total scalar potential and H_c is the magnetic coercive force

and where currents exist

$\bar{H} = -\nabla\phi + \bar{H}_s$ where ϕ is the reduced scalar potential

At magnetic boundaries or interfaces A, B, (fig 1) both normal and tangental equality constraints are satisfied by the following conditional equations in the normal and tangental planes, respectively

$$-\frac{\mu\partial\psi}{\partial n} - \mu H_{cr} = \mu_o\left(H_{sn} - \frac{\partial\phi}{\partial n}\right) \qquad (3)$$

$$\psi_{AB} = \phi_{AB} - \int_A^B H_s\cdot t\ dt + \int_A^B H_c\cdot t\ dt \qquad (4)$$

where t is the unit tangental vector.

The solution of equations 1 and 2 is performed within the CAD program by the Weighted Residual (WR) method. The solution is based on discretising the geometry into finite elements, comprising prisms, tetrahedrons and bricks etc. The problem was posed as steady-state, which assumes no eddy-current effects and all current to be instantaneous. The WR method results in sets of non-linear matrix equations which are solved by Successive Over Relaxation (SOR) techniques to determine the field distribution in the magnetic material and air-gaps.

The force acting on the armature is determined from Maxwell's stress tensor in free space as follows;

$$f = \frac{1}{\mu_o}(\bar{B}\cdot\bar{n})\bar{B} - \frac{1}{2\mu_o}B^2\cdot\bar{n}$$

from which the electromagnetic force is

$F = \oint_s f\ ds$ where n is the unit normal vector of a surface s parallel to the armature face

The integration over the region of the air-gaps may be performed within the TOSCA.FE program to permit calculation of the electromagnetic force acting on the armature. The specification of the problem takes account of the magnetic material properties, displacement angle of the permanent magnet, the shape and dimensions of the magnetic circuit, armature and air-gaps, the number of coil turns and the magnitude of the coil control current.

Actuator Settings

For the armature to remain closed the electromagnetic force must exceed the opposing spring force. For precise current detection the margin of the difference between the two forces is critical and can only be set by permitting the desired trip control current to flow in the coil and to then adjust the angular displacement of the permanent magnet to just effect tripping of the armature. This technique is adopted as a means of assuring good quality control in manufacture and test, and will be returned to later. In analysing the proposed actuator as a field problem it is readily found that the air-gaps have a significant effect on the magnitude of the air-gap flux and consequently on the electromagnetic force acting on the armature, figure 2. To arrive at the optimum air-gap it is necessary to find the radial alignment of the magnet which just produces tripping with no current in the control coil. Variation of the air-gap and angular alignment can be readily simulated using TOSCA and checked by physical measurement.

A number of relays were tested as described and the results were compared with computed predictions. Both studies demonstrated the need to pre-set the permanent magnet angular alignment to between 40° - 50° to reduce the effects of manufacturing tolerances and other vagaries on the performance of the actuator.

Actuator Energised States

As described earlier, when current is injected into the control coil the armature force of attraction reduces until a current is reached at which tripping occurs. Figure 3 shows the computed and measured values of the electromagnetic force and initial spring force against trip current for three values (0°, 40°, 50°) of magnet displacement angle.

Figure 4 shows the trip current against magnet alignment for four relays and confirms the spread of characteristic due to manufacturing tolerances and the need to set the displacement angle to between 40°-50° where the curves converge to enable consistent tripping. The correlation between the measured and computed results is sensible and confirms industrial test practice. It furthermore highlights the dependency of the actuator performance on high precision manufacture and how practical tolerances can be permitted without producing excessive inconsistency of performance.

Summary Conclusions

The TOSCA CAD program was found to be highly suitable for analysing sensitive current-operated electromagnetic actuator designs. The solutions highlighted some peculiar features of a particular design which were known about but not particularly well understood.

The analysis permitted characterisation of the performance of the actuator in terms of the critical design and control variables, which correlated very closely with practice and the results of tests and measurements.

Finally, the TOSCA CAD solution was found to be a reliable tool for optimising the design of electromagnetic actuators of the type described.

References

1 TOSCA CAD Manual, Vector Field Ltd

2 Li Erping, P M McEwan, "Electromagnetic Current-Sensitive RCD Actuator" Report No 1, December 1989, Sheffield City Polytechnic

3 A L Kidd, "Electrical Protection for Domestic and Small Commercial Installations", IEE Power Eng Journal, Vol 251, pp 57-65

4 A L Kidd, "Improvements Relating to Magnetic Tripping Devices", Patent No 51521/69, London

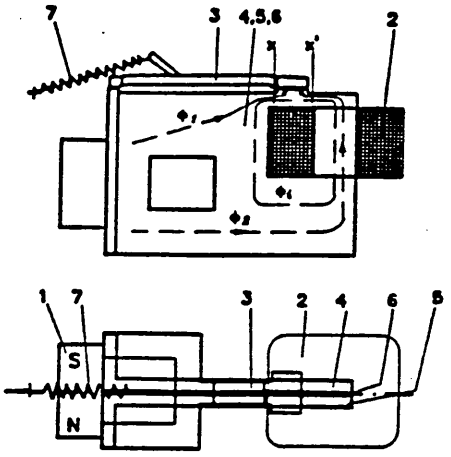

1–Magnet
2–Coil
3–Armature
4,5–Yoke
6–non–ferromagnetic material
7–Spring
Φ_1, Φ_2–flux produced by the permanent magnet through regions x,x'respectively
Φ_i–flux produced by the current in N turns coil

FIGURE 1

Actuator General Arrangement

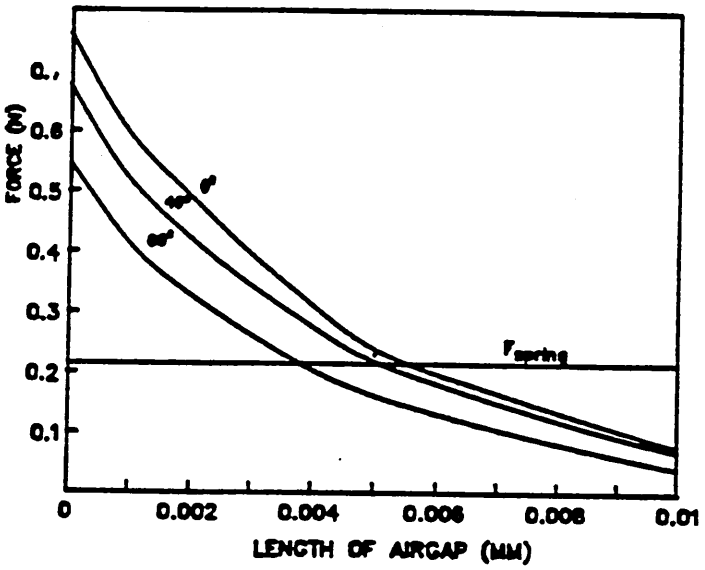

FIGURE 2

Relationships between force and air-gap for different permanent magnet alighment angles

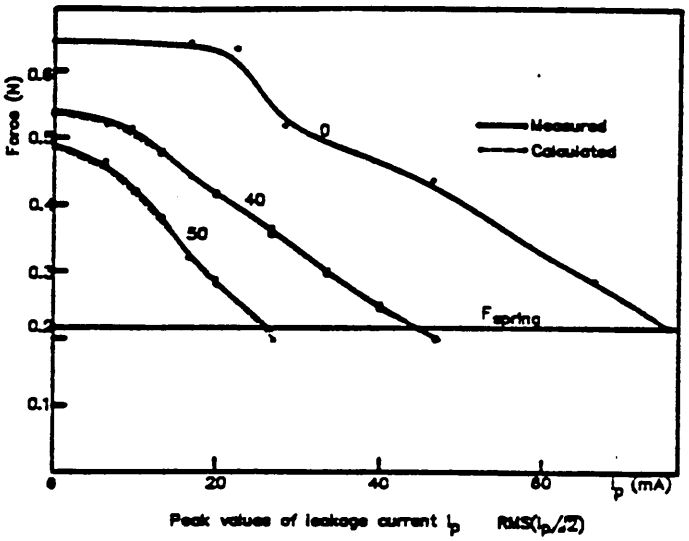

FIGURE 3

Magnetic force against toroid current for different magnetic angle displacements

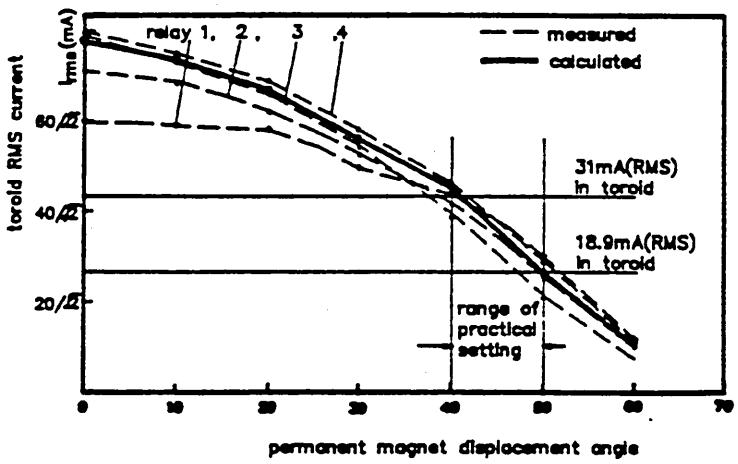

FIGURE 4

Comparison of calculated and measured values of trip current versus magnetic displacement angle for four production type relays

A DECOUPLED INTEGRAL - FINITE ELEMENT CAD METHOD FOR DETERMINING THE TRANSIENT RESPONSE OF CURRENT-SENSITIVE ELECTROMAGNETIC ACTUATORS

LI ERPING[1], A L KIDD[2], P M McEWAN[1]

[1]Sheffield City Polytechnic, UK [2] G H Scholes Ltd, UK

ABSTRACT

A decoupled integral-finite element method is presented for determining the transient response of an electromagnetic current-sensitive actuator. The method involves solving the electromagnetic force acting on an armature, using a three dimensional finite element non-linear electromagnetic field CAD program, for varying armature displacements, and time-varying current and to subsequently solve the resulting governing dynamic equation, by numerical integration.

The technique permits the transient response of a current-sensitive actuator to be accurately computed and characterised for time-varying current.

INTRODUCTION

Previous work on the analysis of current-sensitive electromagnetic actuators (1, 2) demonstrated that the magnetic force holding an armature closed against the opposing pull of a spring can be fully simulated and accurately predicted using a finite element three dimensional electromagnetic CAD program (3). The simulation takes account of the magnetic circuit's geometry, dimensions, material properties, air-gaps, coil current, and the shape of the armature etc.

The force acting on the armature is defined by Maxwell's stress tensor in free space

$$\vec{f} = \frac{1}{\mu_o}(\vec{B}\cdot\vec{n})\vec{B} - \frac{1}{2\mu_o}B^2\cdot\vec{n}$$

from which the electromagnetic force is given by

$$F_e(i,y) = \oint \vec{f}\, ds$$

where n is the unit normal vector of a surface parallel to the armature faces and i,y are the control current and air-gap spacing (displacement), respectively

The electromagnetic field in the actuator air-gap and consequently the electromagnetic force F(i,y) are diminished when current flows in the coil as shown in figure 1. The velocity and impact force of the armature required to actuate a mechanism, is however a function of the component of the spring force in the 'y' axis $F_s(y)$ and the force required to move the trip mechanism F_c. If the field distribution in the air gap is computed, the actuator variables can be reduced to a function of the net force $[F_s(y) - F_e(i,y)]$. It is then possible to solve the dynamic equation for the actuator by numerical integration. The combined field and numerical solutions is referred to here as the decoupled integral-finite element method.

Formulation of the Problem

The physical arrangement of the actuator is shown in figure 1, which also illustrates the forces acting on the armature, where $F_e(i,y)$ is the electromagnetic force directly opposing the spring force $F_s(y)$. The control current is assumed to be sinisoidal in the study,

$$\text{ie} \quad i = f(t) = I_m \sin\omega t \qquad (1)$$

The dynamic equation of the moving armature is solved by reducing the second order differential equation to two first order equations;

$$\frac{dv}{dt} = (F_{s(y)} - F_e(i, y)/m \qquad (2)$$

where m = mass of the armature and y the air-gap spacing

$$\frac{dy}{dt} = v \qquad (3)$$

v is the velocity

The initial conditions are determined by measurement and computation (1) or are prescribed, as follows;

$$y\big|_{t=0} = 0.0009, \quad i\big|_{t=0} = 0, \quad F_e(i,y)\big|_{t=0} = F_o,$$

$$F_{s(y)}\big|_{t=0} = F_{so}, \quad v\big|_{t=0} = 0$$

Here F_o is the magnetic force acting on the armature produced only by the permanent magnet, and F_{so} the maximum force of the spring acting on the armature, in the y axis.

From measurements the armature was found to strike the trip mechanism when y = 0.5 mm, whereupon the spring force is suddenly opposed by the trip mechanism force F_c.

The spring force equations are therefore derived from the force diagram as;

$$F_s(y) = [F_{sz}l_y - F_{sy}l_z]/la, \qquad \text{for } 0<y<0.5\text{mm}$$

and $F_s(y) = [F_{sz}.l_y - F_{sy}.l_z]/la - F_c$, for $y>0.5$mm

Where $F_{sz} = F_s \sin(\beta(y))$

$F_{sy} = F_s \cos(\beta(y))$

The equation for the spring tension force F_s, acting along the axis of the spring, was determined by precise measurement as

$$F_s = 0.48 + 0.38\,(l_s - 4.5)\ \text{N},$$

where l_s = length of spring

The Decoupled Integral - FE CAD Method

The decoupled method is based on pre-determining the electromagnetic force $F_e(i,y)$ for a range of currents and displacement values, using a 3D FE CAD solution, such as TOSCA, and to then store the values in the form of look-up tables. The solution of the dynamic equation then progresses in incremental time steps Δt by substituting the latest computed values of $F_e(i, y)$ and $F_s(y)$ into

the difference equation (equation 2), corresponding to the respective values of the instantaneous current and displacement at the instant $t=n\Delta t$. The latest calculated value of velocity is obtained from

$$V_{n+1} = V_n + (F_s(y) - F(i, y)\frac{\Delta t}{m}$$

where n is the current number of time increments.

The latest value of armature displacement is subsequently determined by substitution of the calculated values V_n, V_{n+1} into the corresponding weighted difference equation

$$y_{n+1} = y_n + \frac{\Delta t}{2}(v_n + v_{n+1})$$

Predicted Actuator Dynamic Performance

The proposed method was used to predict the dynamic performance of the current sensitive actuator, figure 1. Figure 2 illustrates the variation of the electromagnetic force in the air-gap against current. Figure 3 shows the prediction of the electromagnetic force $F_e(i,y)$ before and after the armature moves, when the coil current varies sinusoidally. This figure indicates that for 50 Hz currents the delay, before the armature commences movement, is of the order of 3ms (2.95ms).

Figure 4 shows the prediction of the dynamic response of the armature and prediction of the velocity and the time for the armature to travel the fixed distance before actuating the mechanism. This figure shows the classical rapid declination of the electromagnetic force acting in the air-gap, when the armature commences movement and the air-gap increases. The figure also clearly shows that the opposing spring force $F_s(y)$ increases slightly and suddenly drops when the displacement exceeds the critical value where the 'y' component of the spring force $F_s(y)$ changes sign. This action, of course, has little effect on the transient response of the actuator.

Summary Conclusions

The proposed decoupled method enables solution of the dynamic response of a current-sensitive electromagnetic actuator to time-varying current. The method takes account of the complete magnetic circuit and mechanical design of the actuator and therefore permits the actuator response and design to be optimised for any current waveform. Given that the travel of the armature to actuate the mechanism was of the order of 4-5mm, the analysis indicates that initiation would occur within 2.5ms. This result compared very favourably with measurements.

References

1 Li Erping, Chen Degui, "Numerical Analysis of the Transient Process for Current Limiting Magnetic Drive Mechanism", ECAAA, Int Conf, Xi'an, May 1989

2 Li Erping, A L Kidd, P M McEwan, "CAD Design of Current Sensitive Electromagnetic Actuators", 4th Int Symp on Short Circuit Currents in Power Systems, Liege, Belgium, September 1990

3 TOSCA CAD Manual, Vector Field Ltd, Electromagnetic 3 Dimensional Non-linear Finite Element CAD Package

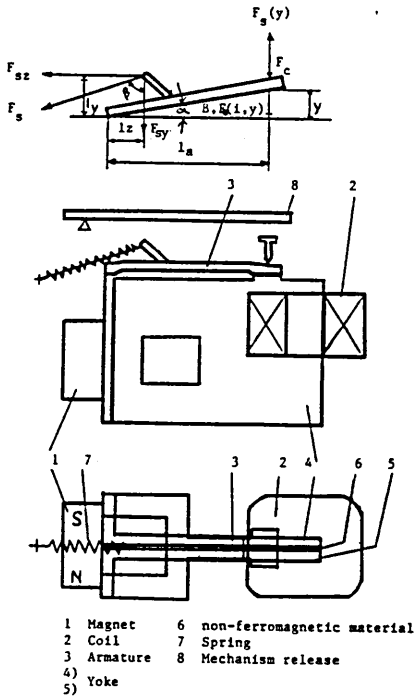

Figure 1 Actuator General Arrangement and Force Diagram

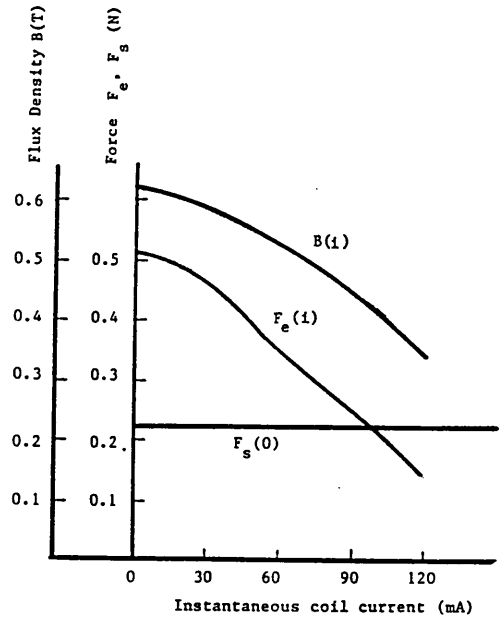

Figure 2 Magnetic force and flux density in air-gap versus coil current

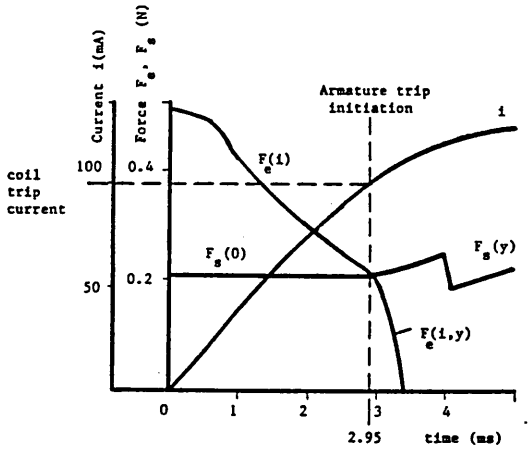

Figure 3 Actuator response characteristics for sinusoidal current detection

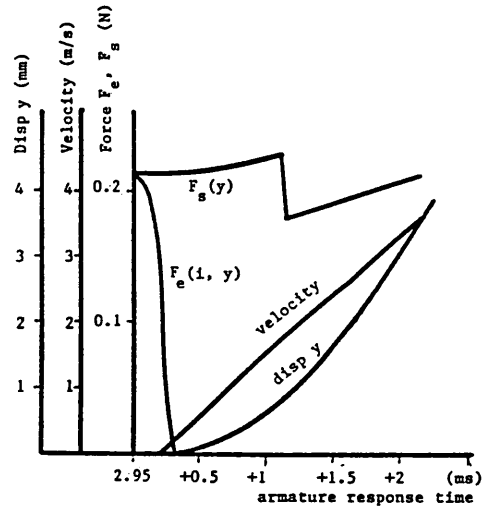

Figure 4 Actuator dynamic characteristics

Analysis of a Circuit Breaker Solenoid Actuator System Using the Decoupled CAD-FE-Integral Technique

Li Erping P M McEwan
School of Engineering Information Technology
Sheffield City Polytechnic
Sheffield, UK

Abstract: **A decoupled three dimensional CAD finite element-integral method, combined with Runge-Kuta method, is proffered to determine the dynamic characteristics and design requirements of a circuit breaker solenoid actuator, when energised from a D.C. supply. The model couples the electric, magnetic and mechanical systems of the device. The presented solution takes account of the non-linear magnetic material properties, dimensions of the magnetic circuit, the coil parameters and load of the trip mechanism system. The predicted dynamic characteristics from the analysis correlate closely with the results from the test performed on the actuator and demonstrate the applicability of the proposed techniques for optimizing circuit breaker actuator performance and electromagnetic solenoid design.**

I INTRODUCTION

Solenoid actuators are commonly used to initiate the tripping mechanism of circuit breakers. These actuators basically consist of a coil which is energised from a D.C. source, typically at 110v. The actuators have a magnetic core and a moving plunger which is used to trip the circuit breaker mechanism as shown in Figure 1. The actuator mechanism is spring loaded. One such actuator was analysed to enable prediction of its dynamic performance and design requirements, when energised from a switched D.C. voltage supply. The analysis involved solving three sets of linked equations for the electric circuit, the electromagnetic force acting on the actuating mechanism and the dynamic response of the system for a given trip load. A decoupled CAD FE-integral method was used in combination with the Runge-Kuta method to solve the equations for the electromagnetic force acting on the system and its dynamic response.

Manuscript received July 7, 1991

II SYSTEM MODELLING

A schematic of a typical solenoid actuator operated from a dc voltage source is shown in figure 1. The physical arrangement of the solenoid actuator is shown in figure 2. This has a stationary coil and a magnetic circuit with cylindrical plunger and rectangular cores. The solution of the dynamic response of the plunger, following energisation of the coil, necessitates determining the field surrounding the plunger and consequently the need for a three dimensional model of the system.

III DECOUPLED-3D FE-INTEGRAL METHOD

The three dimensional finite Element CAD program, TOSCA, was used to model the distribution of the solenoid electromagnetic field and calculate the magnetic force on the plunger for different currents and displacements of the plunger. The mechanical movement of the plunger was determined for the

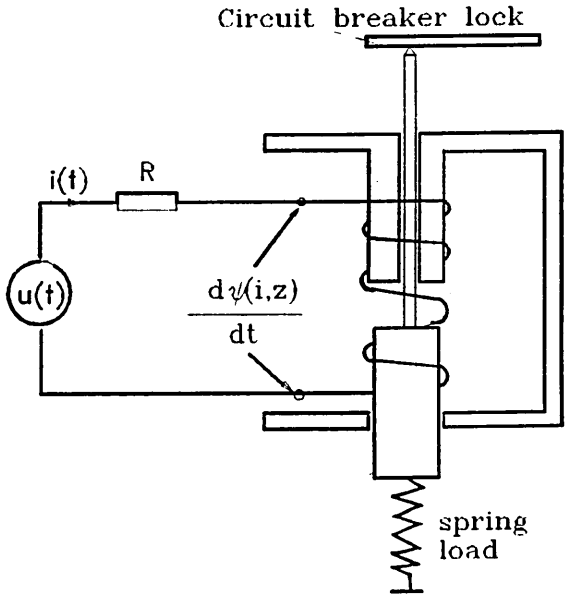

Figure 1 Solenoid actuator operated from a voltage source

current in the solenoid upon application of a D.C. applied voltage source. The solutions of the electromagnetic field are based on Maxwell's equations.

$$\nabla \cdot B = 0 \quad (1)$$

$$\nabla \times H = J \quad (2)$$

and the material constituent relationship $B=\mu H$

The finite element method, which was used to solve the partial differential equations derived from the above equations, is based on dividing the actuator magnetic circuit physically into small volumes. Within each element a simple polynomial is used to approximate the relevant partial differential equation and boundary conditions. The electromagnetic partial differential equations describe the spatial and temporal variation of the field, directly in terms of the field variable, magnetic flux density B.

Discretisation of the magnetic circuit into finite elements as described enables the field distribution in the magnetic material and airgap to be obtained using TOSCA, from which the electromagnetic force acting on the armature is determined from the following equation:

$$F_e = \int_s T ds \quad (3)$$

where T is the Maxwell stress tensor.

The integration over the region of the airgap may also be performed within the TOSCA program to permit calculation of the electromagnetic force acting on the plunger. The specification of the problem takes account of the magnetic material properties, the shape and dimensions of the magnetic circuit, plunger and air-gaps, the number of coil turns and the instantaneous value of the current.

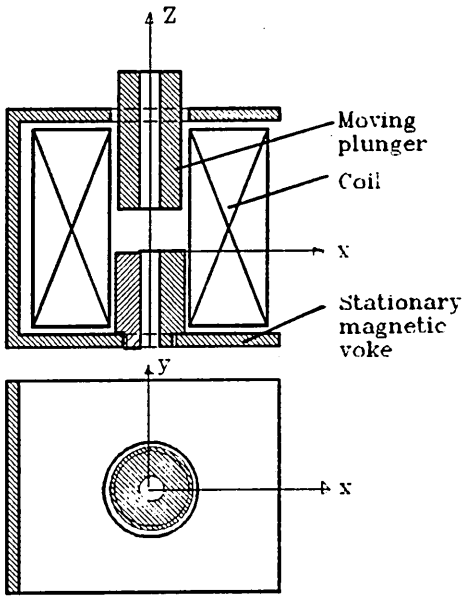

Figure 2 Circuit breaker solenoid actuator

The prediction of the dynamic characteristics of the electromagnetic actuator involves determining the relationships between the coil excitation current,i(t), electromagnetic force,F(t), plunger displacement, z(t), and the velocity of the trip mechanism, v(t), at different times,t.

From the schematic and equivalent electric circuit for the solenoid magnet (fig 1), the electric and magnetic coupled circuit equation is

$$u(t) = iR + \frac{d\psi}{dt} \quad (4)$$

where:

u is the coil applied voltage;

i is the coil current;

R is the total circuit resistance; and

$\psi=\psi(i,z)$ is the coil flux linkages.

The dynamic equation for the system is

$$F_e = m\frac{d^2z}{dt^2} + c\frac{dz}{dt} + F_o \quad (5)$$

where:

Fe=Fe(i,z) is the magnetic force on the plunger obtained from equation(1);

z is the displacements of plunger(armature);

m is the mass of the plunger and trip mechanism;

c is the viscous damping coefficient;

Fo is the spring load force.

and the velocity of the armature is

$$v = \frac{dz}{dt} \quad (6)$$

The corresponding dynamic equations are presented in the form of the following first order differential equations

$$\frac{d\psi}{dt} = u - iR$$

$$\frac{dv}{dt} = (F_e - cv - F_o)/m \quad (7)$$

$$\frac{dz}{dt} = v$$

where the initial conditions are given as;

$\psi|_{t=0}=0$; $i|_{t=0}=0$; $z|_{t=0}=0$;

$Fe|_{t=0}=0$; $Fo|_{t=0}=Fo$; $v|_{t=0}=0$

Fo is the initial opposing force acting on the armature.

The method of solving these equations and boundary conditions involves determining the electromagnetic force Fe(i,z) and flux linkage $\psi(i,z)$ for a range of currents and displacement values which are first stored in the form of data tables. The functions $i=i(\psi,z)$, $Fe=F(\psi,z)$ are required to solve the dynamic equations directly. Therefore the derived data tables $\psi(i,z)$ and F(i,z) from TOSCA are transposed in the form of the look-up data tables,$i(\psi,z)$ and $F(\psi,z)$, for direct insertion into the dynamic difference equations. The first order differential equations are then solved by the the Runge-Kuta method.

IV RESULTS

The computed and measured mechanical force required to trip the toggle mechanism of the circuit breaker is shown in figure 3. The eddy currents in the cores and plunger have been neglected in the computation. Although the figure shows that the measured and calculated static forces are in close agreement. However when the airgap is small, the relative errors between the measured and calculated forces increase due to saturation of the core.

Figure 4 shows the measured forces when the current is held constant and while it is changing at a rate of $0.107 Am^{-1} s^{-1}$, for airgaps of 10mm and 15mm. It can be seen from the figure that the forces differ, because the eddy currents in the cores and plunger exist when the current is changing with time. Since the difference is small, however, it follows that the computed forces using TOSCA can be used to predict the dynamic performance for all practical purposes.

The coil current and corresponding plunger displacement were measured under test with a supply voltage of 110v given a varying spring load force (Fig 3 curve 2), a coil resistance, 60.5Ω, and 3150 turns. The corresponding operating characteristics are given in figure 5 from which it is noticeable that the measured operating time of the actuator is slightly longer than the computed value, due to the existence of eddy currents in the core.

Figure 6 shows the measured and computed dynamic characteristics of the armature at the minimum threshold operating voltage. The correlation is good since the measured threshold coil operating voltage was 57.7V d.c.and the computed threshold voltage was 49V d.c.

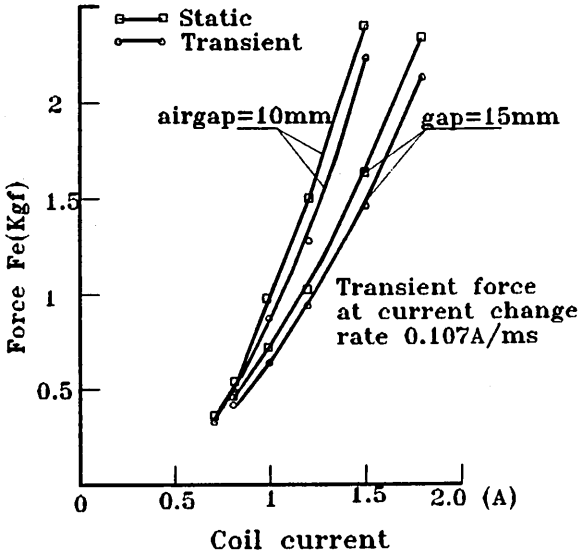

Figure 4 Comparison between static force and transient force at different airgaps

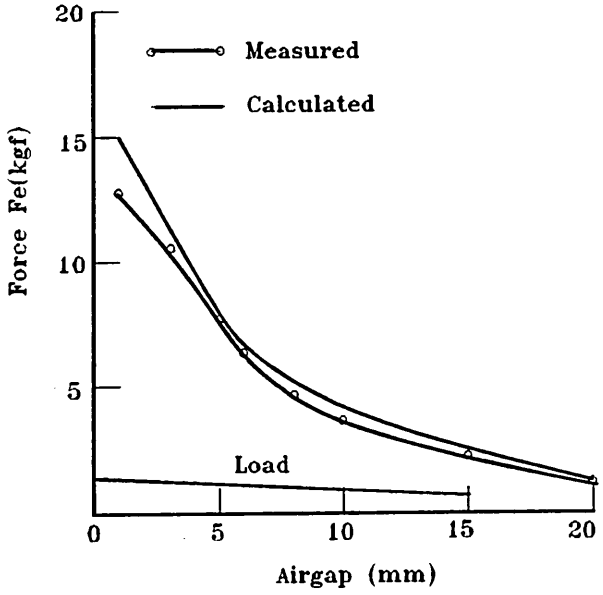

Figure 3 Electromagnetic force on the plunger against the movement displacement

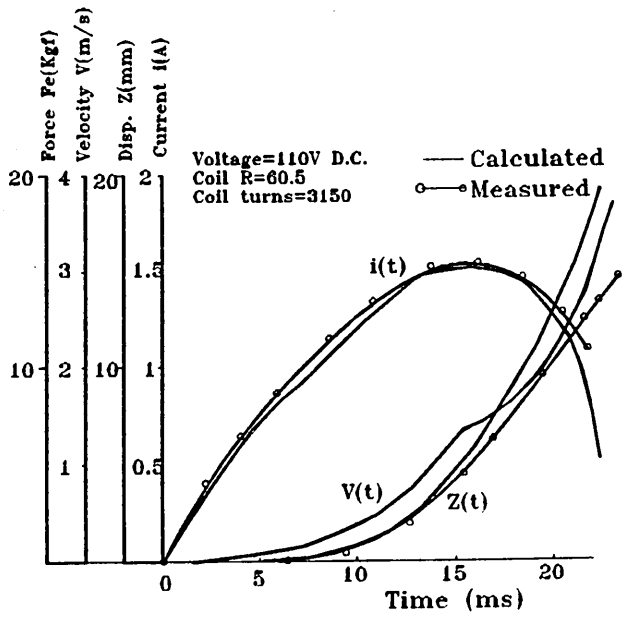

Figure 5 Operating characteristics of solenoid actuator at voltage supply of 110V

Figure 7 shows the operating time of the actuator for different supply voltages. This figure shows that when reducing the supply voltage, the response time of the plunger will increase and that when the supply voltage falls below the threshold voltage , the actuator can not be closed.

V CONCLUSIONS

The 3D finite element method was used to predict the forces produced by a solenoidal actuator. The computed dynamic characteristics were in a good agreement with measured results. From the analysis, the transient forces are slightly smaller than the values corresponding to static current due to neglecting the effect of eddy currents in the TOSCA CAD program. The computed forces can however replace the transient forces to predict the dynamic performance without producing large errors. The decoupled FE CAD method is therefore useful to obtain the solution of the dynamic response of a solenoidal actuator in respect to all the design and control variables.

REFERENCES

[1] Li Erping, Chen Degui, "Numerical Analysis of the Transient Process for Currents Limiting Magnetic Drive Mechanism", ECAAA, Int Conf. Xi'an, May 1989

[2] Li Erping, A L Kidd and P M McEwan, "A Decoupled Integral-Finite Element CAD Method for Determining the Transient Response of Current -sensitive Electromagnetic Actuators", Proceedings of 25 UPEC'90, Vol.2, Aberdeen, September 1990

[3] L. Bompa, P. Schueller and J. C. Sabonnadire " Analysis and Synthesis of an Electromagnet used for Circuit Breaker Operation" IEEE Tran. on MAG. Vol. MAg-21 , No.6, 1985

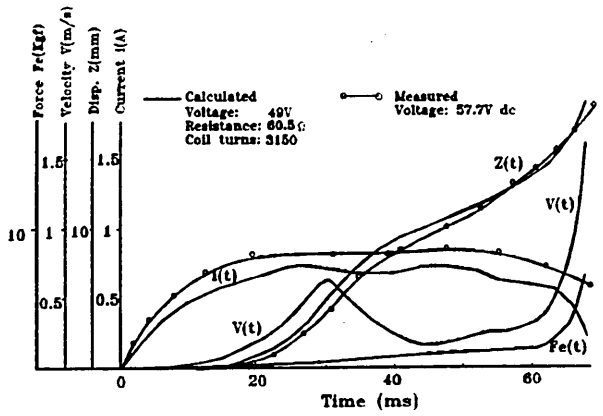

Fig. 6 Solenoid actuator dynamic performance under the threshold operating voltage

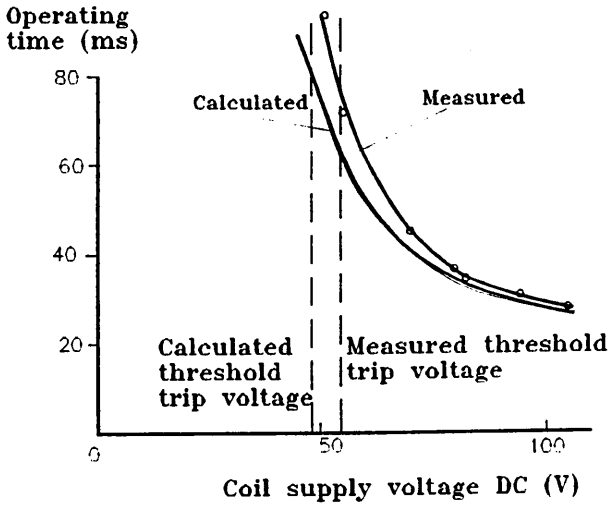

Figure 7 Relationship between operating time and coil supply voltage

Application of 3D Finite Element CAD Techniques in the Design of Current Sensitive Electromagnetic Actuators

Li Erping , P M McEwan
School of Engineering Information Technology
Sheffield City Polytechnic
Sheffield ,UK

A L Kidd
G H Scholes Ltd
Manchester
UK

Abstract: **The paper presents a method for evaluating and optimizing the design of an electromagnetic current-sensitive actuator, using a three dimensional CAD finite element package. The analysis enables the relationship of the actuator sensitivity to manufacturing tolerance, sinusoidal current and a wide range of design and control variables to be examined. The actuator sensitivity is quantified in terms of critical design factors for four practical actuators and a range of airgap settings. The results of all the studies correlated closely with the results from test and measurements.**

I INTRODUCTION

Electromagnetic actuators are used in a wide variety of applications. The types of interest in the reported studies are those which are required to operate with great precision at very low current(less than 30ma) and which are able to produce relatively high mechanical actuating forces(typically up to 0.6N). These actuators fall into the class of current-sensitive relays and have applications in accurately detecting leakage current in electrical systems and in protecting humans against the effects of electric shock.

These systems monitor the difference between the currents carried by the live and neutral conductors connecting a power supply to a load. When the currents are in balance the actuator remains inorperative. An imbalance of currents in the circuit causes current to flow into the control coil of the actuator and when the current exceeds a set value the actuator is designed to trip.

Studies of current-sensitive electromagnetic actuators[1,2] have demonstrated that the actuators performance is critically dependent upon the airgap size and the quality of the gap machined surfaces. The reported study is based on the use of the 3D FE-CAD (TOSCA)[3,4] software package for the determination of the dynamic performance and the optimization of the actuator design when subjected to sinusoidal current.

II CURRENT SENSITIVE ELECTROMAGNETIC ACTUATOR

The actuator general arrangement is shown in figure 1. The magnetic circuit consists of two yoke plates(4) and (5). The plates are separated by a layer of non-ferromagnetic material(6), which acts as a shunt path for the flux from the permanent magnet(1). The permanent magnet bridges the yoke plates, the polarisation strength and angular direction of which may be adjusted to change the electromagnetic force acting on the armature, by rotating the magnet about its N-S axis. The armature is held on the yoke machined faces by the force of attraction produced by the permanent magnet against the opposing force of spring 7.

The magnetic circuit has a constricted section denoted by x and x', which contains flux Φ_1 and Φ_2 from the permanent magnet and flux Φ_i produced by the coil when carrying current. The latter flux produces saturation in one of the constricted sections when current exceeds a specified value, the airgap flux then is diverted to the shunt path. The net flux in the airgap is then reduced which consequently reduces the force of attraction on the armature. The electromagnetic force therefore decreases as the coil current is increased until the armature opens under the action of the spring.

The sensitivity of the attraction force to the residual current in the coil can be varied by rotating the poles of a permanent

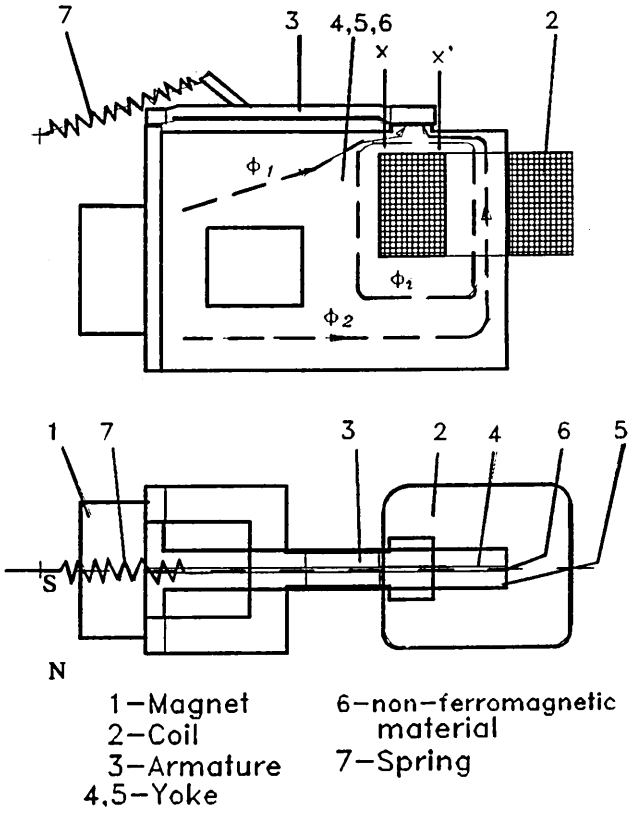

Figure 1 Current-sensitive electromagnetic actuator general arrangement

Manuscript received July 7,1991

magnet. The actuator sensitivity is dependent on many variables including the constricted slot cross section area and the shunt reluctance.

III NON-ENERGISED ACTUATOR PERFORMANCE

The non-energised state applies when the current in the coil is negligible. A 3D finite element analysis package [3,4] was used to solve the electromagnetic field distribution in the magnetic circuit to enable prediction of the force acting on the armature and its dependency on the actuator design parameters. The solution of the electromagnetic field is based on Maxwell's equations $\nabla \cdot B = 0$, $\nabla \times H = J$ and the material constituent relationship $B = \mu H$ which are solved by the two scalar potential finite element method. The magnetic force acting on the armature is determined by integration of Maxwell stress tensor over the armature outside surface.

The variation of the magnetic force with change of airgap is shown in Figure 2. Figure 2 shows the variation of the measured and computed magnetic force acting on the armature over a wide range of the permanent magnet displacement angle. These characteristics indicate the need to adjust the displacement angle to between 40^0 and 50^0 in order to minimise the sensitivity of the actuators to variations in airgap and also to retain the magnetic force (F_m) at 0.49N (2.3 times that of opposing force) in order to withstand the effect of mechanical shock.

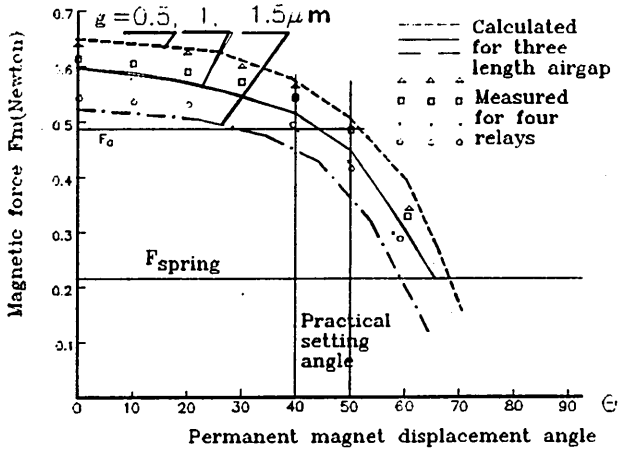

Fig 2 Measured and computed magnetic force acting on armature against magnet angular displacement for three airgap settings

IV ACTUATOR ENERGISED STATE

The energisation state occurs when the coil current is significant. Figure 4 shows the computed relationship between the electromagnetic force (Fe) acting on the armature and the forces (Fi) and (Fm) produced by control current and permanent magnet respectively for a magnetic displacement angle of 50^0. When a low value of sinusoidal current (curve 3 in fig. 3a) flows into the control coil, the force given by $Fe = F_m - F_i$ (curve 3 in fig.3c) is higher than the spring force, thus the armature remains closed on to the yoke plate. For a slightly larger sinusoidal trip current (curve 2 in fig. 3a), at its peak value ,the force approaches the level of the opposing spring force. At the moment the two forces are equal, the armature starts to move under the action of the opposing spring force at which instant the force (Fe) will reduce slowly to zero. However, if the current is only slightly increased (curve 1 figure 3a), the force(Fe) dramatically decreases to the trip level at approximately 3ms as shown in figure 3(c). This variation in performance indicates the precision to which the actuator sensitivity can be set in relation to the trip current setting.

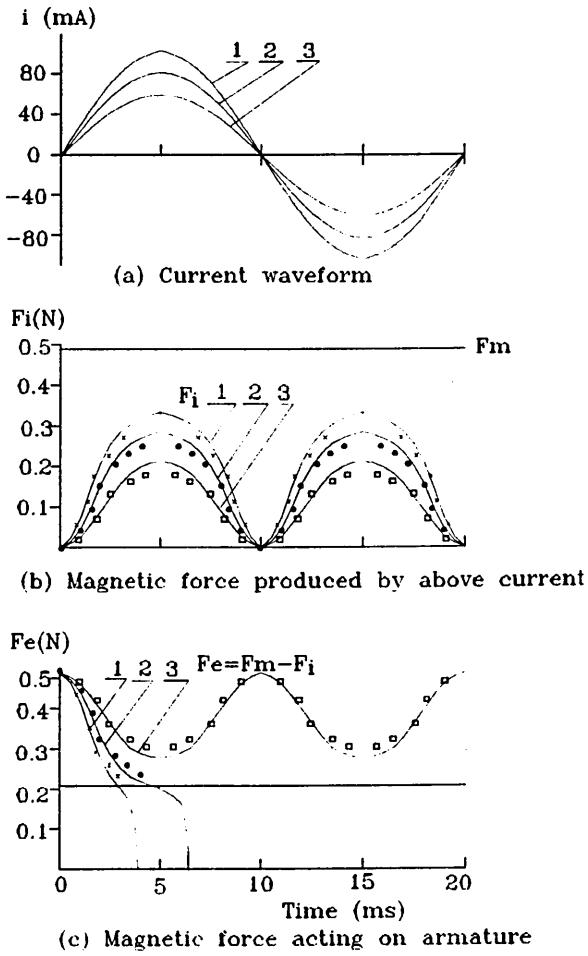

—— Calculated • x □ Measured

Fig. 3 Variation of energised magnetic force with sinusoidal 50Hz current

V ACTUATOR TRIPPING CHARACTERISTICS

The actuator tripping characteristics shown in figure 4 indicate the variation of the trip current with magnet alignment for four actuator designs which confirm the spread of characteristics typically due to manufacturing tolerances. The figure also indicates the practical need to set the displacement angle between 40^0-50^0, where the curves converge, to enable consistent tripping and minimum sensitivity to manufacturing tolerances. The correlation between the measured and computed results is good and confirms industrial test practice for setting the magnet displacement angle. It furthermore highlights the critical dependency of the actuator performance on high precision manufacture and on how practical tolerances can be permitted without producing excessive variations and inconsistency of performance.

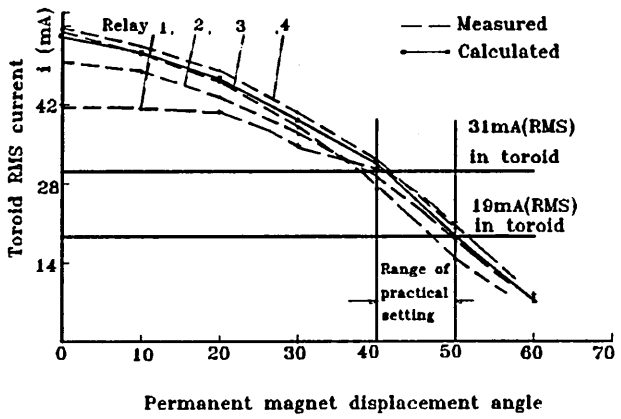

Fig. 4 Trip current versus magnet displacement angles for given four production actuators

VI OPTIMIZATION OF THE ACTUATOR

A. Influences of Shunt Reluctance on Sensitivity

The critical dependency of the actuator sensitivity upon airgap tolerance has been presented above, however, the actuator's other design parameters, such as the shunt reluctance, constricted slot, contact surface and material properties also have a significant effect on the actuator's sensitivity. These other parameters therefore were also investigated to obtain the optimal design.

The value of the shunt reluctance greatly influences the diversion of the flux away from airgap into the shunt path during energisation, which consequently significantly affects the sensitivity of the actuator to control current. The shunt reluctance can be expressed in terms of a factor Ks, which is the ratio of the distance between the two yoke plates to the face-to-face area of plates (see fig. 1). Figure 5 shows the sensitivity, expressed as the change of force ΔF to control ampere turns, $\Delta F/AT$, against the factor Ks. It is observed from the figure that the highest sensitivity occurs between, ks=0.5-1$\mu m/mm^2$, which thus gives the optimal design point of the shunt reluctance.

B. Constricted Slot to the Sensitivity

As described earlier, the area of the constricted section considerably affects the force on the armature due to slot saturation, when the coil carries current. This effect is shown in figure 6 where the constricted section is expressed in terms of a factor, Ko, which is the ratio of slot area to its length. The magnetic force of attraction on the armature increases with increase of the slot factor, whereupon it approximates to a constant value, since a large area of slot diverts more flux to the airgap. A optimum value of the force occurs for a value of slot factor, Ko=0.6. The reason for this result is that over-saturation occurs at small slot factors and the nonsaturation occurs at large slot factors, both of which lead decreasing sensitivity.

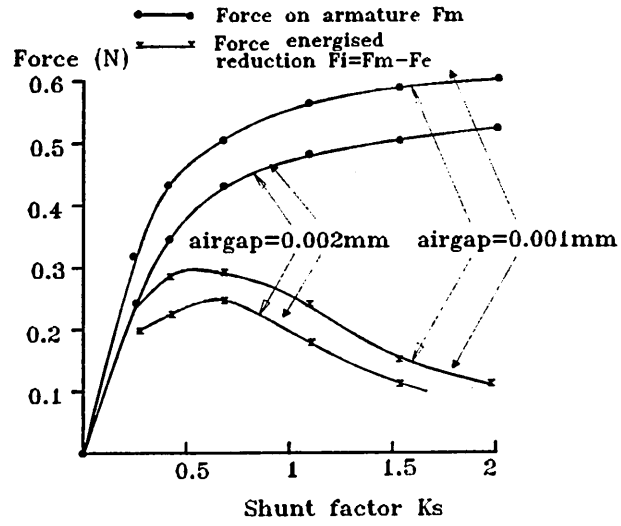

Fig. 5 Force sensitivity as function of shunt factor Ks

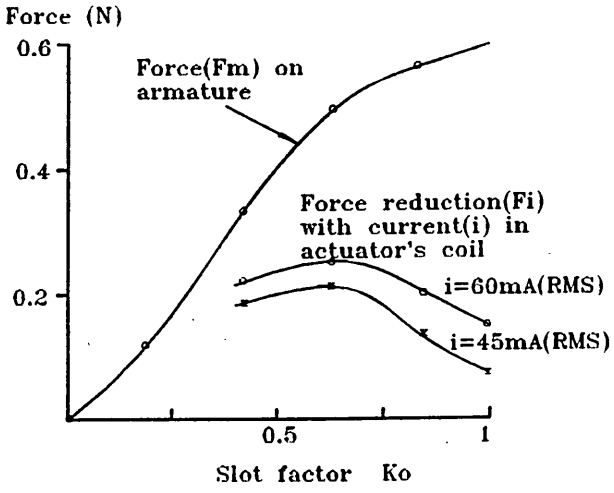

Fig. 6 Force sensitivity as function of slot factor Ko

C. Influence of the Contact Surface Area on the Sensitivity

The sensitivity of the actuator is significantly affected by the excitation MMF of the permanent magnet. Generally, the smaller the MMF the higher is the sensitivity. In the design, therefore, the lowest MMF is to be desired. Figure 7 shows the relationship between source MMF required to produce a force of attraction on the armature (typically,0.5N) and the contact surface area for four different values of airgap with constant constricted section. The greater source MMF is required to produce a force of 0.5N with smaller contact surface for airgaps larger than 0.002mm as is to be expected. However an inverse relationship is obtained for airgap lengths less than 0.001mm and contact areas larger than 1mm^2. The latter result is mostly applicable in the design of current sensitive electromagnetic actuators.

D. Comparison of the Tripping Characteristics

A comparison of the tripping characteristics was made for two production types of current sensitive actuator. The relevant design data are given in the Table 1 for the two types, the construction being as shown in figure 1. The design parameters of type II are based on the above presented optimal approach.

Type	Ks	Contact surface (mm^2)	Slot factor ko	Coil turns
I	0.75	1.52	0.65	20
II	0.5	1.28	0.64	20

Figure 8 shows the variation of electromagnetic force acting on the armature when energised for both types of actuator. It is observed that the decline in the force for type II is greater than that of type I for the same value of tripping current. As a consequence the type II actuator requires a lower tripping current, and is therefore more sensitive to current than type I, and therefore is a more effective current-sensitive electromagnetic actuator.

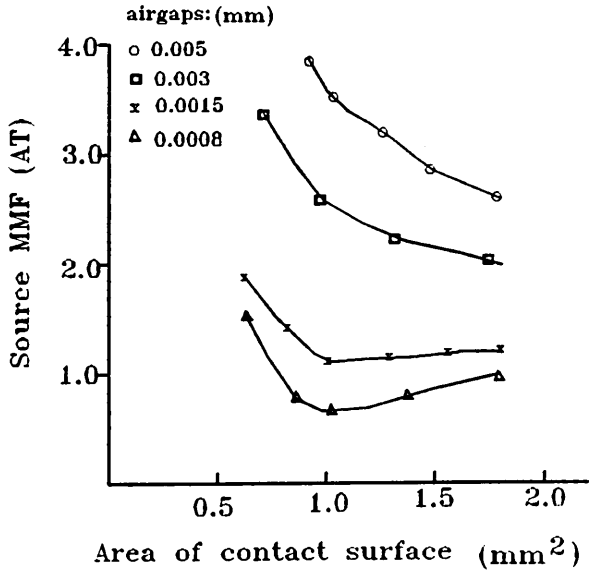

Fig. 7 Relationship between the source MMF and area of contact surface for an magnetic force=0.5N

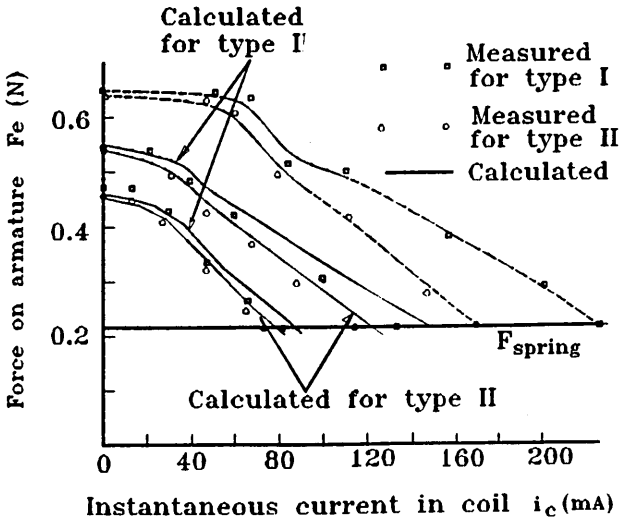

Fig. 8 Variation of computed and measured force on armature with coil current for two types of actuator

VII CONCLUSIONS

The three dimensional finite element CAD TOSCA program was used to accurately predict the operating characteristics of a clapper type current-sensitive actuator for a wide range of manufacturing tolerances. This prediction and analysis highlighted some peculiar features of the particular design which were known about but were not fully understood.

The analysis permitted characterisation of the performance of the actuator in terms of the critical design and control variables. The results were analysed in detail and the sensitivity of actuator for a wide range of design variables and for 50Hz trip current, was presented. All the analytical results correlated very closely with the results of tests and measurements. The presented optimization studies enabled the dependency of the critical dimensions and control variables on the actuator sensitivity to be evaluated, which were examplified for two types of actuator design.

REFERENCES

[1] Li Erping, A L Kidd and P M McEwan, " CAD Design of Curren-Sensitive
Electromagnetic Actuators", Proceedings of 4th int. Sym. on Short-circuit
Currents in Power Systems, Liege, September 1990

[2] Li Erping, A L Kidd and P M McEwan, "A Decoupled Integral-Finite
Element CAD Method for Determining the Transient Response of Current
-sensitive Electromagnetic Actuators", Proceedings of 25th Universities
Power engineering Conf. Aberdeen, September 1990

[3] C.S. Biddlecombe and C.P. Riley, "Postprocessing of 3 Dimensional
Electromagnetic Field Calculations" IEEE Trans. on Magnetics, VOL. 24, No.1 ,1988

[4] TOSCA Manual, Vector Field Ltd, 1989